QUANTUM LIQUIDS AND QUANTUM CRYSTALS

Vortex momentum density and invariants of the hydrodynamic equations of superfluidity and superconductivity

G. A. Kuz'min

*Institute of Thermal Physics, Siberian branch of the Russian Academy of Sciences, 630090 Novosibirsk, Russia**

(Submitted May 12, 1998; revised August 11, 1998)
Fiz. Nizk. Temp. **25**, 3–8 (January 1999)

The gauge transformation of the hydrodynamic equations of superfluidity and superconductivity is considered. The vortex and heat momentum densities are defined and their evolution equations are derived. The physical meaning of these quantities is analyzed. The Lagrangian invariants of the new set of equations, which are similar to those obtained by Hollman for classical hydrodynamics, are derived. © *1999 American Institute of Physics.* [S1063-777X(99)00101-2]

1. INTRODUCTION

Macroscopic properties of superfluid and superconducting systems are described by equations analogous to the hydrodynamic equations. Classical equations for an ideal fluid possess a set of invariants which include integral (energy, momentum, angular momentum, helicity[1]) as well as local invariants. The most common among these are the Lagrangian and freeze-in invariants.

The Lagrangian invariants are preserved along the trajectories of fluid particles. The ratio ω/ρ of vorticity to the density defines another type of invariants, viz., the field frozen into an ideal fluid.[1] Moiseev *et al.*[2,3] have proposed methods for obtaining new integrals of freeze-in and Lagrangian invariants from known invariants. A wide range of invariants was determined by Hollman.[4] These invariants are obscure in Euler equations, but are revealed in the Weber representation.

Earlier, we carried out[5,6] a gauge transformation of the classical hydrodynamics equations, which were presented in a form clearly admitting the presence of many additional invariants. In the particular case of the equations of hydrodynamics of a homogeneous incompressible fluid, the transformation involves a transition from the conventional momentum density $\rho\mathbf{v}$ to the vortex momentum density $\mathbf{q}$ which differs from $\rho\mathbf{v}$ by the gauge function gradient. The new form of equations has a number of advantages that are manifested during simulation of vortices, waves and their interaction.[7]

Equations for the field $\mathbf{q}$ were also derived by Oseledets[8] and Buttke[9] and have been used for computing various flows.[10,11] For a complete reflection of the geometrical meaning of the equations, the theory was also reformulated in terms of differential forms.[12,13] A more complete review of the problem and an extensive list of references can be found in Refs. 12–14.

A superfluid liquid also moves in the form of vortices and waves. The mechanics of such a liquid is described by two velocity fields, and there are two types of vortices and waves. The evolution of such a complex system may be regular or random. The latter case is associated with quantum turbulence.[15] As in the case of classical hydrodynamics, it is expedient to use the gauge transformation of equations and the existing invariants of motion in a theoretical analysis of the interaction of superfluid vortices and waves.

In this work, we consider the analogs of the classical vortex momentum,[1] i.e., vortex and heat momentum of a superfluid and superconducting liquid. Equations for the density of these quantities are derived, their invariants of motion are determined and the decomposition of complete motion into vortices and waves is analyzed for an arbitrary nonlinearity. The hydrodynamic model of superconductivity is considered from analogous positions.

2. DENSITY OF VORTEX MOMENTUM IN AN INCOMPRESSIBLE FLUID

We shall call a bounded vorticity cloud a vortex in this work. Vorticity patches induce in the surrounding space velocity fields $\mathbf{u}(\mathbf{r},t)$ which decrease in proportion to a power of the separation from the vortices. The momentum $\int \rho\mathbf{u}dV$ and the angular momentum of the vortex are defined by diverging integrals since the rate of decrease of integrands at infinity is insufficient. In order to obtain finite integral characteristics of vortices, certain infinite constants have to be subtracted. The finite quantities obtained as a result are expressed in terms of the vorticity field ω and are called the vortex momentum $\mathbf{p}$ and the vortex angular momentum $\mathbf{J}$[1,16]:

$$\mathbf{p}=\frac{1}{2}\int \mathbf{r}\times\omega\, dV,$$
$$\mathbf{J}=\frac{1}{3}\int \mathbf{r}\times(\mathbf{r}\times\omega)dV. \tag{1}$$

Let us determine the distribution of these characteristics in space. The integrand in Eqs. (1) cannot be treated as the

Lamb's vortex momentum density since, at the point where a certain liquid particle is located, $\mathbf{r}\times\omega$ depends on the origin of coordinates. According to Batchelor,[1] $\mathbf{p}$ is equal to the force impulse required for instant generation of the given motion from the state of rest. Similarly, $\mathbf{J}$ is equal to the angular momentum of the force impulse.

Consequently, we can associate a vortex patch bounded in space with the density $\mathbf{q}(\mathbf{r},t)$ of the force impulse, which is bounded in space and is called the vortex momentum density.[5] Its value at a given point does not depend any longer on the origin. The velocity is equal to the solenoidal component of the vortex momentum density. It differs from $\mathbf{q}(\mathbf{r},t)$ by the gradient of a certain gauge function. Hence, a transition from $\mathbf{u}(\mathbf{r},t)$ to $\mathbf{q}(\mathbf{r},t)$ can be treated as a change in the gauge of the hydrodynamic field.

The separation of the solenoidal component induces potential ''tails'' of the velocity field in the surrounding homogeneous liquid. It is obvious that the hydrodynamic structures can be described more locally in this case than in terms of the velocity field. Exaggerating slightly, we can state that the vortex momentum field is just the velocity $\mathbf{u}(\mathbf{r},t)$ divested of its potential ''tails.'' This idea can be extended to a stratified[6] and compressible fluid. In such cases, the total motion can be decomposed into the density of Lamb's momentum (which is equivalent to the force impulse required for instant generation of the non-wave component of motion) and waves. It is expedient to develop this concept for superfluid liquids also.

3. HYDRODYNAMICS OF SUPERFLUIDITY

Two-velocity hydrodynamic equations are used for a macroscopic description of superfluid helium. If we choose the velocities $\mathbf{v}_n$ and $\mathbf{v}_s$ of the normal and superfluid components, the density ρ and the entropy density per unit mass s as the complete set of variables, the complete system of equations of motion can be presented in the form[17]

$$\frac{\partial\rho}{\partial t}+\nabla\cdot(\rho_n\mathbf{v}_n+\rho_s\mathbf{v}_s)=0,$$

$$\frac{\partial\rho_s}{\partial t}+\nabla\cdot(\rho s\mathbf{v}_n)=0, \tag{2}$$

$$\left(\frac{\partial}{\partial t}+\mathbf{v}_s\cdot\nabla\right)\mathbf{v}_s=-\nabla\mu, \tag{3}$$

$$\frac{\partial\rho_n v_{ni}+\rho_s v_{si}}{\partial t}+\frac{\partial}{\partial x_j}(p\,\delta_{ij}+\rho_n v_{ni}v_{nj}+\rho_s v_{si}v_{sj})=0, \tag{4}$$

where $\rho_n+\rho_s=\rho$. Dissipative terms are not taken into account since they are defined by the specific models which are insignificant for the main subject of this communication. Their inclusion in the analysis complicates the formulas and may be done at a later stage. We assume that the equations of state that express the density ρ_n, pressure p, and the chemical potential μ in terms of ρ, s and $(\mathbf{v}_n-\mathbf{v}_s)^2$ are known.

Instead of the equation (4) for the total momentum, we shall use below the equation $w=\rho_n(\mathbf{v}_n-\mathbf{v}_s)/s\rho$, which describes, among other things, *heat vortices* (see Ref. 17):

$$\frac{\partial w_i}{\partial t}+(\mathbf{v}_n\cdot\nabla)w_i=-\frac{\partial T}{\partial x_i}-w_j\frac{\partial v_{nj}}{\partial x_i}+[\mathbf{w}\times(\nabla\times\mathbf{v}_s)]_i, \tag{5}$$

where T is the temperature.

It is usually assumed in the hydrodynamics of superfluid liquids that the velocity of the superfluid component is of the potential type everywhere (probably, except the axes of superfluid vortices: $\nabla\times\mathbf{v}_s=0$. Hence we shall disregard the last term on the right-hand side of Eq. (5). At first, Eqs. (2), (3), and (5) are considered in the framework of classical mechanics. Then the quantization conditions are imposed.

4. HEAT MOMENTUM DENSITY

Let $\delta\mathbf{l}$ be an element of length and $\delta\mathbf{S}$ a surface element which move with a fluid having the velocity field $\mathbf{v}$. It is well known[1] that the time evolution of the elements $\delta\mathbf{l}$ and $\delta\mathbf{S}$ is described by the equations

$$\frac{d\,\delta\mathbf{l}}{dt}=(\delta\mathbf{l}\cdot\nabla)\mathbf{v},\quad \frac{d\rho\,\delta S_i}{dt}=-\rho\,\delta S_j\frac{\partial v_j}{\partial x_i}, \tag{6}$$

where ρ is the density of the fluid. It is also known that the frozen-in fields w are similar to $\delta\mathbf{l}$. It will be proved below that $\mathbf{w}$ evolves in the same way as $\rho\delta\mathbf{S}$ under appropriate gauging. This imparts a geometrical meaning to w, and the algorithm for the quest of Lagrangian invariants becomes obvious.

The vector field $\mathbf{w}$ can be decomposed (to within a harmonic function) into the curl $\mathbf{w}_{\rm curl}$ and the divergence $\mathbf{w}_{\rm div}$ components. In an unbounded liquid which is at rest at infinity, the harmonic correction is zero, and the decomposition can be carried out by using the projection integral operators $\hat{\Pi},\hat{Q}$ whose kernels are given by

$$\Pi_{ij}=-\frac{1}{4\pi}\frac{\partial^2}{\partial x_i\partial x_j}\frac{1}{|\mathbf{x}-\mathbf{x}'|},\quad \mathbf{w}_{\rm div}=\hat{\Pi}\mathbf{w},$$

$$Q_{ij}=\delta_{ij}\delta(\mathbf{x}-\mathbf{x}')-\Pi_{ij},\quad \mathbf{w}_{\rm curl}=\hat{Q}\mathbf{w}.$$

Here $\mathbf{w}_{\rm curl}$ is induced by the vorticity, and $\mathbf{w}_{\rm div}$ is induced by the divergence of the field $\mathbf{w}$. It is natural to associate heat vortices with the component $\mathbf{w}_{\rm curl}$ and the sound with the component $\mathbf{w}_{\rm div}=-\nabla\chi$.

Let us consider the field evolution equation $\mathbf{q}_w=\mathbf{w}+\nabla\psi(\mathbf{x},t)$, where $\psi(\mathbf{x},t)$ is a certain gauge function. If we additionally define this function by the condition

$$\left(\frac{\partial}{\partial t}+\mathbf{v}_n\cdot\nabla\right)(\psi+\chi)+T=0, \tag{7}$$

the equation for $\mathbf{q}_w$ assumes the form

$$\left(\frac{\partial}{\partial t}+\mathbf{v}_n\cdot\nabla\right)q_{wi}=-q_{wj}\frac{\partial v_{nj}}{\partial x_i}. \tag{8}$$

The field $\mathbf{q}_w$ is gauged by Eq. (7) and the initial condition for χ or $\mathbf{q}_w$. It can easily be seen that Eq. (8) coincides with Eq. (6) for $\rho\delta\mathbf{S}$. If we form the scalar product of the field $\mathbf{q}_w$ and the element of length $\delta\mathbf{l}$, we obtain a quantity

similar to an element of mass that is conserved along the Lagrangian trajectory. A direct verification shows that $(\partial/\partial t+\mathbf{v}_n\cdot\nabla)(q_w\cdot\delta\mathbf{l})=0$.

Having chosen an arbitrary contour in the fluid and divided it into a sum of small elements $\delta\mathbf{l}$, we find that the integral $\int\mathbf{q}_\omega\cdot\delta\mathbf{l}$ is conserved over any contour (which need not be closed) entrained by the fluid with a velocity $\mathbf{v}_n$. In the particular case of a closed contour, the circulations of the fields $\mathbf{q}_\omega$ and $\mathbf{w}$ coincide since these fields differ by the scalar function gradient. Hence circulation is conserved over a closed contour of the field $\mathbf{w}$. The overall method of construction of invariants is considered in Sec. 6.

The field $\mathbf{w}$ is found to be divided into two components, the first of which is defined by the field $\mathbf{q}_\omega$ and corresponds to the heat vortices. The second component is defined by the scalar field ψ and corresponds to waves. The motion of the superfluid component will be considered in the following section.

5. VORTEX MOMENTUM DENSITY OF THE SUPERFLUID COMPONENT

Using transformations analogous to the ones carried out above, we can write Eq. (3) for the superfluid component in the form

$$\left(\frac{\partial}{\partial t}+\mathbf{v}_s\cdot\nabla\right)q_{si}=-q_{sj}\frac{\partial v_{sj}}{\partial x_i},$$

$$\left(\frac{\partial}{\partial t}+\mathbf{v}_n\cdot\nabla\right)(\chi_s+\psi_s)=-\mu+\frac{v^2}{2},$$

where $\nabla\chi_s=\hat{\Pi}\mathbf{v}_s$, $\mathbf{q}_s=\hat{Q}\mathbf{v}_s+\nabla\psi$. Calibration of fields is defined by the equation for $\chi_s+\psi_s$ and the initial conditions. Vortices of two types and waves are employed in the two-fluid hydrodynamics while superfluid vortices and waves are described by the fields $\mathbf{q}_s$ and χ_s.

6. LAGRANGIAN INVARIANTS

A comparison with Eq. (8) shows that $\mathbf{q}$ evolves in time in the same way as $\rho\delta\mathbf{S}$. Any field of quantities of this type is denoted by $\mathbf{q}$. Frozen-in fields existing in the liquid satisfy the equation for $\delta\mathbf{l}$. An example of such a field is ω/ρ, where $\omega=\nabla\times\mathbf{w}$. Fields similar to $\delta\mathbf{l}$ are denoted by $\mathbf{J}$. Fields of the third type, which are similar to an element of mass of the liquid $\delta m=\rho\delta\mathbf{S}\cdot\delta\mathbf{l}$, are ''Lagrangian invariants'' and are denoted by I.

This analogy shows (and direct computations prove) that any fields of the type $\mathrm{curl}(\mathbf{q})/\rho$ or $[\mathbf{Q}\times\mathbf{Q}']/\rho$ are frozen-in fields, the fields $\rho[\mathbf{J}\times\mathbf{J}'],\nabla I$ belong to the $\mathbf{q}$ type, while $\mathrm{div}(\rho\mathbf{J}/\rho),(\mathbf{j}\cdot\mathbf{q})$ are Lagrangian invariants I. Using these relations, we can obtain new fields of the same type from known fields of the type $\mathbf{J}$, $\mathbf{Q}$, and I. In this way, fields similar to the Hollman invariants[4] can be obtained.

7. PHYSICAL INTERPRETATION AND QUANTIZATION CONDITIONS

The interpretation of a vortex momentum as a force impulse required for the generation of the given motion from the state of rest is also possible in the case of a superfluid liquid. For a two-velocity medium, two types of external agencies are required. Mass forces generate the total motion of the components. The relative motion (heat vortices) are generated by thermal agencies.

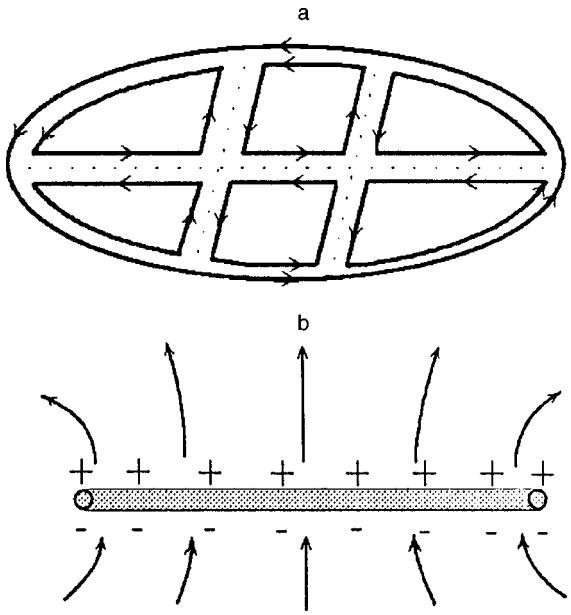

FIG. 1. Replacement of a vortex loop by a system of small vortex loops (b). Side view (a). Equivalent replacement of flow by the double layer potential. The dipole moment density corresponds to the field $\mathbf{q}_s$.

The connection between the vorticity and the vortex momentum density can be explained by using the following simple example. Let us consider the motion of a classical incompressible liquid generated by an impact on a membrane placed in it. The membrane is then removed. A thin vortex tube is formed near the membrane edge. The density of the corresponding vortex momentum is equal to the distribution of the force impulse on the membrane.

Let us consider the inverse problem. Let a closed vortex loop of intensity κ be a source of velocity (see Fig. 1). We divide the surface stretched over this loop into small area elements and place a vortex tube of the same intensity κ along the perimeter of each element. Each vortex loop has the vortex momentum $\rho\varkappa\delta\mathbf{S}$, where $\delta\mathbf{S}$ is the area. Since the vorticity on segments lying within the main loop are mutually compensated, the total flux induced by small loops coincides with the initial field of the flow. The surface can be deformed arbitrarily, which leads to gauge freedom of the vortex momentum density (see Ref. 5 for details).

A similar construction can be carried out for the solenoidal components of the superfluid velocity and field $\mathbf{w}$. The circulation of the superfluid velocity is conserved. Following Onsager, we impose on it the quantization condition $\kappa=nh/m$, where n is an integer, m the mass of a helium atom, and h the Planck constant. The available experimental data are in accord with these assumption. According to the above relations, the vortex momentum density should also be regarded as quantized.

It can be seen from Fig. 1 that the distribution of the vortex momentum density in a superfluid flow can be put in

correspondence with a double layer. The state of a weakly nonideal Bose gas is described by an averaged wave function[17] $\Psi=\sqrt{\rho_s}\exp(i\psi_s)$, the superfluid velocity being proportional to the phase gradient: $\mathbf{v}_s=(h/m)\nabla\psi_s$. In order to define the wave function unambiguously, it is necessary that the phase change by a multiple integer of 2π upon a circumvention of the vortex loop. Consequently, the phase is not single-valued. In order to make it single-valued, we must make a cut. The phase jump appearing at the cut is proportional to $\mathbf{q}_s$. Since the position of the cut surface can be varied arbitrarily, $\mathbf{q}_s$ possesses gauge freedom which can be eliminated by fixing the initial conditions.

The circulation of the field $\mathbf{w}$ is also preserved, but the available experimental data are not sufficient to assume that any quantization conditions are satisfied for it.[17] Consequently, the heat momentum density $\mathbf{q}_\mathbf{w}$ is not quantized. By choosing the gauge properly, we can make it equal to zero outside the regions where the vorticity of the field $\mathbf{w}$ differs from zero (cf. Refs. 5 and 6). In the given case, the field $\mathbf{q}_w$ can be put in correspondence with a layer of heat dipoles. The combination of the force impulse and heat momentum generates a vortex momentum of the superfluid component.

8. TYPE II SUPERCONDUCTIVITY

Hydrodynamic equations for the electron liquid in a type II superconductor are similar to those considered above, Superfluid vortices correspond to fluxoids, viz., quantized magnetic flux tubes. The equation for the superfluid component of the electron liquid has the form (see Refs. 17 and 19)

$$\left(\frac{\partial}{\partial t}+\nabla\cdot\mathbf{v}_s\right)\mathbf{v}_s=-\nabla\mu-\nabla H+\frac{e}{m}\left(\mathbf{E}+\frac{1}{c}\mathbf{v}_s\times\mathbf{B}\right),$$

where $\mathbf{B}$ is the magnetic field, c the velocity of light, and H the nonequilibrium correction to the chemical potential. Its form is immaterial for the subsequent analysis.

Let Φ and $\mathbf{A}$ be the scalar and vector potentials of the electromagnetic field $\mathbf{B}=\nabla\times\mathbf{A}$, $\mathbf{E}=-\nabla\Phi-(1/c)(\partial\mathbf{A}/\partial t)$. If $\mathbf{v}_s+(e/mc)\mathbf{A}=\nabla\chi$, we have

$$\frac{\partial\chi}{\partial t}+\mu+\frac{1}{2}v_s^2+\frac{e}{m}\Phi+H=\text{const}. \tag{9}$$

This equation resembles Bernoulli's law. Let us now suppose that

$$\mathbf{v}_s=\mathbf{q}_s-\frac{e}{mc}\mathbf{A}+\nabla\chi,$$

where χ satisfies condition (9). For $\mathbf{q}_s$, we have

$$\left(\frac{\partial}{\partial t}+\mathbf{v}_s\cdot\nabla\right)q_{si}=-q_{sj}\frac{\partial v_j}{\partial x_i}.$$

In complete analogy with the hydrodynamic equations for a superfluid liquid, this leads to invariants and quantization conditions for the field $\mathbf{q}_s$. In Fig. 1, the closed loop corresponds to a fluxoid. Superconducting current is equivalently generated by the fluxoid or by the field $\mathbf{q}_s$.

9. CONCLUSIONS

In terms of the vortex momentum density, the hydrodynamic equations of superconductivity and superfluidity acquire a clear geometrical meaning. These equations lead to directly the existence of many fields similar to an elementary area element, length, or a passive impurity. The existence of such fields restricts the evolution of the system of vortices and waves, which simplifies the theoretical analysis of the relaxation in a superfluid flow.

The vortex momentum density can be used in vortex models of phase transition to the superfluid state.[18] As the temperature increases from absolute zero, the emerging vortices become larger in size. The role of the smallest blocks is played by rotons,[19] viz. elementary quantum excitations of the vortex momentum density. According to the model,[18] scale-invariant distributions of such blocks are of special interest. It should be noted that Lagrangian invariants may influence the phase equilibrium in a moving continuum.[20]

The obtained invariants can also be useful in the case of a weak dissipation. Different invariants have different dissipation rates. This allows us to consider selective attenuation of some invariants for fixed values of other invariants, and to solve the appropriate variational problems.

This research was carried out under partial support from the Russian Foundation of Basic Research (Grants Nos. 98-01-00681 and 97-01-00773.

*E-mail: kuz'min@itp.nsc.ru

[1] G. K. Batchelor, *An Introduction to Fluid Dynamics* Cambridge Univ. Press, Cambridge (1967).
[2] S. S. Moiseev, R. Z. Sagdeev, A. V. Tur, and V. V. Yanovsky, Dokl. Nauk SSSR **258**, 318 (1981) [Sov. Phys. Dokl. **26**, 479 (1981)].
[3] S. S. Moiseev, R. Z. Sagdeev, A. V. Tur, and V. V. Yanovsky, Zh. Éksp. Teor. Fiz. **83**, 215 (1982) [Sov. Phys. JETP **56**, 117 (1982)].
[4] G. Hollman, Archiv für Meteorologie Geophysik und Bioklimatologie **A4**, 1 (1964).
[5] G. A. Kuz'min, Phys. Lett. **A96**, 88 (1983).
[6] G. A. Kuz'min, Zh. Prilk. Mat. Teor. Fiz. **4A**, 25 (1984).
[7] G. A. Kuz'min, Appl. Sci. Res. **51**, 429 (1993).
[8] V. I. Oseledets, Zap. Mosk. Matem. Obshch. **44**, 210 (1989).
[9] T. F. Buttke, in *Vortex Flows and Related Numerical Methods* (Ed. by J. T. Beale, G. H. Cottet, and S. Huberson), NATO ASI Series, vol. 395, Kluwer, Norwell (1993).
[10] T. F. Buttke and A. J. Chorin, Appl. Numer. Math. **12**, 47 (1993).
[11] R. Cortez, Ph.D Thesis, Univ. of California, Berkeley (1995).
[12] V. P. Goncharov and V. I. Pavlov, *Hydrodynamic Problems in Hamiltonian Description* [in Russian], Izd. MGU, Moscow (1993).
[13] A. V. Tur and V. V. Yanovsky, J. Fluid Mech. **248**, 67 (1993).
[14] U. Frisch, *Turbulence. Legacy of A. N. Kolmogorov*, Cambridge Univ. Press, Cambridge (1996).
[15] R. J. Donnelly and C. E. Swanson, J. Fluid Mech. **173**, 387 (1986).
[16] G. Lamb, *Hydrodynamics* [Russian trans.], GITTL, Moscow (1947).
[17] C. Patterman, *Hydrodynamics of Superfluid Liquid* [Russian transl.], Mir, Moscow (1974).
[18] G. A. Williams, Phys. Rev. Lett. **59**, 1926 (1987).
[19] R. Feynman, *Statistical Mechanics*, Benjamin, Reading, MA, 1972.
[20] G. A. Kuz'min, Izv. Ross. Akad. Nauk, Ser. Fiz. **4**, 48 (1995).

Translated by R. S. Wadhwa

Low-frequency impedance and heat capacity of $LuFe_4Al_8$

A. M. Gurevich, V. M. Dmitriev*), V. N. Eropkin, L. A. Ishchenko, N. N. Prentslau, and L. V. Shlyk

*B. Verkin Institute for Low Temperature Physics and Engineering, National Academy of Sciences of the Ukraine, 310164 Kharkov, Ukraine***)*

(Submitted July 10, 1998; revised August 7, 1998)
Fiz. Nizk. Temp. **25**, 15–24 (January 1999)

Temperature dependences of low-frequency impedance ($0–10^7$ Hz) and heat capacity of $LuFe_4Al_8$ are studied at low temperature in the intervals 4.5–300 K and 1.5–120 K, respectively. The observed singularities suggest that antiferromagnetic phase ordering occurs at $T_N = 100.5$ K. A sharp increase in the resistance is observed at a certain temperature $T_1 < T_N$ below which a negative magnetoresistive effect is detected in a weak magnetic field ($H < 50$ Oe). It is shown that the low- temperature anomalies at $T < 25$ K are associated with the superconducting transition. This is supported by the presence of the Meissner effect, levitation, a decrease in ohmic losses, as well as the influence of a static magnetic field and direct current on the resistance of the compound. A magnetostructural phase transition, which is assumed to occur at $T_1 < T_N$, may be responsible for the peculiarities observed in the physical properties of $LuFe_4Al_8$. © *1999 American Institute of Physics.* [S1063-777X(99)00301-1]

INTRODUCTION

The crystal structure and magnetic properties (susceptibility and magnetization) of ternary compounds of the type RM_4Al_8 (R stands for the rare-earth metals La, Ce, Pr, Nd, Sm, Gd, Tb, Dy, Ho, Er, Tm, Yb, Lu, as well as the elements Y and Th, while M denotes V, Cr, Mn, Fe, Co, Ni and Cu) were described by Buschow *et al.*[1–3] The magnetic structure of compounds like RFe_4Al_8 is distinguished by the fact that it contains three magnetic sublattices, viz., an R-sublattice and two M-sublattices. Hence, following Ref. 3, such materials can be divided into two groups, i.e., compounds in which only atoms of the Fe group have a magnetic moment (R denotes La, Ce, Lu, Th, and Y) and those in which the magnetic moment is possessed by M-atoms as well as R-atoms.

Materials of the first group experience antiferromagnetic ordering at Néel's temperature T_N which has a characteristic value for each one of them. Some compounds (in which R stands for La, Th) display a dependence of magnetization on a strong magnetic field H at $T < T_N$. It was shown[2] by considering YFe_4Al_8 as an example that a magnetic field of tens of kilooersted can destroy the antiferromagnetic structure at low temperatures.

An analysis of the results presented in Refs. 1–3 indicates that the investigated materials RFe_4Al_8 have a complex magnetic system that has not been studied extensively so far. This is evidenced if only by the fact that the values of the phase-transition temperature obtained by various methods differ considerably according to the available data. Hence it is expedient to carry out further investigations by using traditional methods of measuring magnetic parameters as well as the results of measurements of other characteristics like thermal and electrical properties.[4]

It was shown that a comparison of the results of measurements of heat capacity and low- frequency impedance of some complex compounds makes it possible to detect and explain the origin of anomalies in these properties.[5]

However, the available literature does not contain, to our knowledge, any information about the electrical and thermal properties of ternary compounds of the type RM_4Al_8.

In this paper, we present the results of experimental studies of the temperature dependence of low-frequency impedance of the compound $LuFe_4Al_8$ in weak magnetic fields as well as its heat capacity $C_p(T)$.

SAMPLES AND MEASURING TECHNIQUE

Samples of $LuFe_4Al_8$ were synthesized by inductive melting in a cold crucible in argon. The crystal structure of the obtained crystallites was determined by a four- circle diffractometer and was found to match with the available data.[1]

The surface resistance R_s in the rf range was measured by the resonance technique. Since the concept of surface resistance becomes meaningless for direct current, and its measurement at low frequencies is complicated, we also measured the total resistance Z (modulus of impedance) at low and radio frequencies by the four-probe method. The investigated samples of length up to 6 mm and cross-sectional area $1–10\,mm^2$ were obtained from the same monolithic polycrystal.

Figure 1a shows the apparatus used for measuring the total and surface resistance in a weak static magnetic field as well as in zero field over a wide range of temperatures.

The investigated sample *1* was fixed to the substrate *2* and placed in the cavity *3* of the inductance coil *4* of the measuring oscillatory circuit together with the temperature gauge. Coil *4* was placed in a copper screen *5* having solenoid *6* on its surface. The inductance coil with the sample

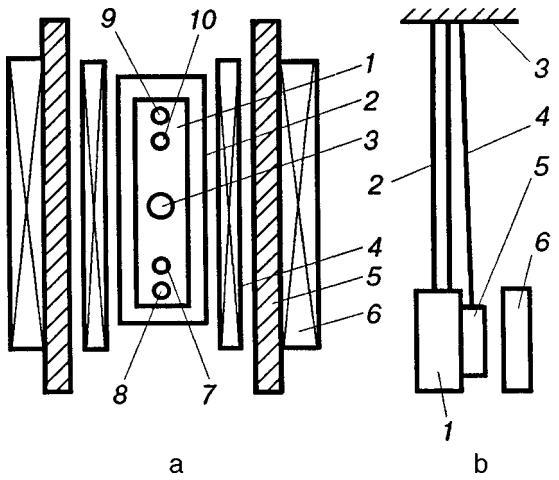

FIG. 1. Apparatus for determining impedance and surface resistance: sample (*1*), substrate (*2*), temperature gauge (*3*), Oscillatory circuit coil (*4*), screen (*5*), solenoid (*6*), current contacts (*8,9*), potential contacts (*7, 10*) (a), and for observing levitation of the sample: permanent magnet (*1*), rod (*2*), platform (*3*), thread (*4*), sample (*5*), and oscillatory circuit (*6*) (b).

could be oriented along any direction relative to the solenoid axis. Sample *1* was connected to external current circuits *8,9* and potential spring-loaded contacts *7,10* made of beryllium bronze. The apparatus shown in Fig. 1a is located in a system permitting a variation of the sample temperature from 4.5 to 300 K by the coolant vapor[6] with an error not exceeding ± 0.25 K in the range 30–300 K and ± 0.1 K below 30 K. The sample impedance Z was defined as the ratio of the amplitudes of the voltage across the samples and the current flowing through it.

While measuring R_s by the resonator technique, we determined ohmic losses taking into account the surface resistance of the standard sample.[7] For this purpose, a mould was prepared and filled with molten metal (indium) with a known surface resistance R_{se}. In turn, the value of R_{se} was checked by using another standard material with surface resistance R_{sd} (copper or aluminum annealed at an optimal temperature).

For investigating the weak dependence of resistance on such physical quantities as temperature T, frequency f, current I, or a static magnetic field H (by measuring Z or R_s within the limits of experimental error), we measured the same quantity repeatedly. The results of measurements were averaged.

While studying the effect of transport current on R_s of the material, we passed the current through contacts *9* and *8* (Fig. 1a) and determined the Q-factor of the circuit.

It will be proved below that the results of some measurements suggest the presence of an insignificant amount of superconducting phase in the compounds at $T<25$ K. In order to verify this, we tested the ability of a $LuFe_4Al_8$ to levitation in a static magnetic field with the help of the device shown in Fig. 1b.

A permanent magnet *1* was fixed rigidly to platform *3* through rod *2*. The sample *5* under investigation was suspended to the platform on thread *4* so that it was located between the magnet *1* and the coil *6* of the oscillatory circuit. As in Refs. 9 and 10, we used a silk fibre of diameter 7 μm as the thread. In contrast to the instrument described in Refs. 9 and 10, the sample in the device shown in Fig. 1b did not twist the thread during levitation, but inclined it, thus approaching coil *6*. The presence of levitation of the sample was detected from the change (decrease) in the Q-factor of the oscillatory circuit.

The temperature dependence of the heat capacity in the interval 1.5–120 K was studied by the method of absolute calorimetry. The experimental error did not exceed 0.5%. Polycrystalline samples having a mass of 2.5 g each were used for measuring heat capacity.

EXPERIMENTAL RESULTS

Heat capacity of $LuFe_4Al_8$

Figure 2a shows the temperature dependence of heat capacity C_p in the interval 1.5–120 K. Fragments of Fig. 2a are shown on a magnified scale in Figs. 2b and 3a.

It can be seen from the figures that at least four temperature intervals with heat capacity anomalies exist on a regular temperature dependence $C_p(T)$.

The first anomaly is observed in the form of ''spikes'' with an appreciable amplitude at temperatures 99–102 K. The peak of $C_p \approx 194.5$ J/mole·K corresponds to the temperature $T_N = 100.5$ K (see Figs. 2a and 3a). According to Buschow *et al.*,[3] the antiferromagnetic transition was detected from magnetic measurements just at this temperature.

The second group of C_p anomalies is also manifested as a series of ''spikes'' of heat capacity values relative to the regular dependence $C_p(T)$ at temperatures 75–90 K (see Figs. 2a and 3a).

The third series of anomalies in C_p is observed at temperatures 50–65 K, but the amplitude is much smaller than in the first and second groups (see Fig. 2a).

The fourth group of singularities of C_p below 30 K (see Fig. 2b) has the form of a few λ-shaped ''spikes.'' The maximum value of heat capacity $C_p = 1.9$ J/mole·K is observed at $T = 24$ K. At lower temperatures, heat capacity anomalies are less pronounced (see Fig. 2b), but their values are considerably larger than the experimental errors.

Temperature and frequency dependences of resistance

The impedance Z and the surface resistance R_s of $LuFe_4Al_8$ were measured in the frequency range 0–10^7 Hz and in the temperature interval 4.5–300 K.

Figure 4a shows the temperature dependences of the impedance of a $LuFe_4Al_8$ sample reduced to $T = 300$ K for the following values of the frequency f, Hz: 0 (curve *1*), 8×10^5 (curve *2*), 4×10^6 (curve *3*), and 10^7 (curve *4*). It can be seen that starting from room temperature up to 100 K, the samples exhibit a virtually linear dependence $Z(T)$ or $\rho(T)$. The dc resistivity of the samples $\rho(300) = 5 \times 10^{-5}$ $\Omega \cdot \mathrm{m}$: $\partial\rho/\partial T = 7.5 \times 10^{-8}$ $\Omega \cdot \mathrm{m} \cdot \mathrm{K}^{-1}$, and $(\partial\rho/\partial T)/\rho(300) = 1.5 \times 10^{-3}$ K^{-1} (curve *1* in Fig. 4a).

Figure 4b shows the $Z(f)$ dependence at 300 (curve *1*) and 95 K (curve *2*). The impedance Z of a sample with the cross-sectional area 3×3 mm is virtually independent of frequency for $0 \leqslant f \leqslant 10^5$ Hz, while for frequencies higher than

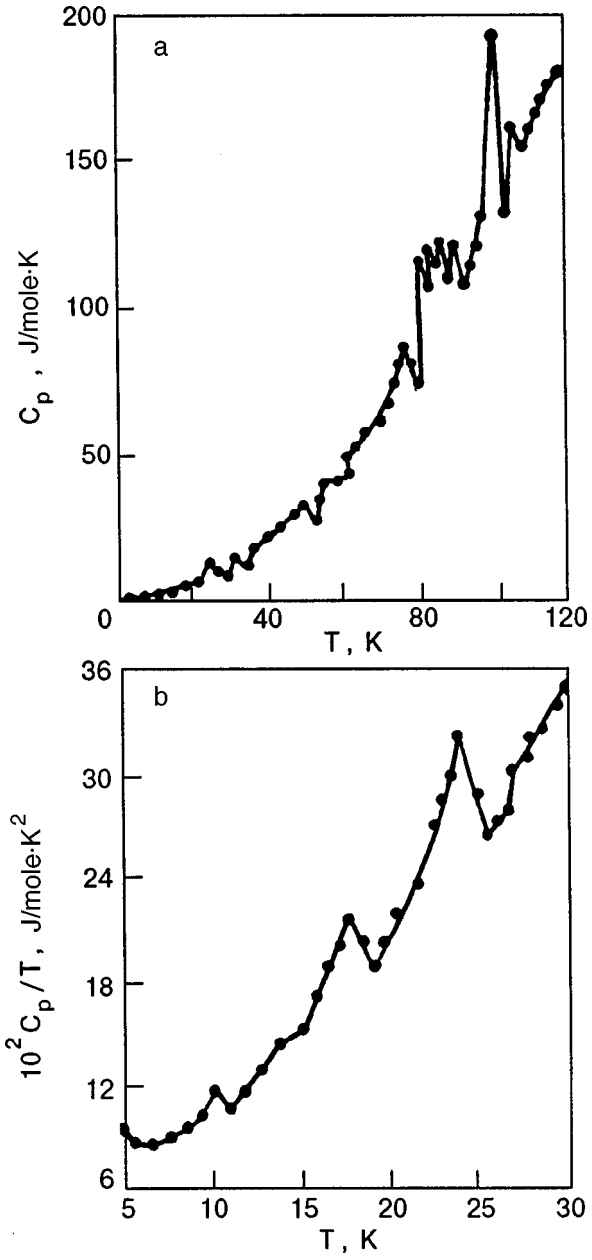

FIG. 2. Temperature dependence of the heat capacity of $LuFe_4Al_8$. (a) Region of heat capacity anomalies on the curve describing the temperature dependence of C_p/T (b).

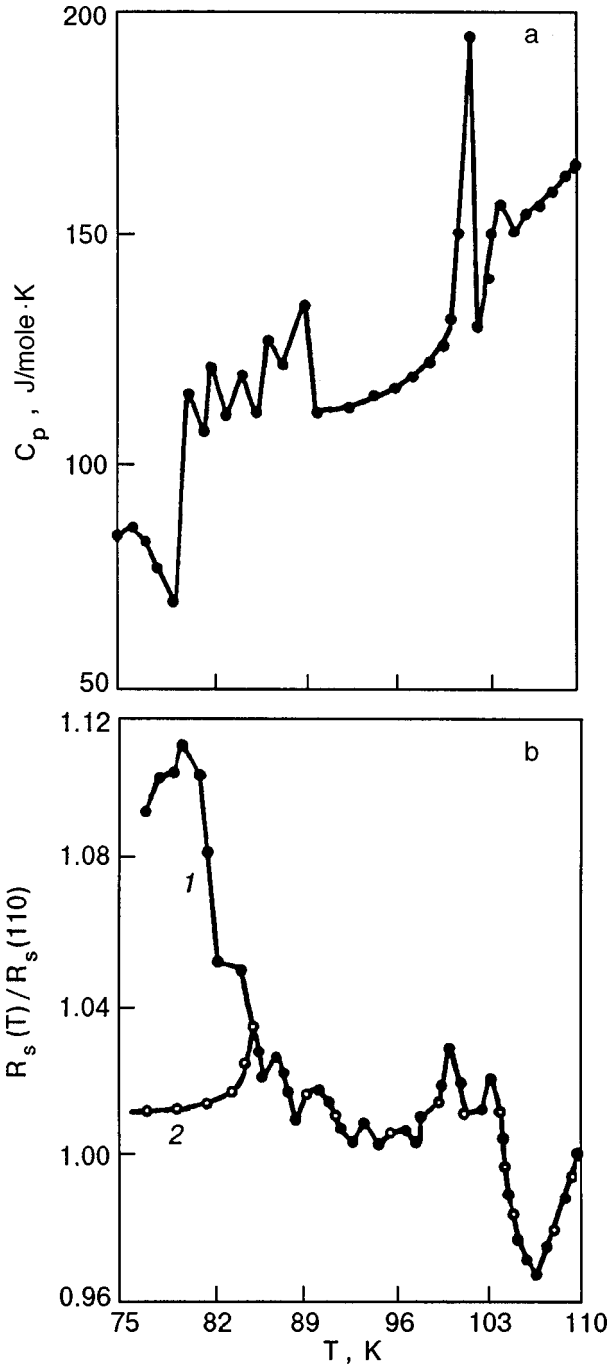

FIG. 3. Temperature dependences $C_p(T)$ in the temperature range 75–110 K (a) and $R_s(T)/R_s(110)$ obtained in simultaneous measurements for all the samples in the same temperature range at a frequency 2×10^6 Hz in zero magnetic field (curve *1*, ●) and in a magnetic field of 50 Oe (curve *2*, ○) (b).

10^5 Hz it increases according to the power law $Z\sim f^n$. The exponent $n=1.5$ at $T=300$ K and increases upon cooling, attaining the value of 2 for some samples. For this reason, $\partial Z/\partial T$ has a complex frequency dependence. The value of $\partial Z/\partial T$ decreases with increasing frequency, is equal to zero for certain frequencies f_1 and f_2, and assumes negative values in the interval from f_1 to f_2 (Fig. 4a). A series of $Z(T)$ curves shown in Fig. 4a was plotted just for frequencies typical of the given sample: $f=0$ (curve *1*), $f=f_1$ (curve *2*), $f_1<f<f_2$ (curve *3*), and $f>f_2$ (curve *4*).

We can note some typical peculiarities of Z in the temperature range under investigation.

1. The compound under investigation exhibits an anomaly in R_s near T_N, which is manifested in the form of a two-hump increase in ohmic losses correlated in temperature with similar anomalies in heat capacity (see Fig. 3a and curve *1* in Fig. 3b). (The latter figure shows the results of simultaneous measurements of R_s for all samples under investigation at a frequency of 2×10^6 Hz in zero magnetic field (curve *1*) and in a magnetic field of 50 Oe (curve *2*.) According to Fig. 4b, a negative value of $\partial\rho/\partial T$ is observed at this frequency.

2. For each sample, there exists a characteristic tempera-

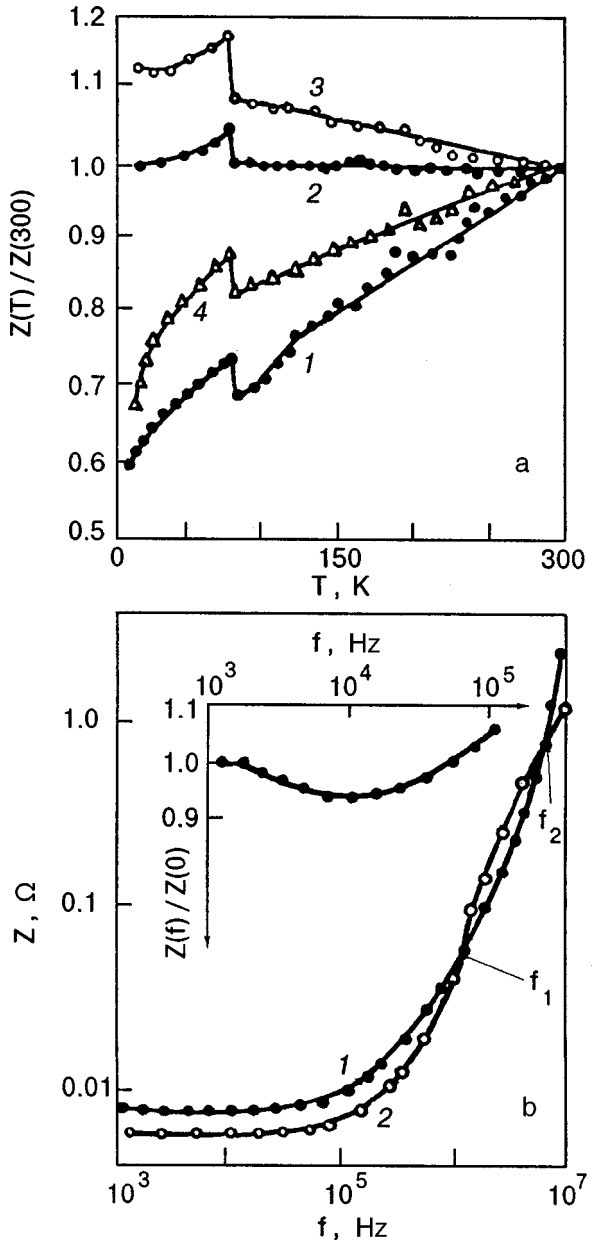

FIG. 4. Temperature dependences of the impedance of $LuFe_4Al_8$ samples normalized to $T=300$ K at frequencies f, Hz: 0 (curve *1*), 8×10^5 (curve *2*), 4×10^6 (curve *3*), and 10^7 (curve *4*) (a). Frequency dependences of impedance at 300 K (curve *1*) and 95 K (curve *2*). The inset shows the frequency dependence of anomalous decrease in the sample resistance (b).

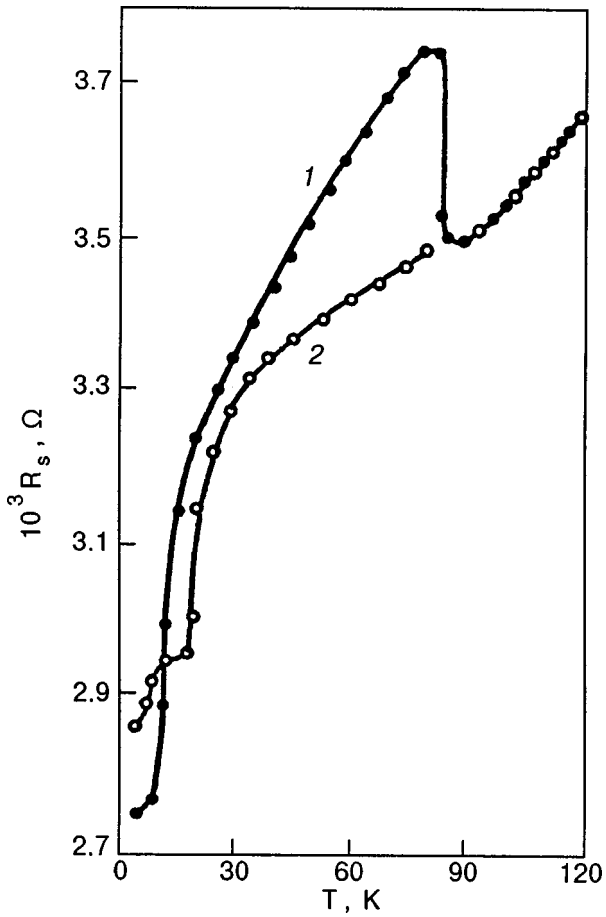

FIG. 5. Temperature dependence of the surface resistance R_s of $LuFe_4Al_8$ samples at a frequency of 10^7 Hz in zero magnetic field (curve *1*) and in a magnetic field of 50 Oe (curve *2*).

ture $T_1<T_N$ at which the resistance increases jumpwise over a step of 2–3 K. This temperature correlates with that at which heat capacity anomalies are manifested (see Fig. 3a) in the temperature range 75–90 K.

Figures 4a and 5 show such jumps in the values of Z and R_s, respectively, for the same sample with $T_1=85$ K.

3. The derivative $\partial Z/\partial T$ reverses its sign not in all samples in spite of the fact that all of them were obtained from the same monolithic $LuFe_4Al_8$ polycrystal.

4. The value of Z decreases insignificantly in a certain frequency range preceding the frequencies at which the frequency dependence of impedance is manifested (see the inset to Fig. 4b). This phenomenon is observed for most of $LuFe_4Al_8$ samples under investigation as well as other materials.[11]

5. Anomalies in the impedance exhibited in the temperature intervals 250–270 K and 160–210 K have the form of deviations from the values corresponding to the regular (linear) temperatures dependences $Z(T)$ in both directions (see Fig. 4a).

One of typical features of the electrical properties of $LuFe_4Al_8$ is that it exhibits a negative magnetoresistance at $T<T_1$ in a weak constant magnetic field. Curve *1* in Fig. 5 shows the temperature dependence of R_s measured in zero magnetic field, while curve *2* shows the same dependence in a magnetic field of 50 Oe. It can be seen that the magnetoresistive effect is not observed in weak magnetic fields at $T>T_1$, and the effect of H on Z or R_s starts being manifested only at $T<T_1$. The magnetic field dependence of R_s at $T=70$ K is shown in Fig. 6. The resistance R_s does not depend on the field H up to values of $H\sim15$ Oe, after which the resistance decreases with increasing field almost linearly. For $H>40$ Oe, the $R_s(H)$ curve attains saturation. No temperature or magnetic hysteresis is observed in these singularities.

It should be noted that a constant transport electric current creating a magnetic field of a few oersted around the sample at $T<T_1$ does not affect the value of R_s either.

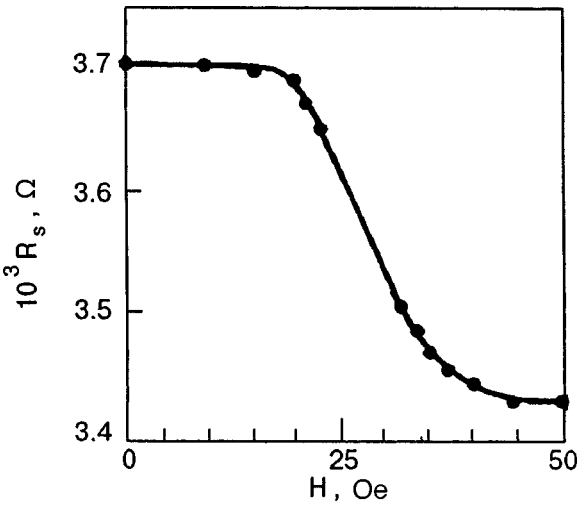

FIG. 6. Magnetic field dependence of the surface resistance R_s of $LuFe_4Al_8$ at $T=70$ K and $f=10^7$ Hz.

A series of R_s and Z anomalies observed in the temperature range 40–65 K correlates with heat capacity anomalies (at 40, 50, and 60 K).

The derivative $|\partial R_s/\partial H|$ changes its sign at a certain temperature T_c which typical of each sample and at which a λ-shaped anomaly in the temperature dependence of heat capacity $C_p(T)$ is observed. For the sample whose $R_s(T)$ curve is shown in Fig. 5, $T_c=12$ K.

Figure 7 shows the temperature dependences $R_s(T)$ of the resistance of the same sample in the vicinity of the temperature T_c, which were measured in zero magnetic field (curve *1*, dark circles), in a static magnetic field of 50 Oe) (curve *2*, dark triangles), in the presence of a transport current passing through the sample in zero magnetic field (curve *3*, light circles), and a transport current passing through the sample in a static magnetic field of 50 Oe (curve *3*, light triangles). The curves in Figs. 7a and 7c were obtained in the first cycle of sample ''cooling,'' while those in Fig. 7b were obtained in the sixth cycle.

We also measured the temperature dependence of $\Delta f = f_p(H=0) - f_p(H=50\,\text{Oe})$, where $f_p(H=0)$ and $f_p(H=50\,\text{Oe})$ are the resonance frequencies of the measuring oscillatory circuit with the sample in zero magnetic field and in magnetic field of 50 Oe respectively (Fig. 7c). A similar relation between Δf and T was established for the case when Δf is the same difference in the frequencies of the oscillatory circuit containing the sample in zero magnetic field without a direct current and with a transport current passing through it.

It should be noted that the value of Δf is proportional to the change in the reactive component of the surface resistance of the compound, and its positive value indicates an enhancement of diamagnetism of the sample at $T<T_c$ in zero magnetic field. The mutual orientation of the magnetic field and transport current does not affect the results of measurements.

It can be seen from Figs. 7a and 7b that the peculiarities of the resistance at $T<T_c$ can be described as follows:

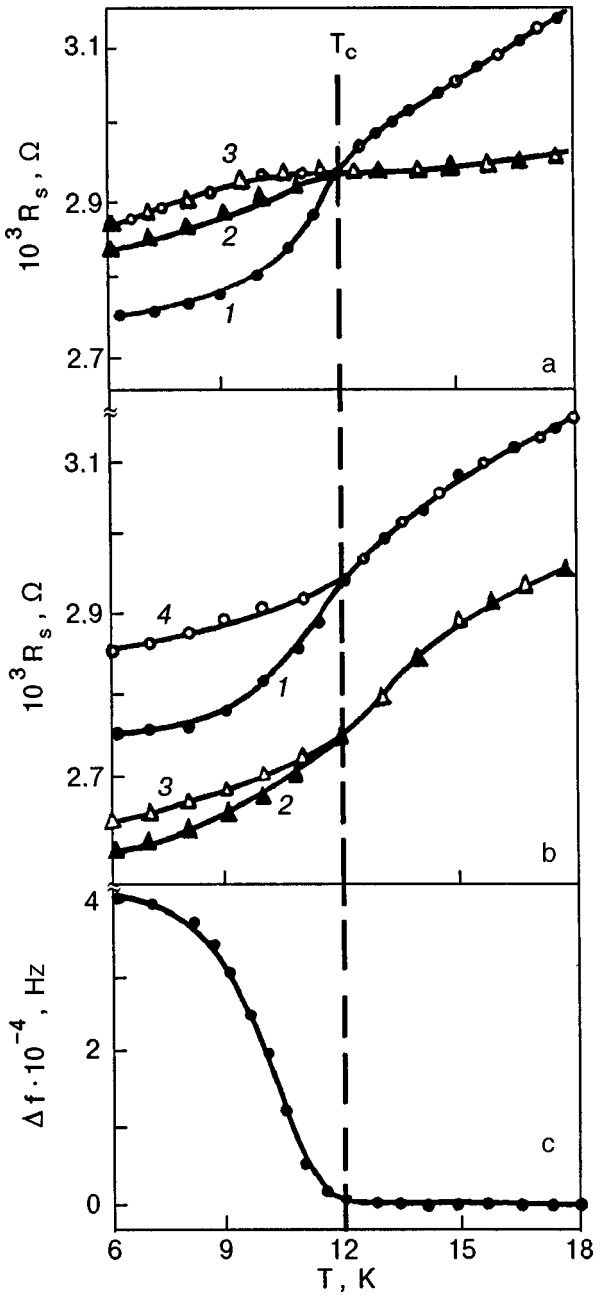

FIG. 7. Temperature dependence of the surface resistance at a frequency of 10^7 Hz in zero magnetic field (dark circles), in a magnetic field of 50 Oe (dark triangles) with a current of 1 A (light circles) and in a magnetic field of 50 Oe with a current of 1 A (light triangles) (a). The same dependence after thermal cycling of the sample (b). Temperature dependence of the difference between the resonance frequencies of the measuring oscillatory circuit with a $LuFe_4Al_8$ sample in zero magnetic field and in a magnetic field of 50 Oe (c).

1. at $T<T_c$, the resistance R_s of the compound in zero magnetic field decreases abnormally (curve *1* in Fig. 7a);

2. at $T=T_c$, the derivative $\partial R_s/\partial T$ changes its sign and becomes positive at $T<T_c$;

3. at temperatures below T_c, the derivative $\partial R_s/\partial I>0$ (curve *3*), while $\partial R_s/\partial T=0$ at $T>T_c$. We also obtained he dependence of R_s at a frequency 10^7 Hz on the value of transport current passing through the sample at 5 K ($T_c=12$ K) (Fig. 8);

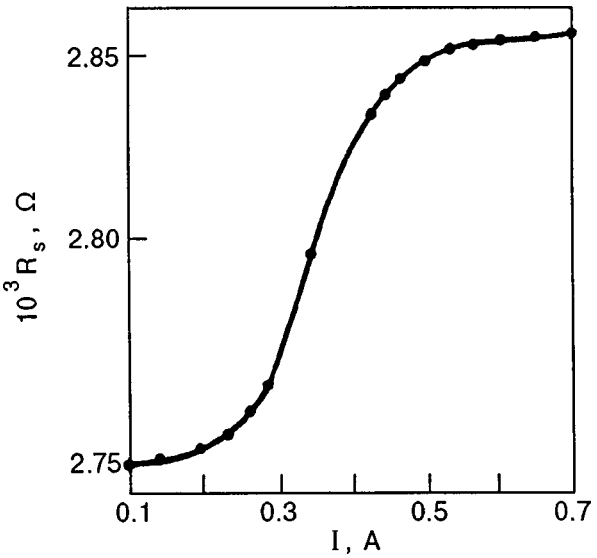

FIG. 8. Dependence of the surface resistance of $LuFe_4Al_8$ samples on direct current at frequency $f=10^7$ Hz and at $T=5$ K.

4. at $T<T_c$, the reactive component of the surface impedance of $LuFe_4Al_8$ changes anomalously (see Fig. 7b).

Levitation of $LuFe_4Al_8$ sample in a magnetic field

The levitation of a sample was detected from the change in the *Q*-factor of the measuring oscillatory circuit. Figure 9 shows the temperature dependences of the *Q*-factor of the same sample reduced to the *Q*-factor of the measuring oscillatory circuit at 7 K with the sample fixed at the magnet (●) and with a free sample ○). It can be seen from the figure that the temperature variations of the *Q*-factor in both cases coincide at $T<T_c$ ($T_c=4.8$ K in the given sample), while the *Q*-factor of a freely suspended sample at $T<4.8$ K decreases, which confirms the existence of levitation.

Similar results were obtained during measurements of the resonance frequency of the oscillatory circuit. Its resonance frequency increases at $T<T_c$, indicating that the sample approaches the inductance coil.

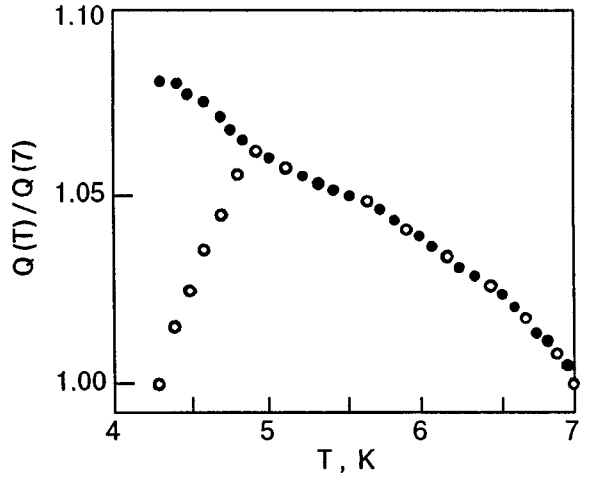

FIG. 9. Dependence of the *Q*-factor of the measuring oscillatory circuit normalized to $T=7$ K for fixed (●) and free (○) sample.

Variation of electrical parameters of $LuFe_4Al_8$ during thermocycling

One of peculiarities of the samples under investigation is the change in their electrical parameters during thermocycling from room to helium temperatures. In this case, new anomalies appear on the temperature dependences of resistance R_s or impedance Z. As the number of thermal cycles increases, the shape of the anomalies changes, or the temperature at which they are observed is displaced.

The magnetic properties of the compound also change. By way of an example, Fig. 7b shows the electromagnetic characteristics of the sample (whose R_s in the first cycle is shown in Fig. 7a) after thermocycling.

After five thermal cycles 4.5–300 K, the sign of the derivative $\partial R_s/\partial H$ did not change (see Fig. 7b), and the value of T_c is actually the temperature at which the direct current starts affecting the value of R_s (curves *3* and *4* in Fig. 7b). After 10–12 cycles, the value of $\partial R_s/\partial H$ decreases for all samples and becomes equal to zero after some time both in the temperature range from T_1 to T_c, and below T_c. The value of $\partial R_s/\partial I$ does not change either, and no levitation is observed.

DISCUSSION OF RESULTS

The linear temperature dependence of resistivity in the paramagnetic region is typical not only of $LuFe_4Al_8$ or a pure lutetium single crystal[13] but also of other materials like complex metaloxides for which it is explained on the basis of the two- band model of conductors.[14] The electrical properties of rare-earth metals and their alloys are also analyzed in many cases with the help of the band model assuming the presence of two (wide and narrow) bands whose interaction causes hybridization.[4] It should be noted that both $LuFe_4Al_8$, and metaloxides exhibit a linear dependence $R(T)$ in the temperature range where paramagnetism exists and where ohmic losses are due to both electron–phonon interaction and scattering at localized magnetic moments (see, for example, Ref. 12 and the literature cited therein). Probably, the linear segment of $R(T)$ for all these compounds can be explained on the basis of the same model.

The derivative $\partial Z/\partial T$ for $LuFe_4Al_8$ changes its sign only at frequencies corresponding to the beginning of the $Z(f)$ dependence. Consequently, the anomaly in $\partial Z/\partial T$ in $LuFe_4Al_8$ is apparently due to the layered nature[14,15] of the material in contrast to metaloxides in which the change in sign is explained by the two-band model. The sample should be treated as a segment of a layered line[16] with a longitudinal[17] and transverse[18] transient resistance between the layers.The complex interaction between these resistances is probably responsible for the decrease in the value of Z in the frequency range preceding the emergence of the $Z(f)$ dependence (see the inset to Fig. 4b).

The anomalies in heat capacity and resistance during phase transitions appear as quite natural. Such singularities correspond to antiferromagnetic ordering at $T_N=100.5$ K and coincide with the results of magnetic measurements on the temperature scale (Fig. 3).[3] The anomalies observed in the temperature range 75–90 K (see Fig. 3) and clearly mani-

fested for one of the samples in Figs. 4a and 5 are astonishing. The resistance increases by 10–20% at temperatures 10–20 K below T_N and decreases in a weak magnetic field at least in the vicinity of T_N. The saturation field has a value of just 40 Oe. The curve in Fig. 6 closely resembles the analogous dependence obtained by Baibich *et al.*[20] for artificial FeCr magnetic superlattices.It is interesting to note that negative magnetoresistance and saturation field in such artificial layered structures depend significantly on the separation between adjacent magnetic layers with antiparallel magnetic moments. Note that the resistance jump $\Delta Z/Z$ at $T=T_1$ is practically independent of frequency. In some samples, the resistance was doubled at $T=T_1$.

The dependence $R_s(H)$ observed in our case in a weak field indicates the existence of a weak magnetic interaction in the magnetic subsystem and a considerable interaction of conduction electrons with magnetic moments, just like in layered magnetic structures and in heavy fermion systems.

Below 30 K, the dependence $C_p(T)$ can be described by the expression $C_p=\gamma T+\beta T^2$, where $\gamma=0.07\,\text{J/mole}\cdot\text{K}^2$. Such a value of γ also suggests that the system contains heavy fermions. Additional investigations must be carried out in order to find the origin of the weak-field magnetoresistance effect with the negative magnetoresistance in the interval between T_1 and T_c.

The obtained results of complex studies of heat capacity as well as the electrical and magnetic parameters of $LuFe_4Al_8$ at $T<25\,\text{K}$ lead to the conclusion that this compound contains a small amount of the superconducting phase (SP) with a transition temperature $T_c\leqslant 24\,\text{K}$.

First, the increase in the reactive component of impedance (see Fig. 7c) and the levitation of the sample at $T<T_c$ indicate an augmentation of the magnetic flux expulsion from the compound, i.e., the existence of the Meissner effect.

Second, a decrease in ohmic losses is observed in the dependence $R_s(T)$ at $T<T_c$.

Third, it was shown above that a constant transport current as well as a static magnetic field affect the ohmic losses in the compound at $T<T_c$. In this case, $\partial R_S/\partial H>0$ and $\partial R_S/\partial I>0$ (see Fig. 7a and 8). Such a behavior is typical of the superconducting phase at temperatures below the transition temperature T_c, and the shape of the current dependence $R_s(I)$ (see Fig. 8) indicates the presence of the critical current in the sample. In this case, weak C_p anomalies of the λ-type observed at the temperatures 5, 10, 15, 19, and 24 K probably reflect the superconducting transitions of the heterogeneous regions of the sample. The absence of a hysteresis in this temperature range allows us to attribute the observed peculiarities to second-order phase transitions.

The model that can describe qualitatively the observed peculiarities can be described as follows. As the temperature decreases below the antiferromagnetic ordering temperature T_1, a magnetostructural phase transition takes place, which results in the formation of antiferromagnetically coupled iron layers separated by the layers of nonmagnetic lutetium. In this case, the spin-dependent scattering of charge carriers, which is responsible for negative magnetoresistance,[21,22] becomes significant, and the resistance experiences a jump. A peculiar magnet–nonmagnet–magnet superlattice is formed. A superconducting state is formed as the temperature decreases below T_c. The emergence of such a state is unlikely in regions with clearly manifested magnetic moments. Assuming that two adjacent layers are coupled antiferromagnetically, it can be surmised that the small boundary region between the layers is nonmagnetic, and superconductivity emerges just in this region. This explains the low concentration of the superconducting phase. The magnetostructural phase transition, and hence the nonuniform state of the sample also explain the peculiarities of thermal cycling and the spread in transition temperatures. Since the samples were polycrystalline, the orientational dependences were not observed.

CONCLUSION

The most important properties observed by us in $LuFe_4Al_8$ can be summarized as follows.

(1) A singularity on the temperature dependence of heat capacity indicating an antiferromagnetic phase ordering at $T_N=100.5\,\text{K}$.
(2) A sharp increase in the sample resistance at $T_1<T_N$. Orientational magnetoresistance is observed below this temperature in a weak ($H<50\,\text{Oe}$) static magnetic field.
(3) The emergence of a small amount of the superconducting phase at temperatures below $T_c=24\,\text{K}$.
(4) The existence of heavy fermions in $LuFe_4Al_8$ is indicated by heat capacity investigations.

It can be assumed on the basis of the entire body of experimental data that a layered magnet– nonmagnet–magnet superlattice is formed at temperatures $T_1<T_N$. Below temperatures $T_c<T_1$, this superlattice is transformed into a magnet–superconductor– magnet superlattice.

Thus, the compound $LuFe_4Al_8$ possesses interesting physical properties and serves as a promising object for further investigations.

The authors are indebted to M. L. Almeida and A. Gonsalves for supplying the samples, and to A. G. Anders and N. I. Glushchuk for fruitful discussions.

*)International Laboratory of Strong Magnetic Fields and Low Temperatures, 53-421 Wroclaw, Poland
**)E-mail: dmitriev@ilt.kharkov.ua

[1] K. H. J. Buschow, J. H. N. van Vucht, and W. W. van den Hoogenhof, J. Less-Common Met. **50**, 145 (1976).
[2] A. M. van der Kraan and K. H. J. Buschow, Physica **86**, 93 (1977).
[3] K. H. J. Buschow and A. M. van der Kraan, J. Phys. F: Metal Physics **8**, 921 (1978).
[4] S. A. Nikitin, *Magnetic Properties of Rare-Earth Metals and Their Alloys* [in Russian], MGU, Moscow (1989).
[5] V. M. Dmitriev, V. N. Eropkin, A. M. Gurevich *et al.*, Fiz. Nizk. Temp. **17**, 53 (1991) [Sov. J. Low Temp. Phys. **17**, 28 (1991)].
[6] M. N. Ofitserov, N. N. Prentslau, N. A. Kucheryavenko *et al.*, Preprint No. 47–88, Inst. for Low Temp. Phys. Eng., Kharkov (1988).
[7] V. M. Dmitriev, M. N. Ofitserov, and N. N. Prentslau, Radiotekhnika, No. 97, 91 (1993).
[8] N. N. Prentslaau, A. P. Bezkorsyi, I. F. Kharchenko *et al.*, Radiotekhnika, No. 87, 120 (1988).
[9] V. M. Dmitriev, M. N. Ofitserov, N. N. Prentslau, and K. Rogatski, Fiz. Nizk. Temp. **19**, 268 (1993) [Low Temp. Phys. **19**, 188 (1993)].
[10] V. M. Dmitriev, M. N. Ofitserov, and N. N. Prentslau, *Proc. Contrib. Papers to Int. Conf. Low Temp. Phys. in Ukraine*, Kiev (1993).

[11] V. M. Dmitriev, M. N. Ofitserov, N. N. Prentslau *et al.*, Fiz. Nizk. Temp. **21**, 397 (1995) [Low Temp. Phys. **21**, 308 (1995)].
[12] L. S. Mazov, Fiz. Nizk. Temp. **17**, 1372 (1991) [Sov. J. Low Temp. Phys. **17**, 738 (1991)].
[13] D. Boys and S. Legvold, Phys. Rev. **174**, 377 (1968).
[14] V. P. Galaiko, Fiz. Nizk. Temp. **19**, 123 (1993) [Low Temp. Phys. **19**, 87 (1993)].
[15] V. P. Galaiko, V. M. Dmitriev, M. N. Ofitserov, and N. N. Prentslau, Fiz. Nizk. Temp. **19**, 135 (1993) [Low Temp. Phys. **19**, 96 (1993)].
[16] A. M. Clogston, Proc. IRE **39**, 767 (1951).
[17] R. A. King, B.S.T.J. **XXXVIII**, No. 2, 5176 (1959).
[18] H. Ataka, Proc. IRE **42**, 1527 (1954).
[19] N. V. Volkenshtein, V. A. Novoselov, and V. E. Startsev, Zh. Éksp. Teor. Fiz. **60**, 1078 (1971) [Sov. Phys. JETP **33**, 584 (1971)].
[20] M. N. Baibich, J. M. Broto, A. Fert *et al.*, Phys. Rev. Lett. **61**, 2472 (1988).
[21] R. E. Camley and R. L. Stamps, J. Phys.: Condens. Matter **5**, 3727 (1993).
[22] P. Zahn, J. Binder, I. Merting *et al.*, Phys. Rev. Lett. **80**, 4309 (1998).

Translated by R. S. Wadhwa

LOW-TEMPERATURE MAGNETISM

Magnetic ordering at the stepped ferro/antiferromagnetic interface

O. K. Dudko and A. S. Kovalev

B. Verkin Institute for Low Temperature Physics and Engineering, National Academy of Sciences of the Ukraine, 310164 Kharkov, Ukraine)*

(Submitted July 13, 1998)
Fiz. Nizk. Temp. **25**, 25–32 (January 1999)

A nonuniform distribution of magnetic disclination type magnetization connected with the atomic size step on the ferro/antiferromagnetic boundary is studied. The obtained results are generalized to the case of periodic stepped ferro/antiferromagnetic interface. © *1999 American Institute of Physics.* [S1063-777X(99)00401-6]

In the light of technical applications of the phenomenon of giant magnetoresistance in recent years, layered magnetic structures and interfaces between different magnetically ordered materials have been subjected widely to theoretical and experimental investigations. Multilayer systems containing alternating layers of ferro- and antiferromagnets[1,2] have been drawing special attention (interface between Co and CoO is an example of such a system). In experimental investigations of layered magnets, some interlayers are often wedge-shaped with a small divergence angle.[3] In this case, the interface between the magnets has a regular stepped form with large separation between steps of atomic size. The presence of a step at the boundary of a layered antiferromagnet leads to local variation of the micromagnetic structure and the possibility of emergence of a ''topological surface antiferromagnetism.''[4,5] A large number of theoretical works have been devoted to this problem (see, for example, Ref. 6). In this communication, we shall show that the presence of an atomic step at the interface between isotropic ferro- and antiferromagnets necessarily leads to the emergence of a nonuniform distribution of the magnetic disclination type magnetization throughout the entire volume of the magnets. The nature of such a distribution depends on the relation between the exchange constants in ferro- and antiferromagnetic half-spaces.

1. MAGNETIZATION DISTRIBUTION FOR AN ISOLATED ATOMIC SIZE STEP AT THE BOUNDARY

Let us consider a plane interface between a ferro- and an antiferromagnetic subspace. For simplicity, we shall assume that both magnets have a strong easy-plane one-ion anisotropy, and disregard the additional weak anisotropy in the easy plane. In this case, it was shown by Gouvea *et al.*[7] that all spins in the magnetic vortex or magnetic disclination configuration, rotate in the easy plane without leaving it, while the spins at lattice sites are characterized simply by their rotation angle in this plane. Thus, the geometry of static configurations is described by using the scalar model. In a layered antiferromagnet with layers ordered parallel to the ideal ferro/antiferromagnet interface, both half-spaces are in the ground state with collinear (in FM) and anticollinear (in AFM) distribution of spins for any kind of exchange interaction through the interface. In a magnet with ''staggered'' ordering and a compensated AFM surface, a noncollinear structure may be formed at the surface.[8,9] In the presence of an atomic size step at this boundary, ideal ferro- and antiferromagnetic ordering in half-spaces can emerge only in the absence of exchange interaction through the interface. Even a weak exchange interaction between the half-spaces makes the spin distribution noncollinear in the ground state and the system acquires a magnetic disclination having Frank's index $k=1$ (Fig. 1) and its center at step. In Ref. 10, such a configuration was associated with the presence of a screw dislocation in the AFM. In the case being considered here, the crystal structure is perfect and the presence of a step is equivalent in the magnetic sense to a ''magnetic dislocation,'' i.e., to the inclusion of an additional spin layer. Since we are interested in the magnetization distribution over distances larger than atomic dimensions (size of a step), we can replace a plane interface by a step at the ideal boundary, having reversed the sign of the exchange interaction through it along one of the semi-axes (on one side of the step).

Let us consider a two-dimensional quadratic lattice with the FM/AFM interface along the x-axis (the direction z of antiferromagnetic ordering is perpendicular to the interface). Confining ourselves to the classical Heisenberg model in the exchange approximation, we can represent the Hamiltonian of the system in the form

$$H=S_0^2\sum_{nm} J_{nm}\cos(\varphi_n-\varphi_m), \tag{1}$$

where S_0 is the lattice site spin, φ_n the spin rotation angle at the site n in the (x,z) plane, and J_{nm} the exchange interaction between spins at lattice sites n and m (summation is carried out over the nearest sites of the quadratic lattice). In the ferromagnetic half-space ($z>0$), $J_{nm}=-J_1$ and $-J_2$ in the x and z directions, respectively, while in the antiferromagetic part ($z<0$), $J_{nm}=-\tilde{J}_1$ and $\tilde{J}_2$ in these directions, where J_i and $\tilde{J}_i>0$. In accordance with our model descrip-

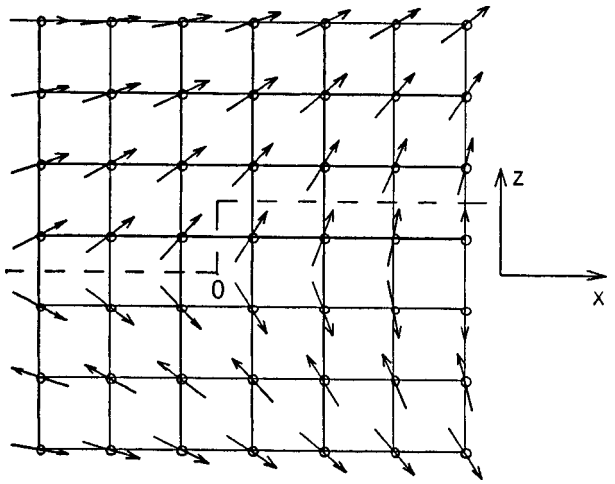

FIG. 1. Structure of a magnetic disclination associated with a step at the FM/AFM interface in the particular case of identical exchange interaction in magnets

tion of the interface containing a step, we propose $J_{nm}=J_s\,\mathrm{sgn}(x)$ as the constant of exchange interaction through this interface. It is convenient to go over in the antiferromagnetic half-space from the angles φ_n to $\varphi_n+\pi$ in even-numbered layers (see Fig. 1). After this we can provide a longwave description for the fields of magnetization and the antiferromagnetism vector in both half-spaces within the framework of Laplace equations:

$$\begin{aligned} &J_1\varphi_{xx}+J_2\varphi_{zz}=0, \quad z>0,\\ &\tilde{J}_1\varphi_{xx}+\tilde{J}_2\varphi_{zz}=0, \quad z<0. \end{aligned} \tag{2}$$

Since the relation between exchange integrals J_i, $\tilde{J}_i$ and J_s is assumed to be arbitrary, relative deviations of spins $\varphi_+=\varphi(z=+0)$ and $\varphi_-=\varphi(z=-0)$ may be quite large ($\simeq\pi$) in layers adjoining the interface and hence the magnetic interaction between these layers must be taken into account exactly:

$$W_s=\mathrm{sgn}(x)S_0^2\cos(\varphi_+-\varphi_-). \tag{3}$$

The nonuniform distribution of the magnetization field in the FM half-space ($z>0$) can be expressed in terms of the density distribution of the effective forces $f_+(x)$ acting at the boundary $z=0$:[11]

$$\varphi(x,z>0)=\frac{1}{2\pi\sqrt{J_1J_2}}\int dx'\,\ln\left[\frac{(x-x')^2}{J_1}+\frac{z^2}{J_2}\right]f_+(x'), \tag{4}$$

where

$$f_+(x)=J_2\left.\frac{\partial\varphi}{\partial z}\right|_{z=+0} \tag{5}$$

(we have put the lattice constant and the spin S_0 equal to unity). Formula (4) leads to the following expression for the magnetization gradient at the interface:

$$\sqrt{J_1J_2}\frac{d\varphi_+}{dx}=\hat{H}f_+(x). \tag{6}$$

Here, we have introduced the following standard notation for the Hilbert transformation:

$$\hat{H}F=\frac{1}{\pi}\int dx'\frac{F(x')}{(x-x')}. \tag{7}$$

For the AFM half-space ($z<0$), formula (6) is replaced by

$$(\tilde{J}_1\tilde{J}_2)^{1/2}\frac{d\varphi_-}{dx}=\hat{H}f_-(x), \tag{8}$$

where $f_-(x)$ are the effective forces acting at the boundary $f_-=-\tilde{J}_2\partial\varphi/\partial z|_{z=-0}$ of the lower region. The dependence of the forces $f_\pm(x)$ on relative orientation of spins at the FM/AFM boundary follows from formula (3) for the surface energy

$$f_\pm(x)=\mp\,\mathrm{sgn}(x)J_s\sin(\varphi_+-\varphi_-). \tag{9}$$

Substituting formula (9) into Eqs. (6) and (8), we obtain, after adding and subtracting, a closed equation for relative spin rotations $\psi=\varphi_+-\varphi_-$ in the layers adjoining the boundary and the relation of the functions φ_+ and φ_- with the distribution $\psi(x)$:

$$\sin\psi+l\,\mathrm{sgn}(x)\hat{H}\left(\frac{d\psi}{dx}\right)=0, \tag{10}$$

$$\begin{aligned} \varphi_+&=\frac{(\tilde{J}_1\tilde{J}_2)^{1/2}}{(J_1J_2)^{1/2}+(\tilde{J}_1\tilde{J}_2)^{1/2}}\psi,\\ \varphi_-&=-\frac{(J_1J_2)^{1/2}}{(J_1J_2)^{1/2}+(\tilde{J}_1\tilde{J}_2)^{1/2}}\psi, \end{aligned} \tag{11}$$

where we have introduced the parameter

$$l=(J_1J_2\tilde{J}_1\tilde{J}_2)^{1/2}/J_s[(J_1J_2)^{1/2}+(\tilde{J}_1\tilde{J}_2)^{1/2}],$$

characterizing the extent of nonuniformity in the distribution of magnetization around the surface step.

Equation (10) was studied in detail by us in Ref. 10. It was shown that it has a local topological soliton solution whose asymptotic forms at large distances from the center and behavior in the vicinity of the step can be described as follows:

$$\psi(\kappa)\cong\begin{cases} \dfrac{1}{\kappa}, & \kappa\to-\infty,\\ \dfrac{\pi}{2}-\dfrac{2}{\pi}\ln|\kappa|, & \kappa\ll 1,\\ \pi-\dfrac{1}{\kappa}, & \kappa\to+\infty, \end{cases} \tag{12}$$

where we have introduced the dimensionless coordinate $\kappa=x/l$.

Spin deviation field distributions at the FM/AFM boundary and in the bulk of the magnets are expressed in terms of the obtained function $\psi(\kappa)$. Thus, spin rotations in layers adjoining the interface are defined by formulas (11). The boundary region in which the spin rotation angles are not small is of the order of l. Hence a decrease in the interaction

through the boundary leads to an increase in the size of the disordered region in proportion to $1/J_s$. Since the total variation of the angle ψ upon a variation of x from $-\infty$ to $+\infty$ amounts to π, we can easily calculate the total rotation of the ferro- and antiferromagnetism vectors in the corresponding half-spaces:

$$\delta\varphi_+ = \varphi_+(+\infty) - \varphi_+(-\infty) = \frac{\pi}{(1+g)},$$
$$\delta\varphi_- = \varphi_-(+\infty) - \varphi_-(-\infty) = -\frac{\pi g}{(1+g)}, \tag{13}$$

where we have introduced the parameter $g=(J_1J_2/\tilde{J}_1\tilde{J}_2)^{1/2}$ characterizing the difference in magnetic properties of FM and AFM. It follows from formulas (13) that the total variation of the angle φ during circumvention of the step at the interface along a closed contour is π, and this spin configuration indeed corresponds to magnetic disclination with Frank's index $k=1$. However, in contrast to the magnetic disclination associated with dislocation in a homogeneous AFM (see Ref. 10), the total spin rotation is different in FM and AFM half-spaces in the present case and depends on the parameter g:

$$\frac{\delta\varphi_+}{\delta\varphi_-} = -g. \tag{14}$$

If magnetic interaction in the AFM half-space is much stronger than the exchange interaction in a ferromagnet ($\tilde{J}_i \gg J_i$, ''frozen'' AFM), the rotation of magnetization occurs mainly in the FM region through an angle close to π. In this case, if we consider even a weak anisotropy in the easy plane, the magnetic disclination is transformed into a ferromagnetic domain wall in the FM half-space which terminates at the step in the interface.

In the opposite case of a ''frozen'' ferromagnet in the case $J_i \gg \tilde{J}_i$, the spin rotation mainly takes place in the AFM region, and the antiferromagnetism vector turns through an angle close to π upon a variation of x from $-\infty$ to $+\infty$. In this case, a 180° AFM domain wall is formed if the intraplane anisotropy is taken into account. Figure 1 shows the spin configuration in the intermediate case $J_i=\tilde{J}_i$. In order to find the magnetization field distribution in the entire two-dimensional region around the interface nonuniformity, we must use formula (4) for the upper half-space ($z>0$) and the corresponding formula for $z<0$ after differentiating them with respect to z and substituting into them formula (9) for the effective forces. Since we are interested in the asymptotic form of the solution at distances $\kappa \gg 1$, we approximate the function $\sin(\varphi_+-\varphi_-)$ by the expression $1/(1+\kappa^2)^{1/2}$. In this case, we obtain the following expression for the upper half-space:

$$\frac{\partial\varphi}{\partial z}(\kappa, z>0) \simeq \frac{zJ_s}{\pi J_2 \lambda}\int d\kappa' \frac{\mathrm{sgn}(\kappa')}{\sqrt{1+\kappa'^2}} \times\left[(\kappa-\kappa')^2+\left(\frac{z}{\lambda}\right)^2\right], \tag{15}$$

where $\lambda = l(J_1/J_2)^{1/2}$ is the characteristic size along the z-axis. For a weak spatial anisotropy in the case $J_2 \simeq J_1$, the quantities λ and l are of the same order of magnitude. The integral in formula (15) is evaluated in elementary functions,[10] and the obtained expression can be expanded in powers of l/x and λ/z at distances $x \gg l$ and $z \gg \lambda$. In terms of the initial variables, the first terms of this expansion have the form

$$\frac{\partial\varphi}{\partial z}(x, z>0) \simeq \frac{J_s}{J_2} f(x,z), \tag{16}$$

where

$$f(x,z) = \frac{x/l}{x^2/l^2+z^2/\lambda^2} \times\left[1-\frac{4|z|}{\lambda\pi(x^2/l^2+z^2/\lambda^2)}+O\left(\frac{l^3}{x^3},\frac{\lambda^3}{z^3}\right)\right]. \tag{17}$$

The corresponding expression for the derivative of the field of the antiferromagnetism vector in the AFM half-space ($z<0$) has the form

$$\frac{\partial\varphi}{\partial z}(x, z<0) \simeq \frac{J_s}{\tilde{J}_2} \tilde{f}(x,z), \tag{18}$$

where $\tilde{f}$ differs from f in the replacement of λ by $\tilde{\lambda} = l(\tilde{J}_2/\tilde{J}_1)^{1/2}$. In the case of a weak spatial anisotropy, when $J_1 \simeq J_2$ and $\tilde{J}_1 \simeq \tilde{J}_2$), the functions f and $\tilde{f}$ actually coincide and

$$\frac{\partial\varphi/\partial z(z>0)}{\partial\varphi/\partial z(z<0)} \approx \frac{\tilde{J}^2}{J_2}. \tag{19}$$

This means that the spin distribution is quite asymmetric relative to the interface in the case of a considerable difference between the exchange constants in FM and AFM.

2. MAGNETIZATION DISTRIBUTION FOR A REGULAR STEPPED SHAPE OF THE INTERFACE

Let us generalize the obtained results to the case of an interface with an infinite number of atomic size steps with a large separation $L \gg a$ between them. The magnetic exchange interaction through the boundary can now be described by the function

$$W = J_s(x) S_0^2 \cos(\varphi_+ - \varphi_-), \tag{20}$$

where $J_s(x)$ has the form of an alternating step function with period $2L$ and amplitude J_s, the constant J_s characterizing the exchange interaction between the half-spaces. Formula (20) leads to the following dependence of the forces $f_\pm(x)$ on the relative orientation of spins at the FM/AFM interface:

$$f_\pm(x) = \mp J_s(x)\sin(\varphi_+ - \varphi_-). \tag{21}$$

Substituting formula (21) into Eqs. (6) and (8), we obtain (after adding and subtracting) an equation analogous to (10) for relative spin rotations $\psi = \varphi_+ - \varphi_-$ in the layers adjoining the boundary and the relation between the functions φ_+ and φ_-:

$$\frac{J_s(x)}{J_s}\sin\psi + l\hat{H}\left(\frac{d\psi}{dx}\right) = 0, \tag{22}$$

$$\varphi_- = -\frac{(J_1J_2)^{1/2}}{(\tilde{J}_1\tilde{J}_2)^{1/2}}\varphi_+, \tag{23}$$

where l is the parameter introduced above to characterize the size of the magnetic nonuniformity associated with the presence of the step boundary in the system.

Let us analyze the solution of Eq. (22) qualitatively. For this purpose, we replace the system under consideration by a model piecewise linear system in which the Heisenberg exchange interaction (20) of spins through the interface is replaced by an interaction in the form

$$W_s \to \begin{cases} S_0^2 J_s \dfrac{(\varphi_+ - \varphi_-)^2}{2} - S_0^2 J_s, & 0 \leqslant \varphi_+ - \varphi_- < \pi/2, \\ -S_0^2 J_s \dfrac{[(\varphi_+ - \varphi_-) - \pi]^2}{2} + S_0^2 J_s, & \pi/2 \leqslant \varphi_+ - \varphi_- \leqslant \pi. \end{cases} \tag{24}$$

In Eq. (22), $\sin\psi$ is replaced by a piecewise linear function

$$\sin\psi \to \begin{cases} \psi, & (2n-1)L < x < 2nL, \\ \pi - \psi, & 2nL < x < (2n+1)L, \end{cases} \tag{25}$$

where n is an integer, and Eq. (22) becomes linear. We shall consider below the simplest case of the ground state of the system in which magnetization distribution becomes uniform at large distances from the interface. This situation corresponds to a regular alternation of the signs of magnetic disclinations associated with the sequence of surface steps. In this case, the distribution of spin deviations (in particular, of the function $\psi(x)$) becomes a periodic function of x with a period $2L$, and we can use the Fourier transformation. Applying it to the above-mentioned linear equation, we obtain the solution for relative deviations of spins near the boundary in the form of a series:

$$\psi(x) = \frac{\pi}{2} + 2\sum_{n=0}^{\infty} \frac{\sin[(2n+1)\pi x/L]}{(2n+1)[1+(2n+1)l\pi/L]}. \tag{26}$$

We shall study the nature of magnetization distribution in the limit of strong and weak bonds between half-spaces.

Limit of weak bond between FM and AFM half-spaces

Even in the presence of an infinitely small exchange interaction through the interface, the spin distribution near it becomes noncollinear. Considering that the size of the inhomogeneity is comparable with the separation between steps or exceeds it (it should be recalled that $l \propto 1/J_s$ and increases with the weakening of bond between the FM and AFM half-spaces), we can confine the converging series (26) containing the factor $1/(2n+1)^2$ (which decreases with increasing n) to the first approximation ($n=0$):

$$\varphi_+ - \varphi_- \simeq \frac{\pi}{2} + \frac{2\sin(\pi x/L)}{1+(l\pi/L)}. \tag{27}$$

In this case, the spin deviations near the interface are obtained by jointly solving Eqs. (23) and (27):

$$\varphi_+ \simeq \frac{\pi}{2}\frac{1}{1+(J_1J_2/\tilde{J}_1\tilde{J}_2)^{1/2}} + \frac{2}{1+(J_1J_2/\tilde{J}_1\tilde{J}_2)^{1/2}}\frac{\sin(\pi x/L)}{1+(l\pi/L)}, \tag{28}$$

$$\varphi_- \simeq -\frac{\pi}{2}\frac{1}{1+(\tilde{J}_1\tilde{J}_2/J_1J_2)^{1/2}} - \frac{2}{1+(\tilde{J}_1\tilde{J}_2/J_1J_2)^{1/2}}\frac{\sin(\pi x/L)}{1+(l\pi/L)}. \tag{29}$$

It follows from these expressions that in the limit of a weak bond between the half-spaces, the spin deviation in the boundary layers is weakly modulated. Spin configuration in both half-spaces is determined by the relation between the exchange constants J_i and $\tilde{J}_i$ in them. (It should be recalled that, since there is no anisotropy, we can measure the angles φ_+ and φ_- from any direction in the easy plane.)

In the particular case when the exchange interaction in the magnets is identical ($\tilde{J}_1\tilde{J}_2 = J_1J_2$), the angle between mean directions of spins in the FM and AFM regions is $\pi/2$, and the amplitude of spin deviations from these mean directions is defined as $[1+(\pi\sqrt{J_1J_2})/2LJ_s]^{-1}$.

If the exchange interaction in AFM is considerably stronger than the exchange in FM ($\tilde{J}_1\tilde{J}_2 \gg J_1J_2$, which corresponds to the ''frozen'' AFM), spin rotation mainly occurs in the FM region in which spins deviate periodically from the mean direction orthogonal to the uniform orientation of spins in the AFM half-space.

In the opposite case of a ''frozen'' FM ($J_1J_2 \gg \tilde{J}_1\tilde{J}_2$), spin rotation mainly occurs in the AFM region.

In order to find the magnetization field distribution in the entire two-dimensional region near the step boundary, we use formula (4) for the upper half-space ($z>0$) and the corresponding formula for $z<0$. We shall take into consideration formulas (6) and (8) after carrying out the Hilbert trans-

formation and substituting the obtained expressions (28) and (29) for spin deviations near the interface. For the upper half-space we obtain the relation

$$\frac{\partial\psi}{\partial z}(x,z>0)=-\frac{2z}{LJ_2[1+(J_1J_2/\tilde{J}_1\tilde{J}_2)^{1/2}](1+l\pi/L)}\times\hat{H}\int dx'\frac{\cos(\pi x'/L)}{(x-x')^2/J_1+z^2/J_2}. \tag{30}$$

Evaluating the integral in Eq. (30) and applying $\hat{H}$-transformation to the result, we finally arrive at an expression for the derivative of magnetization field in the upper half-space:

$$\frac{\partial\psi}{\partial z}(x,z>0)=\frac{2\pi}{L}\left(\frac{J_1}{J_2}\right)^{1/2}\times\frac{1}{[1+(J_1J_2/\tilde{J}_1\tilde{J}_2)^{1/2}](1+l\pi/L)}\times\exp\left[-\pi\frac{z}{L}\left(\frac{J_1}{J_2}\right)^{1/2}\right]\sin\frac{\pi x}{L} \tag{31}$$

(we have used the property $\hat{H}[\cos(\alpha x)]=-\mathrm{sgn}(\alpha)\sin(\alpha x)$ of the $\hat{H}$-transformation).

The expression for the magnetization field distribution in the lower (AFM) half-space is obtained in an analogous manner:

$$\frac{\partial\psi}{\partial z}(x,z<0)=\frac{2\pi}{L}\left(\frac{\tilde{J}_1}{\tilde{J}_2}\right)^{1/2}\times\frac{1}{[1+(\tilde{J}_1\tilde{J}_2/J_1J_2)^{1/2}](1+l\pi/L)}\times\exp\left[\pi\frac{z}{L}\left(\frac{\tilde{J}_1}{\tilde{J}_2}\right)^{1/2}\right]\sin\frac{\pi x}{L}. \tag{32}$$

It can be seen from Eqs. (31) and (32) that the characteristic size of the nonuniform magnetization distribution region near the FM/AFM stepped boundary is of the order of $L\sqrt{J_2/J_1}$ in the FM half-space and $L\sqrt{\tilde{J}_2/\tilde{J}_1}$ in the AFM half-space. However, the nonuniformity in the magnetization distribution upon a weak interaction through the interface is proportional to the quantity $1/l\propto J_s$ and vanishes for $J_s=0$. Note that a decrease in the nonuniformity of magnetization distribution with coordinate z depends only on the properties of the half-space and not on J_s.

Limit of strong bond between FM and AFM half-spaces

In the limit of a strong bond between FM and AFM, let us first consider the case when one of the half-spaces (for definiteness, let it be the AFM half-space) is ''frozen,'' and the spin distribution in it is uniform. If the spins in the lower half-space are collinear to the interface, an indefinitely strong exchange interaction through the interface also ''aligns'' the spins in the FM half-space also along the interface. A transition in the upper half-space through the step along the x-axis turns the spins through an angle π as can be seen from the expression for the exchange interaction (20) and the shape of the function $J_s(x)$ proposed by us.

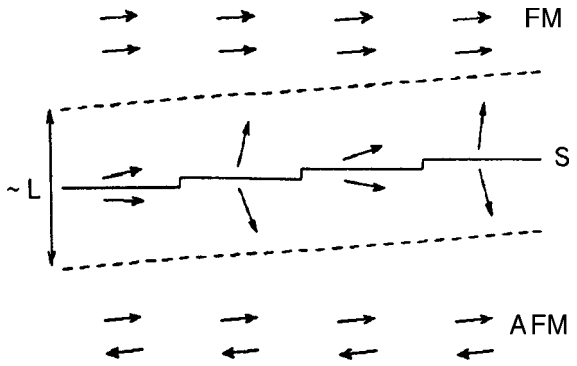

FIG. 2. Schematic representation of magnetization distribution near an FM/AFM step boundary in the limit of strong bond between magnets.

In the general case of ''defrozen'' magnets, it is obvious from the above arguments that, for a strong bond between them, the spins rotate through an angle $\pi/2$ in each half-space upon a change in x by L, while the relative spin deviation varies between 0 and π (Fig. 2). Obviously, the derivatives of spin deviations in the layers adjoining the boundary are described in this case by a sequence of δ-functions:

$$\frac{\partial\varphi_{\pm}}{\partial x}=\pm\frac{\pi}{2}\sum_{n=-\infty}^{+\infty}\delta(x-nl)(-1)^n. \tag{33}$$

In order to determine the nonuniform distribution of magnetization in the FM-half-space, we substitute the expression (33) (with sign ''+'' for the FM) into formula (4) taking into account the relation (6) and the skew-symmetry of the $\hat{H}$-transformation. Differentiation with respect to z gives

$$\frac{\partial\varphi}{\partial z}(x,z>0)=-\frac{2z}{4J_2}\sum_{n=-\infty}^{+\infty}\times(-1)^n\hat{H}\frac{1}{(x-nl)^2/J_1+z^2/J_2}. \tag{34}$$

This expression can easily be transformed (see Ref. 12) into the relation

$$\frac{\partial\varphi}{\partial z}(x,z>0)=\frac{\pi}{4\sqrt{J_1J_2}}\sum_{n=-\infty}^{+\infty}\times(-1)^n\frac{x-nl}{(x-nl)^2/J_1+z^2/J_2}. \tag{35}$$

To calculate the sum of the series (35), it is expedient to decompose it into two sums, one over even values of n and the other over odd values, and to apply the Poisson summation rule to each of the obtained sums:[13]

$$\sum_{s=-\infty}^{+\infty} f(x+sl)=\frac{1}{l}\sum_{m=-\infty}^{+\infty}\exp\left(\frac{2\pi imx}{l}\right)\times\int_{-\infty}^{+\infty}dx' f(x')\exp\left(\frac{-2\pi imx'}{l}\right). \tag{36}$$

Using this relation, we obtain for the sum over even n in (35)

$$\sum_{n=-\infty}^{+\infty}\frac{x-2nL}{(x-2nL)^2/J_1+z^2/J_2}=\frac{J_1}{2L}i\sum_{m=-\infty}^{+\infty}\exp\left(\frac{-2\pi imx}{2L}\right)\times\int_{-\infty}^{+\infty}dx'\frac{x'}{x'^2+z^2(J_1/J_2)}\sin\left(\frac{2\pi mx'}{2L}\right). \tag{37}$$

Obviously, relation (37) is the Fourier sine-transform of the integrand, and the final expression for the sum over even n has the form

$$\sum_{n=-\infty}^{+\infty}\frac{x-2nL}{(x-2nL)^2/J_1+z^2/J_2}=\frac{J_1\pi}{l}\sum_{m=1}^{+\infty}\sin\left(\frac{\pi mx}{L}\right)\exp\left[-\pi\frac{z}{L}\left(\frac{J_1}{J_2}\right)^{1/2}m\right]. \tag{38}$$

Having carried out the above-mentioned transformations on the sum over odd n, we finally arrive at an expression for the derivative of spin deviations in the FM half-space:

$$\frac{\partial\varphi}{\partial z}(x,z>0)=\frac{\pi^2}{2L}\left(\frac{J_1}{J_2}\right)^{1/2}\times\sum_{n=0}^{+\infty}\sin\frac{\pi(2n+1)x}{L}\times\exp\left[-\pi\frac{z}{L}(J_1/J_2)^{1/2}(2n+1)\right]. \tag{39}$$

For the AFM half-space ($z<0$), the analogous expression has the form

$$\frac{\partial\varphi}{\partial z}(x,z<0)=\frac{\pi^2}{2L}\left(\frac{\tilde J_1}{\tilde J_2}\right)^{1/2}\times\sum_{n=0}^{+\infty}\sin\frac{\pi(2n+1)x}{L}\times\exp\left[\pi\frac{z}{L}(\tilde J_1/\tilde J_2)^{1/2}(2n+1)\right]. \tag{40}$$

Since we are interested in the asymptotic form of the expression (39) at distances $z\gg L\sqrt{J_2/J_1}$, we shall confine ourselves to the first term of the series

$$\frac{\partial\varphi}{\partial z}(x,z>0)\simeq\frac{\pi^2}{2L}\left(\frac{J_1}{J_2}\right)^{1/2}\sin\frac{\pi x}{L}\exp\left[-z(J_1/J_2)^{1/2}\frac{\pi}{L}\right]. \tag{41}$$

It can be seen from the above equation that, as in the case of a weak bond between the half-spaces [formulas (31) and (32)], the decrease in the nonuniform magnetization into the bulk of the magnet is exponential in nature, and the region of such a nonuniform magnetization distribution has a characteristic size $\Delta_{\rm FM}\sim L\sqrt{J_2/J_1}$ in the FM half-space (in the AFM half-space, $\Delta_{\rm AFM}\sim L\sqrt{\tilde J_2/\tilde J_1}$, i.e., coincides with the corresponding expression in the limit of weak bond between the magnets).

CONCLUSION

A two-dimensional scalar model is proposed for an easy-plane magnet containing a stepped FM/AFM boundary. Using this model, a system of nonlinear one-dimensional integro-differential equations is obtained for fields of spin rotation around a nonuniform interface. Magnetization field configurations near such a boundary are studied in the limit of strong and weak bonds between FM and AFM half-spaces.

*)E-mail: odudko@ilt.kharkov.ua

[1] R. L. Stamps and R. E. Camley, Phys. Rev. B **54**, 15200 (1996).
[2] R. L. Stamps, R. E. Camley, and R. J. Hicken, Phys. Rev. B **54**, 4159 (1996).
[3] D. Weller and A. Carl, in *Digest of 14th Int. Colloquium on Magnetic Films and Surfaces*, Düsseldorf (1994).
[4] S. Blügel, D. Pescia, and P. H. Dederichs, Phys. Rev. B **39**, 1392 (1989).
[5] R. Wiesendanger, H. J. Güntherodt, G. Güntherodt *et al.*, Phys. Rev. Lett. **65**, 247 (1990).
[6] D. Stoeffler and F. Gautier, in *Digest of 14th Int. Colloquium on Magnetic Films and Surfaces*, Düsseldorf (1994).
[7] M. E. Gouvea, G. M. Wysin, A. R. Bishop, and F. G. Mertens, Phys. Rev. B **39**, 11840 (1989).
[8] A. G. Grechnev and A. S. Kovalev, Fiz. Nizk. Temp. **24**, 340 (1998) [Low Temp. Phys. **24**, 257 (1998)].
[9] A. G. Grechnev and A. S. Kovalev, Fiz. Nizk. Temp. **24**, 839 (1998) [Low Temp. Phys. **24**, 629 (1998)].
[10] O. K. Dudko and A. S. Kovalev, Fiz. Nizk. Temp. **24**, 559 (1998) [Low Temp. Phys. **24**, 422 (1998)].
[11] M. D. Greenberg, *Application of Green's Functions in Science and Engineering*, Prentice–Hall, Englewood Cliffs, N. J. (1971).
[12] G. Bateman and A. Erdeyi, *Tables of Integral Transforms*, McGraw Hill, 1954.
[13] E. Madelung, *Mathematical Apparatus of Physics*, 7th ed., Springer, 1964 (in German).

Translated by R. S. Wadhwa

Hysteretic phenomena and switching effects under phase transitions in external field

L. I. Stefanovich

*A. Galkin Physics and Engineering Institute, National Academy of Sciences of Ukraine, 72 R. Luxemburg St., 340114, Donetsk, Ukraine**

(Submitted July 13, 1998)
Fiz. Nizk. Temp. **25**, 33–37 (January 1999)

The field dependence of the order parameter is investigated theoretically, using a statistical approach within the framework of the Ginzburg–Landau model with respect to the ferroelectric phase transition. It is found that, along with the existence of ordinary non-switching hysteresis is not too high fields ε ($\varepsilon \ll \varepsilon_c$, where ε_c is the coercive field), hysteresis of a switching type can be observed at the fields in excess of the coercive one. © *1999 American Institute of Physics.* [S1063-777X(99)00501-0]

The influence of a quasi-stationary external field on the formation and growth dynamics of 180°-domains was investigated in[1] within the framework of the Ginzburg–Landau model, using a statistical approach.

Our goal in this paper is to follow evolution of the domain structure which has already been formed in ferroelectrics depending on the magnitude and the direction of the external field.

To characterize quantitatively the change of a system state passing through the critical temperature point T_C of a phase transition, one or more values (called order parameters) are introduced. In the case of the ferroelectric phase transition the projection of the polarization vector on a certain crystallographic direction is used as a long-range order parameter $\eta(\mathbf{r},t)$.

To describe the relaxation processes taking place in the system undergoing the phase transition, there is no need to know the spatial distribution of order parameter $\eta(\mathbf{r},t)$ in detail over the total macroscopic specimen. Therefore, in the subsequent discussion, as before,[1] we shall deal with the search of the main physically significant characteristics of this function, such, for example, as the average (over the crystalline grain) value of the order parameter $\langle \eta(\mathbf{r},t)\rangle \equiv \overline{\eta}(t)$ and two-point correlation function

$$\langle \xi(\mathbf{r},t)\xi(\mathbf{r}',t)\rangle \equiv K(\mathbf{s},t), \quad \mathbf{s}=\mathbf{r}-\mathbf{r}', \tag{1}$$

where we have introduced the centered order parameter $\xi(\mathbf{r},t) \equiv \eta(\mathbf{r},t) - \overline{\eta}(t)$. The equations describing the temporal evolution of $\overline{\eta}(t)$ and $K(\mathbf{s},t)$ on all stages of ordering were introduced in[1] on the base of Ginzburg–Landau functional for nonequilibrium order parameter.

Our interest in this work is with the behavior of the order-disorder system for times which are greater in comparison with the time of forming (τ_d), but much less than the time of coalescence (τ_c) of the domain structure ($\tau_d \ll t \ll \tau_c$). Therefore, in the subsequent analysis for field dependence of the order parameter $\overline{\eta} = \overline{\eta}(\varepsilon)$ we shall use the asymptotic system of equation obtained in Ref. 1

$$\begin{cases} \dfrac{d\overline{\eta}}{dt} = \dfrac{1}{2}[(\alpha - 3D(t) - \overline{\eta}^2)\overline{\eta} + \varepsilon], \\ \dfrac{dD(t)}{dt} = (\alpha - D(t) - 3\overline{\eta}^2)D(t), \end{cases} \tag{2}$$

where $D(t) \equiv K(0,t)$; $\alpha = (T_c - T)/T_c$ is a dimensionless parameter which characterizes the proximity of temperature T, up to that the specimen cooled, to the ordering temperature T_c; $\varepsilon = E/T_c$ is an external field in corresponding units.

The singular (stationary) points of the system (2) correspond to the thermodynamic equilibrium states of ordering system and can be found from the conditions of vanishing the first derivatives with respect to time on the left sides of the Eqs. (2) as $t \to \infty$. Hence it follows that the system of two algebraic equations in variables $\overline{\eta}$ and D takes the form

$$\begin{cases} \varepsilon + \alpha\overline{\eta} - 3D\overline{\eta} - \overline{\eta}^3 = 0, \\ (\alpha - D - 3\overline{\eta}^2)D = 0. \end{cases} \tag{3}$$

The roots of the above-mentioned system yield the coordinates of singular points in the plane $(\overline{\eta}, D)$.

In this work we shall consider only the case $T < T_c$, i.e., $\alpha > 0$, when there is a whole system of singular points. However, only the points located in the upper half-plane of the phase pattern (in variables $\overline{\eta}, D$) will have a physical sense. Recall that the positions of these singular points, in the case of weak field ($\varepsilon \ll \alpha^{3/2}$), were found by us in Ref. 1.

The first singular point I [$\overline{\eta} = -(\varepsilon/\alpha)$, $D=0$], which corresponds to a homogeneous disordered state, is an unstable node (Fig. 1).

The second point II ($\overline{\eta} = \sqrt{\alpha} + (\varepsilon/2\alpha)$, $D=0$) corresponds to a homogenous ordered state ''aligned with the external field'' and is a stable node (Fig. 1).

The third point III ($\overline{\eta} = -\sqrt{\alpha} + (\varepsilon/2\alpha)$, $D=0$) corresponds to homogenous ordering, but it is ''opposite to the field.'' This point is also a stable node (Fig. 1).

Both the second and the third singular points correspond to single-domain type of the specimen ordering.

All the rest of the singular points (with $D \neq 0$) correspond to inhomogeneous ordering, i.e., to one or another polydomain structures.

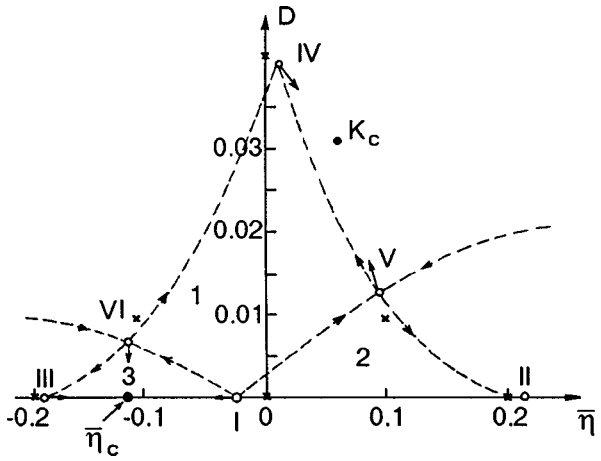

FIG. 1. Phase pattern of order–disorder system. The singular points of the system (2) at $\varepsilon=0$ are marked by the crosses ($\times$); the singular points (I–VI) for the system (2) at $\varepsilon\neq 0$ are marked by circles ($\bigcirc$) and separatrices are indicated by dotted lines. The arrows indicate the directions of motion for the singular points with increasing the external field. The bifurcation points (at $\varepsilon=\varepsilon_c$) for the system (2) ($\eta_c$ and K_c) are shown by black circles ($\bullet$).

The fourth point IV [$\overline{\eta}=\varepsilon/2\alpha; D=\alpha-(3\varepsilon^2/4\alpha^4)$] (Fig. 1) is a stable node and corresponds to the possibility of a polydomain structure realization. The fact that $\eta\neq 0$ in this state corresponds to some non-equivalency of domains of two types. However, in weak fields this distinction is small (to the extent of the ratio ε/α).

Finally, there are another two singular points of the saddle type. One of them V (''right saddle'') with coordinates [$\overline{\eta}=\sqrt{\alpha}/2-\varepsilon/4\alpha;\ D=\alpha/4+3\varepsilon/(4\sqrt{\alpha})$] (Fig. 1) corresponds to a possibility for realizing such a quasi-stationary polydomain structure, where the volume fraction of domains of the same type (e.g., with polarization vector, aligned with field) substantially exceeds the volume fraction of the other type domains (opposed to the field).

The other point (''left saddle'') [$\overline{\eta}=-\sqrt{\alpha}/2-\varepsilon/4\alpha;\ D=\alpha^*/4-3\varepsilon/(4\sqrt{\alpha})$] (the point VI, Fig. 1) corresponds to a possibility for realizing the quasi-stationary polydomain structure as well. However, in this situation the volume fraction of domains with the polarization vector oriented opposite to the field substantially exceeds a volume fraction of domains aligned with the field.

Two separatrices, leaving the origin of coordinates and passing through the ''left'' and ''right'' saddle points, divide the phase pattern into the three parts. The upper central sector (1) is the ''attraction region''of inhomogeneous (polydomain) state, the lower right-hand (2) and lower left-hand sectors (3) correspond to two ''attraction regions'' of homogeneous single-domain states.

In the context of this work our interest will not be with the locations of singular points by itself on a phase pattern at fixed value of external field, but their evolution and bifurcation under changes of a value and direction of external field ε. It is suggested that the field changes slowly enough (quasi-statically) in comparison with time of polydomain structure formation ($\tau_\varepsilon \gg \tau_d$). Recall that for definiteness we shall consider a phase transition in ferroelectrics connected with the appearance of a spontaneous polarization at $T<T_c$.

In order to follow the evolution of singular points on the phase pattern depending on the field ε we direct our attention to the system (3). From the second equation of a system it follows that there are solutions of its satisfying the condition $D(t)=0$. In this case the first equation of the system (3) takes the form

$$\varepsilon=\overline{\eta}^3-\alpha\overline{\eta}. \tag{4}$$

The right-hand side of (4) has extremes in two symmetric points with respect to the ordinate axis

$$\overline{\eta}_c^{(1,2)}=\pm\sqrt{\alpha}/\sqrt{3}. \tag{5}$$

The positive value of parameter ($\overline{\eta}_c>0$) corresponds to the minimum critical field

$$\varepsilon_c^{\min}=-\frac{2\alpha^{3/2}}{3\sqrt{3}}, \tag{6}$$

and the negative value of parameter ($\overline{\eta}_c<0$) corresponds the maximum critical field

$$\varepsilon_c^{\max}=\frac{2\alpha^{3/2}}{3\sqrt{3}}. \tag{7}$$

Since, while writing down the thermodynamic potential (1) in[1] we assumed at $\varepsilon>0$, then it is natural to consider only the maximum critical field ($\varepsilon_c=\neq\varepsilon_c^{\max}$), which we shall call critical field simply. To elucidate its physical sense, we consider what will happen with the singular points of the system (2) under smooth variation of external field beginning from values $\varepsilon\ll\varepsilon_c$.

Studying a behavior of the algebraic system (3) roots it is easy to verify that as the field ε is increased, the singular points I, III and VI located in the second quadrant begin to approach each other gradually. Simultaneously, the mutual approach of the singular points IV and V occurs. And only the second singlet pint (II), corresponding to the homogeneous (monodomain) ordering of the system (crystallite) as a whole, will recede further and further from the rest of the singular points, moving towards the right along the abscissa axis.

The approach of the above-mentioned groups of singular points will cause the sectors *1* and *3* to decrease (Fig. 1). It testifies that the potentialities both for the polydomain and for the monodomain ordering ''opposite to the field'' will be decreased gradually. The sector *2*, on the contrary, grows to extend the range of conceivable initial conditions, beginning with these, the system will be ordered homogeneously, ''aligned with the field.'' That is, the external field specifies the direction of the preferential ordering.

When the critical value of the field $\varepsilon=\varepsilon_c$ is achieved, the confluence of the singular points I, III and VI into a single point η_c will occur. Simultaneously, i.e., at the same value of critical field, the singular points IV, V are merged into the singular point K_c with the coordinates ($1/2\sqrt{\alpha/3}$; $3\alpha/4$). At the same moment (i.e., in merging two groups of singular points) the sectors *1* and *3* disappear on the phase pattern (Fig. 1). In other words, at the critical value of the external field bifurcation of the ordering system trajectories takes place.

The further increasing of the external field up to the values $\varepsilon > \varepsilon_c$ gives all the singular points to disappear, except point II. The fields higher than critical ones should be considered to be strong. Therewith, in the range of the strong field ($\varepsilon \gg \varepsilon_c$), the average value of order parameter in the single-domain state does not depend on temperature to a first approximation, and it is defined only by the value of the field

$$\overline{\eta} \sim \varepsilon^{1/3}. \tag{8}$$

Let us consider the manner in which the character of the ferroelectric domain structure will vary under the influence of the external field. With this in mind we shall trace the variation of the order parameter average value $\overline{\eta}$ in relation to the magnitude and the direction of the applied field ε, identifying $\overline{\eta}$ with the average polarization of the specimen and the field ε—with the uniform electric field.

Analysis will be based on treating the behavior of the solutions for the system of Eqs. (3) under slow, continuous variation of the parameter ε, i.e., on the study of the influence of the external field on the evolution of the ordering system singular points on the phase pattern (Fig. 1).

Initially let us take up the manner in which the ordering system which in the polydomain state corresponds to the singular point IV on the phase pattern (Fig. 1), behaves oneself with time in a weak varying external field. If the external field is changed slowly (quasi-statically) (i.e., $\tau_\varepsilon \gg \alpha^{-1}$), according to the phase diagram (Fig. 1) at the small deviations of field magnitude from zero, the system is limited by the polydomain state. The external field brings into disbalance between volume fractions of the phases: oriented ''opposed to the field'' and ''aligned with the fields'' in favor of the latter. In this case under small changes of the field ($|\varepsilon| \ll \varepsilon_c$) the order parameter $\overline{\eta}$ turns out to be proportional to the field

$$\overline{\eta} \sim \varepsilon/\alpha. \tag{9}$$

The inhomogeneities of the order parameter are therewith smoothed out by the external field

$$D \cong \alpha - 3\varepsilon^2/4\alpha^2. \tag{10}$$

Decreasing the dispersion of the order parameter, in accordance with (10), appears to be a second order effect in the field.

On further increasing the external field, as soon as the dependence $\overline{\eta} = \overline{\eta}(\varepsilon)$ ceases to obey the linear law (9), the order parameter $\overline{\eta}$ in cyclic change of the field will not follow the line *OAOA′*. This change of the order parameter will have the form of a hysteretic loop (dotted line in Fig. 2). The hysteresis involved (in the limits of the polydomain states) has nothing to do with the switching one and it will appear to be more significant if the amplitude of varying of the external field is larger (naturally, within the area $|\varepsilon| < \varepsilon_c$).

However such a behavior of the order parameter $\overline{\eta}$ as a function of the slowly varied external field ε takes place only in the range of relatively weak field, when $|\varepsilon \ll \varepsilon_c$. As soon as the external field reaches its critical value ε_c, the confluence of the singular points IV and V on the phase pattern (Fig. 1) into a single singular point K_c, with coordinates $(1/2\sqrt{\alpha/3},\ 3\alpha/4)$, occurs. Just at such a value of the external field ($\varepsilon = \varepsilon_c$) any polydomain structure appears to be absolutely unstable with respect to further growth of field. In stronger fields ($\varepsilon > \varepsilon_c$) the singular points IV, V disappear at all, that is any polydomain state becomes energetically disadvantageous and order-disorder system switches sharply (practically by a leap) to the thermodynamically stable monodomain state oriented ''with the field,'' with the average value of the order parameter $\overline{\eta} = 2\sqrt{\alpha/3}$ and with dispersion equal to zero ($D = 0$). This single-domain state corresponds to the singular point II on the phase pattern (Fig. 1).

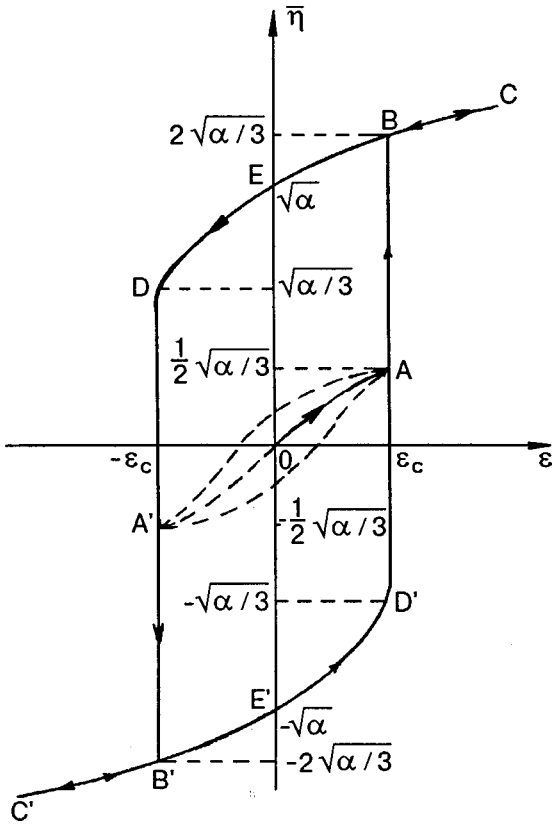

FIG. 2. Field dependences of the order parameter average value $\overline{\eta}$: the ordinary nonswitching hysteresis is indicated by a dotted line; the hysteresis of switching type is marked by a solid line.

Further increasing the field will cause polarization, in accordance with (8), i.e., the average value of order parameter $\overline{\eta}$ at the section of the curve from *B* to *C* (Fig. 2) grows insignificantly ($\sim \varepsilon^{1/3}$).

The field dependence of the order parameter $\overline{\eta} = \overline{\eta}(\varepsilon)$ follows the curve *CB* (Fig. 2) as the value of the field decreases, i.e., decreasing the average value of the order parameter up to the field value $\varepsilon = \varepsilon_c$ in a reversible way. However, when the field ε becomes less than a critical one ($\varepsilon < \varepsilon_c$), the average value of the order parameter does not return to the polydomain branch *OA*, i.e., the ordering character of a specimen remains homogeneous (monodomain). Furthermore, as the field magnitude decreases, the average value of the order parameter will continue to decrease monotonely, following the curve *BE* (Fig. 2) and attaining the residual magnitude $\sqrt{\alpha}$ in total switching off the field ($\varepsilon = 0$). To relieve this residual value of the order parameter $\overline{\eta}$, i.e., to switch the specimen into the alternative ordering

state, it is enough to change the sign of the field ε. In increasing the field of the opposite polarity in the range of values $-\varepsilon_c<\varepsilon<0$ the further decreasing of the average order parameter to the value $\sqrt{\alpha/3}$ (the curve *ED* on Fig. 2) will proceed. The ordering character will not be changed here until the critical value of the field $-\varepsilon_c$ has been attained. At the part of the curve from *E* to *D*, when the external field ε and the order parameter $\overline{\eta}$ have the opposite polarity, the states of the system are unstable thermodynamically, it would be advantageously energetic for the system, if the sign of the order parameter coincided with the field sign. In other words, the section *ED* (as well as $E'D'$) corresponds to the metastable states of the order–disorder system.

The further increasing of the external field magnitude will produce ''the frustration'' of the value $\overline{\eta}$ to the magnitude $-2\sqrt{\alpha/3}$ (the point B', Fig. 2). This fact indicates the switching of the crystallite from the monodomain state with one direction of the spontaneous polarization into a state like this but with opposite direction of polarization in response to the electric field over the whole volume simultaneously. Thus the field $-\varepsilon_c$ is nothing but a coercive field. In accordance with (7), the magnitude of this coercive field depends on temperature through the parameter $\alpha=(T_c-T)/T_c$, which characterizes a proximity of the system considered to the phase transition critical point. To evaluate the coercive field ε_c obtained by us theoretically for really achieved values of α, one should go to corresponding dimensional notations in (7). The transition in triglycine sulphate crystal is one of the most completely studied ferroelectric second order phase transitions. The departure of behavior answering to Landau theory are not observed in this ferroelectrics up to $\alpha\sim10^{-4}$–10^{-5}.[2] For these values of α it turns out that the magnitude of coercive field E_c found by us will achieve quite large values ~50–100 kV/cm. However, the experimental investigations of ferroelectric hysteretic phenomena in the fields such as these or even larger ones ($E\sim10^6$ V/cm) are known (see, e.g., Refs. 3 and 4).

The analysis of the following order parameter average values $\overline{\eta}$ behavior depending on magnitude and direction of the applied external field indicates that it is described by the curve $C'B'E'D'$ (Fig. 2), which is nothing but symmetric doubling of the line *CBED* with respect to the origin of the coordinates. When the field value ε_c has been reached, the order-disorder system falls from the point D' to the point B', i.e., it switches from one monodomain state into another one. Thus, the large loop $BDB'D'$, known as the switching hysteresis, is closed.

However it should be borne in mind that the hystersis pattern described theoretically above is restricted to the idealized order-disorder system. It is unlikely that ''the repolarization'' of the system from one monodomain state to another monodomain one (under the changes of an external field sign) will proceed over the whole volume of the specimen (crystallite) simultaneously. Actually in a volume of monodomain crystal the energetically ''advantageous'' regions with the opposite signs of the order parameter occur in a fluctuational way and grow rapidly.[5] In other words, along the way from one monodomain state to another monodomain one the system passes through a number of the intermediate polydomain states. Besides, different defects and imperfections of the crystalline structure give rise to the obstacles to the free motion of the domain boundaries and for their passing out of the volume. All this will make the hysteresis loop to narrow and ''to smooth out;'' so that, for example, the coercive field may turn out to be less than the value E_c obtained theoretically.

The author thanks to Professor E. P. Feldman for fruitful discussions. This work was partially supported by the State Foundation of Fundamental Investigation of Ukraine, Grant No. 2, 4/220–97.

*E-mail: listef@host.dipt.donetsk.ua

[1] L. I. Stefanovich, Fizika Nizkikh Temperatur **24**, 856 (1998) [Low Temp. Phys. **24**, 643 (1998)].
[2] M. E. Lines and A. M. Glass, *Principles and Application of Ferroelectrics and Related Materials*, Clarendon Press, Oxford (1977).
[3] O. E. Fesenko, R. V. Kolesova, and Y. G. Syndeyev, Ferroelectrics **20**, 177 (1978).
[4] S. Sawada, T. Yamaguchi, and H. Suzuki, Ferroelectrics **63**, 3 (1985).
[5] B. A. Strukov and A. P. Levanyuk, *Physical Principles of Ferroelectric Phenomena in Crystals* [in Russian], Nauka, Moscow (1995).

This article was published in English in the original Russian journal. It was edited by R. T. Beyer.

Effect of linearly polarized light on metamagnetic phase transition in $Ca_3Mn_2Ge_3O_{12}$ garnet

V. A. Bedarev, V. I. Gapon, and S. L. Gnatchenko

*B. Verkin Institute for Low Temperature Physics and Engineering, National Academy of Sciences of the Ukraine, 310164 Kharkov, Ukraine**)*

(Submitted July 22, 1998)
Fiz. Nizk. Temp. **25**, 38–42 (January 1999)

It has been found that the field H_t of a metamagnetic phase transition in $Ca_3Mn_2Ge_3O_{12}$ garnet changes as a result of illumination of the crystal with linearly polarized light. The value of H_t decreases under the illumination with the light polarization $\mathbf{E}\|[110]$ and increases in the case of the light polarization $\mathbf{E}\|[1\bar{1}0]$. The difference in the values of transition field in these two cases amounts to ~ 100 Oe at the temperature $T=7$ K, for which $H_t \simeq 31.2$ kOe in an unexposed crystal. The change in the value of the metamagnetic phase transition field is attributed to the photoinduced magnetic moment whose magnitude and direction depend on the polarization of the inducing radiation. © *1999 American Institute of Physics.* [S1063-777X(99)00601-5]

The exposure of $Ca_3Mn_2Ge_3O_{12}$ garnet to linearly polarized light affects the magnetization reversal in the sublattices of this antiferromagnet (AFM).[1] The observed effect was attributed to the emergence of a photoinduced magnetic moment in the crystal, the magnitude and direction of this moment depending on the polarization of the inducing light. The photoinduced magnetic moment was measured recently in $Ca_3Mn_2Ge_3O_{12}$ on a SQUID magnetometer.[2] Its magnitude ~ 0.03 G at $T=5$ K.

The change in the magnetic state of a Mn–Ge garnet (MnGeG) under the action of light must not only be manifested in the magnetization reversal of the sublattices in the antiferromagnetic state, but also affect the metamagnetic (MM) phase transition observed in this crystal in a magnetic field.[3–5] The present research aims at clarifying and analyzing the effect of linearly polarized light on the metamagnetic phase transition in $Ca_3Mn_2Ge_3O_{12}$ garnet.

The sample under investigation was a monocrystalline plate of thickness $\sim 130\ \mu$m, cut at right angles to the tetragonal axis [001] of the crystal. Surface stresses appearing in the plate after mechanical treatment were eliminated by annealing for 6 h at a temperature of 1000 °C. The MnGeG plate free of mechanical stresses was subjected to additional thermal treatment according to the technique described in Ref. 6 for the sake of monodomainization. As a result of thermal treatment of the sample, its crystalline domain structure emerging in MnGeG as a result of a Jahn–Teller transition from the cubit to the tetragonal phase at $T \approx 520$ K was destroyed.[6,7] The sample was placed on the cold finger in an optical He cryostat and was in vacuum. The temperature was measured by a resistance thermometer to within 0.1 K. A superconducting solenoid produced a magnetic field parallel to the tetragonal axis of the crystal and coinciding with the direction of light propagation.

The effect of illumination with linearly polarized light on the first-order MM phase transition in MnGeG was studied by measuring field dependences of the angle of rotation of the light polarization plane as well as by visual observation of the two-phase domain structure formed during the phase transition. The optical diagram of the experimental setup used for visual observation of the two-phase domain structure is shown in Fig. 1. The light from a incandescent lamp *1* passing through polarizer *6* was incident on the sample *7* whose image was constructed with the help of the objective *9* at the photocathode of a television camera *11*. The image formed was supplied to monitor *12* or recorder by a VCR *13*. The light from the incandescent lamp was attenuated by filters. Its intensity did not exceed $0.01\ \mathrm{W/cm^2}$ and did not affect the magnetic state of the crystal under investigation. The two-phase domain structure observed in the vicinity of the MM phase transition in MnGeG had a weak contrast between the domains of the AFM and MM states. For this reason, computer processing of the image was carried out to enhance its contrast. The sample was exposed to light from a He–Ne laser *16* having a wavelength $\lambda = 633$ nm and a power of approximately $0.1\ \mathrm{W/cm^2}$. The optical system of the setup used for illumination was supplemented with rotating mirrors *14* and *15* as well as the field diaphragm *4* of an appropriate shape, which made it possible to illuminate locally the chosen region of the sample. The image of the diaphragm was formed on the sample by lens *5*. The setup described above allowed us to observe visually and to record on a tape the transition of MnGeG from the AFM to the MM state in an unexposed sample and in a sample exposed to He–Ne laser radiation.

The field dependences of the polarization plane of light were measured by using the method of light modulation in the polarization plane and synchronous detection. The source of light in these measurements was a He–Ne laser ($\lambda = 633$ nm). In order to eliminate the influence of the measuring beam of light on the magnetic state of the crystal, the luminous flux density of the measuring light was reduced to

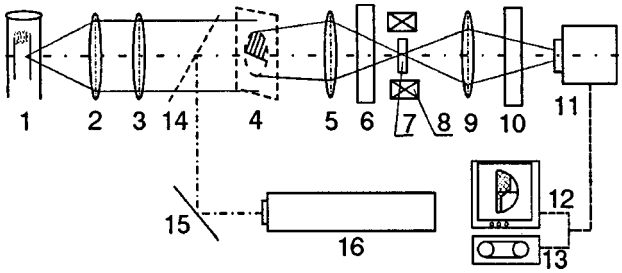

FIG. 1. Optical system of the experimental setup for visual observation of the domain structure: incandescent lamp (*1*), lenses (*2, 3, 5*), field diaphragm (*4*), polarizer (*6*), sample (*7*), solenoid (*8*), objective (*9*), analyzer (*10*), television camera (*11*), monitor (*12*), VCR (*13*), mirrors (*14, 15*), and He–Ne laser (*16*).

$0.01\,\mathrm{W/cm^2}$ as in the case of visual observation of the two-phase domain structure, while the sample was illuminated by light from a He–Ne laser having a power of $\sim 0.1\,\mathrm{W/cm^2}$.

When the inducing light propagates in the antiferromagnetic $Ca_3Mn_2Ge_3O_{12}$ garnet along the tetragonal axis $z\|[001]$, the induced magnetic moment $\mathbf{m}^{\mathrm{ph}}$ is parallel to this axis, and its magnitude and direction are defined by the relation

$$m_z^{\mathrm{ph}} = A\cos 2\varphi + B\sin 2\varphi, \tag{1}$$

where φ is the angle between the light polarization plane and the [100] direction in the crystal, and A and B are constants.[1] According to this relation, m_z^{ph} has opposite signs for the polarizations $\mathbf{E}\|[110]$ and $\mathbf{E}\|[1\bar{1}0]$ of the inducing light. Therefore, we can expect that illumination of the crystal with light having such polarizations produces different effects on the MM transition. In order to verify this assumption, we made the following experiment. At first, a uniform antiferromagnetic state was produced in the sample by applying a magnetic field sufficient for magnetization. It is well known[8] that monodomainization of an antiferromagnet containing collinear domains requires, in addition to the longitudinal field component H_z, also the H_x and H_y components. These field components were present in the experiment due to departures from exact orientation of **H** along the tetragonal axis of the crystal. According to estimates, the deviation of the field from the tetragonal axis was $\sim 3°$. Under such conditions, the monodomainization of the sample requires the application of a field $H \approx 20\,\mathrm{kOe}$ ($H_z \approx 20\,\mathrm{kOe}$, H_x and $H_y \approx 1\,\mathrm{kOe}$.[1] Just such a value of the external magnetic field was required for the monodomainization of the sample in our experiment. The magnetization of the sample was monitored visually.

After the completion of monodomainization and switching off the magnetic field, the upper half of the crystal was exposed to laser radiation with polarization $\mathbf{E}\|[110]$, while the lower part was illuminated by light with $\mathbf{E}\|[1\bar{1}0]$ for 5 min. Then the transition from the antiferromagnetic to the metamagnetic state was observed visually. Figure 2 shows photographs of the two-phase domain structure formed during the field-induced phase transition in the exposed sample. The dot-and-dash curve denotes the boundary between the AFM and MM phases, and two dashed lines indicate the interface between the regions of the crystal exposed to light with the polarizations $\mathbf{E}\|[110]$ and $\mathbf{E}\|[1\bar{1}0]$ (the region between the dashed lines is due to inaccuracy in setting the field diaphragm for illuminating first one part of the sample with $\mathbf{E}\|[110]$, and then the other part of the sample with $\mathbf{E}\|[1\bar{1}0]$). It can be seen from Fig. 2a that the AFM–MM transition in the upper part of the sample occurs earlier than in the lower part. In order to make sure that the difference in the transition fields in the upper and lower parts of the sample is due to illumination and not random factors (like internal mechanical stresses or temperature gradients), the upper part of the sample in the second stage of the experiment was exposed to light with the polarization $\mathbf{E}\|[1\bar{1}0]$ and the power part by light with the polarization $\mathbf{E}\|[110]$. In this case, an inverse effect was observed, i.e., the AFM–MM transition in the upper part of the sample was delayed (Fig. 2b). Thus, our visual observations lead to the conclusion that light with the polarization $\mathbf{E}\|[110]$ stimulates a phase transition from the AFM to the MM state in $Ca_3Mn_2Ge_3O_{12}$ garnet, while light with the polarization $\mathbf{E}\|[1\bar{1}0]$ delays it.

In order to determine the magnitude of the photoinduced displacement ΔH_t of the phase-transition field, we measured the field dependences $\varphi(H)$ of the angle of rotation of the polarization plane shown in Fig. 3. These dependences were measured on the same segment of the sample having a diameter $\sim 100\,\mu\mathrm{m}$ and exposed first to light with the polarization $\mathbf{E}\|[110]$, and then to light with the polarization $\mathbf{E}\|[1\bar{1}0]$. In

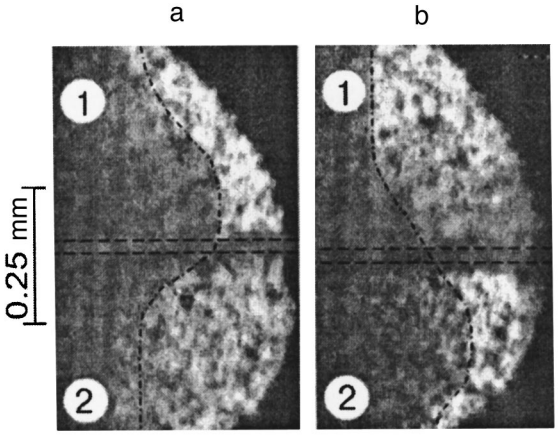

FIG. 2. Two-phase domain structure formed in a $Ca_3Mn_2Ge_3O_{12}$ garnet plate during an AFM–MM phase transition upon illumination of the crystal with linearly polarized light. The dot-and-dash curve marks the AFM–MM interface: region *1* of the plate (above the dashed line) is exposed to light with polarization $\mathbf{E}\|[110]$, while region *2* (below the dashed line) to light with polarization $\mathbf{E}\|[1\bar{1}0]$ (a); region *1* is exposed to light with polarization $\mathbf{E}\|[1\bar{1}0]$, while region *2* to light with polarization $\mathbf{E}\|[110]$ (b).

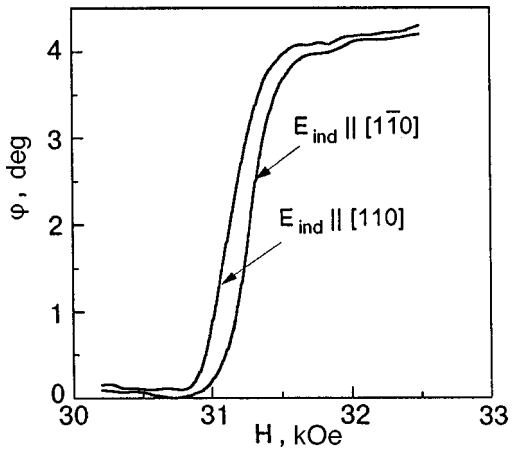

FIG. 3. Field dependences of the angle of rotation of light polarization plane, measured in a region of the $Ca_3Mn_2Ge_3O_{12}$ sample having a diameter $\sim 100\ \mu$m and exposed preliminarily to linearly polarized light with polarization $\mathbf{E}\|[110]$ or $\mathbf{E}\|[1\bar{1}0]$. The sample temperature $T=7$ K.

both cases, the intensity and duration of illumination were the same. The first-order metamagnetic phase transition corresponds to a jump on the $\varphi(H)$ curve. It can be seen from Fig. 3 that the difference $2\Delta H_t = H_{t2} - H_{t1}$ in the transition fields for the cases when the crystal was exposed to light with polarizations $\mathbf{E}\|[110]$ and $\mathbf{E}\|[1\bar{1}0]$ amounts approximately to 100 Oe at the sample temperature $T=7$ K, i.e., $\Delta H_t \approx 50$ Oe. The field corresponding to the MM transition in the investigated region of the sample prior to illumination, which was determined from the position of the midpoint of the segment on the $\varphi(H)$ curve in which the angle of rotation changes strongly, was $H_t \approx 31.2$ kOe, i.e., close to the value of $(H_{t1}+H_{t2})/2$.

Using the value of the photoinduced magnetic moment obtained in Ref. 2, we can estimate the magnitude of the shift ΔH_t in the field of the metamagnetic phase transition in MnGeG, induced by illumination with linearly polarized light. For this purpose, we write the energy of the magnet in a field in the form of the power expansion in H (see Ref. 9):

$$E = E_0 - m_i^0 H_i - \chi_{ij} H_i H_j + \ldots, \tag{2}$$

where E_0 is the energy of the magnet in zero magnetic field, $\mathbf{m}^0$ the spontaneous magnetic moment, and χ_{ij} the magnetic susceptibility. The induction of magnetic moment by light leads to a change in the energy of the magnet by $\mathbf{m}^{\rm ph}\mathbf{H}$. Taking this correction into account and confining the power expansion in H to the second-order term, we can write expression (2) for the energy of the magnet in the form

$$E = E_0 - m_i^0 H_i - \chi_{ij} H_i H_j - m_i^{\rm ph} H_i\,. \tag{3}$$

It was noted above that linearly polarized light induces a magnetic moment in the AFM state. As regards the MM state, no linear magneto-optical effect (LMOE) is observed in MnGeG in this state according to the results of measurements of linear birefringence[10,11] and linear dichroism.[11] In the absence of LMOE in the MM state, there is no photoinduced magnetic moment either in this state since the effect of induction of $\mathbf{m}^{\rm ph}$ in MnGeG by linearly polarized light is inverse to LMOE.[1] Assuming that $m^{\rm ph}=0$ in the MM state and taking into account the absence of a spontaneous magnetic moment in the AFM state, we can use the condition of equality of the energies of the AFM and MM states at the phase-transition point to write the following equation for the cases when a crystal is exposed to light with the polarizations $\mathbf{E}\|[110]$ and $\mathbf{E}\|[1\bar{1}0]$:

$$E_0^A - \chi_A H_{t1}^2 + m_z^{\rm ph} H_{t1} = E_0^M - m_z^0 H_{t1} - \chi_M H_{t1}^2, \tag{4}$$

$$E_0^A - \chi_A H_{t2}^2 - m_z^{\rm ph} H_{t2} = E_0^M - m_z^0 H_{t2} - \chi_M H_{t2}^2. \tag{5}$$

In these equations, the subscripts A and M correspond to the AFM and MM phase respectively, and m_z^0 is the spontaneous magnetization in the MM state. While writing these equations, we took into account the fact that, in accordance with (1), $m_z^{\rm ph}$ has opposite signs for $\mathbf{E}\|[110]$ and $\mathbf{E}\|[1\bar{1}0]$. Solving the system of equations (4) and (5), we obtain the following expression for the photoinduced displacement of the field corresponding to a metamagnetic phase transition:

$$\Delta H_t = m_z^{\rm ph}/[2(\chi_M - \chi_A) + m_z^0/H_t]. \tag{6}$$

While deriving this expression, we considered that $H_t = (H_{t1}+H_{t2})/2$. Substituting the value of $m_z^{\rm ph}$ obtained in Ref. 2 as well as the values of $(\chi_M - \chi_A)$ and m_z^0 from Refs. 3 and 5 into (6), we obtain $\Delta H_t \simeq 15$ Oe. It should be noted that the value of m_z^0 was determined by extrapolating the linear field dependence of magnetization in the MM state to $H=0$. The calculated value of ΔH_t is smaller than the experimentally measured value by a factor of several units. However, the agreement of the experimental value of ΔH_t and the value estimated from (6) can be regarded as quite satisfactory on account of the fact that the value of $m^{\rm ph}$ was measured in Ref. 2 for the direction of light propagation and the direction of magnetic field along the [100] axis of the crystal as well as large errors in the measurements of the values of $(\chi_M - \chi_A)$ and m_z^0 in polydomain samples.[3,5]

Thus, our investigations proved that linearly polarized light induces a change on the magnitude of the field corresponding to a metamagnetic phase transition in $Ca_3Mn_2Ge_3O_{12}$ garnet. The magnitude of the transition field can increase or decrease as compared to the value of H_t in an unexposed crystal depending on the polarization of the inducing light.

The authors are grateful to Dr. J.-M. Desvignes, a scientist from the Laboratoir de Physique des Solides, CNRS, Meudon-Bellevue, France, for supplying MnGeG single crystals for the experiments.

This research was partly supported by the INTAS Grant No. 97.0366.

*)E-mail: bedarev@ilt.kharkov.ua

[1] N. F. Kharchenko and V. A. Bedarev, Fiz. Nizk. Temp. **19**, 72 (1993) [Low Temp. Phys. **19**, 52 (1993)].
[2] S. L. Gnatchenko, N. F. Kharchenko, M. Baran, and R. Szymczack, Abstracts of the ICM'97, Australia, M3-9 (1997).
[3] Z. A. Kazei, B. V. Mil', and V. I. Sokolov, Pis'ma Zh. Éksp. Teor. Fiz. **31**, 338 (1980) [JETP Lett. **31**, 308 (1980)].
[4] Z. A. Kazei, N. P. Kolmakova, D. I. Sirota, and V. I. Sokolov, Pis'ma Zh. Éksp. Teor. Fiz. **37**, 240 (1983) [JETP Lett. **37**, 285 (1983)].

[5] D. Esteve, R. Plumier, P. Feldmann, and H. Le Gall, Phys. Status Solidi A **57**, K83 (1980).
[6] S. L. Gnatchenko, V. V. Eremenko, S. F. Sofroneev *et al.*, Zh. Éksp. Teor. Fiz. **90**, 179 (1986) [Sov. Phys. JETP **63**, 102 (1986)].
[7] W. Grraeff, J. Kub, and K. Wieteska, Phys. Status Solidi A **126**, 477 (1991).
[8] A. V. Bibik, N. F. Kharchenko, and S. V. Petrov, Fiz. Nizk. Temp. **15**, 1280 (1989) [Sov. J. Low Temp. Phys. **15**, 707 (1989)].
[9] G. Gorodetsky, B. Sharon, and S. Shtrikman, Solid State Commun. **5**, 739 (1967).
[10] V. V. Eremenko, S. L. Gnatchenko, N. F. Kharchenko *et al.*, Acta Phys. Pol. A **68**, 419 (1985).
[11] N. F. Kharchenko, V. V. Eremenko, S. L. Gnatchenko *et al.*, Fiz. Nizk. Temp. **11**, 215 (1985) [Sov. J. Low Temp. Phys. **11**, 113 (1985)].

Translated by R. S. Wadhwa

ELECTRONIC PROPERTIES OF METALS AND ALLOYS

Collective electromagnetic mode in layered conductors

V. M. Gokhfeld

*A. Galkin Physicotechnical Institute, National Academy of Sciences of the Ukraine, 340114 Donetsk, Ukraine**)

V. G. Peschansky

*B. Verkin Institute for Low Temperature Physics and Engineering, National Academy of Sciences of the Ukraine, 310164 Kharkov, Ukraine***)

(Submitted July 22, 1998)
Fiz. Nizk. Temp. **25**, 43–48 (January 1999)

The transverse zero-sound wave in a one-component charged Fermi liquid with quasi-two-dimensional electron energy spectrum is considered in the framework of the Landau theory. In contrast to conventional metals, the electromagnetic wave propagation in such media along the weak conductivity direction is possible even for low intensities of the Fermi-liquid interaction. The field distribution in the sample under unilateral excitation is determined, the wave impedance is calculated, and the possibility of observing the effect in the pulse mode is considered. © *1999 American Institute of Physics.* [S1063-777X(99)00701-X]

Conducting synthetic crystals with a layered or chain structure and with a nearly metal-type but strongly anisotropic electric resistance have been studied intensely during recent years in many laboratories. By way of an example, we can mention polymers based on tetrathiafulvalene, polyacetylene, dichalcogenides of transition metals and their intercalates, as well as HTSC ceramics in the nonsuperconducting phase. Among simple metals, similar (although not so well pronounced) properties are observed only in graphite.

The theory of high-frequency properties of layered conductors can be constructed on the basis of concepts of effectively reduced dimensionality of the motion of charge carriers, i.e., the quasi-two-dimensional nature of the single-electron energy spectrum,[1–3] which is in accord with experimental data on the whole (see, for example, Ref. 4). However, many-electron phenomena, including the propagation of various types of zero-sound vibrations, are also of considerable interest. The concentration of free charge carriers in synthetic conductors is usually lower, i.e., the screening of the electron–electron interaction in them is apparently lower in such materials than in ''good'' metals. Along with anisotropy, this can lead to a clearer manifestation of many-particle effects in the electrodynamics of layered materials. A longitudinal zero-sound wave in a quasi-two-dimensional two-band Fermi liquid and its interaction with elastic waves were considered earlier in Ref. 5.

In this communication, we propose a model analysis of the skin effect near the surface parallel to conducting layers, (x,y) on the basis of the Landau Fermi liquid theory[6] (see also Refs. 7–9). We analyze the conditions for the existence of collective electromagnetic (i.e., transverse) modes and prove that these conditions are considerably less stringent than in the isotropic case. We shall determine the dispersion relation for collective excitations and calculate the relevant contribution to the impedance.

Our basic assumption is that all energy characteristics of quasiparticles near the Fermi level (both the one-particle Hamiltonian and the Landau interaction function) weakly depend on the z-component of quasimomentum, i.e., can be expanded into rapidly converging Fourier series in the variable $t \equiv ap_z/\hbar$ (a is the lattice period in the z-direction). Retaining only the zeroth and first harmonics and neglecting anisotropy in the plane of the layers, we can present the dispersion law for charge carriers in the form

$$\varepsilon(\mathbf{p}) = p_\perp^2/2m - (\hbar v_0/a)\cos t, \tag{1}$$

where $p_\perp^2 \equiv p_x^2 + p_y^2$. The corresponding Fermi surface is a weakly corrugate open cylinder. In the given problem, it is sufficient to assume that it is either its only sheet, or other sheets are equivalent to it. For this model, we can write the expression

$$v_z = v_0 \sin t, \quad v_x = v_\perp(t)\cos\varphi,$$

$$v_\perp^2 = v_F^2 + (\hbar v_0/2ma)\cos t, \tag{2}$$

the number of states per unit volume and their energy density are given by the formulas

$$N = \varepsilon_F\langle 1\rangle, \quad \langle 1\rangle = m/a\pi\hbar^2, \tag{3}$$

respectively, and the role of the anisotropy parameter is played by the small ratio of velocities $v_0/v_F \ll 1$.

In complete analogy with (1), the Landau function connecting the true and effective distributions of quasiparticles can be written in the form

$$L(\mathbf{p},\mathbf{p}') = L_0(\varphi,\varphi') + (v_0/v_F)L_1(\varphi,\varphi',t,t'). \tag{4}$$

In this expansion, we confine ourselves only to the first terms. In accordance with the symmetry of the problem, it is natural to assume that it is an even (and, naturally, periodic) function of the difference between the azimuthal angles $\varphi-\varphi'$.

Directing the electric vector **E** in the electromagnetic wave along the x-axis, we can present the kinetic equation in the form

$$kv_z\Phi-\omega\Psi-i\nu(\Phi-\langle\Phi\rangle/\langle 1\rangle)=ieEv_x; \tag{5}$$

$$\Phi=\Psi+(2\pi)^{-2}\int_{-\pi}^{\pi}dt'\int_{-\pi}^{\pi}d\varphi' L_0(\varphi-\varphi')\Psi(\varphi',t'), \tag{6}$$

where k is the wave number ($\mathbf{k}\|0z$), ω the electromagnetic wave frequency, ν the effective frequency of dissipative scattering of charge carriers, and the angle brackets indicate, as before, standard integration over the Fermi surface with the weight $2v^{-1}(2\pi\hbar)^{-3}$. The system of equations (5) and (6) can be solved easily by introducing the harmonics of unknown functions Φ, Ψ and the kernel L_0 by the formula

$$F_1\equiv(2\pi)^{-1}\int_{-\pi}^{\pi}d\varphi F(\varphi)\cos\varphi.$$

Then it follows from (6) that $\Phi_1=\Psi_1+\overline{\Psi}_1 L_0$, where the bar indicates averaging over the variable t (i.e., over p_z). Eliminating Ψ in this way, we obtain from (5) the following expression for the function $\Phi_1(t)$:

$$\Phi_1=(eE/2i\tilde{\omega})R[v_\perp+\lambda\omega\overline{Rv_\perp}(\tilde{\omega}-\lambda\omega\overline{R})^{-1}], \tag{7}$$

where $\tilde{\omega}\equiv\omega+i\nu$, R is the resolvent factor defined as

$$R(t)=\tilde{\omega}/[\tilde{\omega}-kv_z(t)], \tag{8}$$

and the intensity of the Fermi-liquid interaction (abbreviated below as FLI) is characterized by the coefficient $\lambda\equiv L_{01}/(L_{01}+1)$. In the further analysis, we assume that $\lambda>0$.

Using the definitions

$$j_x\equiv-e\langle v_x\Phi\rangle=-e\langle 1\rangle\overline{\Phi_1 v_\perp},\quad \varepsilon\equiv 1+4\pi i j_x/\omega E,$$

for current and dielectric function, we obtain the following expression for the latter quantity:

$$\varepsilon=1-\frac{2\pi e^2\langle 1\rangle}{\omega\tilde{\omega}}\left[\overline{Rv_\perp^2}+(\overline{Rv_\perp})^2\frac{\lambda\omega}{\tilde{\omega}-\lambda\omega\overline{R}}\right]. \tag{9}$$

The averaged values appearing in this formula can be easily evaluated by using formula (2):

$$\overline{Rv_\perp^2}=v_F^2\overline{R},\quad \overline{Rv_\perp}=v_F\overline{R};\quad \overline{R}=\tilde{\omega}/\sqrt{\tilde{\omega}^2-k^2v_0^2}$$

(the second of these equalities holds to within $\sim(v_0/v_F)^2$; in the third equality we choose for the radical the branch with arguments between $-\pi/2$ and $\pi/2$). Thus, the final expression for the transverse dielectric function has the form

$$\varepsilon(k,\omega)=1+\frac{\omega_p^2}{\lambda\omega^2-\omega\sqrt{\tilde{\omega}^2-k^2v_0^2}}. \tag{10}$$

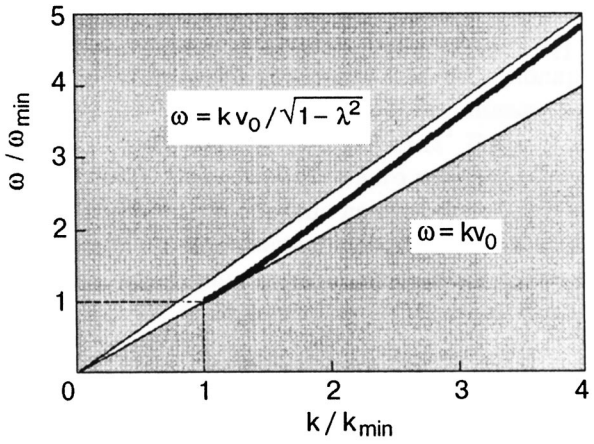

FIG. 1. Dispersion relation for collective mode (bold curve) for $\lambda=0.6$.

Here $\omega_p^2\equiv 4\pi Ne^2/m$ is the ''gas'' value of the squared plasma frequency. It should be noted that the transverse plasmon spectrum in the chosen model starts from $\Omega_p=\omega_p/\sqrt{1-\lambda}$.

We shall be interested in much lower frequencies for which the unity on the right-hand side of (10) can be neglected. At the same time, in view of the high purity of samples at low temperatures, we assume in subsequent formulas that $\omega\gg\nu$ and go over to the collisionless limit (i.e., $\tilde{\omega}\to\omega+i0$). If necessary, the dependence of the results on the relaxation frequency ν can be easily reconstructed by the reader.

It is convenient to write the dispersion equation $k^2c^2=\omega^2\varepsilon$ in the variables $f\equiv\omega c/v_0\omega_p$, $q\equiv kv_0/\omega$ (reduced frequency and wave vector):

$$1+f^2q^2(\sqrt{1-q^2}-\lambda)=0. \tag{11}$$

As in the case of a gas (see Ref. 2), this equations for any frequency has a conventional purely imaginary solution with the asymptotic forms

$$\begin{aligned} &k_0(\omega)\approx i(\omega\omega_p^2/c^2v_0)^{1/3}\quad (f\ll 1);\\ &k_0(\omega)\approx i\omega_p/c\sqrt{1-\lambda}\equiv i\Omega_p/c\quad (f\gg 1). \end{aligned} \tag{12}$$

In this case, the FLI is manifested only in the range of ''infrared'' skin effect, where is slightly accelerates the field damping.[1)]

The qualitative difference from the gaseous approximation is that if $f\sqrt{\lambda}\geqslant 1$, i.e., $\omega\geqslant\omega_{\min}$, Eq. (11) has a real root q_1 describing the collective mode with the phase velocities $V=v_0/q_1$ in the interval

$$v_0\leqslant v_0/q_1(f)<v_0/\sqrt{1-\lambda^2};\quad \omega_{\min}=\omega_p v_0/c\sqrt{\lambda} \tag{13}$$

(see Fig. 1). The simple form of the dispersion equation (12) makes it possible to write explicitly the dispersion relation for collective excitations:

$$\begin{aligned} \omega(k_1)&=\frac{k_1v_0}{\sqrt{1-\lambda^2[1-(k_{\min}/k_1)^2]^2}}\ (k_1\geqslant k_{\min}\\ &=\omega_p/c\sqrt{\lambda}). \end{aligned} \tag{14}$$

The frequency $\omega_{\min}$ has the meaning of the ''activation energy'' of the collective mode. Its excitation also requires a certain degree of spatial inhomogeneity: $k \geqslant \omega_{\min}/v_0$.

A similar theoretical result is well known for quasi-isotropic metals (see, for example, Refs. 7 and 9). However, this requires a high-intensity of FLI: the parameter corresponding to L_{01} must be larger than 3. This is hardly possible for conventional metals with a high density of free charge carriers, and the electronic zero-sound of the type considered above has not been observed in these metals so far.[9] On the contrary, the only requirement in our case is that the quantity $\lambda \equiv L_{01}/(L_{01}+1)$ must be positive. To be more precise, we require that $\lambda \gg v_0/v_F$ in view of the expansions in $v_0/v_F \ll 1$ used in our analysis. Such a condition actually does not limit the existence of the effect in layered conductors.

Let us now discuss the structure of the electromagnetic field in a metal under the conditions of the given effect. Since $|v_z| \ll v_F$, all electrons are incident at small angles on the surface parallel to the layers, so that their reflection can be rightfully regarded as specular.[10] In this case, the field in a semi-infinite sample is described (see, for example, Refs. 2 and 11) by the following integral representations:

$$E(z) = \frac{i\omega H(0)}{\pi c} \int_{-\infty}^{\infty} dk \frac{\exp(ikz)}{\varepsilon(k,\omega)\omega^2/c^2 - k^2} = \frac{2H(0) f^2 \nu_0}{i\pi c} \int_0^{\infty} \frac{dq}{D(q)} \cos\left(qf \frac{z\omega_p}{c} \right), \tag{15}$$

where

$$D(q) = f^2 q^2 + [\sqrt{(1+i0)^2 - q^2} - \lambda]^{-1}, \tag{16}$$

and $2H(0)$ is the amplitude of the magnetic field of the wave at the sample surface. The skin effect itself corresponds to the term (residue) damping with the decrement $|k^0|$ (see (11)). The presence of the collective mode (14), i.e., the pole of the integrand in $k = k_1(\omega)$ indicates that a part of the incident electromagnetic wave penetrates the metal to a considerable depth of the order of the electron mean free path l since we assume that $k_{\min} l = \omega_{\min}/v \gg 1$. In other words, we have

$$[c/\nu_0 H(0)] E(z) = \sum_i A_i \exp\left(iq_i f \frac{z\omega_p}{c} \right) + \frac{2f^2}{\pi} \times \int_1^{\infty} dq \frac{\sqrt{q^2-1}\exp(iqfz\omega_p/c)}{(1-\lambda f^2 q^2)^2 + f^4 q^4 (q^2-1)^2};$$

$$A_i(f) = q_i^{-1}(1 + f^2 q_i^4/2\sqrt{1-q_i^2})^{-1}, \quad i = 0,1, \tag{17}$$

where $q_0(f)$ and $q_1(f)$ are the imaginary and real solutions of Eq. (11), respectively. It should be noted that the penetrating component of the field also exists in the gas approximation ($\lambda = 0$): it is the third (quasi-wave) term in (17), i.e., the contribution from the branching point $k = \tilde{\omega}/v_0$ of the function $\varepsilon(k,\omega)$ associated with the presence of the boundary Fermi velocity v_0 (see, for example, Refs. 11 and 2). However, the asymptotic form of the quasi-wave at a large depth ($z \gg v_0/\omega$) contains small factors (as compared to the collective mode) of the type $(v_0/\omega x)^n$, i.e., it attenuates much more rapidly with increasing distance and frequency in the collisionless limit.

Formulas (15) and (16) are quite simple and can be used directly for numerical calculations on a PC. The results of such calculations are presented in Fig. 2.

For $z = 0$, expressions (15)–(17) give the surface impedance of the metal, which is defined as $Z \equiv E(0)/H(0)$, and make it possible to calculate its frequency dependence. The imaginary component of $Z(\omega)$ is connected with the skinned component of the field and is determined by the first term in (16) (depending on q_0). In the range under investigation, it increases monotonically with frequency. The real component of the impedance, which determines the electromagnetic wave absorption is associated with the collective mode and quasiwave. Although the collective mode exists only for $\omega \geqslant \omega_{\min}$, the total contribution of the penetrating components of the field to the impedance is a smooth function of frequency passing through the peak at $\omega \sim \omega_{\min}$. The real component of Z increases, while the imaginary decreases with increasing intensity of the FLI (parameter λ; see Fig. 3).

In conclusion, we consider the possibility of observing the effect in question. For not very small values of λ, the boundary frequency $\omega_{\min}$ lies in the submillimeter range ($\omega_{\min} \sim 10^{12}\,\mathrm{s}^{-1}$). The quality of synthetic conducting crystals is still inferior to that attained for conventional metals (especially for refractory or fusible ones). Nevertheless, the available information of a sharp cyclotron resonance in layered conductors such as an α-$(ET)_2TlHg(SCN)_4$ single crystal at frequencies ~ 50–$100\,\mathrm{GHz}$[12] indicates that the condition $\omega_{\min} \gg \nu$ which is important for us can be easily satisfied in low-temperature experiments.

Experiments in the pulse mode which was successfully used by Fil's group for observing ''electron sound'' (elastic vibrations that are apparently associated with the longitudinal zero sound in a two-component Fermi liquid) in Al, Ga, and W are preferable.[13] However, in our case it is reasonable to use instead of acoustic pulses directly electromagnetic pulses which are shorter than the minimum transit time for electrons in the sample ($\tau \ll d/v_0$).

By way of a simple example, we consider a Gaussian pulse for which the field on the metal surface is defined in the form

$$H(0,t) = h \exp(-i\Omega t - t^2/4\tau^2), \tag{18}$$

and confine ourselves to the so-called radio pulse: $\Omega\tau \gg 1$. In order to obtain the distribution and evolution of the field in the sample, it is sufficient to multiply the monochromatic expression (17) by the Fourier component of the signal (18) and carry out the inverse Fourier transformation in frequency. Since we are interested only in the weakly attenuating contribution of the collective mode, we obtain

$$E(z,t) \approx \frac{h\tau\nu_0}{c\sqrt{\pi}} \int^{\infty} d\omega A_1(\omega) \exp[-i\omega T - (\omega-\Omega)^2\tau^2], \tag{19}$$

where $T = T(\omega) = t - q_1(\omega) z/v_0$.

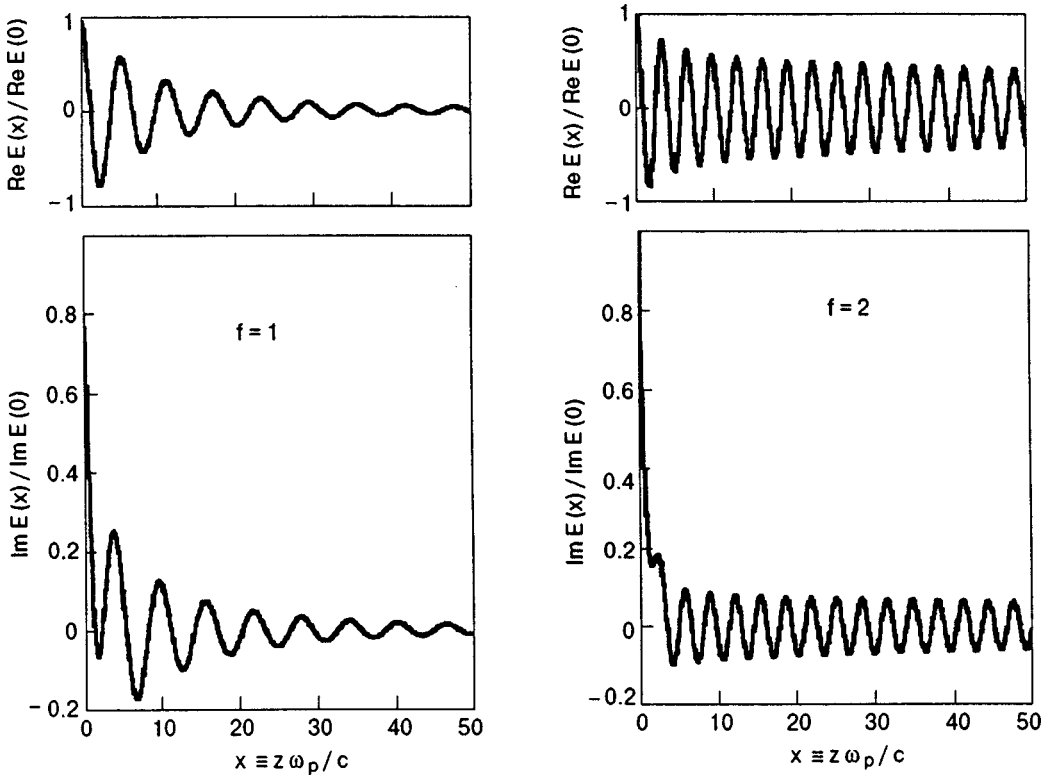

FIG. 2. Distribution of monochromatic electromagnetic field in the sample at frequencies lower and higher than $\omega_{\min}$ for $\lambda=0.5$. In the second case ($f=2$), the field component penetrating the metal is determined by the collective mode, while in the first case ($f=1$) it is a quasiwave attenuating at a relatively high rate.

However, according to (13), the dispersion is low: the quantity $q_1(\omega)$ remains in the interval $[(1-\lambda^2)^{1/2},1]$ in the entire frequency range from $\omega_{\min}=\omega_p v_0/c\sqrt{\lambda}$ to $\omega\sim\omega_p$. For this reason, we can approximately substitute $T(\omega=\Omega)$ and $A_1(\omega=\Omega)$ into (19) for not very large depths z (at least, up to $z\sim(\Omega\tau)v_0\tau$). This gives a self-similar propagation of the pulse with a velocity $V(\Omega)=v_0/q_1(\Omega)$:

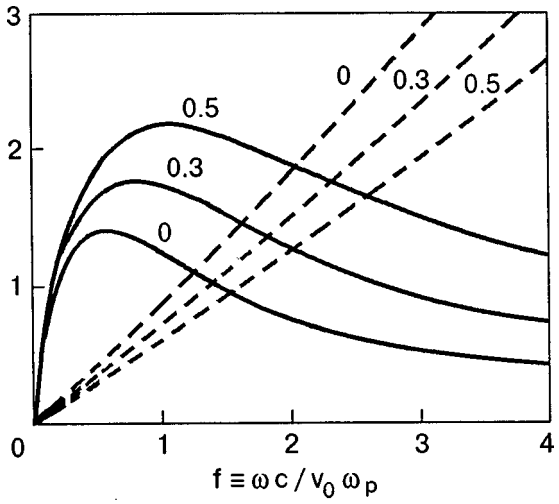

FIG. 3. Frequency dependences of the real (solid curves) and imaginary (dashes curves) components of impedance (in the units of v_0/c) for different values of the FLI parameter: λ.

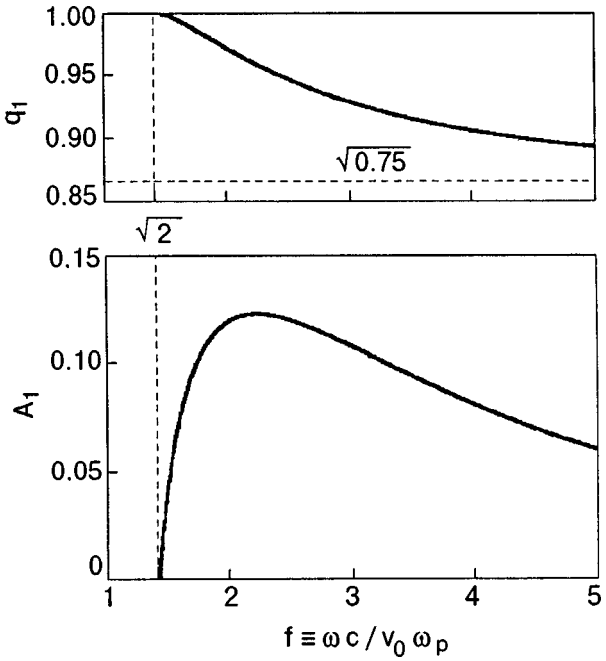

FIG. 4. Dispersion and frequency dependence of the amplitude of collective vibrations ($\lambda=0.5$).

$$E(z,t)\approx\frac{\nu_0}{c}A_1(\Omega)[0,t-z/V(\Omega)]. \quad (20)$$

When obvious inequalities (stipulated above) are satisfied, this expression is quite general: it is not very stringent as regards the shape of the input pulse, and only concrete frequency dependences of the quantities A_1 and q_1 are associated with the chosen model of the electron spectrum in it (see Fig. 4). Consequently, measuring the time of passing of a signal through the sample (whose thickness d must be of the order of or smaller than the electron mean free path v_0/ν) for various values of carrier frequency Ω, we can compare the true dispersion relation of zero-sound with the model relation obtained and estimate the value of the parameter λ characterizing the intensity of the FLI.

This research was carried out under the support of the Foundation of Fundamental Studies of the Ukrainian Ministry of Science (Project No. 2.4/192).

*)E-mail: gokhfeld@host.dipt.donetsk.ua
**)E-mail: vpeschansky@ilt.kharkov.ua

1)It should be mentioned that the characteristic frequency $\omega_p v_0/c$ separating the limiting cases (12) is much lower in a quasi-two-dimensional metal than in an isotropic metal with the same carrier concentration.

[1] V. M. Gokhfeld, M. I. Kaganov, and V. G. Peschansky, Fiz. Nizk. Temp. **12**, 1173 (1986) [Sov. J. Low Temp. Phys. **12**, 661 (1986)].
[2] V. M. Gokhfeld and V. G. Peschansky, Ukr. Fiz. Zh. **37**, 1594 (1992).
[3] V. M. Gokhfeld, O. V. Kirichenko, and V. G. Peschansky, Zh. Éksp. Teor. Fiz. **108**, 2147 (1995) [JETP **81**, 1171 (1995)].
[4] J. Vosnitza, *Fermi Surfaces of Low-Dimensional Organic Metals and Superconductors*, Springer, Heidelberg (1996).
[5] V. M. Gokhfel'd and V. G. Peschansky, in *Nonlocal Acoustoelectronic Effects in Metals and Layered Conductors* (ed. by I. M. Khalatnikov), Harwood Academic Publ. (1993).
[6] L. D. Landau, Zh. Éksp. Teor. Fiz. **32**, 59 (1957) [Sov. Phys. JETP **5**, 101 (1957).
[7] D. Pines and Ph. Nozieres, *The Theory of Quantum Liquids*, Benjamin, New York–Amsterdam (1966).
[8] E. M. Lifshitz and L. P. Pitaevskii, *Physical Kinetics* [in Russian], Nauka, Moscow (1979).
[9] A. A. Abrikosov, *Fundamentals of the Theory of Metals*, No. Holland, 1988.
[10] A. F. Andreev, Usp. Fiz. Nauk **105**, 113 (1971) [Sov. Phys. Usp. **14**, 609 (1971).
[11] V. M. Gokhfeld, M. A. Gulyanskii, M. I. Kaganov, and A. G. Plyavenek, Zh. Éksp. Teor. Fiz. **89**, 3985 (1985) [Sov. Phys. JETP **62**, 566 (1985).
[12] A. Polisski, J. Singleton, and N. D. Kushch, Czech. J. Phys. **46**, Suppl. S5. *Proceedings of LT-21*, Prague (1996)).
[13] E. V. Bezuglyi, N. G. Burma, E. Yu. Deineka, and V. D. Fil', Sverkhprovodimost: Fiz., Khim., Tekh. **4**, 661 (1991).

Translated by R. S. Wadhwa

LOW-DIMENSIONAL AND DISORDERED SYSTEMS

Low-temperature luminescence of thin C_{60} films of different structures

A. A. Avdeenko, V. V. Eremenko, P. V. Zinoviev, N. B. Silaeva, and Yu. A. Tiunov

B. Verkin Institute for Low Temperature Physics and Engineering, National Academy of Sciences of the Ukraine, 310164 Kharkov, Ukraine[*)]

N. I. Gorbenko, A. T. Pugachev, and N. P. Churakova

Kharkov State Polytechnical University, 310002 Kharkov, Ukraine
(Submitted July 23, 1998)
Fiz. Nizk. Temp. **25**, 49–52 (January 1999)

We present the results of investigation of low-temperature (5 K) photoluminescence of thin fullerite C_{60} films of various structures obtained on monocrystalline NaCl substrates by vacuum deposition at temperatures in the interval 290–400 K. Depending on the conditions of deposition, the film structure, which was controlled by the standard transmission high-energy electron diffraction (THEED) technique, varies from a disoriented structure to an oriented structure with different average sizes of microcrystals. The effect of the film structure on the photoluminescence spectral band of fullerite, associated with the luminescence of structural defects (*X*-traps), is attributed to the peculiarities of transport and capture of coherent singlet excitons in single crystals of various sizes.
[S1063-777X(99)00801-4]

Among the physical and chemical properties of fullerenes which have been studied intensely over recent years (see reviews in Refs. 1–3), the photophysical properties of fullerite C_{60} are of special interest. This is primarily due to the unique symmetry of the C_{60} molecule, and consequently the specific nature of the spectrum of its excited states. Radiative dipole–dipole transitions from the lowest excited states to the ground state are forbidden by symmetry considerations, and hence special attention is paid in the literature[4–11] to the study of mechanisms responsible for the luminescence of C_{60} molecules and crystals. The obtained results led to the assumption that the formation of the photoluminescence (PL) spectra involves the participation of the singlet and triplet excitons of different types,[4–9] excimers,[9,12] as well as *X*-traps whose nature is associated with structural defects and residual impurities.[8,13–16] Photoluminescence of *X*-traps is an important tool for studying the exciton dynamics.[14,15,17]

The results of investigations of the effect of C_{60} thin film structure on PL were reported recently in a number of publications.[9,18,19] The choice of thin films deposited on substrates as objects of investigations is not accidental since films with quite different structures can be obtained as a result of variation of deposition conditions and an appropriate choice of the substrate material.[14,15]

In this paper, we present the results of investigations of low-temperature PL of C_{60} thin films of different structures, which was monitored by the electron diffraction technique. The variations of the luminescence spectra of these films are explained by the peculiarities of the transport and capture of excitons in microcrystals of various sizes.

Layers of fullerite C_{60} were obtained by evaporation and deposition of the initial material of no worse than 99.9% purity on the (001) cleavage plane of a NaCl single crystal in vacuum of the order of 10^{-3}Pa at selected temperatures in the interval 290–400 K. The layer thickness was determined with the help of a quartz vibrator. The deposition rate was about 0.1 $\text{nm}\cdot\text{s}^{-1}$. According to the results of electron diffraction and electron microscopic studies, C_{60} films of thickness 35 nm obtained at the substrate temperature $T_{\text{sub}} \approx 370$ K were continuous and had the fcc lattice with a period close to that of bulk fullerite. Electron diffraction patterns contained reflexes of the type (220) and (422), indicating that the (111) plane of the C_{60} film is parallel to the (001) plane of NaCl. The size of microcrystals in such films was of the order of 40–50 nm.

Electron diffraction patterns of films having a thickness of 25 nm and obtained at $T_{\text{sub}} \approx 290$ K had broad halo-like rings (Fig. 1). A preliminary analysis proved that rings in such disoriented films can be identified in the fcc structure. The average size of microcrystals in the films was 4–5 nm. Thus, C_{60} films may have strongly disoriented structure with the ultimate degree of dispersion as well as well-oriented structure determined by the epitaxial growth at a monocrystalline substrate depending on the deposition conditions.

A high-pressure mercury lamp DRSh-500 was used as a source of excitation in PL studies of C_{60} films. The 2.84eV line of the mercury spectrum was separated with the help of appropriate optical filters and a monochromator SPM-2. Photoluminescence was recorded in light reflected at an angle of 45° relative to the incident radiation. The spectra were recorded by using a scanning monochromator MDR-3 and a

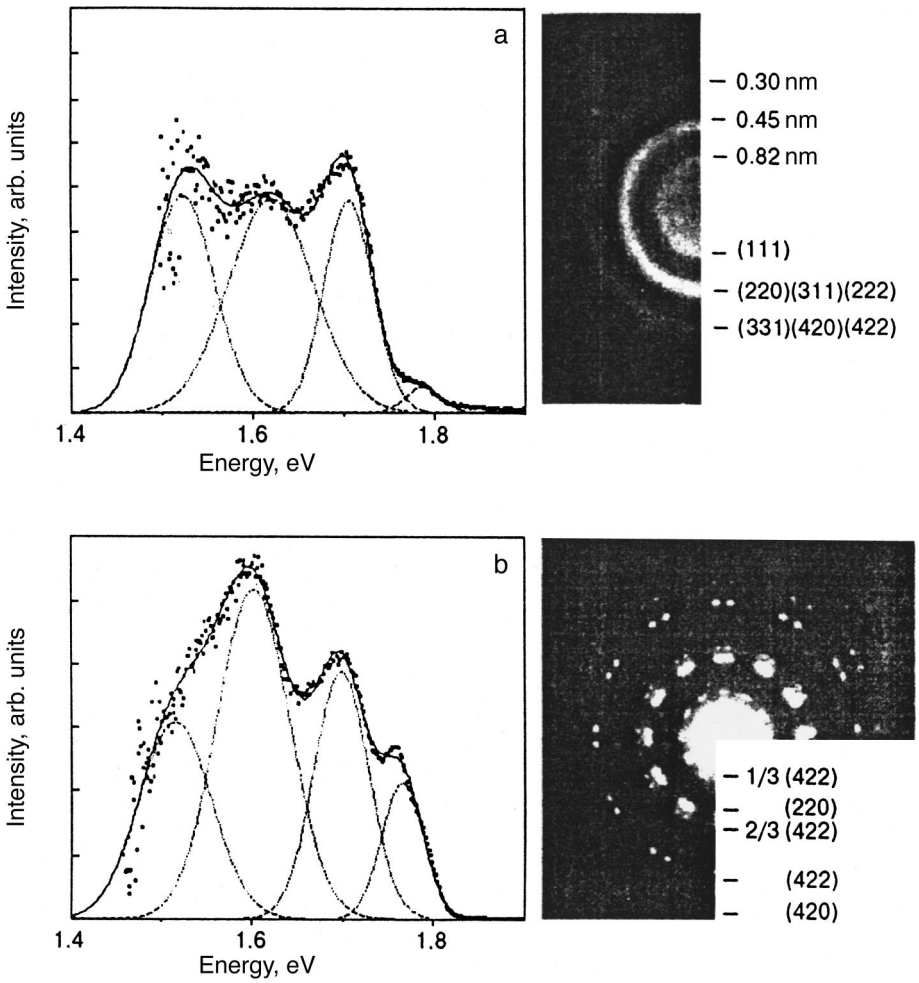

FIG. 1. PL spectra and THEED patterns of disoriented highly dispersive (grain size ~5 nm) (a) and oriented epitaxial (grain size ~40 nm) (b) films of C_{60} fullerite.

photoelectric multiplier FEU-79 operating in the photon counting mode. Signal storage, processing, reading, as well as monitoring of the experiment were executed by a computer. Luminescence spectra were corrected according to the spectral sensitivity of the recording apparatus. The spectral width of the gap was ~5 nm. The sample was held in gaseous helium, and cooling of the film to ~5 K was ensured by the design of the cryostat and by the manner in which the sample was fastened.

Figure 1 shows the PL spectra and electron diffraction patterns of two types of C_{60} fullerite films on a NaCl substrate at 5 K. Since the spectral structure is weakly manifested, they were decomposed by the computer into Gaussian-shaped bands. The details of the procedure of the PL spectral decomposition are described in Ref. 20. Four bands with peaks at 1.78, 1.71, 1.6, and 1.52 eV are clearly manifested in the PL spectrum after decomposition (see Fig. 1).

It can be seen from Fig. 1 that the intensity of the luminescence band with a peak at 1.78 eV depends strongly on the film structure. In order to determine the reasons for such a behavior of the luminescence band, let us consider the modern versions concerning the origins of excited states of the C_{60} fullerite.

The results of experiments[6] and calculations[7] show that the bandwidth for singlet excitons in C_{60} fullerite is unusually large (20–40 meV) taking into account the fact that radiative 0–0 exciton transitions are forbidden in the dipole approximation. This fact can be explained by assuming that the lowermost state of a Frenkel exciton is modified owing to the contribution from interactions with a charge transfer.[7,11,12,21] In other words, photoexcitation leads to partial or complete charge transfer to a neighboring molecule, and as a result, a broader exciton band corresponds to the new state.[22] The 0–0 exciton transition was observed experimentally in two-photon absorption (1.846 eV).[6]

The principal PL band of C_{60} fullerite (with a peak around 1.69 eV) is usually associated with a self-trapped singlet exciton[23,24] with a probable contribution from states with charge transfer.[9,11,21,23,25] We assume that the PL band observed by us and having a peak around 1.71 eV is of the same origin, i.e., corresponds to the excimer state.

It was shown earlier that the structurally sensitive band with a peak at 1.78 eV corresponds to radiative transitions from the excited *X*-traps.[16] In our opinion, these traps are of the excimer type, which apparently explains their large depth relative to the exciton band. The atomic concentration of such *X*-traps is relatively low and usually does not exceed 10^{-3}–10^{-4} in molecular crystals.[8,14] A large contribution from *X*-trap luminescence to the general PL intensity (Fig.

1b) indicates that singlet excitons captured by these traps are quite mobile.

Since the Debye temperature of C_{60} fullerite is not high (of the order of 75 K),[26,27] the width of the singlet exciton bands (20–40 meV[6,7]) is much larger than the Debye energy. Consequently, the transport of singlet excitons at low temperatures must be coherent.[28]

Transport and trapping of coherent excitons during scattering at the boundaries of microcrystals was studied by Agranovich and Galanin.[29] Using the concepts developed by them, it can be proved that the probability of capturing by the traps decreases as the size of microcrystals decreases to the exciton mean free path. Thus, the influence of the structure of C_{60} thin fullerite films on the PL spectrum is associated with the size effect when the mean free path of a coherent singlet exciton becomes comparable with the size of microcrystals.

The authors thank M. A. Strzhemechny for fruitful discussions of the results.

*)E-mail: avdeenko@ilt.kharkov.ua

[1] H. W. Kroto, J. E. Fisher, and D. E. Cox (Eds.), *The Fullerenes*, Pregamon Press, Oxford (1993).
[2] J. H. Weaver and D. M. Poirier, in Solid State Physics (ed. by H. Ehrenreich and F. Spaepen), Vol. 48, Academic Press, Cambridge (1994).
[3] P. R. Birkett, Ann. Rep. Progr. Chem. **A93**, 611 (1997).
[4] M. Matsushita, A. M. Frens, E. J. J. Groenen *et al.*, Chem. Phys. Lett. **214**, 349 (1993).
[5] T. W. Ebbesen, Y. Mochizuki, K. Tanigaki, and H. Hiura, Europhys. Lett. **25**, 503 (1994).
[6] M. Muccini, R. Danieli, R. Zamboni *et al.*, Chem. Phys. Lett. **245**, 107 (1995).
[7] E. L. Shirley, L. X. Beenedict, and S. G. Louie, Phys. Rev. B **54**, 10970 (1996).
[8] V. V. Kveder, V. D. Negrii, E. A. Shteinman *et al.*, Zh. Éksp. Teor. Fiz. **113**, 734 (1998) [JETP **86**, 405 (1998)].
[9] P. P. Pippenger, R. D. Averitt, V. O. Papanyan *et al.*, J. Phys. Chem. **100**, 2854 (1996).
[10] D. J. van den Heuvel, G. J. B. van den Berg, E. J. J. Groenen *et al.*, J. Phys. Chem. **99**, 11644 (1995).
[11] A. Nakamura, M. Ichida, M. Sakai, and T. Yajima, in *Springer Series in Excited State Sciences* (ed. by K. Nasu), vol. 124, Springer Verlag, Berlin (1997).
[12] V. M. Farztdinov, A. L. Dobryakov, V. S. Letokhov *et al.*, Phys. Rev. B **56**, 4176 (1997).
[13] K. W. Benz, W. Hacker, and Y. C. Wolf, Z. Naturforsch. A **25**, 657 (1970).
[14] H. Baessler, Phys. Status Solidi B **107**, 9 (1981).
[15] E. A. Silinsh (Ed.), *Electron Processes in Organic Molecular Crystals* [in Russian], Zinatne, Riga (1992).
[16] W. Guss, J. Feldman, E. O. Göbel *et al.*, Phys. Rev. Lett. **72**, 2644 (1994).
[17] D. J. van den Heuvel, I. Y. Chan, E. J. J. Groenen *et al.*, Chem. Phys. Lett. **233**, 284 (1995).
[18] K. Kaneto, K. Rikitake, T. Akiyama, and H. Hasegava, Jpn. J. Appl. Phys., Part 1 **36**, 910 (1997).
[19] V. Capozzi, G. F. Lorusso, T. Trovato *et al.*, J. Lumin. **72–74**, 473 (1997).
[20] A. A. Avdeenko, V. V. Eremenko, N. I. Gorbenko *et al.*, Sverkhtverd. Mat. No. 3 (107), 56 (1997).
[21] S. Kazaoui and S. Minami, Synth. Met. **86**, 2345 (1997).
[22] P. Petelenz and V. H. Smith Jr., Chem. Phys. Lett. **82**, 430 (1981).
[23] T. Zoo, J. Liu, Y. Li, and D. Zhu, Appl. Phys. Lett. **67**, 1028 (1992).
[24] M. Matus, H. Kuzmany, and E. Sohmen, Phys. Rev. Lett. **68**, 2822 (1992).
[25] M. A. Terekhin, N. Yu. Svechnikov, A. A. Kolmakov *et al.*, Fiz. Nizk. Temp. **21**, 773 (1995) [Low Temp. Phys. **21**, 600 (1995)].
[26] W. P. Beyerman, M. F. Handley, and J. D. Thomson, Phys. Rev. Lett. **68**, 2046 (1992).
[27] R. C. Yu, M. V. Salamon, D. Lorents, and R. Malhotra, Phys. Rev. Lett. **68**, 2050 (1992).
[28] B. I. Verkin and A. F. Prikhot'ko (Eds.) *Cryocrystals* [in Russian], Naukova Dumka, Kiev (1983).
[29] V. M. Agranovich and M. D. Galanin, *Electron Excitation Energy Transport in Condensed Media* [in Russian], Nauka, Moscow (1978).

Translated by R. S. Wadhwa

PHYSICAL PROPERTIES OF CRYOCRYSTALS

Recombination of charge carriers in neon cryocrystals containing oxygen impurity

A. G. Belov

*B. Verkin Institute for Low Temperature Physics and Engineering, National Academy of Sciences of the Ukraine, 310164 Kharkov, Ukraine**

(Submitted July 6, 1998)
Fiz. Nizk. Temp. **25**, 53–62 (January 1999)

The recombination of electrons and holes in neon crystals containing deep electron traps due to impurity oxygen along with weakly localized electron states of the matrix is investigated experimentally. Measurements are made by the method of cathode-luminescence spectroscopy in VUV, UV, and visible wavelength ranges at temperatures varying from 2 to 8 K. It is found that the temperature dependences of integral intensities of intrinsic and extrinsic luminescence in solid solutions of oxygen in neon are similar and nonmonotonic by nature. The observed effect is analyzed in the model of two coexisting channels of energy relaxation of electron excitations: through the $\Gamma(1/2,3/2)$ exciton subsystem and through the recombination of self-trapped two-center holes and electrons. It is shown that temperature variations of integral parameters of luminescence are mainly due to peculiarities of the recombination channel whose efficiency is determined by the probability of electron localization in the matrix lattice in the low-temperature regions (2.5–5 K) and by the probability of trapping at impurity centers in the temperature range 6–8 K. Additional proofs are obtained for the possibility of electron self-trapping in the Ne lattice with the formation of shallow localized states. [S1063-777X(99)00901-9]

In view of comparatively strong electron–phonon coupling, low barriers for self-trapping, and high plasticity of the lattice, solid neon is the only noble cryocrystal which does not exhibit the coexistence of free (FE) and self-trapped (STE) excitons. The luminescence spectra for Ne contain transitions only from STE states, in which bands corresponding to one-center quasi-atomic luminescence a-STE dominate.[1–4] The complete energy spectrum of a-STE excitations in Ne includes two types of transitions: (1) transitions from the $^1P_1$, $^3P_1$, and $^3P_2$ states to the ground state as a result of self-trapping of the lowermost $\Gamma(3s,3s')$ excitons in the VUV range, and (2) transitions from high-energy atomic energy levels $(3p,3p')$ associated with $X(3p,3p')$ excitons in the visible spectral range.[5–7] Apart from exciton self-trapping, Ne cryocrystals also exhibit self-trapping of holes with the formation of Ne_2^+ centers.[7,8] Indications of possible electron localization in the temperature range below 5 K were obtained recently in Ref. 9. Effective self-trapping of electron (both neutral and charge) excitations indicates peculiarities of the electron–phonon interaction in the Ne lattice, distinguishing neon from the series of heavier inert cryocrystals. Among other things, this necessitates the inclusion of migration of self-trapped excitons and charge centers (polarons) in the course of their hopping diffusion along with the traditional mechanisms of motion of free quasiparticles in an analysis of energy transport in neon.

This research is a continuation of the experiments started in Ref. 9 and pertaining to excitation energy relaxation and possible self-trapping of electrons with the formation of a microcavity in pure and doped Ne cryocrystals at low temperatures. We analyze the effect of an impurity possessing considerable affinity to an electron on the efficiency of radiative annihilation in intrinsic and extrinsic electron excitations in Ne cryocrystals. It is found that the integral intensity of luminescence of solid solutions of oxygen in Ne is a nonmonotonic function of temperature. The observed effect is analyzed under the assumption on two possible relaxation channels for excitation energy: the exciton channel and the recombination channel. It is shown that the temperature variations of integral parameters of both intrinsic and extrinsic luminescence are mainly determined by the recombination channel. The efficiency of the recombination contribution in the low-temperature region (2.5–5 K) depends on the probability of electron self-trapping in the bulk of the crystal accompanied with the formation of a ''shallow trap.'' In the region of higher temperatures (5–8 K), the efficiency of the recombination channel is controlled by electron trapping at an electronegative impurity, resulting in the formation of deep centers with a negative charge.

1. EXPERIMENTAL TECHNIQUE

The measurements were made on a setup for studying luminescence parameters of cryocrystals and their solid solutions in the spectral range from 1.5 to 25 eV.[10,11] We investigated high-purity Ne cryocrystals as well as crystals with oxygen impurity with a concentration 10^{-2}–1%. Prior to experiments, optically pure Ne was additionally purified by passing the gas through a column containing liquid

lithium at $T=200\,^{\circ}$C. The preset concentrations of oxygen in neon were attained by consecutive dilution of gas mixtures. The samples under investigation were prepared by the condensation of the gas mixture on the substrate of an optical He cryostat at a temperature close to the neon sublimation temperature. After thermal annealing, the samples were cooled slowly to the required temperature.

The excitation of the samples was carried out by monochromatic electrons with energy $E_e=2.3$ keV and current density $i_e=0.03$ mA/cm^2, in which luminescence from bulk centers dominates over the emission from the surface. Under such conditions of excitation, the sample does not experience sputtering for several hours, which was controlled both visually and from the spectrum stability under isothermal holding.

The spectra were recorded simultaneously in the VUV and visible regions at an angle of 45° to the substrate plane. The intrinsic and extrinsic VUV luminescence was studied with the help of a vacuum normal-incidence monochromator VMR-2 with a grating having 600 lines/mm. Intrinsic luminescence of neon was recorded in the third order with a resolution of 0.2 Å. The resolution for oxygen impurity bands was 0.5 Å. In the visible and near IR regions, the luminescence was detected by a double-beam monochromator DFS-24 with a spectral resolution not lower than 0.2 Å. The details of experimental procedure are described in Ref. 9.

2. EXPERIMENTAL RESULTS

2.1. Identification of the structure of intrinsic and extrinsic luminescence spectra. Concentration variations

The measured luminescence spectrograms for pure Ne are similar to those reported earlier[9,12,13] and mainly contain transitions from one-center (quasi-atomic) self-trapped states (a-STE). They include luminescence bands lying in two wavelengths intervals with essentially different energies. Transitions from the lowermost $2p^5 3s(3s')$ states ($^1P_1$, $^3P_1$, and $^3P_2$ states in terms of the Russell–Saunders coupling) to the ground $^1S_0$ energy level $2p^6$ are observed in the extreme VUV region. A series of bands corresponding to transitions from the $2p^5 3p(3p')$ to $2p^5 3s(3s')$ energy levels appears in the near IR and visible ranges. The characteristic regions of the luminescence spectrograms for crystalline neon are shown in Fig. 1. Vertical strokes in the upper regions of the figure denote the positions of lines in the luminescence spectrum of gaseous neon. It can be seen from the figure that each transition in a free atom corresponds to a band including the components ''2,'' ''1,'' ''d,'' ''0,'' and ''s.'' It was shown earlier[6,9,12,13] that the first three of these components appear as a result of formation of a-STE in the bulk of the sample. Their position and half-width reflect various extents of deformation of the nearest crystalline environment of an excited center during energy relaxation to stable configurations of a-STE.[6,9,12] The last two components (''0'' and ''s'') are due to self-trapping of excitations at the free surface of the crystal.[5,6,13]

Extrinsic luminescence spectrum of oxygen in the Ne matrix mainly contains bands of quasi-atomic excited O*-centers in spite of the fact that the solid Ne–O_2 mixture initially contained only molecular oxygen. The spectrum contains luminescence bands for valence transitions ($^1S-{}^1D$, $^1S-{}^3P$ and $^1D-{}^3P$), as well as Rydberg transitions $3s^5S\rightarrow 2p^4\,{}^3P$, $3s^3S\rightarrow 2p^4\,{}^3P$, $3s'\,{}^1D\rightarrow 2p^4\,{}^1D$, $3s'\,{}^3D\rightarrow 2p^4\,{}^3P$ (Fig. 2). The structure of bands for all Rydberg transitions in O* turned out to be similar to the structure of the a-STE bands in the intrinsic luminescence of neon in the VUV range. Luminescence from the bulk includes two relatively broad components ''2'' and ''1'' and one or several narrow components ''d'' depending on the multiplicity index. Luminescence from impurity centers lying near the free surface of the crystal contain narrow components ''s'' and ''0.'' The latter component coincides with the luminescence spectrum of a free excited O* atom to within the resolution of our apparatus. The structure of the Rydberg states of O* in neon was analyzed in Ref. 11. It was shown that the components ''2,'' ''1,'' and ''d'' correspond to different stages of lattice deformation around an excited impurity atom, while the ''0'' component emerges as a result of desorption of O* from the crystal surface to the vacuum.

The most intense band of valence transitions in the visible wavelength range corresponds to the band of the $^1S-{}^1D$ transition (Fig. 2a). Its multicomponent structure is associated with various positions of the O* atoms in the crystal

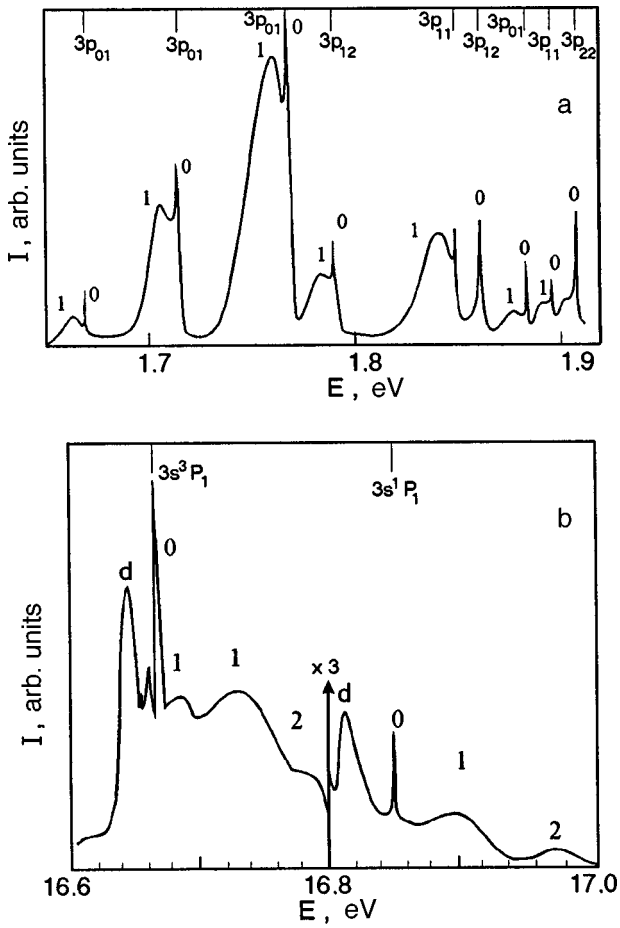

FIG. 1. Characteristic regions of luminescence spectrogram of solid Ne in visible (a) and VUV (b) regions.

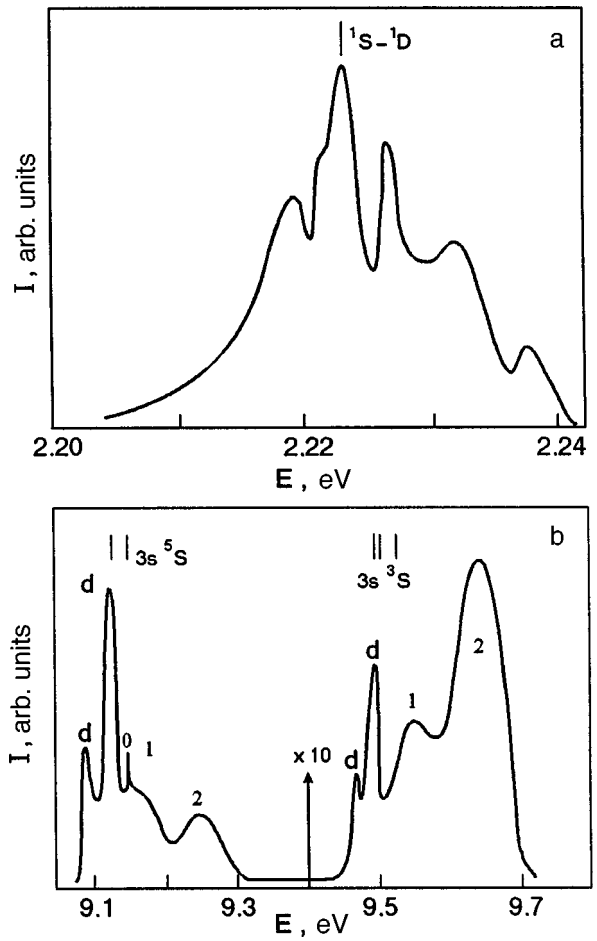

FIG. 2. Characteristic regions of spectrogram of extrinsic luminescence of oxygen in solid Ne–O_2 solution for $c \simeq 10^{-2}$ mol.%: valence transition $^1S \rightarrow {}^1D$ region (a), Rydberg transition region (b).

lattice: interstitial and substitutional sites as well as the centers near defects and at grain boundaries.[11]

Molecular luminescence of oxygen in neon is represented by a series of relatively low-intensity bands $A^2\Pi_u \rightarrow X^2\Pi_g$ corresponding to a transition between the energy levels of the O_2^+ ion. The series lies at the boundary between the visible and UV regions.

The formation of luminescent impurity centers of oxygen in neon includes a series of cryochemical reactions connected with the localization of energy $E \geqslant 17$ eV of high-energy electron excitations in the matrix at impurity centers and its subsequent relaxation in the system: effective dissociation of molecules, accelerated superthermal migration of impurity atoms over the lattice, defect formation, etc. The VUV luminescence intensity of Rydberg excitations is determined by the concentration of O radicals in the Ne lattice, while the luminescence of valence transitions is determined by the concentration of O_2 centers in the mixture. Under steady-state excitation conditions, the balance between O_2 and O centers is maintained by radiation-stimulated diffusion of O* centers and depends on the intensity of the exciting electron beam.[14]

After the introduction of oxygen in the concentration range $10^{-3}\% \leqslant c < 10^{-1}\%$, the integral intensity of the intrinsic luminescence of neon decreases gradually, but the structure of the bands remains unchanged. The rate of the decrease in the intensity of VUV luminescence is higher than that for $3p(3p') \rightarrow 3s(3s')$ IR and visible transitions. The impurity spectrum of oxygen contains only the bands of quasi-atomic luminescence: the VUV region is characterized only by transitions from ^3S and ^5S Rydberg states of O* atoms, while the visible range mainly contains the band corresponding to the $^1S-{}^1D$ valence transition. The intensity of these transitions increases with the oxygen concentration. For $c = 0.1\%$, the impurity VUV luminescence spectrum acquires additional low-intensity bands corresponding to transitions from $3s'{}^1D$ and $3s'{}^3D$ states.

In the region of higher concentrations ($c \geqslant 0.3\%$), a considerable transformation of the intrinsic and extrinsic luminescence spectra was observed. Intrinsic luminescence bands for neon (both bulk and surface) are suppressed abruptly, while the intensity of extrinsic luminescence increases significantly. The enhancement of Rydberg transitions in O* is accompanied by a redistribution of intensity between ''2,'' ''1,'' and ''d'' components. The intensity of ''d'' components increase significantly relative to the ''1'' and ''2'' components, and the intensity of ''1'' components becomes higher than that of ''2'' components. The intensity of the band corresponding to the transition $^1S \rightarrow {}^1D$ in the visible range also increased. In addition to this band, the spectrum also acquires a molecular series $A^2\Pi_u - X^2\Pi_g$ indicating the existence of positive molecular oxygen ions in irradiated O_2–Ne crystals.

2.2. Effect of temperature on luminescence spectra of solid O_2–Ne mixtures

The variation of temperature in the sample in the range from 2 to 8 K does not change the spectral structure of luminescence, but leads to a redistribution of intensity between individual components within the contour of complex bands and to a considerable change in the integral intensity of luminescence on the whole. The temperature dependences of integral intensities I_{VUV} and I_{VIS} of bulk VUV luminescence [$3s(3s') \rightarrow {}^1S_0$ transitions] and of visible luminescence [$3p(3p') \rightarrow 3s(3s')$ transitions] for the case of pure Ne cryocrystals are shown in Fig. 3. The same figure shows the temperature dependence of the total integral intensity I_{tot} of the bulk luminescence of pure neon ($I_{\mathrm{tot}} = I_{\mathrm{VIS}} + I_{\mathrm{VUV}}$). It can be seen from Fig. 3 that the luminescence intensities I_{VUV} and I_{VIS} vary with temperature in different ways: the value of I_{VIS} increases virtually by an order of magnitude in the interval from 2.5 to 8 K, while I_{VUV} increases only by 10% of the initial value in the interval from 2 to 5 K, and then decreases weakly. As a result, the total intensity increases by a factor of 1.4 in the interval between 2.5 and 6 K, after which it attains saturation.

The introduction of oxygen into the neon matrix in the concentration range 10^{-3}–$10^{-2}\%$ practically does not affect the temperature dependence of the intensities I_{VUV} and I_{VIS} in the matrix in the temperature interval between 2.5 and 6 K (Fig. 4a). AT higher temperatures ($T > 6$ K), a further decrease in intensity (especially in I_{VIS}) is observed. As a

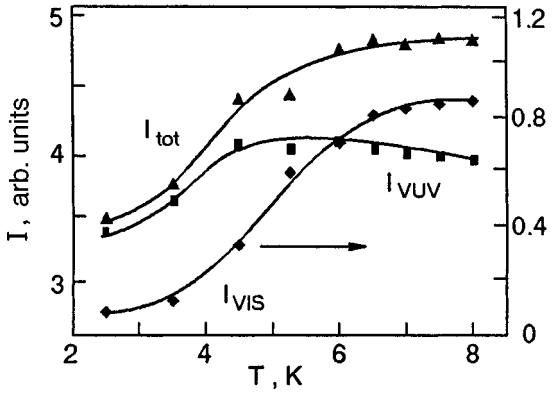

FIG. 3. Temperature dependence of integral luminescence intensities of transitions from the lowest excited states $^3P_{1,2}$ and $^1P_1$ (I_{VUV}), $3p\rightarrow 3s$ transitions (I_{VIS}), and their sum (I_{tot}) in pure Ne cryocrystals.

result, the temperature dependence of the total intensity I_{tot} of the crystal becomes nonmonotonic and can be represented as the sum of two segments, one depicting an increase in the interval 2.5–6 K and the other showing a decrease in the range 6–8 K. As the oxygen concentration in the sample increases, the steepness of the decrease in the intensities I_{VIS}, I_{VUV}, and I_{tot} rises in the high temperature interval 6–8 K (Fig. 4b and 4c), and the value of I_{tot} at 8 K becomes much smaller than the intensity at $T=2$ K for $c=1\%$. The inflection on the curves I_{VIS}, I_{VUV}, and I_{tot} is displaced slightly towards lower temperatures, the shift being especially noticeable on the $I_{VIS}(T)$ curve.

The temperature dependence of the integral intensity of impurity luminescence for samples with different oxygen concentrations is shown in Fig. 5. The I_R curves describe the general variation of the integral intensity of Rydberg transitions, the I_V curves correspond to valence transitions, and I_{R+V} to the total sum of the Rydberg and valence luminescence. It can be seen from Fig. 5 that the temperature dependence of integral intensity of impurity luminescence of low-concentration solid mixtures Ne–O_2 ($c\leqslant 10^{-2}\%$) is similar to that for intrinsic luminescence of the matrix. The values of I_R, I_V, and I_{R+V} increase in the interval 2.5–6.5 K and decrease insignificantly in the range of higher temperature (see Fig. 4). An increase in the impurity concentration to $10^{-1}\%$ leads to a decrease in the rate of intensity increase in the low-temperature range, an increase in steepness, and a displacement of the point of inflection on the I_R, I_V, and I_{R+V} curves in the high temperature region (Fig. 5b). In the region of high oxygen concentrations ($c=1\%$) in which the luminescence intensity of the matrix decreases abruptly and the impurity luminescence spectrum is transformed significantly (see above), the temperature variation of the integral intensity of impurity luminescence also experiences considerable changes (Fig. 5c). The I_V curve has practically no initial low-temperature segment where it increases, and the characteristic segment of a decrease in intensity in the high-temperature range starts from $T=4$ K. On the contrary, the $I_R(T)$ curve demonstrates a considerable increase in the intensity of Rydberg's transitions in the temperature range 4–8 K. As a result, the total integral intensity I_{R+V} of impurity luminescence for the concentration $c\approx 1\%$ has a segment on which the intensity decreases in the temperature range up to $T\approx 5$ K, which anticorrelates with an analogous segment on the I_{tot} curve describing the intrinsic luminescence of the matrix (see Fig. 4c). At higher temperatures, I_{tot} virtually attains saturation.

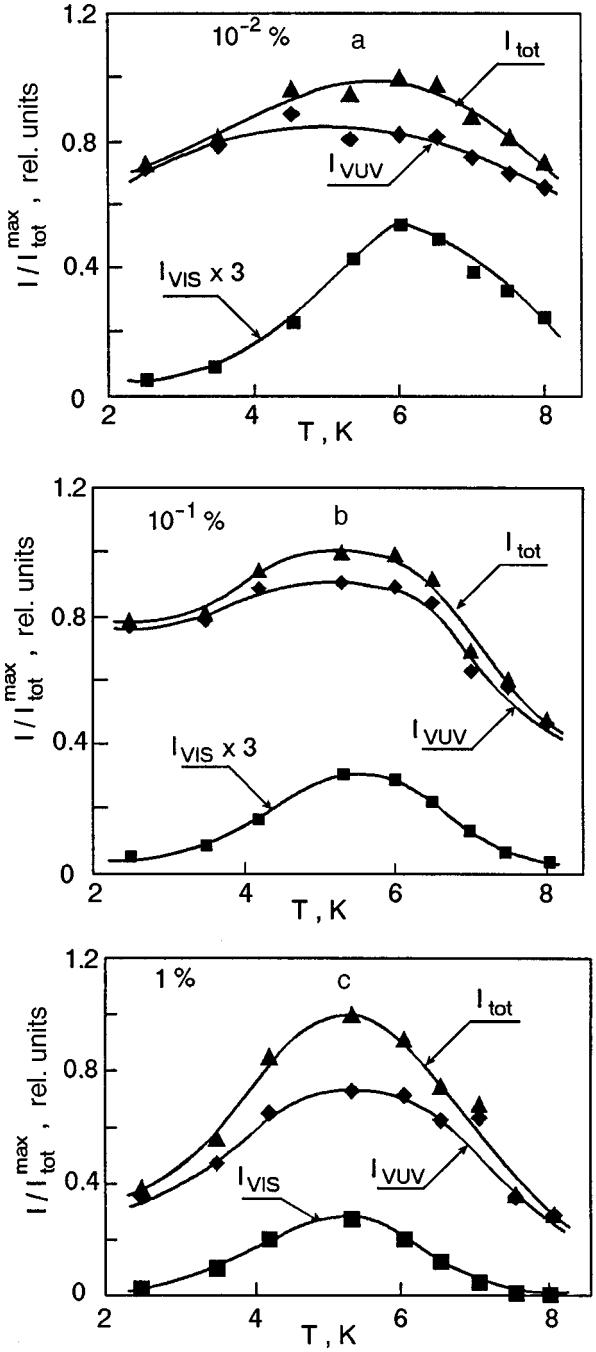

FIG. 4. Temperature dependence of integral intensities of intrinsic luminescence of neon in Ne–O_2 solid solutions for oxygen concentrations 10^{-2} (a), 10^{-1} (b), and 1 mol.% (c) Here I_{VUV} is the integral intensity of transitions from the lowermost excited states to the VUV spectral region, I_{VIS} the integral intensities of transitions between excited states in the visible range, and I_{tot} the total integral intensity in the VUV and visible regions.

It was noted in Ref. 9 that prolonged attenuation of intrinsic as well as extrinsic luminescence (afterglow) is observed after the irradiation is terminated. The attenuation

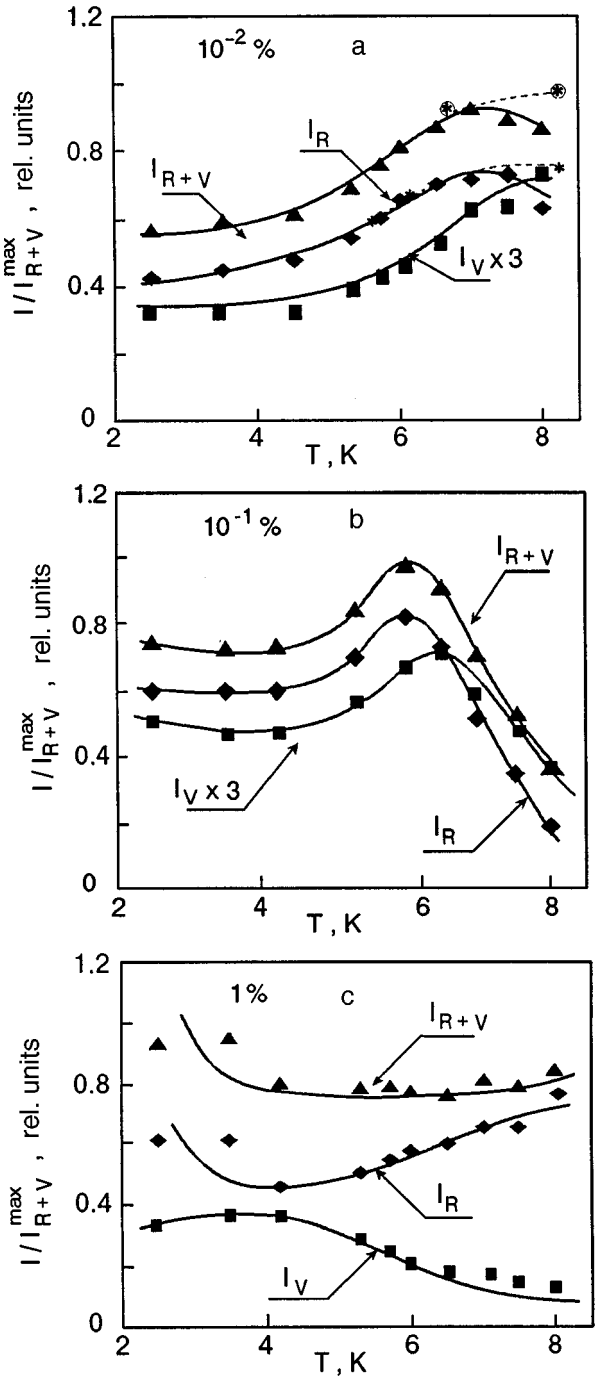

FIG. 5. Temperature dependence of integral intensities of extrinsic luminescence of O* centers for oxygen concentrations 10^{-2} mol.% (a), 10^{-1} mol.% (b), and 1 mol.% (c). Here I_{R+V} is the total integral intensity of O* centers, I_R the integral intensity of Rydberg transitions in this range, and I_V the integral intensity of luminescence of the valence transition $^1S \rightarrow {}^1D$. The dashed curves show the temperatures dependence of the luminescence of Ar impurity centers in Ne–Ar solid mixture.[15]

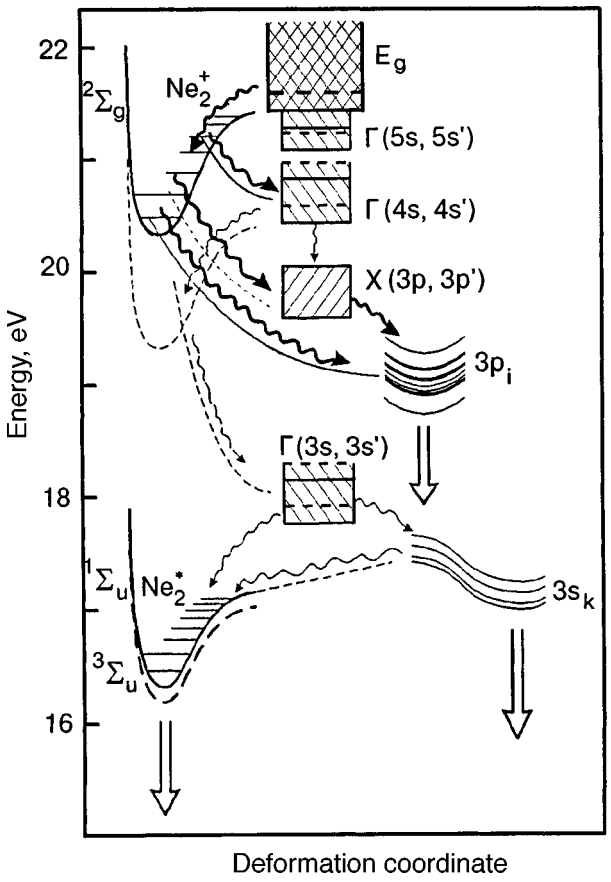

FIG. 6. Schematic diagram of energy relaxation for electron excitations in Ne cryocrystals.

curves for different transitions are found to be similar.[9] For a low oxygen concentration, the initial segment of the main segment of afterglow (1–2 min) is correctly described by the law $I \sim 1/t$. As the oxygen concentration increases, the intensity of afterglow of intrinsic transitions in the matrix in the VUV and visible ranges decreases significantly, while the intensity of impurity luminescence increases. The duration of impurity afterglow in this case also increase due to the emergence of an additional component characterized by a larger time constant. An increase in the temperature of solid mixtures subjected to preliminary irradiation leads to intensive thermoluminescence observed for all impurity bands and accompanied by thermal spikes of luminescence at $T \geqslant 9$ K.

3. DISCUSSION OF RESULTS

The most important results of this experimental investigation include (1) a consistent study of the transformation of the intrinsic and extrinsic luminescence spectra upon a change in the oxygen concentration in neon crystal and (2) observation and detailed analysis of the nonmonotonic temperature dependence of intrinsic and extrinsic luminescence. The first group of the results reflects peculiarities of migration of electron excitation energy in the matrix and trapping of the energy by impurity centers upon the variation of their concentration. It will be proved below that the second group of the results is due to temperature variation of the efficiency of recombination in the solid mixture during its high-energy ($E > E_g$) excitation.

Let us consider in greater detail the relaxation of electron energy and the formation of luminescent centers in Ne cryocrystals. It was proved in Ref. 9 that the excitation of neon by an electron beam with energy $E \geqslant 100$ eV leads to the coexistence of two energy relaxation channels in it: the exciton channel and the pure recombination channel (Fig. 6).

The exciton channel of energy relaxation for electron excitations dominates in heavy inert crystals.[1–4] It leads to an effective energy release from high-energy Γ-excitons formed directly during irradiation (including that involving secondary (polarization) braking radiation (PBR))[20] as well as excitons formed during the recombination of band electrons and holes to the lowermost $(n=1)$ $\Gamma(1/2,3/2)$-states. Energy relaxation through the exciton channel occurs in a sequence of relaxation processes inside the bands and in the course of interband transitions. The latter processes are accompanied by the self-trapping of high-energy $(n>1)$ Γ-excitons in two-center bound Ne_2^{**} states and their subsequent dissociation in repulsive potentials of unstable $[Ne_2^*]$ states generated by lower-lying ns-energy levels. The entire sequence of processes can be presented in the form

$$\left.\begin{matrix} e^* \\ \hbar\omega_{\mathrm{PBR}} \\ e^- + h^+ \end{matrix}\right\} \rightarrow \mathrm{Ne}^{**} + \mathrm{Ne} \rightarrow [\mathrm{Ne}_2^{**}] \rightarrow \mathrm{Ne}^* + \mathrm{Ne} \rightarrow h\nu_{\mathrm{VUV}} + \mathrm{Ne} + \mathrm{Ne}, \quad (1)$$

where e^*, e^-, and h^+ are, respectively, band excitons, electrons, and holes created by the exciting beam, and $\hbar\omega_{\mathrm{PBR}}$ are the polarization braking radiation quanta. The excitation relaxation process in Ne cryocrystals leads to the population of the lowest $(n=1)$ $\Gamma(1/2,3/2)$-excitons whose self-trapping results in the formation of $^1P_1$, $^3P_1$, and $^3P_2$ luminescence centers.[2]

The recombination relaxation channel of the electron energy is manifested most clearly in crystalline neon, although its contribution can also be observed in other crystals of inert gases. This is mainly due to a strong electron–phonon interaction which is characteristic of neon and is responsible for the rapid self-trapping of hole carriers, which precedes the recombination act and is accompanied by the formation of Ne_2^+ centers (m-STh).[7,9] The initial stage of hole localization involves the emergence of m-STh in higher vibrational states. Their recombination with electrons may lead to the population of Γ-excitons with $n>2$. On the other hand, two-center localized holes in excited vibrational states can transport energy rapidly over the lattice as well as over the oxygen impurity atoms (in analogy with the energy transport by m-STE centers in Ne).[18] The latter process is accompanied by the emission of phonons into the lattice and facilitates a rapid energy relaxation of m-STh centers to the lowest vibrational levels. Recombination of vibrationally relaxed m-STh centers, which occurs through the dissociative mechanism, leads to the population of $3p(3p')$ localized centers directly or through X-exciton states. Radiative $3p(3p')\rightarrow 3s(3s')$ transitions (visible luminescence) do not lead to the formation of $^{1,3}P_{1,2}$-centers in view of the axial symmetry possessed by $3p(3p')$ centers, but are rather accompanied by the population of Ne_2^* states:[6,7,9]

$$e^- + \mathrm{Ne}_2^+ \rightarrow [\mathrm{Ne}_2^{**}] \rightarrow \mathrm{Ne}^{**}_{3p(3p')} + \mathrm{Ne} \rightarrow \mathrm{Ne}^{*}_{3s(3s')} + \mathrm{Ne} + h\nu_{\mathrm{VIS}} \rightarrow h\nu_{\mathrm{VIS}} + \mathrm{Ne}_2^*. \quad (2)$$

Thus, a simultaneous analysis of the intensity of the luminescence spectra of the lowest self-trapped (VUV) centers $^1P_1$, $^3P_1$, and $^3P_2$ and the higher (visible) $3p(3p')a$-STE centers makes it possible to separate the contributions from different energy relaxation channels of electron excitations in the formation of radiative states by varying the experimental parameters. It was shown in Ref. 9 that the efficiency of the recombination channel decreases sharply with temperature in the interval 6–2 K. This indicates the possible existence of localized electrons of shallow polaron states in Ne-type cryocrystals.

Let us consider the influence of neon doping by oxygen on this effect. Figure 4 demonstrates a consecutive variation of temperature dependences of integral luminescence parameters of Ne matrix with decreasing oxygen concentration. A comparison of Figs. 4 and 3 shows that the variation of I_{tot}, I_{VUV}, and I_{VIS} in the low-temperature region 2.5–5 K in pure neon as well as in solid mixtures with oxygen is the same for all concentrations. On the contrary, the intrinsic luminescence intensity of the matrix in solid mixtures of Ne with oxygen at higher temperatures decreases, the decrease being the sharper, the higher the impurity concentration. This can be due either to an increase in the rate of energy transport from the matrix to the impurity upon an increase in temperature, or to a decrease in the efficiency of the formation of luminescence centers in the recombination process caused by the localization of charge carriers in the sample. The role of the former process can be determined from the type of temperature dependence of extrinsic luminescence. It can be seen from Fig. 5 that an increase in temperature does not cause any significant increase in the intensity of extrinsic luminescence at temperature above 5–6 K. On the contrary, the extrinsic luminescence of oxygen, like the intrinsic luminescence of the matrix, decreases the intensities I_{R} and I_{V} of transitions. This fact contradicts the first of the assumption made above and supports the second. It should be noted that the temperature dependence of the spectral characteristics of the luminescence of Ne–O solid solutions differs significantly from that of the luminescence spectra of Ne–Xe and Ne–Ar solid mixtures,[15–17] which were recorded under conditions similar to those in our experiments (dashed curves in Fig. 5a). The intensity of the extrinsic luminescence of Xe or Ar increases consistently with temperature in the interval 6–10 K, while the intensity of the VUV luminescence of the matrix exhibits a slight decrease. (The visible radiation of the $3p(3p')\rightarrow 3s(3s')$ transitions was not observed by us in these works.) A comparison of the results obtained in Refs. 15–17 with those presented in Fig. 5a suggests that a sharp attenuation of the intrinsic and extrinsic luminescence in $Ne–O_2$ solid solutions at $T>6$ K is due to a peculiar feature of the oxygen impurity, viz., its close affinity to an electron, which is equal to 0.54 eV for O_2 and 1.46 eV for the radical O. The considerable affinity of oxygen impurity atoms and molecules to the electron enables the localization of electrons at impurity centers, accompanied by the formation of low mobility negative impurity ions O^- or O_2^-:

$$\begin{aligned} &e^- + \mathrm{O}_2 \rightarrow \mathrm{O}_2^-, \\ &e^- + \mathrm{O} \rightarrow \mathrm{O}^-. \end{aligned} \quad (3)$$

On the other hand, charge transport from intrinsic hole

carriers in the matrix to neutral O_2 or O centers is accompanied by the formation of O_2^+ or O^+ local centers. These centers can also be formed as a result of trapping of the exciton excitations of the matrix by neutral oxygen centers since the exciton energy $E_{exc} \geqslant 17$ eV considerably exceeds the impurity ionization energy ($\geqslant 12$ eV):

$$\begin{aligned} &h_2^+ + O_2 \rightarrow O_2^+, \\ &h_2^+ + O \rightarrow O^+, \\ &e^* + O_2 \rightarrow (NeO_2)^* \rightarrow O_2^+ + Ne + e^-, \\ &e^* + O \rightarrow (NeO)^* \rightarrow O^+ + Ne + e^-. \end{aligned} \tag{4}$$

The existence of these processes is indicated by a more noticeable decrease in the intensity of VUV luminescence of the matrix in comparison with I_{VIS} upon an increase in oxygen concentration (see Fig. 4). Thus, spatially separated stationary charge centers are accumulated in an irradiated $Ne–O_2$ solid solution, and the recombination channel of formation of intrinsic luminescence states becomes ineffective. This also follows from the observed prolonged afterglow and thermoluminescence (see above).

Within the framework of the above model and under the assumption of self-trapping of electrons in the neon matrix, we can easily explain such a bell-shaped temperature dependence of integral characteristics for intrinsic and extrinsic luminescence shown in Figs. 4 and 5. At low temperatures, the efficiency of the recombination channel in the solid solution is determined by the mobility of weakly coupled electron states in the Ne matrix. The probability of self-trapping of electrons decreases with increasing temperature, while their mobility increases, and hence the rate of formation of luminescence centers increases sharply during recombination. This leads to an enhancement of intrinsic as well as extrinsic luminescence. However, a decrease in the probability of electron self-trapping in the matrix lattice leads to an increase in the probability of localization of electrons at oxygen impurity centers, accompanied by the formation of deep negatively charged states, as well as to the accumulation of both types of charges separated in the bulk of the crystal. The latter process is also enhanced by an increase in the mobility of exciton excitations in the matrix upon heating.[18] All these processes lead to a further decrease in the luminescence intensity due to a decrease in the efficiency of the recombination channel, which is controlled in this temperature range by charge localization in the oxygen impurity subsystem.

An increase in the concentration of the solid solution augments the influence of the latter process, causing an increase in the steepness of declining integral luminescence characteristics in the range of relatively high temperatures, and a displacement of the points of inflection on the curves in Figs. 4 and 5 towards lower temperatures. Similar phenomena were observed in several wide-band semiconductors and alkali-halide crystals and were given the common name of charge reversal effect in a system of shallow and deep electron traps.[19]

For very high oxygen concentrations $c \geqslant 1\%$, the effect of electron self-trapping has a strong effect only on the intrinsic luminescence of the matrix (Fig. 5c). The extrinsic luminescence spectrum at temperatures 2.5–5 K shows only a slight decrease in I_{R+V} due to a decrease in the efficiency of the recombination channel, after which it remains practically unchanged. At relatively high temperatures 4.5–8 K, the intensities I_R and I_V exhibit just the opposite temperature dependence, which apparently reflects the possibility of electron jumps over a system of closely spaced molecular centers to quasi-atomic centers O having a strong affinity to the electron. It was mentioned above that this effect is accompanied by a strong variation of the spectral composition of radiation, including the emergence of high-energy $3s'^1D$ and $3s'^3D$ Rydberg states of O* and an enhancement of the contribution of the ''*d*''-components to the combined contour of each band (see Figs. 2 and Sec. 2.2). The effect of recombination processes on the formation of different excited states and their structure will be discussed in subsequent publications.

Finally, it should be remarked that the increase in the intrinsic luminescence of the matrix in the temperature range 2.5–5 K over a wide range of impurity concentrations right up to $c \geqslant 1\%$ is a strong argument in favor of the hypothesis about the possible localization of electrons in Ne cryocrystals put forth in Ref. 9.

4. CONCLUSION

An analysis of the temperature dependence of intrinsic and extrinsic luminescence of neon–oxygen solid mixtures of various concentrations carried out by us has revealed the contribution of the recombination channel to the population of the luminescence states. It is shown that its efficiency depends on the probability of electron localization in the matrix lattice at low temperatures 2.5–5 K, while in the interval 6–8 K it is determined by the probability of trapping at the oxygen impurity centers with a large negative charge having a strong affinity to an electron. As a result of these processes, the luminescence intensity in Ne–O solid mixtures has a bell-shaped temperature dependence with a peak near 5–6 K. The evidence of the possible self-trapping of electrons in Ne cryocrystals supplements the results obtained in Ref. 9.

*E-mail: belov@ilt.kharkov.ua

[1] I. Ya. Fugol', Adv. Phys. **27**, 1 (1978).
[2] I. Ya. Fugol' and E. V. Savchenko, in *Cryocrystals* [in Russian] (ed. by B. I. Verkin and A. F. Prikhot'ko), Naukova Dumka, Kiev (1983).
[3] A. Schwentner, E. E. Koch, and J. Jortner, *Electronic Excitations in Condensed Rare Gases*, Springer Verlag, Berlin (1985).
[4] G. Zimmerer, in *Excited State Spectroscopy in Solids* (ed. by U. M. Grassano and N. Tarzi), North-Holland, Amsterdam (1987).
[5] I. Ya. Fugol', A. G. Belov, and V. N. Svishchev, Solid State Commun. **66**, 503 (1988).
[6] I. Ya. Fugol', Adv. Phys. **37**, 1 (1988).
[7] A. G. Belov, V. N. Svishchev, and I. Ya. Fugol', Fiz. Nizk. Temp. **15**, 61 (1989) [Sov. J. Low Temp. Phys. **15**, 34 (1989)].
[8] W. E. Spear and P. G. LeComber, in *Rare Gas Solids* (ed. by H. L. Klein and J. A. Venables), Vol. II, Acad. Press, London (1978).
[9] A. G. Belov, G. M. Gorbulin, I. Ya. Fugol', and E. M. Yurtaeva, Fiz. Nizk. Temp. **23**, 439 (1997) [Low Temp. Phys. **23**, 322 (1997)].
[10] E. M. Yurtaeva, I. Ya. Fugol', and A. G. Belov, Fiz. Nizk. Temp. **13**, 165 (1987) [Sov. J. Low Temp. Phys. **13**, 90 (1987)].

[11] A. G. Belov, I. Ya. Fugol', and E. M. Yurtaeva, Fiz. Nizk. Temp. **18**, 177 (1992) [Sov. J. Low Temp. Phys. **18**, 123 (1992)].
[12] E. V. Savchenko, Yu. I. Rybalko, and I. Ya. Fugol', Pis'ma Zh. Éksp. Teor. Fiz. **42**, 210 (1985) [JETP Lett. **42**, 260 (1985)].
[13] F. J. Coletti, J. M. Debever, and G. Zimmerer, J. Chem. Phys. **83**, 49 (1985).
[14] A. G. Belov, I. Ya. Fugol', and E. M. Yurtaeva, Fiz. Nizk. Temp. **19**, 591 (1993) [Low Temp. Phys. **19**, 421 (1993)].
[15] Yu. I. Rybalko, Ph.D. Thesis, Kharkov (1987).
[16] Yu. I. Rybalko, E. V. Savchenko, and I. Ya. Fugol', Fiz. Nizk. Temp. **11**, 637 (1985) [Sov. J. Low Temp. Phys. **11**, 349 (1985)].
[17] I. Ya. Fugol', Yu. I. Rybalko, and E. V. Savchenko, Solid State Commun. **60**, 495 (1986).
[18] A. M. Ratner, I. Ya. Fugol', A. G. Belov, and Yu. I. Steshenko, Phys. Lett. A **137**, 403 (1989).
[19] E. D. Aluker, V. V. Gavrilov, R. G. Deich, and S. A. Chernov, *Rapid Radiation-Stimulated Processes in Alkali-Halide Crystals* [in Russian], Zinatne, Riga (1987).
[20] A. G. Belov, I. Ya. Fugol', and E. M. Yurtaeva, Fiz. Nizk. Temp. **21**, 238 (1995) [Low Temp. Phys. **21**, 183 (1995)].

Translated by R. S. Wadhwa

LATTICE DYNAMICS

Peculiarities of the resonant phonon scattering from a plane defect in an fcc crystal

A. M. Kosevich and S. E. Savotchenko

*B. Verkin Institute for Low Temperature Physics and Engineering, National Academy of Sciences of the Ukraine, 310164 Kharkov, Ukraine**

D. V. Matsokin

Kharkov State University, 310077 Kharkov, Ukraine
(Submitted July 24, 1998; revised September 8, 1998)
Fiz. Nizk. Temp. **25**, 63–71 (January 1999)

Resonant peculiarities of phonon scattering from a plane defect in an fcc crystal with the central interaction between nearest neighbors are investigated. It is shown that resonance effects are associated with the interaction of phonons of two bulk branches on a plane defect. Dispersion curves for the frequencies of resonance transmission and reflection are derived. To clarify the physical nature of resonances under investigation, the dispersion relations of vibrations localized at the defect are calculated in a wide range of wavelengths. The frequency curves of localized symmetric vibrations continue in the bulk spectrum in the form of dispersion curves of the frequencies of resonant phonons transmitted through the defect. [S1063-777X(99)01001-4]

INTRODUCTION

The study of interaction between different types of waves in media with plane defects has a long history and is not only of theoretical, but also of purely applied interest. Examples of plane defects in crystals are twin and phase boundaries as well as two-dimensional stacking faults. Resonant scattering of transverse elastic waves by a plane defect was described in recent publications.[1,2] It was found that the phase velocities of elastic waves scattered resonantly or transmitted through the defect lie in the interval between the velocities of transverse and longitudinal acoustic waves. It would be interesting to generalize these results obtained in the theory of elasticity to the vibrations of a discrete lattice and to study peculiarities of resonant scattering in a wide range of wavelengths. In this communication, we propose a description of resonant peculiarities of phonon scattering by a plane defect and eigenvibrations of the Rayleigh polarization in the model of a discrete fcc lattice with the interaction between nearest neighbors. The boundary conditions formulated in the framework of the lattice model under investigation can obviously be used to obtain the boundary condition in the theory of elasticity through a limiting transition in the long-wave approximation.[2,3] The choice of Rayleigh polarization of vibrations is dictated by their wide application in engineering. The fact that phonons polarized in the sagittal plane have a displacement component perpendicular to the surface facilitates their experimental observation.[4,5]

It was shown earlier[6–8] that an analysis of the interaction of the vibrations of a crystal with a plane defect by the methods of crystal lattice dynamics makes it possible to describe high-frequency peculiarities of phonon scattering by a plane defect as well as new essentially short-wave local vibrations in a wide range of wavelengths.

A general theory of resonance phenomena of the type under investigation was proposed recently in Ref. 9. The conditions of resonant scattering and transmission determine the frequencies of steady-state vibrations which are not symmetric relative to the defect plane and which can be formed owing to the presence of two branches in the bulk spectrum. Resonant scattering of a phonon corresponds to a standing wave of one of the bulk (e.g., transverse) branches only in one half-space in the presence of a localized mode of another branch on both sides of the defect. Resonant transmission also corresponds to two modes of waves, viz., a bulk wave propagating in the same direction on both sides of the defect and a wave which is localized also on both sides of the defect.

1. BOUNDARY CONDITIONS AND ANALYSIS OF THE BULK VIBRATIONAL SPECTRUM

Let us consider the simplest model of a plane defect coinciding with the crystallographic plane (001) of an fcc crystal. The coordinate axes are directed along the edges of the cube, and the z-axis is perpendicular to the defect plane. We confine our analysis to interactions of atoms only with their nearest neighbors. Let the interaction of atoms be characterized by a force constant α in the entire volume of the crystal except the interaction between the layers $n_z=0$ and -1, where it is characterized by the parameter β differing from α (Fig. 1). We assume that the edge of the cube is equal to $2d$. For convenience of notation, we put $d=1$.

We start with an analysis of the bulk dispersion relation required for determining the spectral regions in which the

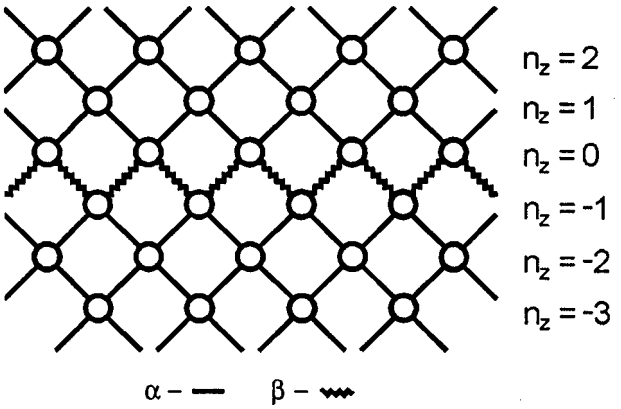

FIG. 1. Schematic diagram of a plane defect in a crystal.

frequencies of localized or pseudolocalized eigenvibrations as well as the frequencies of resonance scattering of waves on the defect can be determined.

The displacements of atoms can be represented in the form

$$\mathbf{u}(\mathbf{n})=\begin{cases}\mathbf{u}^{+}(n_z)e^{i(k_x n_x+k_y n_y-\omega t)}, & n_z\geqslant 0,\\ \mathbf{u}^{-}(n_z)e^{i(k_x n_x+k_y n_y-\omega t)}, & n_z<0,\end{cases}$$

where $\mathbf{u}^{\pm}(n_z)$ is the dependence of the displacement amplitude on the number of the layer.

We choose the [110] direction as the direction of wave propagation along the plane defect ($k_x=k_z=k$) and recall the basic features of phonons polarized in the xz sagittal plane [$\mathbf{u}=(u_x,0,u_z)$].

The system of equations of motion for a perfect crystal (infinitely large crystal without defects) can be written in the form

$$\hat{L}(\mathbf{k},\lambda)\mathbf{u}=0, \tag{1}$$

where

$$L_{11}(q)=2-\cos 2k-\cos k\cos q-\lambda;$$

$$L_{12}(q)=L_{21}(q)=\sin k\sin q;$$

$$L_{22}(q)=1-\cos k\cos q-\frac{\lambda}{2};\quad \lambda=\frac{m\omega^2}{4\alpha};$$

m is the mass of an atom, and $\mathbf{u}(n_z)=\mathbf{u}_0\exp[i(qn_z)]$ the change in the vibrational amplitude with the depth. Equating the determinant of the system (1) to zero, we obtain the characteristic equation for bulk vibrations of the crystal:

$$L_{11}L_{22}=L_{12}^2. \tag{2}$$

Solving this equation for λ, we obtain the dispersion relation for two bulk vibrational branches

$$\lambda_{\pm}(k,q)=\frac{1}{2}(4-\cos 2k-3\cos k\cos q\pm\sqrt{D}), \tag{3}$$

$$D=(4-\cos 2k-3\cos k\cos q)^2-8[2+(\cos 2k-3)\cos k\cos q-\cos^2 k+\cos^2 q],$$

where the ''+'' sign corresponds to the vibrational branch with a higher frequency (conditionally longitudinal l-branch), and the ''−'' sign to the vibrational branch with a lower frequency (conditionally transverse t-branch). Figure 2 shows the vibrational spectra for these two bulk vibrational branches along the [110] direction in a fcc crystal within the first Brillouin zone. The lower boundary of the continuous spectrum $\lambda_{t\,\min}(k)$ is the envelope of the minimum values of frequency for different values of q (curve *1* in Fig. 2). Curve *2* in Fig. 2 given by the formula

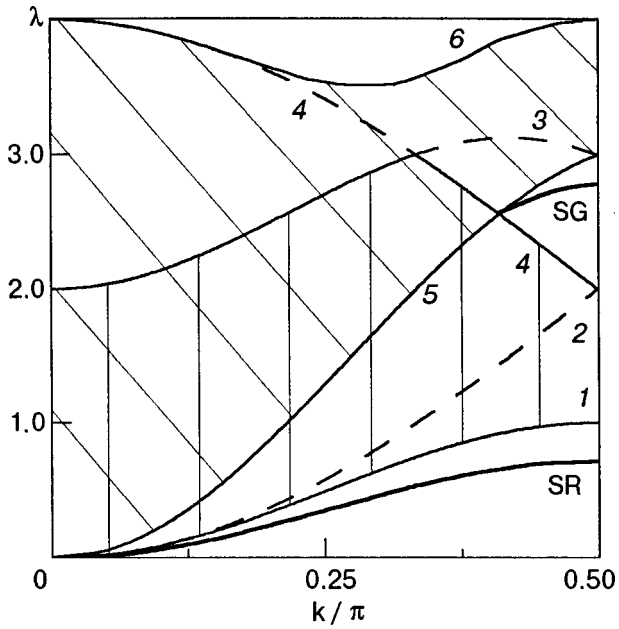

FIG. 2. Frequency spectra for surface waves (*SR* and *SG* curves) and bulk vibrations (hatched regions) as functions of the wave vector k. The vertical hatching corresponds to pseudotransverse branch and slanted hatching to the pseudolongitudinal branch.

$$\lambda_{0t}(k)=2(1-\cos k) \tag{4}$$

is obtained from (3) for $q=0$ and bounds the region of the t-branch in which each value of k corresponds to a pair of real roots $\pm q_t(k)$ of the characteristic equation (2) and a pair of complex-conjugate roots $q_l(k)=\pm i\kappa_l$. This region is bounded from above by the lower boundary of the l-branch (curve *5* in Fig. 2), i.e.,

$$\lambda_{l\,\min}(k)=2-\cos 2k-\cos k, \tag{5}$$

which can be obtained from (3) for $q=0$. The upper boundary of the l-branch is the envelope of the maximum values of frequencies in (3) (curve *6* in Fig. 2), while the upper boundary of the t-branch can be obtained from (3) for $q=\pi$ (solid segments of curves *3* and *4* in Fig. 2).

The boundaries of pseudotransverse and pseudolongitudinal branches intersect at the point $\lambda_0(k_0)=1/2(1+\sqrt{17})$ for $k_0=\arccos(1/4)(\sqrt{17}-3)$, forming a gap in the continuous spectrum, in which the frequencies of local vibrations can be located.

The transverse and longitudinal phase velocities ($c=\omega/k$) of acoustic waves in the long-wave approximation $kd\ll 1$ (the wavelength is much larger than the lattice constant) along the [110] direction can be obtained from (3) for $q=0$:

$$c_t^2=\frac{4\alpha}{m}, \quad c_l^2=\frac{10\alpha}{m}. \tag{6}$$

It is well known[10] that the cross sections of constant-frequency surfaces by the plane kq along the [110] direction of an fcc crystal are always nonconvex for the corresponding anisotropy parameter $\eta=(c_{11}-c_{12})/2c_{44}=1/2$, where elastic moduli of the cubic crystal are expressed in terms of the force constant of interaction: $c_{11}=4\alpha$, $c_{12}=c_{44}=2\alpha$.

Consequently, the velocities of surface waves in an fcc crystal cannot exceed the value $c_{\min}^2=c_t^2 4(\sqrt{5}-2)$. This minimal velocity can be determined from $\lambda_{t\,\min}(k)$ in the long-wave limit $kd\ll 1$.

Having discussed the properties of bulk vibrations, we write the dynamic equations for atomic layers adjoining the plane defect ($n_z=0,-1$). These equations differ from (1) and can be written in the form

$$\begin{cases} u_x^+(0)[4-\varepsilon-2\lambda-2\cos 2k]-u_x^+(1)\cos k-u_z^+(1)i\sin k \\ -u_x^-(-1)(1-\varepsilon)\cos k+u_z^-(-1)i(1-\varepsilon)\sin k=0, \\ u_x^+(1)i\sin k+u_z^+(1)\cos k-u_z^+(0)(2-\varepsilon-\lambda) \\ -u_x^-(-1)i(1-\varepsilon)\sin k+u_z^-(-1)(1-\varepsilon)\cos k=0 \end{cases} \tag{7}$$

for the layer $n_z=0$ and

$$\begin{cases} u_x^-(-1)[4-\varepsilon-2\lambda-2\cos 2k]-u_x^-(-2)\cos k \\ +u_z^-(-2)i\sin k-u_x^+(0)(1-\varepsilon)\cos k \\ -u_z^+(0)i(1-\varepsilon)\sin k=0, \\ u_x^-(-2)i\sin k-u_z^-(-2)\cos k+u_z^-(-1)(2-\varepsilon-\lambda) \\ -u_x^+(0)i(1-\varepsilon)\sin k-u_z^+(0)(1-\varepsilon)\cos k=0, \end{cases} \tag{8}$$

for the layer $n_z=-1$, where $\varepsilon=(\alpha-\beta)/\alpha$ is the parameter characterizing the relative change in the force interaction between atoms near the interface.

Using Eqs. (7) and (8), we can easily obtain the boundary conditions at a plane defect for dynamic equations in the theory of elasticity. We assume that the plane defect is concentrated in the plane $z=0$. Expanding the displacements in the dynamic equations (7) and (8) relative to the chosen lattice sites into power series in (n_x,n_z) and confining our analysis to the first terms, we obtain the following boundary conditions:

$$\sigma_{iz}^+-\sigma_{iz}^-=\Lambda_i\frac{\partial}{\partial x}(u_j^--u_j^+),$$

$$\sigma_{iz}^++\sigma_{iz}^-=\frac{\Omega_i}{d}(u_i^+-u_i^-)+\Lambda_i\frac{\partial}{\partial x}(u_j^+-u_j^-),$$

$$i,j=x,z; \quad i\neq j,$$

where σ_{ij}^+ and σ_{ij}^- are the stress tensors above and below the defect, respectively, whose components in the model under investigation are

$$\sigma_{xz}=2\alpha\left(\frac{\partial u_x}{\partial z}+\frac{\partial u_z}{\partial x}\right), \quad \sigma_{zz}=4\alpha\left(\frac{\partial u_x}{\partial x}+\frac{\partial u_z}{\partial z}\right),$$

and the effective parameters of the defect can be expressed in terms of the force constant β of interaction between boundary layers:

$$\Lambda_x=2\beta, \quad \Lambda_z=\Omega_x=4\beta, \quad \Omega_z=8\beta.$$

Such boundary conditions were formulated (accurate to the notation) phenomenologically on the basis of equations in the theory of elasticity.[2] The possibility of a transition from the dynamic equations for the lattice to the boundary conditions at a plane defect in the theory of elasticity were illustrated earlier for a hexagonal crystal.[8]

Let us determine the types of vibrations that can be characterized by frequencies lying in different regions of the bulk spectrum and outside it (see Fig. 2). An analysis of the roots of the characteristic equation (2) shows that

(1) In the regions $\omega<\omega_{t\,\min}(k)$ (under the spectrum), $\omega_{t\,\max}(k)<\omega<\omega_{l\,\min}(k)$ for $k>k_0$ (in the gap) and $\omega>\omega_{l\,\max}$ (above the spectrum), the characteristic equation (2) has four complex-valued roots from which we can choose the pair $i\kappa_\mu=q_\mu(k)$ $(\mu=l,t)$ satisfying the condition of attenuation of vibrations as we move from the defect to the bulk of the crystal ($\mathrm{Re}\,\kappa_\mu>0$ for $z>0$). These spectral regions can contain the frequencies of two-partial localized waves of the Rayleigh polarization;

(2) in the regions $\omega_t(k,q=0)<\omega<\omega_{l\,\min}(k)$, $\omega_{t\,\max}(k)<\omega<\omega_{l\,\max}(k)$ the characteristic equation (2) has two real and two complex-conjugate roots from which we choose a pair of real-valued roots $\pm q$ and a purely imaginary solution $\pm i\kappa$ with the sign ensuring attenuation of the wave towards the bulk of the crystal. Pseudolocalized phonons can exist in these regions of the bulk spectrum;

(3) in the region $\omega_{l\,\min}(k)<\omega<\omega_{t\,\max}(k)$, Eq. (2) has four real roots $q(k)$ from which we can choose a pair q_t and $-q_l$ (or $-q_t$ and q_l) that determines the transformation of the wave upon the reflection at the defect (transformation waves were considered in detail in Ref. 8).

2. EIGENVIBRATIONS LOCALIZED AT THE DEFECT

The boundary Eqs. (7) and (8) show that the solutions of the problem of eigenvibrations can be of two types: symmetric solutions

$$u_x^+(n_z+1)=-u_x^-(-n_z), \quad u_z^+(n_z+1)=u_z^-(-n_z)$$

and the antisymmetric solutions

$$u_x^+(n_z+1)=u_x^-(-n_z), \quad u_z^+(n_z+1)=-u_z^-(-n_z)$$

where u_i^+ is the displacement in the upper half-space ($n_z\geqslant 0$) and u_i^- the displacement in the lower subspace ($n_z<0$).

Since the equations are linear, we can analyze the symmetric and antisymmetric solutions separately. For such an analysis, we can take any of the boundary conditions (7) and (8) (say, (7)).

An analysis of the characteristic equation (2) proved that the solutions of the boundary-value problem outside of the continuous spectrum should be sought for $n_z\geqslant 0$ in the form

$$\begin{cases} u_x^+(n_z)=u_t^0 e^{-\kappa_t n_z}+u_l^0 e^{-\kappa_l n_z}, \\ u_z^+(n_z)=u_t^0\Gamma_t e^{-\kappa_t n_z}+u_l^0\Gamma_l e^{-\kappa_l n_z}, \end{cases} \tag{9}$$

where

$$\Gamma_\mu \equiv \frac{u^0_{z\mu}}{u^0_{x\mu}} = -\frac{L_{11}(q_\mu)}{L_{12}(q_\mu)} = -\frac{L_{12}(q_\mu)}{L_{22}(q_\mu)},$$

$\mu = l,t$ are the eigenvectors of the bulk equations of motion (1). The roots κ_μ ($\mu = l,t$) of the characteristic equation (2) were chosen for $\mathrm{Re}\,\kappa_\mu > 0$. The displacements in the lower half-space are determined by the choice of the symmetry of vibrations. Substituting (9) into the boundary conditions (7), we obtain the system of boundary equations

$$\sum_{\mu=l,t} u^0_\mu C^{(A,S)}_{j\mu} = 0 \quad (j = 1,2), \tag{10}$$

$$\begin{cases} C^{(A,S)}_{1\mu} = 3 - 2\lambda - 2\cos 2k - (1-\varepsilon)(1 \mp \cos k) \\ \quad - e^{-\kappa_\mu}\cos k - i\Gamma_\mu[e^{-\kappa_\mu} \pm (1-\varepsilon)]\sin k, \\ C^{(A,S)}_{1\mu} = \Gamma_\mu[1 - \lambda - e^{-\kappa_\mu}\cos k + (1-\varepsilon)(1 \pm \cos k)] \\ \quad - i[e^{-\kappa_\mu} \mp (1-\varepsilon)]\sin k. \end{cases} \tag{11}$$

The upper signs in (11) correspond to antisymmetric states (superscripts A) while the lower signs to the symmetric states (superscripts S). Equating the determinant of the system (10) to zero, we obtain the dispersion equation for frequencies of localized eigenvibrations:

$$C^{(A,S)}_{1t} C^{(A,S)}_{2l} - C^{(A,S)}_{1l} C^{(A,S)}_{2t} = 0. \tag{12}$$

This equation can be solved analytically only at the boundary points of the Brillouin zone, while for arbitrary values of k has been solved numerically (on a computer).

An analysis of Eq. (12) shows that in the case of weakened interaction between the boundary atomic layers $\beta < \alpha (0 < \varepsilon < 1)$, frequencies of localized vibrations appear below the spectrum.

The frequency curve for antisymmetric localized vibrations lie slightly above the frequencies of symmetric vibrations for the same value of ε for $0 < k < \pi/2$. At the boundaries of the Brillouin zone, these curve converge to a point (Fig. 3). As the parameter of the defect varies in the interval $0 < \varepsilon < 1$, the frequencies of local phonons fill the region $\omega_{\mathrm{Re}}(k) < \omega < \omega_{t\,\min}(k)$ where $\omega_{\mathrm{Re}}(k)$ is the dispersion relation for a Rayleigh wave localized at the free surface for $\varepsilon = 1 (\beta = 0)$ (the *SR* curve in Figs. 2 and 3). In the long-wave region, the phase velocity of the SR wave $c_{\mathrm{Re}} \approx 0.85 c_t$, and the value of the frequency in the other limiting case (at the boundary of the Brillouin zone $k = \pi/2$) is $\lambda_{\mathrm{Re}}(\pi/2) = (7 - \sqrt{17})/4$.

The amplitudes of symmetric and antisymmetric vibrations decrease in an oscillating manner on both sides of the defect (i.e., behave as generalized surface waves) since the attenuation parameters $\kappa_\mu(k)$ are complex-valued.

As the coupling between the atomic boundary layers $\beta > \alpha$ increases ($-\infty < \varepsilon < 0$), localized vibrations with frequencies higher than those in continuous spectrum are excited (curves *S* in Fig. 4 correspond to the symmetric mode and *A* to the antisymmetric mode). Antisymmetric states are formed even for an infinitely small perturbation ($\varepsilon < 0$) in a thresholdless manner, their frequencies at the boundary point $k = 0$ being $\lambda_A = 4\beta^2/[\alpha(2\beta - \alpha)]$.

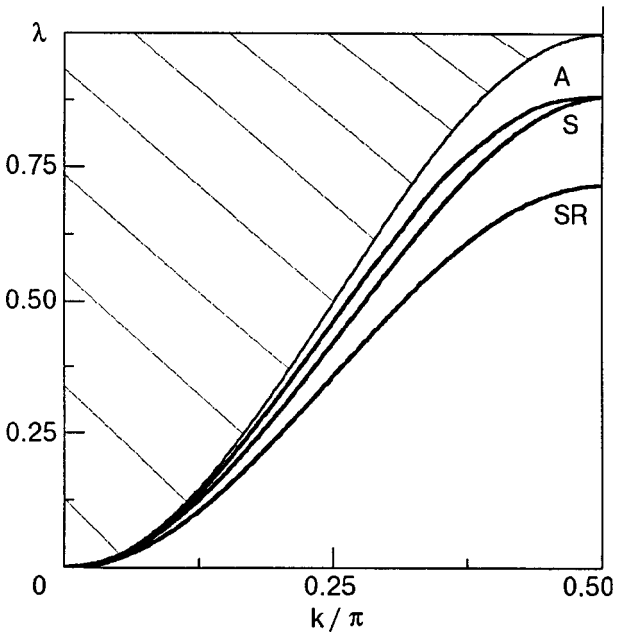

FIG. 3. Frequency spectra for localized low-frequency vibrations of the symmetric (curve *S*) and antisymmetric (curve *A*) types for $\beta = \alpha/4$; *SR* corresponds to the dispersion frequency curve localized near the free surface of a Rayleigh-type wave ($\beta = 0$). Hatched regions correspond to the continuous spectrum.

The frequencies of antisymmetric vibrations lie above the frequencies of symmetric vibrations for the same ε. The curves corresponding to symmetric and antisymmetric vibrations converge at a point on the boundary of the Brillouin zone ($k = \pi/2$). This point is separated (without a threshold) from the upper edge of the continuous spectrum upon an enhancement of coupling between defect layers. Symmetric

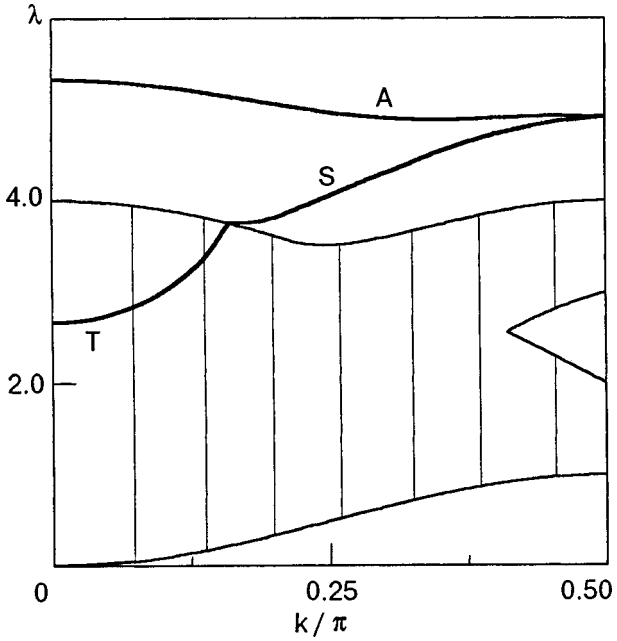

FIG. 4. Spectra for high-frequency localized vibrations of the symmetric (curve *S*) and antisymmetric (curve *A*) types and resonant transmission frequency spectra (curve *T*) for $\beta = 2\alpha$. Hatched regions correspond to the continuous spectrum of bulk vibrational frequencies.

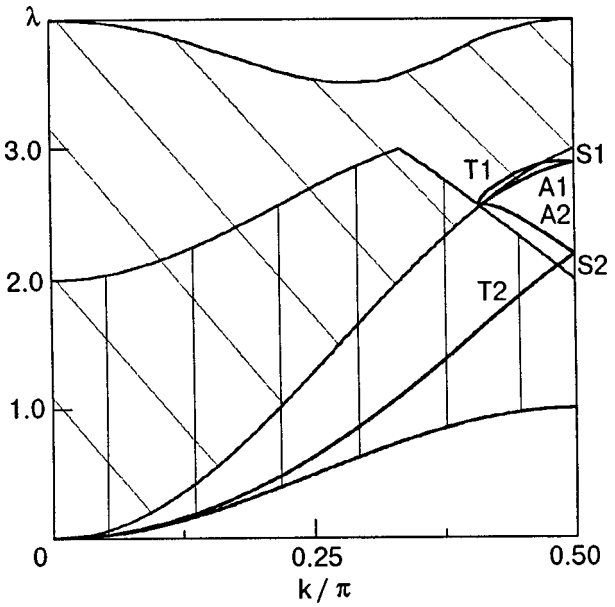

FIG. 5. Dispersion curves for the resonant transmission frequencies (*T1*) and localized gap vibrations of the symmetric (*S1*) and antisymmetric (*A1*) types for $\beta=0.35\alpha$ and *T2*, *S2*, and *A2* for $\beta=3\alpha$. Hatched regions correspond to the continuous spectrum of bulk vibrational frequencies.

vibrations exist above the spectrum for $k>k_S^*(\varepsilon)$, where $k_S^*(\varepsilon)$ is the point at which the frequency curve for symmetric vibrations touches the boundary of the continuous spectrum. For $k<k_S^*(\varepsilon)$, the curve corresponding to local frequencies of symmetric vibrations continues in the bulk spectrum in the form of an isolated frequency curve corresponding to complete transmission of a *t*-phonon through a plane defect (see Sec. 3). The frequencies of symmetric vibrations at point $k=0$ correspond to $\lambda_S=2\beta^2/[\alpha(2\beta-\alpha)]$.

In this region, local modes of a symmetric type are formed for $\beta>\beta_c\equiv\alpha(2+\sqrt{2})$.

The properties of localized high-frequency vibrations described above are analogous to those observed while studying shear waves with horizontal polarization.[6]

Symmetric and antisymmetric vibrations can be formed in the gap of the continuous spectrum in the case when the defect coupling is weakened ($\beta<\alpha$) as well as in the case when it is enhanced ($\beta>\alpha$) (Fig. 5). For a small excitation $\varepsilon>0$, the frequencies of localized gap vibrations split downwards from the lower boundary of the *l*-branch of the bulk spectrum in the case of weakening of the interaction between the boundaries values. In the case of a free surface ($\beta=0$), the frequency curve of the gap surface wave (*SG* curve in Fig. 2) starts from the point of intersection of the *t*- and *l*-branches of bulk vibrations $\lambda_0(k_0)=(1/2)(1+\sqrt{17})$ for $k_0=\arccos(1/4)(\sqrt{17}-3)$ and arrives at the point $\lambda_{\text{gap}}(\pi/2)=(1/4)(7+\sqrt{17})$ for $k=\pi/2$.

For a small perturbation of opposite polarity ($\varepsilon<0$), local gap modes of the symmetric and antisymmetric types split from the upper boundary of the bulk *t*-branch (*S2* and *A2* curves in Fig. 5). The frequency curves for gap vibrations of both types converge at the same point at the boundary of the Brillouin zone for the same value of the defect parameter.

The dispersion curves of antisymmetric gap vibrations emerge from the point $\lambda_0(k_0)$ for any value of ε. Gap vibrations of the symmetric type arrive either at the lower boundary of the *l*-branch, or at the upper boundary of the *t*-branch of bulk vibrations depending on the sign of the perturbation.

3. PECULIARITIES OF RESONANT SCATTERING OF PHONONS BY A PLANE DEFECT

Let us consider the problem of resonant scattering of phonons with frequencies belonging to a branch of eigenvibrations of the crystal, but differing from the eigenfrequencies of the other branch, by a plane defect. In such regions defined in Sec. 1, pseudolocal states (quasi-surface phonons) can exist. Such a pseudolocalized phonon consists of an incident and reflected waves of one of the bulk branches as well as the mode of the other bulk branch localized at the defect.

In a resonantly scattered wave, either *l*- or *t*-branch can be localized in various regions of the bulk spectrum. We shall conventionally mark by *a* the quantities pertaining to the bulk branch and by *b* the quantities corresponding to the localized branch. For frequencies $\omega<\omega_{l\,\min}(k)$, $b=l$ and $a=t$, while $b=t$ and $a=l$ for $\omega>\omega_{t\,\max}(k)$. The displacement vector for a wave of the Rayleigh type in the scattering problem is sought in the form

$$\begin{cases} u_x^+(n_z)=e^{-iq_a n_z}+Re^{iq_a n_z}+Me^{-\kappa_b n_z}, \\ u_z^+(n_z)=-\Gamma_a e^{-iq_a n_z}+R\Gamma_a e^{iq_a n_z}+M\Gamma_b e^{-\kappa_b n_z}, \end{cases}$$

$$\begin{cases} u_x^-(n_z)=Te^{-iq_a n_z}+Ne^{\kappa_b n_z}, \\ u_z^-(n_z)=-T\Gamma_a e^{-iq_a n_z}-N\Gamma_b e^{\kappa_b n_z}, \end{cases} \tag{13}$$

where q_a is the real-valued wave vector (the root of the characteristic equation (2)) and $i\kappa_b$ the complex root of (2) satisfying the condition $\operatorname{Re}\kappa_b>0$ for the localization of solutions. Substituting (13) into the boundary conditions (7) and (8), we obtain the matrix system of nonhomogeneous linear equations for the amplitudes *R*, *T*, *M*, and *N*:

$$\begin{pmatrix} R \\ M \\ T \\ N \end{pmatrix} \begin{pmatrix} D_{1R} & D_{1M} & D_{1T} & D_{1N} \\ D_{2R} & D_{2M} & D_{2T} & D_{2N} \\ D_{3R} & D_{3M} & D_{3T} & D_{3N} \\ D_{4R} & D_{4M} & D_{4T} & D_{4N} \end{pmatrix} = \begin{pmatrix} D_1 \\ D_2 \\ D_3 \\ D_4 \end{pmatrix}, \tag{14}$$

where the coefficients are given by

$$\begin{aligned} D_{1R}&=D_{3T}=4-\varepsilon-2\lambda-2\cos 2k-e^{iq_a}(\cos k+i\Gamma_a\sin k); \\ D_{1M}&=D_{3N}=4-\varepsilon-2\lambda-2\cos 2k-e^{-\kappa_b}(\cos k+i\Gamma_b\sin k); \\ D_{1T}&=D_{3R}=(\varepsilon-1)(\cos k+i\Gamma_a\sin k); \\ D_{1N}&=D_{3M}=(\varepsilon-1)(\cos k+i\Gamma_b\sin k); \\ D_{2R}&=D_{4T}=-\Gamma_a(2-\varepsilon-\lambda)+e^{iq_a}(\Gamma_a\cos k+i\sin k); \\ D_{2M}&=D_{4N}=-\Gamma_b(2-\varepsilon-\lambda)+e^{-\kappa_b}(\Gamma_b\cos k+i\sin k); \\ D_{2T}&=D_{4R}=(\varepsilon-1)(\Gamma_a\cos k+i\sin k); \end{aligned} \tag{15}$$

$$D_{2N}=D_{4M}=(\varepsilon-1)(\Gamma_b\cos k+i\sin k);$$

$$D_1=-D_{1R}^*;\quad D_2=D_{2R}^*;\quad D_3=-D_{3R}^*;\quad D_4=D_{4R}^*$$

(* marks complex conjugation).

We can easily write the coefficients of reflection $|R|^2$ and transmission $|T|^2$ in the form

$$|T|^2=\left|\frac{\Delta_T}{\Delta}\right|^2,\quad |R|^2=\left|\frac{\Delta_R}{\Delta}\right|^2, \tag{16}$$

where

$$\Delta=\begin{vmatrix} D_{1R} & D_{1M} & D_{1T} & D_{1N}\\ D_{2R} & D_{2M} & D_{2T} & D_{2N}\\ D_{3R} & D_{3M} & D_{3T} & D_{3N}\\ D_{4R} & D_{4M} & D_{4T} & D_{4N}\end{vmatrix},$$

$$\Delta_T=\begin{vmatrix} D_{1R} & D_{1M} & D_1 & D_{1N}\\ D_{2R} & D_{2M} & D_2 & D_{2N}\\ D_{3R} & D_{3M} & D_3 & D_{3N}\\ D_{4R} & D_{4M} & D_4 & D_{4N}\end{vmatrix},$$

$$\Delta_R=\begin{vmatrix} D_1 & D_{1M} & D_{1T} & D_{1N}\\ D_2 & D_{2M} & D_{2T} & D_{2N}\\ D_3 & D_{3M} & D_{3T} & D_{3N}\\ D_4 & D_{4M} & D_{4T} & D_{4N}\end{vmatrix}.$$

The conditions of resonant reflection $|T|^2=0$ or transmission $|R|^2=0$ can be satisfied for a certain relation between the frequency ω and the wave number k, which can be derived from the equations

$$|\Delta_T(\omega,k,\varepsilon)|=0 \tag{17}$$

and

$$|\Delta_R(\omega,k,\varepsilon)|=0, \tag{18}$$

for reflection and transmission respectively.

The explicit form of Eqs. (17) and (18) is extremely cumbersome and hence will not be given here. For the same reason, we present only the results of numerical analysis.

Let us analyze in greater detail the case of resonant reflection. The solution of the equations of motion (7) and (8) in this case is a superposition of the fields $\mathbf{u}=\mathbf{u}_a+\mathbf{u}_b$ of a nonsymmetric form, where the localized mode

$$\mathbf{u}_b(n_z)=\begin{cases}\mathbf{M}e^{-\kappa_b n_z}, & n_z\geqslant 0,\\ \mathbf{N}e^{\kappa_b n_z}, & n_z<0,\end{cases} \tag{19}$$

$\mathbf{M}=(M,0,M\Gamma_b)$, $\mathbf{N}=(N,0,-N\Gamma_b)$ and the bulk standing a-wave exists only in one of the half-spaces:

$$\mathbf{u}_a(n_z)=\begin{cases}\mathbf{A}(\cos q_a n_z+\delta), & n_z\geqslant 0,\\ 0, & n_z<0,\end{cases}$$

where $\mathbf{A}=(2e^{i\delta},0,2\Gamma_a e^{i\delta})$; and the phase δ of the wave is determined from the condition $R=e^{2i\delta}$.

Condition (17) defines the frequency $\omega_R=\omega_R(k,\varepsilon)$ of resonant scattering. The frequency spectrum for resonant reflection depends significantly on the type of the defect. When the interaction between the boundary layers is weakened ($\beta<\alpha$), the frequencies of resonant scattering lie in the region of t-branch of the continuous spectrum: $\omega_t^0(k,q=0)<\omega_R<\omega_p(k)$ (the lower range of the pseudolocalized states), where

$$\omega_p(k)=\begin{cases}\omega_{l\,\min}(k), & 0<k<k_0,\\ \omega_{t\,\max}(k), & k_0<k<\dfrac{\pi}{2}.\end{cases}$$

Figure 6 shows the frequency of resonant reflection as a function of the wave number for $\beta=0.1\alpha$ (curve *1*). An analysis of Eq. (17) shows that in the limiting case $\beta\to\alpha(\varepsilon\to 0)$, such a frequency tends to the lower boundary of the l-branch of bulk vibrations (5).

Similar conclusions concerning the phase velocities of a resonantly reflected elastic wave in the long-wave limit $kd\ll 1$: $c_R=\omega_R/k\to c_l$. were drawn in Refs. 1, 2, and 11.

In the case of enhancement of the interaction between defect layers, i.e., $\beta>\alpha(\varepsilon<0)$, new high-frequency peculiarities of resonant reflection of phonons appear. The dispersion curves $\omega_R(k,\varepsilon)$ in this case lie in the upper part of the spectrum of pseudolocal states, i.e., in the region of the l-branch of bulk vibrations, which is bounded by the dependence

$$\lambda(k)=\begin{cases}2-\cos 2k+\cos k, & k<\pi/3 \quad \text{(Fig. 2, solid part of curve } 3),\\ 2(1+\cos k), & \pi/3<k<k_0 \quad \text{(Fig. 2, solid part of curve } 4),\\ 2-\cos 2k-\cos k, & k_0<k<\pi/2 \quad \text{(Fig. 2, solid part of curve } 5),\end{cases}$$

from below and by the dispersion curves

$$\lambda(k)=\begin{cases}2(1+\cos k), & k<\pi/3 \quad \text{(Fig. 2, dashed part of curve } 4),\\ 2-\cos 2k+\cos k, & \pi/3<k<\pi/2 \quad \text{(Fig. 2, dashed part of curve } 3)\end{cases}$$

from above.

Figure 6 shows the calculated frequencies of resonant reflection for various values of $\beta>\alpha$ (curves *2–4*). The frequencies ω_R split from $\omega_{t\,\min}$ for small values of ε exist in the continuous spectrum for $k=0$ up to the value of $\beta\approx 3.345\alpha$. As the parameter β of defect coupling increases further, the curves describing resonant frequencies emerge from the upper boundary $\omega_{l\,\max}(k)$ of the continuous spec-

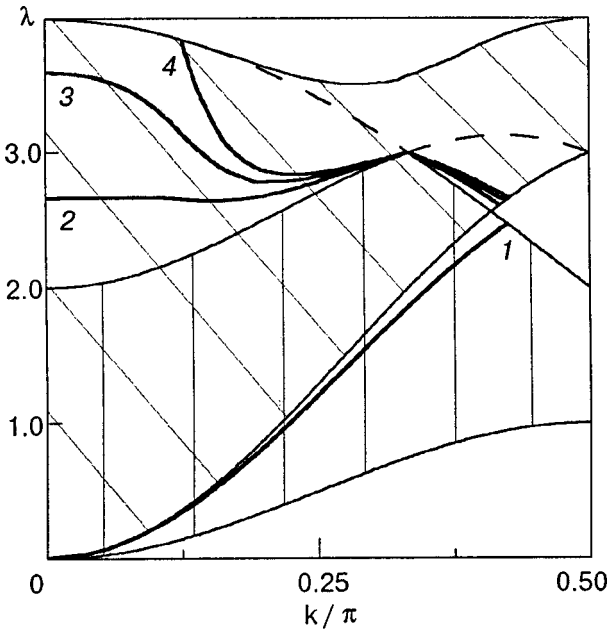

FIG. 6. Dispersion curves for frequencies of total reflection of phonons by a defect: $\beta=0.1\alpha$ (curve *1*), $\beta=2\alpha$ (curve *2*), $\beta=3\alpha$ (curve *3*), and $\beta=5\alpha$ (curve *4*).

trum at a certain point $k_R^*(\varepsilon)$ (curve *4* in Fig. 6). All such curves intersect for $\varepsilon<0$ at the point $\lambda_{t\,\max}(\pi/3)=3$.

If the condition $|R|^2=0$ is satisfied, the transmission of a *t*-phonon through a plane defect is complete. The resonant transmission frequencies $\omega_T(k,\varepsilon)$ can be determined from Eq. (18). An analysis proved that in the case when the defect coupling is weakened, Eq. (18) has solutions in the short-wave range above the lower boundary of the *l*-branch extending from k_0 to a certain value $k_{T1}^*(\varepsilon)$ of the wave number. Starting from this point, the transmission frequency curves are transformed into the dispersion curves of localized gap vibrations of the symmetric type (curve *T1* in Fig. 5).

In the case when the interaction between the boundary layers is enhanced, two branches corresponding to complete transmission frequencies $\omega_T(k,\varepsilon)$ are formed for the same value of the defect parameter. One of the transmission branches (curve *T* in Fig. 4) exists in the continuous spectrum (in the high-frequency region of pseudolocal states) up to a certain value of the wave number $k_{T2}^*(\varepsilon)$ and emerges from the spectrum of bulk vibrations in the form of local frequencies of symmetric high-frequency modes for $k>k_{T2}^*(\varepsilon)$ and for the same value of ε. Resonant transmission can take place in this spectral region only for values of the defect parameter in the interval $\alpha<\beta<\beta_c$, where $\beta_c=\alpha(2+\sqrt{2})$. For $k=0$, transmission frequencies are given by $\lambda_T^0=2\beta^2/[\alpha(2\beta-\alpha)]$.

The other transmission frequency branch lies in the lower range of pseudolocalized states. Such curves (curve *T2* in Fig. 5) split from the lower boundary (4) of this region. As the value of the defect parameter β increases, such curves fall, starting from $k_{T3}^*(\varepsilon)$, into the gap of the continuous spectrum, where they are continued as dispersion curves for local gap-type symmetric vibrations for the same value of β.

The behavior of the dispersion curves for resonant transmission and reflection described above is in accord with the conclusions drawn in Ref. 11 concerning the continuation of the frequency curves corresponding to total transmission in the form of frequency dependences of local vibrations outside the continuous spectrum as well as the termination of the frequency lines for resonant reflection at the boundary of the bulk vibrational spectrum.

CONCLUSION

The results obtained in this work allow us to draw more definite conclusions from the general theory[9] concerning the physical nature of resonant interaction of phonons with a plane defect for a discrete fcc lattice. The frequencies and wave vectors of resonant peculiarities of scattering lie in the vibration spectrum regions for a perfect crystal in which quasi-localized vibrational states can exist. Such states can be formed due to the fact that the above-mentioned spectral regions of bulk vibrations correspond to the conditions for the existence of waves with a continuous spectrum of one vibrational branch and the frequencies of localized vibrations split from the continuous spectrum of the other vibrational branch.

The resonant nature of scattering of an elastic wave by a plane defect is manifested in the existence of frequencies ω and wave vectors k for which the reflection coefficient vanishes (total transmission of the wave), or the transmission coefficient vanishes (total reflection of the wave) if we disregard the absorption of wave in the bulk. The curves of resonant phenomena in the (k,ω) plane are determined. It is shown that two resonant transmission curves exist for the same value of the defect parameter. Starting from a certain value of the wave number, resonant transmission frequency curves are continued outside the continuous spectrum in the form of frequency curves for symmetric local vibrations.

This research was carried out under the support of the Ukrainian Ministry of Science and Technology, Project No. 2.4/163.

*E-mail: kosevich@ilt.kharkov.ua

[1] A. N. Darinskii and G. A. Maugin, Wave Motion **23**, 363 (1996).
[2] A. M. Kosevich and A. V. Tutov, Phys. Lett. A **248**, 271 (1998).
[3] A. M. Kosevich and A. V. Tutov, Phys. Lett. A **213**, 256 (1996).
[4] J. Strocio, M. Persson, S. Bare, and W. Ho, Phys. Rev. Lett. **54**, 1428 (1995).
[5] G. Braco, R. Tatarek, F. Tomasini *et al.*, Phys. Rev. B **36**, 2928 (1987).
[6] A. M. Kosevich, E. S. Syrkin, and A. V. Tutov, Fiz. Nizk. Temp. **22**, 804 (1996) [Low Temp. Phys. **22**, 617 (1996)].
[7] A. M. Kosevich, D. V. Matsokin, and S. E. Savotchenko, Fiz. Nizk. Temp. **23**, 92 (1997) [Low Temp. Phys. **23**, 69 (1997)].
[8] A. M. Kosevich, D. V. Matsokin, and S. E. Savotchenko, Fiz. Nizk. Temp. **24**, 992 (1998) [Low Temp. Phys. **24**, 748 (1998)].
[9] A. M. Kosevich, Zh. Éksp. Teor. Fiz. (1998) (in press).
[10] A. M. Kosevich, Yu. A. Kosevich, and E. S. Syrkin, Fiz. Tverd. Tela (Leningrad) **28**, 1946 (1985) [Sov. Phys. Solid State **28**, 1089 (1985)].
[11] A. M. Kosevich and D. A. Semagin, Cond. Mat. Phys. (Lviv) (1998) (in press).

Translated by R. S. Wadhwa

SUPERCONDUCTIVITY, HIGH-TEMPERATURE SUPERCONDUCTIVITY

Flux vortex pinning in a thick $Ba_{0.64}K_{0.36}BiO_y$ film

S. N. Barilo, V. I. Gatalskaya, S. V. Shiryaev, D. I. Zhigunov, and L. A. Kurochkin

Institute of Solid State and Semiconductor Physics, National Academy of Sciences of Byelorussia, 220072 Minsk)*

H. Szymczak, R. Szymczak, and M. Baran

*Institute of Physics, Polish Academy of Sciences, 02-688 Warsaw, Poland**)*
(Submitted August 4, 1998)
Fiz. Nizk. Temp. **25**, 9–14 (January 1999)

The magnetic properties of a $Ba_{1-x}K_xBiO_y$ film ($x=0.36$) of thickness 18 μm are investigated. It is shown that the field dependences $J_c(B)$ of critical currents at 5–20 K in fields above the peak-effect field H_p are correctly described in the collective pinning theory for a vortex lattice with a small bundle size. © *1999 American Institute of Physics.* [S1063-777X(99)00201-7]

1. INTRODUCTION

In a recent publication,[1] the liquid-phase epitaxy technique is used for obtaining epitaxial superconducting monocrystalline films of $Ba_{1-x}K_xBiO_y$ with various concentrations of potassium in an electrochemical cell. The choice of single crystals of $BaBiO_3$ (100) and $Ba_{0.8}K_{0.2}BiO_3$ used as substrates ensured good coincidence of the lattice parameters of the film and the substrate. The high quality of films grown on both types of substrate was confirmed by a detailed x-ray diffraction analysis. Some of the critical parameters of superconducting films were given earlier in Ref. 1. However, the possibility of application of BKBO films in microelectronic devices employing such properties as the ideal hysteresis of Josephson tunneling in *SIS* junctions[2] as well as tunneling parameters of *SIS* junctions which are in accord with the BCS model[3–5] combined with the isotropic structure and a large coherence length (as compared to the lattice constant) undoubtedly call for a thorough and systematic analysis of superconducting BKBO films.

We were the first to observe and analyze systematically[6] the peak effect in an isotropic system, viz., copper-free $Ba_{1-x}K_xBiO_y$ single crystals ($x>0.33$) in a wide temperature range (from 4.2 K to T_c) in fields up to 6 T. We drew the conclusion concerning the origin of the peak effect, which is associated with the presence of regions containing superstoichiometric oxygen in a crystal grown by electrochemical deposition. The measurements of the irreversibility curve $H_{\rm irr}(T)$ near T_c revealed that the $H_{\rm irr}(T)$ dependence for a single crystal with $x=0.34$ obeys the law $H_{\rm irr}(T) \sim H_{\rm irr}(0)(1-T/T_c)^{1.45}$. The magnitude of the exponent close to 3/2 suggests that the flux creep model[7] can be used for explaining the behavior of $H_{\rm irr}(T)$. The exponent in the dependence $H_p(T)\sim(1-T/T_c)^{0.59}$ differs significantly from the value 1.45 for $H_{\rm irr}(T)$. Peak effect, which is typical of type II superconductors, was observed in copper-based HTSC systems.[8–12] All the above-mentioned superconductors possess anisotropic layered structure containing CuO_2 planes. The mechanism underlying the peak effect is extensively discussed in the literature. Various statistical models proposed for explaining the peak effect are associated with (1) the presence of regions with a nonstoichiometric concentration of oxygen in the crystal,[8,13] (2) anisotropy in electron properties,[14] (3) $3D-2D$ phase transition in the vortex lattice,[15] (4) commensurability of the periods of the vortex lattice and the lattice of defects in the vicinity of the peak field,[9] and (5) the formation of regions with reversible magnetization in the crystal.[16] In addition, the model of dynamic peak effect proposed by Kruzin-Elbaum *et al.*[17] explains the emergence of an extra peak on the $M(H)$ curves by a decrease in the magnetization relaxation rate due to a change in the nature of the flux creep. Nevertheless, an exhaustive explanation of this effect has not been obtained yet. In this paper, we report on the results of measurements of magnetic parameters of an epitaxial monocrystalline thick $Ba_{0.64}K_{0.36}BiO_y$ films with $T_c=30$ K and thickness ~ 18 μm, which enabled us to study the mechanism of vortex lattice pinning in a wide range of magnetic fields and temperatures.

2. SAMPLES AND EXPERIMENTAL TECHNIQUE

The films of $Ba_{0.64}K_{0.36}BiO_y$ were grown on monocrystalline $BaBiO_3$ (100) substrates. The discrepancy in the crystal lattice parameters of the film and the substrate did not exceed 2%. The monoclinic monocrystalline substrate was grown from a nearly stoichiometric melt with a subsequent slow cooling (at a rate $\sim 0.2\,^\circ$C/h). The details of the method of obtaining the substrate and electrochemical deposition of the monocrystalline film are given in Ref. 1. The chemical compositions of the film and the substrate were determined from the ratio of potassium concentrations and parameters of pseudocubic lattice.[18]

The magnetization and susceptibility of the monocrystalline BKBO film in weak fields (~ 4 Oe) as well as magne-

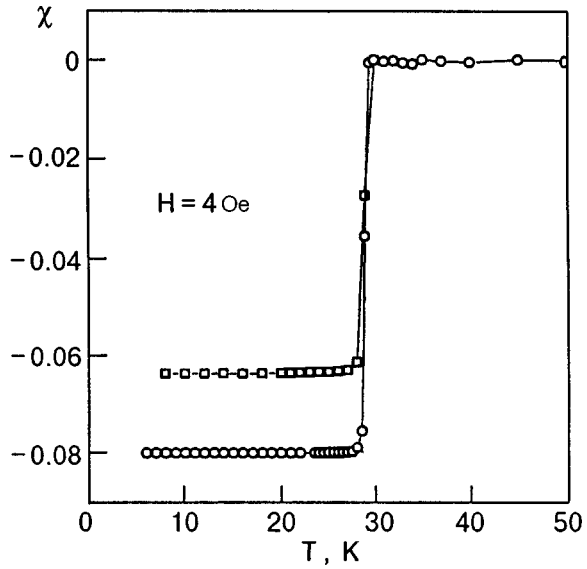

FIG. 1. Temperature dependences of signals for a thick $Ba_{0.64}K_{0.36}BiO_y$ film on a $BaBiO_3(100)$ substrate for ZFC (○) and FC (□) ($d=18\ \mu$m and $T_c=30$ K).

tization hysteresis loops $M(H,T)$ in fields up to 50 kOe were measured on a SQUID magnetometer (QUANTUM Design, MPMS-5) in a wide temperature range. The susceptibility of the film in the normal state was determined in the field of 50 kOe, and this contribution was then subtracted from the $M(H,T)$ dependence in order to determine the response associated with the superconducting state of the crystal. The magnetization isotherms $M(H)$ were obtained in fields 0–50 kOe at temperatures 5–26 K for the **H** orientation at right angles to the film surface.

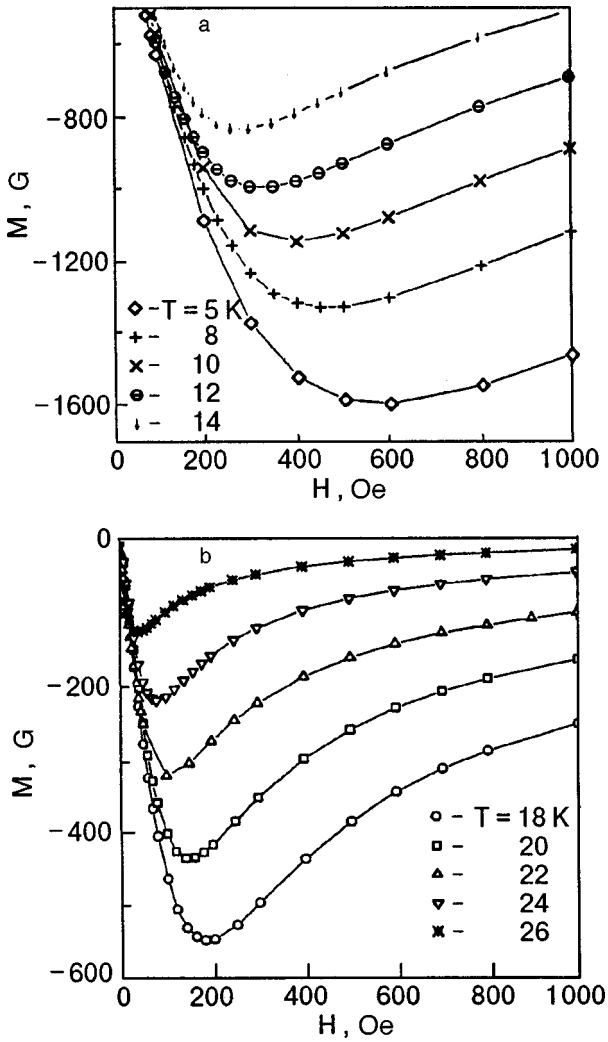

FIG. 2. Fragment of a hysteresis loop for a BKBO film at 5–14 K (a) and 18–26 K (b) in weak magnetic fields ($H\leqslant 1$ kOe).

3. DISCUSSION OF RESULTS

The temperature dependences of the shielding effect (ZFC) and the Meissner effect (FC) in a weak magnetic field for a BKBO film with $x=0.36$ are shown in Fig. 1 taking into account the demagnetizing factor. In a magnetic field of 4 Oe, the onset of the superconducting transition corresponds to $T_c^0=30$ K, and the superconducting transition field is $\Delta T<1$ K at a level of 10–90%. It can be seen that almost complete screening and only an 80% Meissner signal are observed in the film. This effect is associated with a strong pinning in weak fields and is typical of traditional and high-T_c superconductors. BKBO single crystals[19] as well as thick films in weak fields (but higher than H_{c1}) exhibit a magnetization peak at H_{p1} whose position and magnitude depend on temperature (Fig. 2). As the temperature increases, the peak is shifted towards lower fields: $H_{p1}=600$ Oe at $T=5$ K and 180 Oe at 20 K, while the peak height decreases by a factor of three. The emergence of such a magnetization peak (and hence the critical current peak J_c) in weak fields is attributed either to a strong field dependence of J_c as a result of vanishing of the repulsion between vortices,[20] or a strong deformation of the vortex lattice by pinning centers.[21] The magnitude of the critical current calculated by Bean's formula $J_c=30\Delta M/l$ (l is the average size of two broad sides of the film) attains the value 5×10^5 A/cm^2 at 5 K in the field 600 Oe (cf. the value of J_c (42 K, 0 Oe) for a single crystal with $x=0.4$, which is 4.2×10^5 A/cm^2).[19]

A further increase in the magnetic field leads to a decrease in critical current, but this dependence $J_c(H)$ is not monotonic, i.e., the film exhibits the peak effect. Figure 3 shows fragments of magnetization curves for a BKBO film at various temperatures. The field H_p corresponding to the peak effect depends on temperature and decreases with heating. The temperature dependence of H_p for a film with $x=0.36$ is described by a relation close to a linear dependence: $H_p(T)=A(1-T/T_c)^n$, where $n\approx1.17$ (Fig. 4). The value of J_c of the film at 10 K near the peak effect field increases with the field by 10%, i.e., the pinning of the vortex lattice increases in this range of magnetic fields, and the critical current density in the film amounts to $\sim1.1\times10^5$ A/cm^2 (in the field 15 kOe) and $\sim1.2\cdot10^5$ A/cm^2 (30 kOe).

Our measurements of the temperature dependence of irreversibility line $H_{\rm irr}(T)$ for the film resulted in the exponent 1.52 (see Fig. 4), which is close to the value 1.45 for a single crystal. The value of $H_{\rm irr}(0)$ amounts to 172 kOe, which is in good agreement with the corresponding value for the single

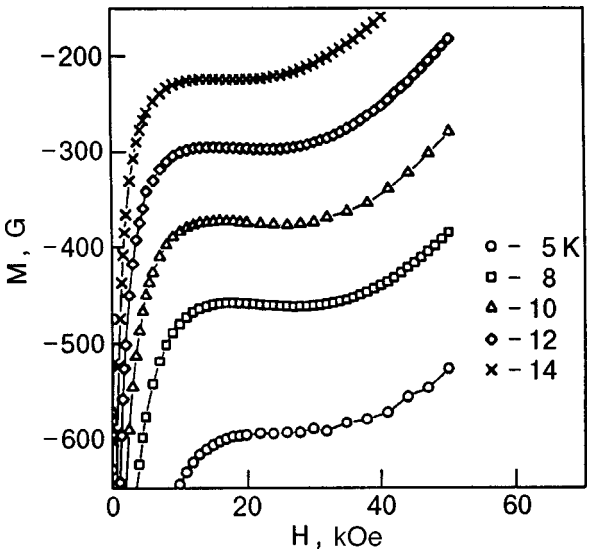

FIG. 3. Fragment of a hysteresis loop for a BKBO film at 5–14 K in strong magnetic fields.

crystal. The noticeable difference in the values of the exponents in the $H_p(T)$ and $H_{\rm irr}(T)$ for the single crystal as well as for the BKBO film makes it possible to disregard the emergence of reversible regions as a source of the peak effect in BKBO.[16] Such regions are formed when the magnetic field passes through the threshold values $H_{\rm irr}$ for the presumed regions with a nonstoichiometric oxygen concentration, the more so that the values of $H_p(0)\approx 40$ kOe are noticeably smaller than $H_{\rm irr}(0)\approx 172$ kOe (by more than a factor of four for the film under investigation). The models described in Refs. 14 and 15 are also inapplicable to the isotropic cubic compound BKBO as well as the model[9] presuming the independence of H_p of temperature, which contradicts our results (see Fig. 4).

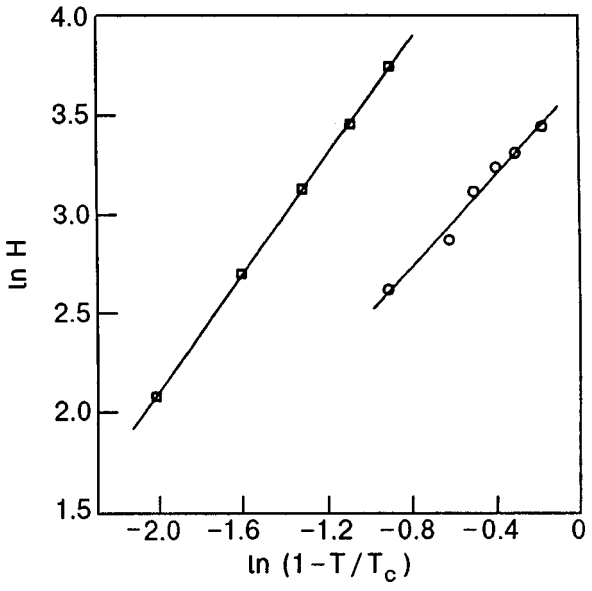

FIG. 4. Temperature dependences of the irreversibility field (□) and peak-effect field (○) for a BKBO film.

The theory of collective pinning was first put forth by Larkin and Ovchinnikov[21] for describing the behavior of $J_c(B)$ in type II superconductors and was developed by Feigel'man and Vinokur[22] who took into account the flux creep effects and the formation of vortex bundles. This theory presumes that a vortex can be pinned by a large number of randomly distributed defects. In weak fields, the mode of solitary vortices is observed [$J_c\sim(\xi/L_c)^2$, where L_c is the characteristic longitudinal size of a vortex]. As the magnetic field increases, the separation a_0 between vortices becomes smaller ($a_0=(\varphi_0/B)^{1/2}$, where φ_0 is the magnetic flux quantum), and vortices start interacting with one another, forming bundles with the transverse dimension R_c depending on the elastic modulus of the vortex lattice.[23] For small bundles with $a_0<R_c<\lambda$ (λ is the magnetic field penetration depth), the quantity R_c is connected with the longitudinal dimension L_c of the bundle of vortices through the expression

$$R_c\sim a_0\exp(L_c/a_0)^3. \tag{1}$$

This equation is valid for temperatures and magnetic fields away from the irreversibility line. Feigel'man and Vinokur[22] proved that vortex lattice fluctuations at temperatures above the depinning temperature $T_{\rm dp}$ can noticeably reduce the values of critical current in the crystal, but this effect is negligibly small for our system ($T_{\rm dp}=600$ K for 1 T for BKBO).[24]

The value of the critical current for small size bundles is defined by the relation[23]

$$J_c\sim B\exp[-2(L_c^2(T)B/\varphi_0)^{3/2}] \tag{2}$$

with a maximum for $B\sim B_{\rm sb}/2$, where $B_{\rm sb}=\varphi_0/L_c^2(T)$. This expression is valid for fields $B>B_{\rm sb}$. Consequently, using formula (2), we can describe the behavior of $J_c(B)$ in fields higher than those corresponding to the peak effect.

The construction of the dependence of $J_c(B)$ on $B^{3/2}$ on the semilogarithmic scale makes it possible to determine the range of magnetic fields and temperatures in which the regime of vortex bundles with a small R_c is observed as well as the temperature dependence $L_c(T)$ for a thick BKBO film and to compare the obtained results with the data[24,25] for BKBO single crystals.

It should be noted that a BKBO superconductor is a model system for verifying the concepts of the collective pinning theory for a vortex lattice for a number of reasons. First, this is due to its isotropic cubic structure as well as the experimentally attainable values of $H_{c2}(0)\sim 350$ kOe. Second, the shape of the magnetization curves $M(B)$ for BKBO in a certain temperature range is not distorted by flux creep since, according to estimates,[24] the pinning potential values $U_c\sim 700\,{\rm K}\gg T_c$. The effect of flux creep in this system with $T_c\sim 30$ K becomes significant at temperatures above ~ 24 K; this was observed on the bases of $M(B)$ measurements on a SQUID magnetometer and in pulsed magnetic fields.[24] Thus, the peak on the $\Delta M(B)$ dependence in intermediate fields $B_{c1}\leqslant B\leqslant B_{c2}$ and at temperatures lower than ~ 24 K corresponds to the true value of the critical current density $J_c(B)$.

Figure 5 shows the J_c/B dependences on $B^{3/2}$ on a semilogarithmic scale for a BKBO film with $x=0.36$. Typical (linear) dependences for small-size bundles are clearly seen

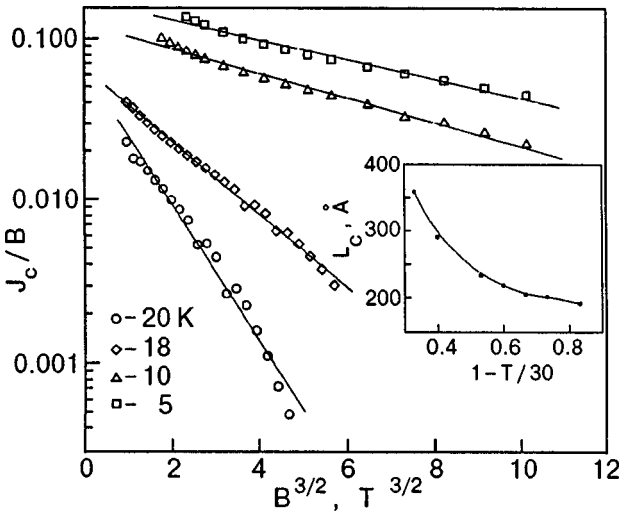

FIG. 5. Dependence of J_c/B on $B^{3/2}$ for a BKBO film in small-size bundle mode at different temperatures. The inset shows the temperature dependence of the collective pinning length $L_c(T)$.

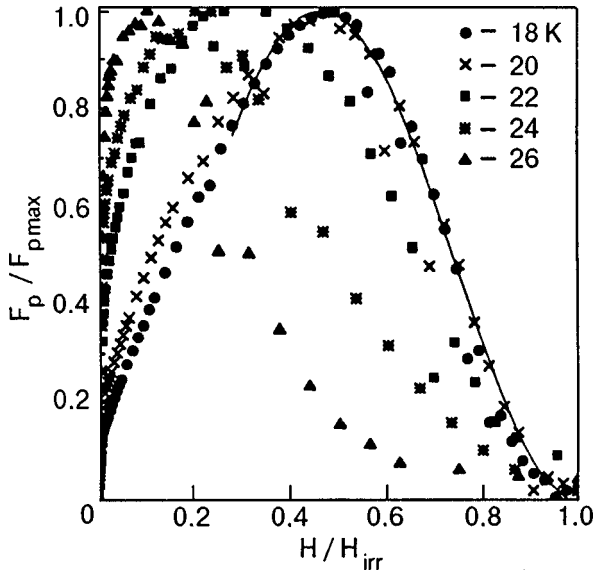

FIG. 7. Normalized pinning force density as a function of reduced field for a BKBO film at different temperatures; solid curve is approximation according to the dependence $F_p \sim b^2 \exp(-2b^{3/2})$ for $T=18$ K.

in the temperature range 5–20 K. Using Eq. (2), we obtain the temperature dependence of the collective pinning length $L_c(T)$ from the slope of the straight lines (see the inset to Fig. 5). This dependence can be approximated by the expression $L_c(T)=L_c(0)(1-T/T_c)^{-n}$, where $n\approx 0.7$ and $L_c(0)\approx 160$ Å. The values of L_c allow us to estimate the field $B_{sb}\sim \varphi_0/L_c^2$ above which the dominating pinning mechanisms changes from the single vortex mode to the bundle of vortices with the transverse size R_c [see Eq. (1)]. The values of B_{sb} for a film with $x=0.36$ (Fig. 6) are on the whole comparable with the values of B_{sb} for our BKBO single crystals[25] with $x=0.34$, 0.37 and 0.46 and for a BKBO single crystal with $x=0.4$.[24]

Figure 6 also shows experimental values of peak-effect fields H_p and irreversibility fields H_{irr} for the film. In spite of the fact that the collective pinning theory correctly describes the field dependence $J_c(B)$ in strong fields, further investigations are required to determine the change in the pinning mechanism as a source of the peak effect. The H–T diagram (see Fig. 6) also confirms the above statement that the peak effect should not be associated with the emergence of reversible regions in the film.

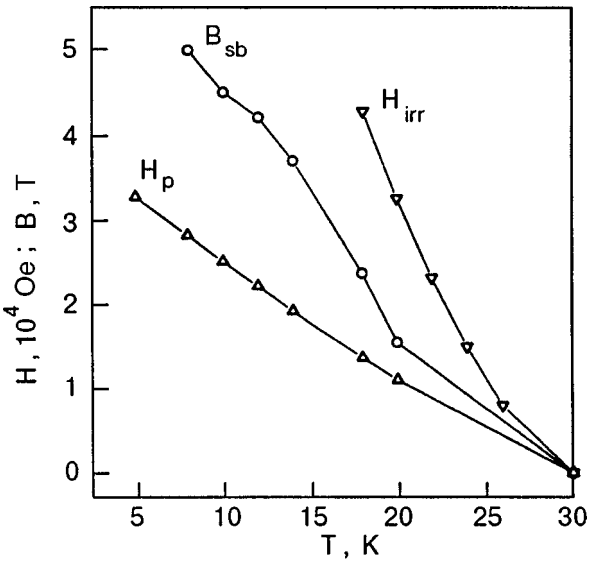

FIG. 6. H–T phase diagram for a BKBO film: $H_p(T)$ and $H_{irr}(T)$ correspond to experimental data, $B_{sb}(T)$ curves are calculated from the field dependence of $J_c(B)$.

Useful information can be gained by studying the volume pinning force $F_p=J_cB\sim\Delta MB$.[6,25] Figure 7 presents the experimental values of the normalized pinning force as a function of the reduced field for temperatures 18–26 K. As the normalizing field, we choose the fields H_{irr} whose experimental values were measured in the indicated temperature range. Approximation in the form $F_p\sim b^p(1-b)^q$, where $b=H/H_{irr}$, and p and q are determined by the origin of pinning,[26] gives a clearly manifested peak of F_p for $b_{max}=p/(p+q)=0.48$ ($T=18$–20 K) with $p=1.74$ and $q=2.17$. At higher temperatures, poor scaling is observed (Fig. 7). In order to compare the obtained results with the concepts of the collective pinning theory, the dependence of the reduced pinning force on B/B_{sb} is shown in Fig. 8. The solid curve is an approximation given by the dependence $F_p\sim b^2\exp\times(-2b^{3/2})$ for $T=18$ K and $B_{sb}=23.6$ kOe (here $b=B/B_{sb}$). Our experimental data are in good agreement with Eq. (2).

The pinning of the vortex lattice in type II superconductors can be associated with a spatial variation of the Landau–Ginzburg parameter, and the interaction of the vortex lattice with pinning centers can be described in terms of the variation of the critical temperature T_c (δT_c-pinning) or of the mean free path (δl-pinning).[23] In order to determine the type of pinning on a BKBO film with $x=0.36$, we must compare the $L_c(T)$ and $H_{c2}(T)$ dependences since the δT_c-pinning presumes that $L_c\approx\xi^{2/3}$, while the δl-pinning requires that $L_c\approx\xi^2$ (ξ is the coherence length).[23] Such measurements of $H_{c2}(T)$ for the film are planned.

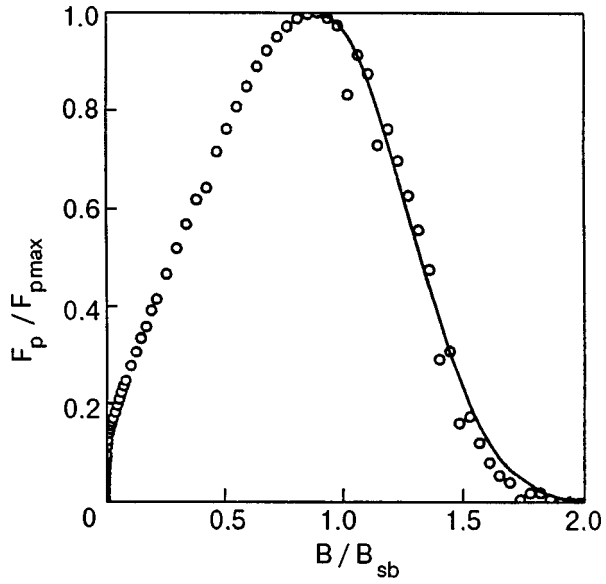

FIG. 8. Normalized pinning force density as a function of B/B_{sb} at $T=18$ K.

CONCLUSION

We studied the vortex lattice pinning in an epitaxial monocrystalline $Ba_{0.64}K_{0.36}BiO_y$ film having a thickness of 18 μm and $T_c=30$ K. The critical current density J_c (5 K, ~ 0.1 T) is $5\cdot 10^5$ A/cm^2. The peak effect observed in the film is presumably associated with extra pinning of the vortex lattice in regions with a nonstoichiometric oxygen (and/or potassium) concentration. The field dependence of critical current in a BKBO film is correctly described by the collective pinning theory in the temperature range 5–20 K; the value of $J_c(B)$ decreases sharply as the pinning mode emerges for small-size bundles. Direct measurements of $H_{c2}(T)$ will allow us to draw final conclusions concerning the nature of pinning in the film (δT_c- or δl-pinning) from a comparison of the dependences $H_{c2}(T)$ and $L_c(T)$.

The research carried out in Minsk and Warsaw was partly supported by the International organization CRDF (Grant No. BP1-111) and the State Committee on Scientific Research of Polish Republic (Contract 2P30211407).

*)E-mail: bars@ifttp.bas-net.misk.by
**)E-mail: baran@ifpan.edu.pl

[1] S. V. Shiryaev, S. N. Barilo, N. S. Orlova *et al.*, J. Cryst. Growth **172**, 396 (1997).
[2] A. N. Pargellis, F. Sharifi, R. C. Dynes *et al.*, Appl. Phys. Lett. **58**, 95 (1991).
[3] Q. Huang, J. F. Zasadinski, N. Tralshawala *et al.*, Nature (London) **347**, 369 (1990).
[4] F. Sharifi, A. N. Pargellis, R. C. Dynes *et al.*, Phys. Rev. B **44**, 12521 (1991).
[5] M. Kosugi, J. Akimitsu, T. Uchida *et al.*, Physica C **229**, 389 (1994).
[6] S. N. Barilo, V. I. Gatalskaya, S. V. Shiryaev *et al.*, Physica C **254**, 181 (1995).
[7] I. Yeshurum and A. P. Malozemoff, Phys. Rev. Lett. **60**, 2202 (1988).
[8] M. Dauemling, J. M. Seuntjens, and D. C. Larbalestier, Nature (London) **346**, 332 (1990).
[9] G. Yang, J. S. Abell, and C. E. Gough, IEEE Trans. Appl. Supercond. **3**, 1671 (1993).
[10] T. Kimura, K. Kishio, T. Kobayashi *et al.*, Physica C **192**, 247 (1992).
[11] V. N. Kopylov, I. F. Schegolev, and T. G. Togonidze, Physica C **162–164**, 1143 (1989).
[12] A. Maignan, S. N. Putilin, V. Haroly *et al.*, Physica C **266**, 173 (1996).
[13] J. L. Vargas and D. C. Larbalestier, Appl. Phys. Lett. **60**, 1741 (1992).
[14] V. Hardy, A. Wahl, A. Ruyter *et al.*, Physica C **232**, 347 (1994).
[15] G. Yang, J. S. Abell, and C. E. Gough, in *Proc. 7th Int. Workshop on Crit. Currents in Supercond.*, Alpbach, Austria (1994).
[16] L. Klein, E. R. Yacoby, I. Yeshurum *et al.*, Phys. Rev. B **49**, 4403 (1994).
[17] L. Kruzin-Elbaum, L. Civale, V. M. Vinokur, and F. Holtzberg, Phys. Rev. Lett. **G69**, 280 (1992).
[18] Sh. Pei, J. D. Jorgensen, B. Dabrowski *et al.*, Phys. Rev. B **41**, 4126 (1990).
[19] V. I. Gatalskaya, G. V. Gatalskii, L. A. Kurochkin *et al.*, Phys. Status Solidi A **143**, 123 (1994).
[20] S. Senoussi, C. Aguillon, and P. Manuel, Physica C **175**, 202 (1991).
[21] A. I. Larkin and Y. N. Ovchinnikov, J. Low Temp. Phys. **34**, 409 (1979).
[22] M. V. Feigel'man and V. M. Vinokur, Phys. Rev. B **41**, 8986 (1990).
[23] G. Blatter, M. V. Feigel'man, A. I. Larkin, and V. M. Vinokur, Rev. Mod. Phys. **66**, 1125 (1994).
[24] W. Harneit, T. Klein, L. Baril, and C. Esribe-Filippini, Europhys. Lett. **36**, 141 (1996).
[25] M. Baran, H. Szymczak, R. Szymczak *et al.*, J. Magn. Magn. Mater. **166**, 124 (1997).
[26] D. Dew-Hughes, Philos. Mag. **30**, 293 (1974).

Translated by R. S. Wadhwa

Effect of local defects on vibrational characteristics of infinite and semi-infinite one-dimensional structures in an external periodic field

M. A. Mamalui, E. S. Syrkin, and S. B. Feodosyev

*B. Verkin Institute for Low Temperature Physics and Engineering, National Academy of Sciences of the Ukraine, 310164 Kharkov, Ukraine**

(Submitted August 14, 1998)
Fiz. Nizk. Temp. **25**, 72–82 (January 1999)

Exact analytic expressions for Green's functions of the chain type structures with defects in an external periodic field are obtained by the method of Jacobi matrices. A diatomic impurity molecule in a monatomic chain as well as adsorbed chains with a monatomic and a diatomic unit cell are considered. The conditions for the formation and the characteristics of local and gap vibrations are investigated. The evolution of the threshold values of mass of the defect required for the formation of localized vibrations by two isotopic impurities upon a change in the separation between them is analyzed. © *1999 American Institute of Physics.* [S1063-777X(99)01101-9]

The interest to the investigation of dynamic parameters of low-dimensional and quasi-low-dimensional structures with defects is due to considerable advancement in the synthesis of such compounds and their application in modern high technologies on the one hand and fascinating physical features of these compounds on the other hand. It is well known that the conditions of formation and properties of bound states in systems with defects depend qualitatively on the dimensionality of the system as well as the dimensionality of the defect. In our earlier publication,[1] we formulated the general criterion for obtaining exact solutions (on the basis of the Jacobi matrices method)[2–4] for vibrational parameters of linear one-dimensional systems with defects. This communication is devoted to an analysis of changes occurring in the phonon spectrum of such systems in the presence of various defects as well as in a periodic external field. The external (relative to the chain) periodic field eliminates the divergence of root-mean-square displacements typical of one-dimensional lattices, and the exactly solvable problem under investigation can be applied directly to real objects. We studied the models of monatomic and diatomic chains containing impurities differing from the matrix atoms in mass and force constants characterizing their interaction with nearest neighbors as well as impurity clusters possessing an internal structure, e.g., a diatomic impurity molecule in a monatomic chain. The analysis is carried out for an infinite and semi-infinite chain.

1. DIATOMIC IMPURITY MOLECULE IN A MONATOMIC LINEAR CHAIN IN AN PERIODIC EXTERNAL FIELD

Let us consider a one-dimensional monatomic lattice with a defect in the form of two impurity atoms with the mass m', whose coupling constant α' differs from the coupling constant α between matrix atoms whose masses are denoted by m, in an external periodic field (Fig. 1).

It is obvious from the symmetry of the problem that atoms in the chain exhibit two types of independent vibrations: antiphase vibrations of isotopes and their synphase vibrations. The spectral characteristics of these two types of vibrations will be henceforth marked by the indices $(-)$ and $(+)$, respectively. In terms of the method of $\mathscr{J}$-matrices, this means that all the space H of atomic displacements of the lattice is the direct sum of the subspaces: $H=H^{(-)}+H^{(+)}$, each of which is generated by the $(+)$- or $(-)$-displacement of defect atoms.

It should be noted that, with such a separation, $(-)$-vibrations ''perceive'' distortions of coupling as well as mass, while the $(+)$-vibrations perceive only the mass defect.

For an ideal chain in a periodic external field, the dynamic operator $\hat{\mathscr{L}}$ of the system, which is defined as

$$\hat{\mathscr{L}}(n,n')=\frac{\alpha(n,n')}{\sqrt{m_n m_{n'}}},$$

where $\alpha(n,n')$ is the force constant describing the interaction between atoms located at sites n and n', and m_n and $m_{n'}$ are the masses of these atoms, can be written in the form

$$\hat{\mathscr{L}}(n,n')=\begin{cases}\dfrac{\lambda_m+\lambda_0}{2}, & |n-n'|=0,\\ -\dfrac{\lambda_m-\lambda_0}{4}, & |n-n'|=1,\\ 0, & |n-n'|>1,\end{cases} \tag{1}$$

where $(\lambda_m-\lambda_0)/4=\alpha/m$; $n,n'=0,\pm1,\pm2,\ldots$. Here λ_0 is the square of the ''activation frequency'' associated with the external periodic field, and λ_m the square of the maximum vibrational frequency of atoms in the chain. Thus, the eigenvalues λ of the operator $\hat{\mathscr{L}}$ belong to the interval $[\lambda_0,\lambda_m]$, owing to which the divergence of root-mean-square displacements is removed. The parameter λ_0 may emerge in a natural way, e.g., while considering the scalar model of a simple cubic lattice, taking into account the interaction λ_0

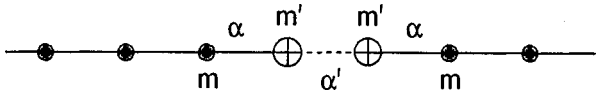

FIG. 1. Schematic diagram of the model of a diatomic impurity molecule in a monatomic chain.

$=(2\alpha/m)(2-\cos k_x-\cos k_y)$, between nearest neighbors, k_x and k_y being the components of the two-dimensional wave vector in the (x,y) plane.

With such a defect, the lattice vibrations are described by the operator $\hat{\mathscr{L}}+\hat{\Lambda}$, where the perturbation operator $\hat{\Lambda}$ is defined as

$$\begin{aligned}\hat{\Lambda}(n,n')=&\frac{\eta(\lambda_m-\lambda_0)-2\varepsilon(\lambda_m+\lambda_0)}{4(\varepsilon+1)}(\delta_{n,1}\delta_{n',1}\\&+\delta_{n,-1}\delta_{n',-1})-\frac{\lambda_m-\lambda_0}{4}\left(\frac{\eta-\varepsilon}{\varepsilon+1}\right)\\&\times(\delta_{n,1}\delta_{n',-1}+\delta_{n,-1}\delta_{n',1})\\&-\frac{\lambda_m-\lambda_0}{4}\left(\frac{1}{\sqrt{\varepsilon+1}}-1\right)(\delta_{n,1}\delta_{n',2}+\delta_{n,2}\delta_{n',1}\\&+\delta_{n,-1}\delta_{n',-2}+\delta_{n,-2}\delta_{n',-1}),\end{aligned}\tag{2}$$

where $\eta\equiv(\alpha'-\alpha)/\alpha$; $\varepsilon\equiv(m'-m)/m$ are dimensionless parameters describing local variations of coupling and mass. In this case, the operator $\hat{\mathscr{L}}$ in the subspaces $H^{(+)}$ and $H^{(-)}$ can be written in the form of a $\mathscr{J}$-matrix with the elements

$$\begin{aligned}&a_0^{(-)}(\eta,\varepsilon)=\frac{(\lambda_m-\lambda_0)(2\eta+3)+4\lambda_0}{4(\varepsilon+1)};\\&b_0^{(-)}(\eta,\varepsilon)=\frac{\lambda_m-\lambda_0}{4\sqrt{\varepsilon+1}};\quad a_0^{(+)}(\varepsilon)=\frac{\lambda_m+3\lambda_0}{4(\varepsilon+1)};\\&b_0^{(+)}(\varepsilon)=\frac{\lambda_m-\lambda_0}{4\sqrt{\varepsilon+1}};\quad a_{n>0}^{(-)}=a_{n>0}^{(+)}=\frac{\lambda_m+\lambda_0}{2};\\&b_{n>0}^{(-)}=b_{n>0}^{(+)}=\frac{\lambda_m-\lambda_0}{4};\end{aligned}\tag{3}$$

where $a_n^{(\pm)}$ are diagonal and $b_n^{(\pm)}$ off-diagonal elements of the $\mathscr{J}$-matrix of the operators $\hat{\mathscr{L}}^{(\pm)}$, and $n=1,2,\ldots$. The Green's function (i.e., the first diagonal element of the operator $\hat{\mathscr{G}}=(\lambda\hat{I}-\hat{\mathscr{L}})^{-1}$, where λ is the square of frequency) can be written in the form[3,4]

$$\mathscr{G}_{00}(\lambda)=\frac{Q_{n+1}(\lambda)-b_nQ_n(\lambda)K_\infty(\lambda)}{P_{n+1}(\lambda)-b_nP_n(\lambda)K_\infty(\lambda)},\tag{4}$$

where $K_\infty(\lambda)$ is a continued fraction whose all elements are equal to their limiting values $a\equiv a_n=(\lambda_m+\lambda_0)/2$; $b\equiv b_n=(\lambda_m-\lambda_0)/4$ [(see Eq. (3) for $n\geqslant 1$)]. The function $K_\infty(\lambda)$ can be written in the form

$$K_\infty(\lambda)=\frac{8}{(\lambda_m-\lambda_0)^2}\left[\lambda-\frac{\lambda_m+\lambda_0}{2}+\sqrt{|(\lambda-\lambda_0)(\lambda-\lambda_m)|}\right].\tag{5}$$

where $P_n(\lambda,\eta,\varepsilon)$ are n-degree polynomials in λ, calculated from the elements of the $\mathscr{J}$-matrix of the operator $\hat{\mathscr{L}}$ (the quantities $a_n(\eta,\varepsilon)$ and $b_n(\eta,\varepsilon)$) by using the recurrence relation

$$\begin{aligned}b_n(\eta,\varepsilon)P_{n+1}(\lambda,\eta,\varepsilon)=&[\lambda-a_n(\eta,\varepsilon)]P_n(\lambda,\eta,\varepsilon)\\&-b_{n-1}(\eta,\varepsilon)P_{n-1}(\lambda,\eta,\varepsilon)\end{aligned}\tag{6}$$

with the initial conditions $P_{-1}=0$ and $P_0=1$. The polynomials $Q_n(\lambda)$ are defined by the same relation (6) with the initial conditions $Q_0=0$ and $Q_1=1/b_0$.

For this reason, for the cyclic subspaces $H^{(-)}$ and $H^{(+)}$ we obtain respectively

$$\begin{aligned}\mathscr{G}_{00}^{(-)}(\lambda,\lambda_0,\varepsilon,\eta)=&\frac{2(\varepsilon+1)}{R^{(-)}(\lambda,\lambda_0,\varepsilon,\eta)}[\lambda(2\varepsilon+1)\\&-(\lambda_m(1+\eta)-\lambda_0\eta)\\&+\mathscr{Z}_1(\lambda)\sqrt{|(\lambda-\lambda_m)(\lambda-\lambda_0)|}];\end{aligned}\tag{7}$$

$$\begin{aligned}\mathscr{G}_{00}^{(+)}(\lambda,\lambda_0,\varepsilon)=&\frac{2(\varepsilon+1)}{R^{(+)}(\lambda,\lambda_0,\varepsilon)}[\lambda(2\varepsilon+1)-\lambda_0\\&+\mathscr{Z}_1(\lambda)\sqrt{|(\lambda-\lambda_m)(\lambda-\lambda_0)|}],\end{aligned}\tag{8}$$

where

$$\begin{aligned}R^{(-)}(\lambda,\lambda_0,\varepsilon,\eta)=&4\varepsilon(\varepsilon+1)\lambda^2-\lambda\{(\lambda_m-\lambda_0)(2\eta+1)\\&+4\varepsilon[\lambda_m(1+\eta)-\lambda_0\eta]\}+(\lambda_m-\lambda_0)\\&\times[\lambda_m(1+\eta)^2-\eta^2\lambda_0];\end{aligned}\tag{9}$$

$$\begin{aligned}R^{(+)}(\lambda,\lambda_0,\varepsilon)=&4\varepsilon(\varepsilon+1)\lambda^2+\lambda[(\lambda_m-\lambda_0)-4\varepsilon\lambda_0]\\&-\lambda_0(\lambda_m-\lambda_0);\end{aligned}\tag{10}$$

$$\begin{aligned}\mathscr{Z}_1(\lambda)=&\Theta(\lambda)(\lambda_0-\lambda)+i\Theta(\lambda-\lambda_0)\Theta(\lambda_m-\lambda)\\&-\Theta(\lambda-\lambda_m)\end{aligned}\tag{11}$$

($\Theta(x)$ is the Heaviside step function). Consequently, the spectral densities of the $(-)$- and $(+)$-vibrations defined in the band $[\lambda_0,\lambda_m]$ as $\rho^{(\pm)}(\lambda,\lambda_0,\eta,\varepsilon)=(1/\pi)\mathrm{Im}\,\mathscr{G}_{00}^{(\pm)}\times(\lambda,\lambda_0,\eta,\varepsilon)$ are given by

$$\begin{aligned}\rho^{(-)}(\lambda,\lambda_0,\varepsilon,\eta)=&\frac{2(\varepsilon+1)\sqrt{|(\lambda-\lambda_m)(\lambda-\lambda_0)|}}{\pi R^{(-)}(\lambda,\lambda_0,\varepsilon,\eta)},\\\rho^{(+)}(\lambda,\lambda_0,\varepsilon)=&\frac{2(\varepsilon+1)\sqrt{|(\lambda-\lambda_m)(\lambda-\lambda_0)|}}{\pi R^{(+)}(\lambda,\lambda_0,\varepsilon)}.\end{aligned}\tag{12}$$

It should be noted that the external field does not change qualitatively the type of spectral densities in the band of the continuous spectrum: as in the case of zero field (i.e., $\lambda_0=0$), $\rho^{(-)}(\lambda,\lambda_0,0,0)$ vanishes at the left edge of the spectrum $(\lambda=\lambda_0)$ and turns to infinity at the right edge of the

spectrum ($\lambda=\lambda_m$), while $\rho^{(+)}(\lambda,\lambda_0,0)$ vanishes at the maximum frequency of the continuous spectrum ($\lambda=\lambda_m$) and turns to infinity for $\lambda=\lambda_0$.

Thus, discrete frequencies of (+)-vibrations must split to the region $[0,\lambda_0]$ without a threshold, while the localization of (−)-vibrations in this region requires a threshold. The splitting of discrete frequencies from the upper boundary λ_m of the continuous spectrum must occur in the threshold manner for (+)-vibrations and without a threshold for (−)-vibrations in the special case of a purely isotopic defect or with a distortion of only the force coupling constant between the two atoms.

The poles $\mathcal{G}_{00}^{(-)}(\lambda,\lambda_0,\varepsilon,\eta)$ and $\mathcal{G}_{00}^{(+)}(\lambda,\lambda_0,\varepsilon)$, of the Green's functions that define the squares of discrete frequencies of (+)- and (−)-vibrations of the chain as functions of the parameters of the defect have the form

$$\lambda_{g,l}^{(-)}=\frac{1}{8\varepsilon(\varepsilon+1)}\{(\lambda_m-\lambda_0)(2\eta+1)+4\varepsilon[\lambda_m(1+\eta)-\lambda_0\eta] \pm\sqrt{(\lambda_m-\lambda_0)^2(2\eta+1)^2-8\varepsilon(\lambda_m-\lambda_0)[\lambda_m(1+\eta)+\lambda_0\eta]+16\varepsilon^2\lambda_m\lambda_0}\}; \tag{13}$$

$$\lambda_{g,l}^{(+)}=\frac{1}{8\varepsilon(\varepsilon+1)}\{4\varepsilon\lambda_0-(\lambda_m-\lambda_0) \pm\sqrt{(\lambda_m-\lambda_0)^2+8\varepsilon\lambda_0[\lambda_m(2\varepsilon+1)-\lambda_0]}\}. \tag{14}$$

Let us first consider the conditions for the existence of discrete states for (−)-vibrations. The intensity of the discrete state is the residue of the function $G_{00}(\lambda)$ at the corresponding pole.[3,5] Thus, for (−)-vibrations we obtain

$$\mu_g^{(-)}=\frac{4(\varepsilon+1)\{\lambda_g(2\varepsilon+1)-[\lambda_m(1+\eta)-\lambda_0\eta]\}\Theta(\varepsilon-(\lambda_m-\lambda_0)(1+\eta)/2\lambda_0)}{\sqrt{(\lambda_m-\lambda_0)^2(2\eta+1)^2-8\varepsilon(\lambda_m-\lambda_0)[\lambda_m(1+\eta)+\lambda_0\eta]+16\varepsilon^2\lambda_m\lambda_0}};$$
$$\mu_l^{(-)}=\frac{-4(\varepsilon+1)[\lambda_l(2\varepsilon+1)-(\lambda_m(1+\eta)-\lambda_0\eta)]\Theta((\lambda_m-\lambda_0)\eta/(2\lambda_m)-\varepsilon)}{\sqrt{(\lambda_m-\lambda_0)^2(2\eta+1)^2-8\varepsilon(\lambda_m-\lambda_0)[\lambda_m(1+\eta)+\lambda_0\eta]+16\varepsilon^2\lambda_m\lambda_0}}. \tag{15}$$

It can easily be seen from the expressions for $\lambda_{g,l}^{(-)}$ and $\mu_{g,l}^{(-)}$ that the antiphase vibrations of defect atoms lead to the formation of discrete vibrations both in the ''gap'' region ($(0,\lambda_0)$) [with the square of the gap frequency $\lambda_g^{(-)}$ (the ''+'' sign in front of the radical) and with intensity $\mu_g^{(-)}$] and in the region $(\lambda_m,+\infty)$ [with the square of the local frequency $\lambda_l^{(-)}$ (the ''−'' sign in front of the radical) and intensity $\mu_l^{(-)}$]. For splitting of the gap vibration, the mass of the isotopes must exceed the threshold value defined by the relation

$$\varepsilon\geqslant\varepsilon_g\equiv\frac{\lambda_m-\lambda_0}{2\lambda_0}(1+\eta). \tag{16}$$

The equality in this expression corresponds to the ''boundary'' case when $\lambda=\lambda_0$, which indicates the emergence of a root singularity in the spectral density $\rho^{(-)}(\lambda\to\lambda_0)\sim 1/\sqrt{|\lambda-\lambda_0|}\to\infty$. It should be noted that this threshold is positive for all values of η except $\eta=-1$ (the rupture of the bond between two isotopes). As the value of ε increases, the intensity of the gap vibration increases from zero for $\varepsilon=\varepsilon_g[\lambda_g^{(-)}(\varepsilon_g)=\lambda_0]$ to unity in the limit $\varepsilon\to+\infty$:

$$\lim_{\varepsilon\to+\infty}\lambda_g^{(-)}=0,\quad \lim_{\varepsilon\to+\infty}\mu_g^{(-)}=1.$$

The splitting of the local vibration takes place when the following condition holds for the mass of isotopes and the coupling between them:

$$\varepsilon\leqslant\varepsilon_l\equiv\frac{\lambda_m-\lambda_0}{2\lambda_m}\eta. \tag{17}$$

It can be seen that, in the presence of only one type of defect (i.e., for $\varepsilon=0$ or $\eta=0$), the local vibration emerges without a threshold. Both the gap and the local vibration appear with zero intensity, i.e.,

$$\mu_l^{(-)}(\varepsilon_l)=0;\quad \lambda_l^{(-)}(\varepsilon_l)=\lambda_m,$$

which corresponds to the emergence of a singularity in the spectral density $\rho^{(-)}(\lambda\to\lambda_m)\sim 1/\sqrt{|\lambda-\lambda_m|}\to\infty$. For extremely light isotopes ($\varepsilon\to-1$), we have

$$\lim_{\varepsilon\to-1}\lambda_l^{(-)}=\infty,\quad \lim_{\varepsilon\to-1}\mu_l^{(-)}=1.$$

The evolution of spectral densities $\rho^{(-)}(\lambda,\lambda_0,\eta,\varepsilon)$ is shown in Fig. 2 (curves *6–10*). It was noted above that discrete (+)-vibrations of the chain split without a threshold from the lower boundary of the continuous spectrum band, while their splitting from the upper boundary of the spectrum occurs with a threshold. The squares of the frequencies of discrete (+)-vibrations is defined by formula (14) in which the

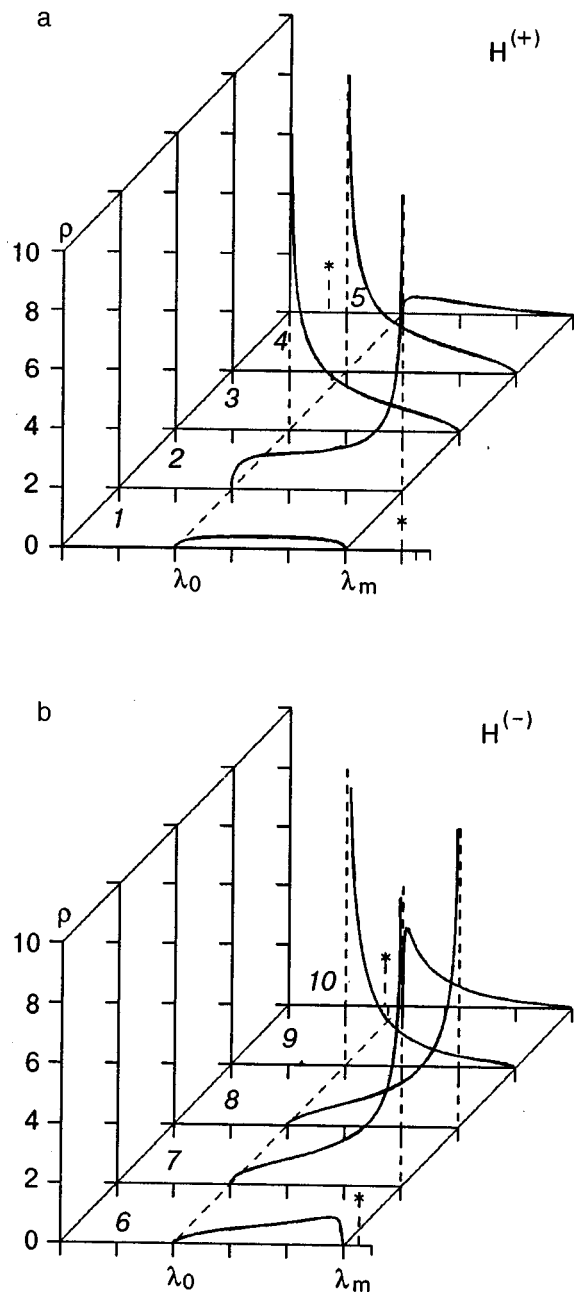

FIG. 2. Spectral densities in the subspaces $H^{(+)}$ (curves *1–5*) and $H^{(-)}$ (curves *6–10*) generated by synphase and antiphase displacements of a diatomic impurity molecule in an external periodic field of a monatomic linear chain: curves *1* and *6* correspond to the presence of a local vibration in the system $\int_{\lambda_0}^{\lambda_m}\rho^{(\pm)}(\lambda)d\lambda=1-\mu_l^{(\pm)}$, curves *2* and *7* are the threshold values required for the formation of local vibrations (root singularity for $\lambda=\lambda_m$), curves *3* and *8* are the spectral densities $\rho^{(\pm)}(\lambda)$ of an ideal linear chain (root singularity in $\rho^{(+)}(\lambda)$ for $\lambda=\lambda_0$ and in $\rho^{(-)}(\lambda)$ for $\lambda=\lambda_m$), curves *4* and *9* are threshold values for the formation of gap vibrations (root singularity for $\lambda=\lambda_0$); curves *5* and *10* correspond to the presence of a gap vibration in the system $\int_{\lambda_0}^{\lambda_m}\rho^{(\pm)}(\lambda)d\lambda=1-\mu_g^{(\pm)}$.

''gap'' vibration is marked by the subscript g and the ''+'' sign in front of the radical, while the local vibration has the subscript l and the sign ''−.''

The frequency $\lambda_g^{(+)}$ of the gap vibration coincides with the lower boundary of the continuous spectrum band for $m'\to m(\varepsilon\to+0)$ and tends to zero upon an increase in the mass of the isotopes ($\varepsilon\to+\infty$). The intensity $\mu_g^{(+)}$ of this discrete vibration increases from zero for $\varepsilon\to+0$ to unity for $\varepsilon\to+\infty$ and is described by the formula

$$\mu_g^{(+)}=\frac{4(\varepsilon+1)[\lambda_g(2\varepsilon+1)-\lambda_0]}{\sqrt{(\lambda_m-\lambda_0)^2+8\varepsilon\lambda_0[\lambda_m(2\varepsilon+1)-\lambda_0]}}\Theta(\varepsilon). \tag{18}$$

The frequency of the local vibration coincides with the upper boundary of the continuous spectrum band for the threshold value of the isotope mass, which corresponds to $\varepsilon_l=-(\lambda_m-\lambda_0)/2\lambda_m$, and tends to infinity in the case when the mass of the isotopes is extremely small, i.e., for $\varepsilon\to-1$. The intensity of the local vibration has the form

$$\mu_l^{(+)}=-\frac{4(\varepsilon+1)[\lambda_l(2\varepsilon+1)-\lambda_0]}{\sqrt{(\lambda_m-\lambda_0)^2+8\varepsilon\lambda_0[\lambda_m(2\varepsilon+1)-\lambda_0]}}\Theta \times\left(\frac{\lambda_m-\lambda_0}{2\lambda_m}+\varepsilon\right) \tag{19}$$

and increases from zero for the threshold value of the mass of the isotopes ($\mu_l^{(+)}(\varepsilon_l)=0$) to unity in the case when their mass tends to zero:

$$\lim_{\varepsilon\to-1}\mu_l^{(+)}=1.$$

The evolution of spectral densities $\rho^{(+)}(\lambda,\lambda_0,\varepsilon)$ is shown in Fig. 2 (curves *1–5*).

It should be noted that the results presented here for $\varepsilon=0$, $\lambda_0=0$ (which corresponds to the model of a monatomic chain with a modified coupling constant between an arbitrary pair of atoms in zero external field) coincide with the results presented in Ref. 5.

The case when $\eta=-1$ for $\lambda_0>0$ is a model of a semi-infinite monatomic chain with an isotopic impurity at its end in an external field. Obviously, in this case the subspaces $H^{(+)}$ and $H^{(-)}$ coincide with each other and with the entire space of displacements of atoms in the chain. Since the spectral characteristics in the subspace $H^{(+)}$ do not depend on the coupling parameter η, the vibrations of the given semi-infinite chain with the isotopic impurity can be described by the expressions obtained for (+)-vibrations of a semi-infinite chain with the defect considered above.

Concluding the section, let us discuss the results of a more general nature, which were obtained for systems containing purely isotopic defects in a periodic external field. Let us suppose that an infinite symmetric chain of atoms of mass m contains two substitutional impurities having the same mass m' and separated by an ''interlayer'' containing k matrix atoms. The threshold value of the isotope mass required for the emergence of discrete states at frequencies above as well as below the continuous spectrum band is a function of the number of atoms in this ''interlayer.'' The case $k=0$ must obviously correspond to the results of the previous problem on the spectral characteristics of a diatomic impurity molecule in a monatomic chain for $\eta\equiv0$, when the coupling constant between the impurities is equal to the coupling constant between matrix atoms.

It follows from Eqs. (4)–(6) that the threshold values of ε leading to the splitting of discrete vibrations from the boundaries of the continuous spectrum are solutions of the equation

$$R(\lambda,\varepsilon)\equiv P_{n+1}(\lambda_b,\varepsilon)-b_nP_n(\lambda_b,\varepsilon)K_\infty(\lambda_b)=0, \quad (20)$$

where λ_b stands for one of the boundaries $[\lambda_0,\lambda_m]$.

In a perfect infinite atomic chain, the center of symmetry of the system can be placed either at the point corresponding to the equilibrium position of an atom, or at the midpoint of the atomic separation. In both cases, the space H of displacements of lattice atoms can be divided into two mutually orthogonal subspaces whose direct sum gives the entire displacement space. The first version of the choice corresponds to the direct sum of the subspaces $H^{(0)}$, which is generated by a displacement of the atom located at the symmetry center and, subsequently, by synphase vibrations of its nearest neighbors, and $H^{(\pm)}$, which is generated by antiphase displacements of nearest neighbors of the atom at the symmetry center. The second version of the choice of the position of the symmetry center, which has already been considered by us, corresponds to the direct sum of the subspaces $H^{(+)}$ and $H^{(-)}$. We can prove that in all the subspaces mentioned above, the polynomials $P_n(\lambda)$ at the edges λ_b of the continuous spectrum band exhibit a simple dependence on the number n:

$$\begin{aligned}
&P_n^{(0)}(\lambda_0)=(-1)^n\sqrt{2}, \quad P_n^{(0)}(\lambda_m)=\sqrt{2};\\
&P_n^{(\pm1)}(\lambda_0)=(-1)^n(n+1), \quad P_n^{(\pm1)}(\lambda_m)=(n+1);\\
&P_n^{(+)}(\lambda_0)=(-1)^n, \quad P_n^{(+)}(\lambda_m)=2n+1;\\
&P_n^{(-)}(\lambda_0)=(-1)^n(2n+1), \quad P_n^{(-)}(\lambda_m)=1.
\end{aligned} \quad (21)$$

The presence of impurities changes the values of the corresponding matrix elements a_n and $b_n\,(n\geqslant 1)$ of the dynamic operator:

$$a_n=\frac{a}{\varepsilon+1}, \quad b_{n-1}=b_n=\frac{b}{\sqrt{\varepsilon+1}}, \quad (22)$$

where $n=(k-1)/2$ if the number k of atoms between the isotopes is odd and $n=k/2$ if k is even. Proceeding from the recurrence relations (6) for the polynomials $P_n(\lambda)$ and the form of the matrix of the operator L for the system under investigation that contains two isotopic impurities separated from each other by k atoms, we obtain the following dependence of the functions $P_n(\lambda,\varepsilon)$ on the mass parameter for the impurity:

$$\begin{aligned}
&P_{n-1}(\lambda,\varepsilon)=P_{n-1}(\lambda),\\
&P_n(\lambda,\varepsilon)=\sqrt{\varepsilon+1}P_n(\lambda),\\
&P_{n+1}(\lambda,\varepsilon)=\frac{\lambda\varepsilon}{b}P_n(\lambda)+P_{n+1}(\lambda).
\end{aligned} \quad (23)$$

Consequently, the presence of the given defect leads to the emergence of an additional term in the denominator of the Green's function (4):

$$R(\lambda,\varepsilon)=\frac{\lambda\varepsilon}{b}P_n(\lambda)+R(\lambda), \quad (24)$$

where $R(\lambda)\equiv R(\lambda,0)$. At the boundaries of the continuous spectrum band, $R(\lambda)$ is transformed to

$$R(\lambda)=\frac{1}{2}[P_{n-1}(\lambda_b)-P_{n+1}(\lambda_b)], \quad (25)$$

which allows us to obtain the threshold value of the mass parameter of the defect as a solution of Eq. (20):

$$\varepsilon_b=\frac{b}{\lambda_b}\frac{[P_{n-1}(\lambda_b)-P_{n+1}(\lambda_b)]}{2P_n(\lambda_b)}. \quad (26)$$

The final result can be obtained by substituting into (26) the polynomials $P_n(\lambda_b)$ (21) corresponding to a definite [(+) or (−)] type of independent vibrations of the chain, i.e., a definite subspace, where (+)-vibrations are described by $H^{(0)}$ for odd k and $H^{(+)}$ for even k, while (−)-vibrations correspond to $H^{(\pm1)}$ for odd k and $H^{(-)}$ for even k.

Thus, in the model of a chain containing two isotopic impurities having the same mass and separated by k atoms from each other, the critical mass defect required for the formation of a local discrete state generated by synphase displacements of isotopes (discrete (+)-vibrations) is given by

$$\varepsilon_l^{(+)}=-\frac{1}{2(k+1)}\frac{\lambda_m-\lambda_0}{\lambda_m}<0. \quad (27)$$

In this case, the square of frequency corresponding to the ''gap'' (+)-vibration splits to the frequency region $[0,\lambda_0]$ without any threshold.

For (−)-vibrations, a discrete ''gap'' state is formed in the threshold manner, while the splitting of the local state occurs for $\varepsilon<0$, i.e., without any threshold. The threshold value of the mass defect parameter corresponding to the ''gap'' vibration is given by

$$\varepsilon_g^{(-)}=\frac{1}{2(k+1)}\frac{\lambda_m-\lambda_0}{\lambda_0}>0. \quad (28)$$

Naturally, the threshold values for $k\to\infty$ are $\varepsilon_l^{(+)}\to\varepsilon_l^{(-)}\equiv-0$ and $\varepsilon_g^{(-)}\to\varepsilon_g^{(+)}\equiv+0$, and the squares of discrete frequencies are $\lambda_d^{(+)}\to\lambda_d^{(-)}$.

2. ADSORBED MONATOMIC CHAIN IN A PERIODIC EXTERNAL FIELD

Let us consider the model of an absorbed monatomic chain taking into account the effect of an applied periodic field. The terminal atom of the chain is connected to a certain ''wall'' (whose mass is regarded as infinitely large). The force constant characterizing this coupling is denoted by α' (Fig. 3). As in the previous section, we denote $\eta\equiv(\alpha'-\alpha)/\alpha$. The perturbation operator $\hat{\Lambda}^{af}(n,n')$ for the system under investigation is defined as

$$\hat{\Lambda}^{af}(n,n')=\frac{\eta(\lambda_m-\lambda_0)}{4}\delta_{n,0}\delta_{n',0}-\hat{\mathscr{L}}(n,n')\Theta(-n)\Theta(-n'), \quad (29)$$

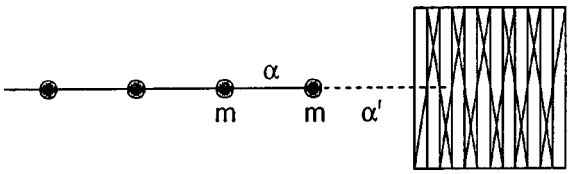

FIG. 3. Schematic diagram of the model of a monatomic chain adsorbed at the surface of a stationary solid.

where $\hat{\mathscr{L}}(n,n')$ is defined by (1).

The matrix elements a_n and b_n of the dynamic operator $\hat{\mathscr{L}}+\hat{\Lambda}^{af}$ coincide with similar elements from (3) for $n\geqslant 1$, which is natural since these elements describe the interaction between atoms in the chain that are separated from the defect by distances exceeding the atomic spacing. The elements a_0 and b_0 determining the changes emerging in the spectrum of the chain due to the rupture and formation of an additional bond are given by

$$a_0^{af}=\frac{\lambda_m-\lambda_0}{4}(\eta+2)+\lambda_0, \quad b_0^{af}=\frac{\lambda_m-\lambda_0}{4}. \tag{30}$$

The Green's function of the given model has the form

$$\mathscr{G}_{00}^{af}(\lambda,\lambda_0,\eta)=\frac{2}{\eta(\lambda_m-\lambda_0)(\lambda_l^{af}-\lambda)} \times\left[\lambda-\frac{\lambda_m(\eta+1)-\lambda_0(\eta-1)}{2} +\mathscr{Z}_1(\lambda)\sqrt{|(\lambda-\lambda_m)(\lambda-\lambda_0)|}\right], \tag{31}$$

where

$$\lambda_l^{af}=\frac{\lambda_m(\eta+1)^2-\lambda_0(\eta-1)^2}{4\eta}. \tag{32}$$

The corresponding spectral density is defined in the band $[\lambda_0,\lambda_m]$ of the continuous spectrum as $\rho^{af}(\lambda,\lambda_0,\eta)=(1/\pi)\mathrm{Im}\,\mathscr{G}_{00}^{af}(\lambda,\lambda_0,\eta)$ and is given by

$$\rho^{af}(\lambda,\lambda_0,\eta)=\frac{2\sqrt{(\lambda_m-\lambda)(\lambda-\lambda_0)}}{\pi\eta(\lambda_m-\lambda_0)(\lambda_l^{af}-\lambda)}. \tag{33}$$

The evolution of these spectral densities upon an increase in the parameter η is shown in Fig. 4. It can easily be seen that (33) vanishes at both boundaries of the continuous spectrum. Such a behavior of the spectral density is typical of one-dimensional systems containing a defect of the type ''surface plus additional bond,'' which can be conventionally referred to as adsorbed chains. Green's pole λ_l^{af} (31) is the square of the local frequency split to the region $(\lambda_m,+\infty)$ for $\eta\geqslant 1$ with the intensity

$$\mu_l^{af}=\frac{\eta^2-1}{\eta^2}\Theta(\eta-1). \tag{34}$$

It should be noted that the values of the local frequency λ_l^{af} (32) can also fall in to the interval $[0,\lambda_0]$, but in this case the intensity vanishes identically. Thus, irrespective of the smallness of the coupling constant α' between the chain and in certain adsorbing surface, this does not lead to splitting of the discrete vibration from the lower boundary of the continuous spectrum band. At the same time, the weakening of the coupling α' is accompanied by the ''pumping'' of phonons to the region of squares of frequencies near the bottom of the acoustic band. In the limiting case of an unperturbed semi-infinite chain, the spectral density of vibrations in the model acquires a root singularity.[6]

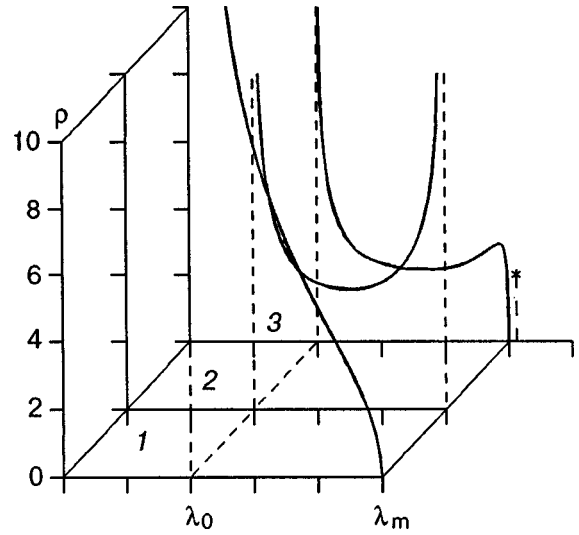

FIG. 4. Spectral densities of the terminal atom in an adsorbed semi-infinite linear chain: curve *1* corresponds to the free end (root singularity for $\lambda=\lambda_0$), curve *2* to the threshold value of the coupling parameter required for the formation of a local vibration (root singularities at both boundaries of the continuous spectrum band), and curve *3* corresponds to the presence of a local vibration in the system.

3. ADSORBED CHAIN WITH A DIATOMIC UNIT CELL

Let us consider a semi-infinite chain with a diatomic unit cell, which is adsorbed at the surface of a solid through its terminal atom. The masses of atoms are m_1 and m_2. As in the previous section, the terminal atom of the chain (for definiteness, we assume that its mass is m_1) is fixed to a certain ''wall,'' the force constant characterizing this coupling being $\alpha'\equiv\alpha(1+\eta)$ (Fig. 5).

The perturbation operator (defined in the same way as operator (29) in the previous problem) in the system under investigation has the form

$$\hat{\Lambda}(n,n')=-\hat{\mathscr{L}}(n,n')\Theta(-n)\Theta(-n') -\frac{\lambda_1-\lambda_*}{2}\delta_{n,0}\delta_{n',0}, \tag{35}$$

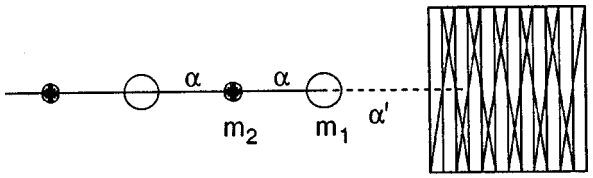

FIG. 5. Schematic diagram of the model of a diatomic chain adsorbed at the surface of a stationary solid.

where $\hat{\mathscr{L}}(n,n')$ is the dynamic operator describing vibrations of an ideal infinite diatomic chain:[1] $\lambda_*=2\alpha'/m_1$, $\lambda_i=2\alpha/m_i$, $i=1,2$. The matrix elements of the $\mathscr{J}$-matrix of the operator $\hat{\mathscr{L}}+\hat{\Lambda}$ of the given system are defined as

$$a_0=\frac{\lambda_1+\lambda_*}{2};\quad \alpha_{2(n+1)}=\lambda_1;\quad a_{2n+1}=\lambda_2;$$
$$b_n=\frac{\sqrt{\lambda_1\lambda_2}}{2};\quad n=0,1,2,... \tag{36}$$

and the Green's function has the form

$$\mathscr{G}_{00}(\lambda,\lambda_*)=\frac{2}{R(\lambda,\lambda_*)}[(\lambda-\lambda_*)(\lambda-\lambda_2)+\mathscr{Z}_2(\lambda)\sqrt{|\lambda(\lambda-\lambda_1)(\lambda-\lambda_2)(\lambda-\lambda_1-\lambda_2)|}], \tag{37}$$

where

$$\mathscr{Z}_2(\lambda)=i[\Theta(\lambda)\Theta(\lambda_1-\lambda)+\Theta(\lambda-\lambda_2)\Theta(\lambda_1+\lambda_2-\lambda)]+\Theta(\lambda-\lambda_1)\Theta(\lambda_2-\lambda)-\Theta(\lambda-\lambda_1-\lambda_2);$$
$$R(\lambda,\lambda_*)=2\lambda^2(\lambda_1-\lambda_*)-\lambda[(\lambda_1+\lambda_*)(\lambda_1-\lambda_*)-\lambda_2(2\lambda_*-\lambda_1)]-\lambda_2\lambda_*^2.$$

It follows from (37) that the continuous vibrational spectrum of the system is formed by two bands of equal width: $[0,\{\lambda_1,\lambda_2\}_{\min}]$ and $[\{\lambda_1,\lambda_2\}_{\max},\ \lambda_m=\lambda_1+\lambda_2]$, which are separated by the gap $\Delta=|\lambda_1-\lambda_2|$.

Thus, it can be seen that the spectral density of vibrations of a diatomic adsorbed chain vanishes at each boundary of the continuous spectrum. In the limiting case of a free (uncoupled and unperturbed) semi-infinite chain ($\lambda_*\equiv 0$), the spectral density tends to infinity for $\lambda=0$ in proportion to $1/\sqrt{\lambda}$ (which leads to the divergence of rot-mean-square displacement in such a system). The perturbation in question eliminates this singularity for $\lambda_*>0$.

The function $R(\lambda,\lambda_*)$ has the following roots $\lambda_{g,l}$:

$$\lambda_{g,l}=\frac{1}{4(\lambda_1-\lambda_*)}[(\lambda_1+\lambda_*)(\lambda_1-\lambda_*)-\lambda_2(2\lambda_*-\lambda_1)\pm\sqrt{[(\lambda_1+\lambda_*)(\lambda_1-\lambda_*)+\lambda_2(2\lambda_*-\lambda_1)]^2+2\lambda_1\lambda_2(\lambda_1-\lambda_*)^2}], \tag{38}$$

which define the poles of Green's function (37), i.e., the values of the squares of the frequencies of the gap and local vibrations (the ''+'' and ''-'' signs of the radical respectively). For $\lambda_*>0$, the splitting of discrete vibrational frequencies does not differ in principle from the systems for which the spectral density at a boundary of the continuous spectrum turns to infinity and occurs in the same way as in the case of splitting of a discrete frequency from the edge of the spectrum at which the vibrational density is zero. It can be easily proved that the pole λ_g (37) tends to one of the boundaries λ_1 of the gap as $\lambda_*\to\lambda_1$:

$$\lim_{\lambda_*\to\lambda_1\pm 0}\lambda_g=\lambda_1.$$

Similarly, for $\lambda_*=\lambda_{\max}$, the other root λ_l of the denominator of the Green's function coincides with the square of the maximum frequency in the spectrum. It can be seen that for a certain nonzero value of the coupling parameter λ_*, the spectral density acquires a root singularity at the boundary of the continuous spectrum from which the discrete frequency is split. Thus, there exists a threshold for the formation of the gap state as well as the local state in the given system, which should be expected in view of the form of the spectral density of vibrations of a free semi-infinite chain.

The terminal atom of the chain can obviously belong to the light or to the heavy sublattice. These two situations will be considered separately.

If the extreme atom m_1 of the chain is light (see curves *1–5* in Fig. 6), λ_2 is the upper boundary of the acoustic band and λ_1 is the lower boundary of the optical band. The intensities of discrete vibrations are defined in this case as follows:

$$\mu_g(\lambda_*)=\frac{4(\lambda_g-\lambda_*)(\lambda_g-\lambda_2)\Theta(\lambda_*)\Theta(\lambda_1-\lambda_*)}{\sqrt{[(\lambda_1+\lambda_*)(\lambda_1-\lambda_*)+\lambda_2(2\lambda_*-\lambda_1)]^2+2\lambda_1\lambda_2(\lambda_1-\lambda_*)^2}}, \tag{39}$$

$$\mu_l(\lambda_*)=-\frac{4(\lambda_l-\lambda_*)(\lambda_l-\lambda_2)\Theta(\lambda_1+\lambda_2-\lambda_*)}{\sqrt{[(\lambda_1+\lambda_*)(\lambda_1-\lambda_*)+\lambda_2(2\lambda_*-\lambda_1)]^2+2\lambda_1\lambda_2(\lambda_1-\lambda_*)^2}}. \tag{40}$$

An analysis of the expressions for the gap frequency λ_g (38) and its weight (39) shows that a discrete gap state exists in the limiting case $\lambda_*=0$ corresponding to the rupture of the bond:

$$\lambda_g(0)=\frac{\lambda_1+\lambda_2}{2},\quad \mu_g(0)=\frac{\lambda_1-\lambda_2}{\lambda_1}, \tag{41}$$

which is in accord with the results obtained in Refs. 1 and 7. The enhancement of the bond in the range $\lambda_*\in[0,\lambda_1]$ leads to an increase in the gap root λ_g to the value $\lambda_g=\lambda_1$ (i.e., to the lower boundary of the optical band) and is accompanied by a monotonic decrease in μ_g to zero.

It should be noted that the relation $\lambda_*=\lambda_1$ indicates the equality of the force constant α' characterizing the interaction of the extreme atom of the chain with the surface and the coupling constant α for the remaining atoms in the chain. As the coupling parameter λ_* increases further, the spectral density of vibrations acquires a peak near the upper boundary of the optical band, and the fulfillment of the inequality $\lambda_*>\lambda_{\max}$ [i.e., $\alpha'>\alpha(1+m_1/m_2)$] leads to the formation of a local vibration with the square of the frequency λ_l (38). The weight μ_l (40) of this vibration increases monotonically from zero at $\lambda_*=\lambda_{\max}$ to unity for $\lambda_*\to\infty$.

Let us now consider the situation when a chain is fixed to an adsorbing surface through a heavy atom (see curves *6–10* in Fig. 6). The gap vibration splits from the upper boundary of the acoustic band if λ_* exceeds the threshold value ($\lambda_*\geqslant\lambda_1$).

A further enhancement of the coupling leads to the splitting of the local vibration from the upper boundary of the spectrum in analogy to the case $m_1<m_2$ with the same threshold: $\lambda_*\geqslant\lambda_{\max}$. In the limit $\lambda_*\to\infty$, the gap state approaches the lower boundary of the optical band asymptotically, and the frequency of the local state in this case tends to infinity:

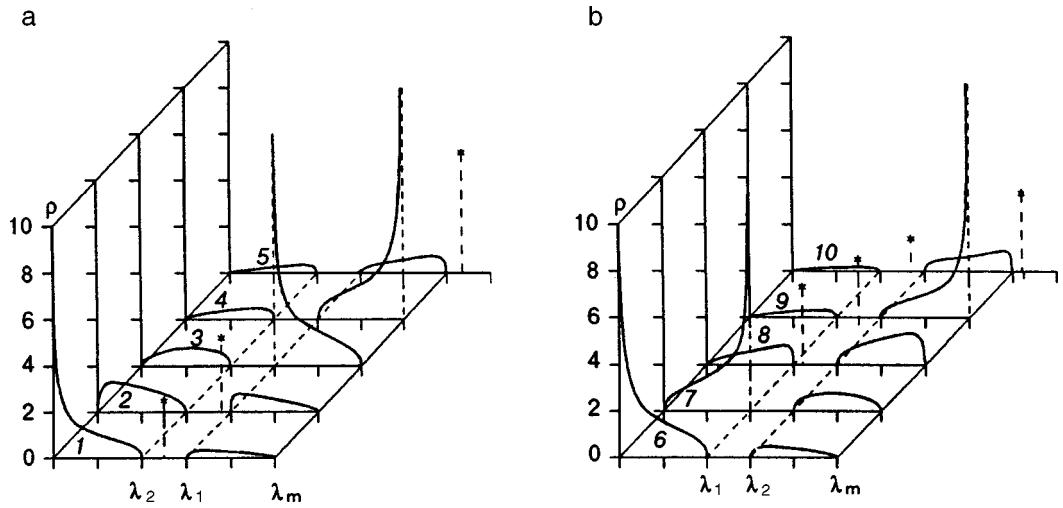

FIG. 6. Spectral densities of the terminal atom of an adsorbed semi-infinite linar chain with a diatomic unit cell.

$$\lim_{\lambda_* \to \infty} \lambda_g = \lambda_2; \quad \lim_{\lambda_* \to \infty} \lambda_l = \infty.$$

Thus, in the case of a quite strong interaction between the heavy terminal atom of the chain with the surface of the solid ($\alpha' > \alpha(1+m_1/m_2)$), the spectrum contains both the local vibration with the square of the frequency λ_l, and the gap vibration λ_g.

The intensity

$$\mu_g = \frac{4(\lambda_g - \lambda_*)(\lambda_g - \lambda_2)\Theta(\lambda_* - \lambda_1)}{\sqrt{[(\lambda_1 + \lambda_*)(\lambda_1 - \lambda_*) + \lambda_2(2\lambda_* - \lambda_1)]^2 + 2\lambda_1\lambda_2(\lambda_1 - \lambda_*)^2}} \qquad (42)$$

of the gap state depends nonmonotonically on the parameter λ_*. It can easily be proved that μ_g vanishes both for $\lambda_* = \lambda_1$ and for $\lambda_* \to \infty$. At the same time, the intensity μ_l (40) of the local state increases monotonically with the enhancement of the coupling between the chain and the adsorbing surface. The suppression of the discrete state upon an increase in the distance from the defect occurs in accordance with Refs. 1 and 6, where it was shown that the intensity of a discrete vibration of an atom with number n due to a local defect situated at the origin in the linear chain with interaction between nearest neighbors is proportional to $P_n^2(\lambda_d)$, and the polynomials $P_n(\lambda_d)$ outside the defect cluster form a descending geometrical progression. Thus, the degree of localization of the gap vibration with the square of the frequency $\lambda_g \in [\lambda_1, \lambda_2]$ is lower than that for the local vibration whose square of frequency is $\lambda_l > \lambda_m$.

It should be noted that a similar model was considered by Glushko and Khrisanov.[7] In contrast to the approach developed in Ref. 7, the introduction of the quantity $\mu_{g,l}$, viz., the intensity of the localized state as the residue of the function $\mathscr{G}_{00}(\lambda, \lambda_*)$ at the relevant pole makes it possible to select the poles corresponding to the true discrete vibrations. For example, no gap level is formed in a diatomic semi-infinite linear chain with a free end if the terminal atom of the chain is heavy since the value of μ_g in this case is zero. On the contrary, a light atom of the sublattice at the end of the chain leads to the formation of the gap state (41).

The obtained results can also be used for an analysis of other quasiparticle excitations in one-dimensional systems. It is interesting to note in this connection that various characteristics including the transport[8] and optical[9] properties as well as resonant tunneling[10], many-particle effects and plasmon excitations,[11] the role of impurities,[12] peculiarities of the electron–phonon interaction,[13] and the spectrum of collective vibrations of a one-dimensional electron system over liquid helium[14,15] are being studied intensely (in experiments also) for one-dimensional degenerate electron systems.

The authors express their gratitude to A. M. Kosevich for fruitful discussions of the results.

This research was carried out under support of the Ukrainian Foundation for Fundamental Studies, Grant No. 2.4/165 (''USKO'').

*E-mail: mamalui@ilt.kharkov.ua

[1] M. A. Mamalui, E. S. Syrkin, and S. B. Feodosyev, Fiz. Nizk. Temp. **24**, 773 (1998) [Low Temp. Phys. **23**, 583 (1998)].
[2] V. I. Peresada, in *Physics of Condensed State* [in Russian], B. Verkin Inst. for Low Temp. Phys. and Eng., Kharkov (1968).
[3] V. I. Peresada, V. N. Afanas'ev, and V. S. Borovikov, Fiz. Nizk. Temp. **1**, 461 (1975) [Sov. J. Low Temp. Phys. **1**, 227 (1975)].
[4] R. Haydock, in Solid State Phys. vol. 35 (ed. by H. Ehrenreich, F. Seitz, and D. Turnbull), Academic Press, New York (1980).
[5] E. S. Syrkin and S. B. Feodosyev, Fiz. Nizk. Temp. **20**, 586 (1994) [Low Temp. Phys. **20**, 463 (1994)].
[6] M. A. Mamalui, E. S. Syrkin, and S. B. Feodosyev, Fiz. Tverd. Tela (St. Petersburg) **38**, 3683 (1996) [Phys. Solid State **38**, 2006 (1996)].
[7] E. Ya. Glushko and V. A. Khrisanov, Fiz. Nizk. Temp. **23**, 1215 (1997) [Low Temp. Phys. **23**, 910 (1997)].
[8] C. W. S. Beenakker and H. van Houton, in Solid State Phys. **44** (ed. by H. Ehrenreich and D. Turnbull), Academic Press, New York (1991), p. 1.
[9] A. S. Plaut, H. Lage, P. Grambow *et al.*, Phys. Rev. Lett. **67**, 1642 (1991).
[10] S. Tarucha, Y. Hirayama, T. Saku, and T. Kimura, Phys. Rev. B **41**, 5459 (1990).
[11] L. Wendler and V. G. Grigoryan, Phys. Rev. B **49**, 14 531 (1994).
[12] A. Ferreira da Silva, Phys. Rev. B **41**, 1684 (1990).
[13] Vl. L. Ginzburg and Yu. P. Monarkha, Fiz. Nizk. Temp. **4**, 1236 (1978) [Sov. J. Low Temp. Phys. **4**, 580 (1978)].
[14] S. S. Sokolov and O. I. Kirichek, Fiz. Nizk. Temp. **20**, 764 (1994) [Low Temp. Phys. **20**, 599 (1994)].
[15] V. A. Nikolaenko, H. Yayama, Yu. Z. Kovdrya, and A. Tomokiyo, Fiz. Nizk. Temp. **23**, 642 (1997) [Low Temp. Phys. **23**, 482 (1997)].

Translated by R. S. Wadhwa

LOW-TEMPERATURE PHYSICS OF PLASTICITY AND STRENGTH

Low-temperature dislocation and magnetomechanical acoustic effects in high purity Fe single crystals

P. P. Pal-Val

*B. Verkin Institute for Low Temperature Physics and Engineering, National Academy of Sciences of the Ukraine, 310164 Kharkov, Ukraine**

(Submitted July 23, 1998)
Fiz. Nizk. Temp. **25**, 83–93 (January 1999)

The effect of preliminary plastic deformation $\varepsilon_{\rm pl}<3\%$ and an external magnetic field $H \leqslant 3.35$ kOe on linear and nonlinear acoustic properties of high purity Fe single crystals is studied. Measurements were made at frequencies ~ 90 kHz in the temperature interval 5.5–300 K using the two-component composite oscillator technique. The wave vector of the longitudinal standing wave and the magnetic field direction coincide with the crystallographic axis $\langle 731 \rangle$. In the linear range, the main attention is paid to the influence of the deformation level and subsequent low-temperature recovery on parameters of the relaxation α-peak near 50 K. The increase in $\varepsilon_{\rm pl}$ leads to a considerable rise in the height of the peak, while the height and temperature of the peak are considerably lowered in the recovery process. An increase in the amplitude ε_0 of the ultrasonic deformation beyond a certain threshold ε_{0c} is accompanied by the emergence of strong amplitude dependences of acoustic parameters of the crystals under investigation. As a result of plastic deformation, the amplitude dependences of the decrement and the Young's modulus are displaced towards lower amplitudes. Magnetoacoustic effects in a saturating external field are practically independent of the amplitude and display a weak monotonic dependence on temperature in the region of the α-peak. It is concluded that the amplitude dependences as well as the α-peak are of the dislocation nature. Possible microscopic mechanisms of the observed effects are discussed.
[S1063-777X(99)01201-3]

INTRODUCTION

A large number of linear and nonlinear acoustic effects observed during investigations of crystals are associated with the presence of dislocations in them (see, for example, Refs. 1–6). As a rule, linear effects are responsible for the emergence of peaks on temperature or frequency dependences of the absorption of sound as well as step-like variations of the elastic moduli (modulus defect) of the crystal associated with them. Nonlinear effects are manifested in the form of a strong dependence of absorption as well as the elastic moduli on the amplitude of the alternating deformation ε_0 produced in the crystal by sound. Acoustic effects are usually considered to be of dislocation origin in cases in which their manifestation depends directly on the presence of dislocations in the samples, whose density and/or mobility can be changed in the course of the experiment over a wide range as a result of plastic deformation, introduction of impurities, irradiation, annealing, etc.

In order to explain the dislocation acoustic effects, a number of microscopic models of the behavior of dislocations in the field of an ultrasonic wave were proposed.[1,4,7–17] Together with reliable experimental data on dislocation contributions to the sound absorption and modulus defect, these models could have provided in principle detailed information on the dynamic behavior of dislocations in crystals. Such attempts were undertaken repeatedly but it was found in almost all cases that the obtained experimental results differ significantly from the predicted behavior in the framework of any theory.[10,13,14,18–22] This is especially true for the amplitude dependent acoustic effects whose theoretical description is still confined to simplified dislocation models. The main reasons for this situation are the complexity and diversity of real dislocation processes in excitation of sound (including high-amplitude sound) on the one hand, and a comparatively small body of the accumulated experimental results in this field on the other hand. Hence it is expedient to obtain new experimental data and provide their phenomenological description in order to form a reliable experimental base for constructing subsequently a more appropriate microscopic description of the investigated phenomena.

In this paper, we continue our systematic studies of linear and nonlinear dislocation effects in single crystals of high-purity iron in the temperature interval 5.5–300 K, which were started in Refs. 23–25. Ultrasonic studies in ferromagnets become complicated due to the presence of spontaneous magnetization regions (magnetic domains) in them. A change in the magnetization of ferromagnets in the field of an ultrasonic wave may lead to additional linear and nonlinear absorption of sound and a variation in dynamic elastic

moduli.[26] The magnitude and relative role of magnetoacoustic effects can be changed by applying a constant magnetic field to the investigated samples. Unlike the previous publications,[23–25] the present paper aims at studying the effect of the applied magnetic field on the amplitude-independent as well as amplitude-dependent acoustic effects at low temperatures.

1. EXPERIMENT

High-purity single crystals of iron grown by the recrystallization technique were chosen as the objects of investigation.[27] The high purity of samples was ensured by a seven-fold zone purification of the original commercial metal (supplied by Johnson and Mathey, England) followed by a prolonged (for about seven days) annealing of the grown single crystals in an atmosphere of dehydrated hydrogen with a heated zirconium absorber.[28] The final concentration of interstitial impurities (C, N, etc.) was less than 1×10^{-4} at. %. The orientation of the samples was determined with the help of Laue's diffraction pattern. The longitudinal axis of the samples, which coincided with the longitudinal standing wave vector in samples and loading axis in the case of plastic deformation, was at the center of a standard crystallographic triangle and had an orientation close to $\langle 731\rangle$ which is coplanar with the directions $\langle 111\rangle$ and $\langle 101\rangle$ and forms angles of about 45° with them. The initial density of growth dislocations was $\sim10^5-10^6\ \mathrm{cm}^{-2}$.

Acoustic measurements were made by using the two-component composite oscillator technique.[29,30] Longitudinal standing waves with a vibrational frequency of about 90 kHz and the ultrasonic deformation amplitude in the interval $5\times10^{-9}<\varepsilon_0<7\times10^{-5}$ were excited in undeformed and deformed samples. Temperature and amplitude dependences of the decrement δ and the resonance frequency f_r of the composite oscillator were measured in the temperature interval $5.5\ \mathrm{K}<T<300\ \mathrm{K}$, and were subsequently used to determine the dynamic elastic Young's modulus E.[30]

In order to establish a relation between the acoustic properties of samples and the dislocation processes in them, fresh dislocations were introduced by deformation at room temperature up to the residual plastic deformation $\varepsilon_{\mathrm{pl}}=0.84$ and 2.76%. The chosen orientation of the samples ensured a singlet slip in the $(\bar{1}01)$ plane with the maximum resolved shear stress along the Burgers vector [111].[31]

The external magnetic field was produced by a superconducting solenoid. The direction of the magnetic field vector coincided with the wave vector of the ultrasound (i.e., with the longitudinal axis of the sample). In view of technical constraints, measurements in a magnetic field were made in the temperature interval 5.5–60 K.

2. RESULTS OF MEASUREMENTS

2.1. Measurements in zero magnetic field

Temperature Dependences in the Amplitude-Independent Region. Figure 1 shows the temperature dependences of the decrement $\delta(T)$ and the dynamic Young's modulus $E(T)$ measured in an undeformed sample as well as after

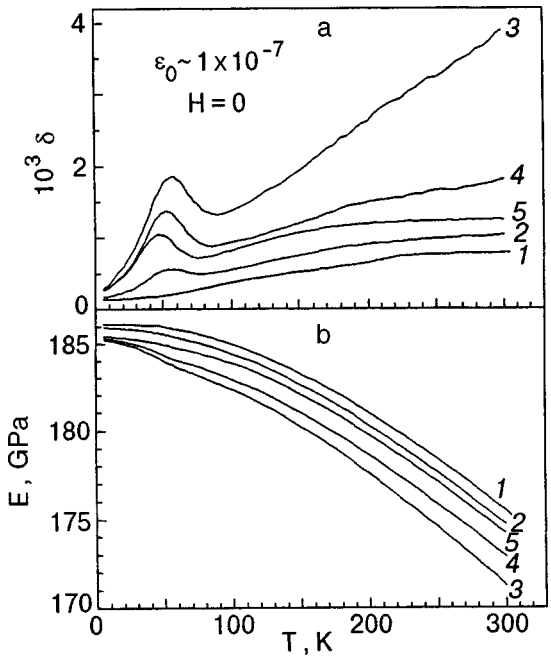

FIG. 1. Temperature dependences of decrement (a) and dynamic elastic modulus (b) measured in zero magnetic field for an undeformed sample (curve *1*), a sample deformed at room temperature to residual plastic deformation $\varepsilon_{\mathrm{pl}}=0.84\%$ (curve *2*), immediately after deformation $\varepsilon_{\mathrm{pl}}=2.76\%$ (curve *3*), 3 days after the deformation (curve *4*), and 11 years after the deformation (curve *5*). The ultrasonic deformation amplitude is denoted by ε_0.

deformation at room temperature up to values of the residual plastic deformation $\varepsilon_{\mathrm{pl}}=0.84$ and 2.76%. Measurements were made at the ultrasonic deformation amplitude $\varepsilon_0\sim1\cdot10^{-7}$, which corresponds in all cases to the amplitude-independent region $\delta(\varepsilon_0)$ and $E(\varepsilon_0)$. Preliminary deformation increases the decrement and decreases the Young's modulus in the entire investigated intervals of temperatures and residual plastic deformations. The growth of decrement in deformed samples depends nonmonotonically on the temperature. Near $T\sim52\ \mathrm{K}$, the $\delta(T)$ dependence acquires a peak whose height increases with $\varepsilon_{\mathrm{pl}}$. In the same temperature interval, the peak on the $\delta(T)$ dependence corresponds to the emergence of smeared steps on the dependences $E(T)$ (modulus defect). Samples held at room temperature recover to a considerable extent their properties that had undergone a change during deformation: the decrement becomes smaller and the Young's modulus increases again (cf. curves *3, 4, 5* in Fig. 1).[1)] It should be noted that the recovery of acoustic properties is also accompanied by a noticeable shift in the peak on the $\delta(T)$ dependence as well as the steps on the $E(T)$ dependence towards lower temperatures, and also by a decrease in their height.

Amplitude dependences. The amplitude dependences of the decrement $\delta(\varepsilon_0)$ and relative variations in the dynamic Young's modulus $(\Delta E/E)(\varepsilon_0)\equiv[E(\varepsilon_0)-E(\varepsilon_0\to0)]/E(\varepsilon_0\to0)$ were measured at fixed temperatures in undeformed and deformed samples after holding them at room temperature for seven days following each act of deformation, i.e., after stabilization of the defect structure created in them. Figure 2 shows the dependences $\delta(\varepsilon_0)$ and $(\Delta E/E)(\varepsilon_0)$ in

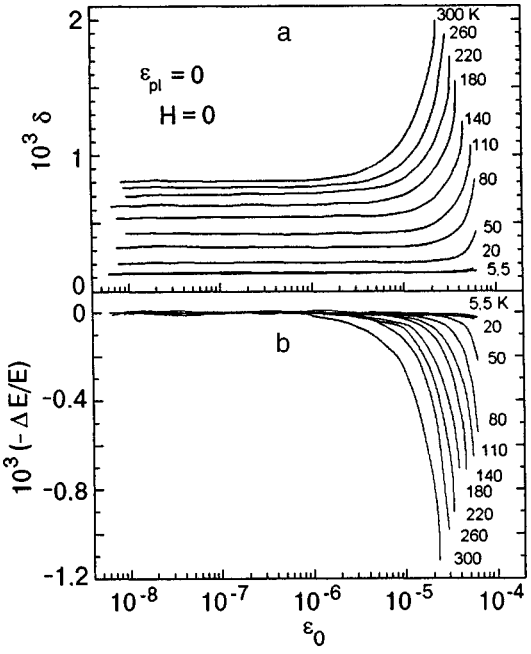

FIG. 2. Amplitude dependences of decrement (a) and modulus defect (b) in an undeformed sample at different temperatures in zero magnetic field.

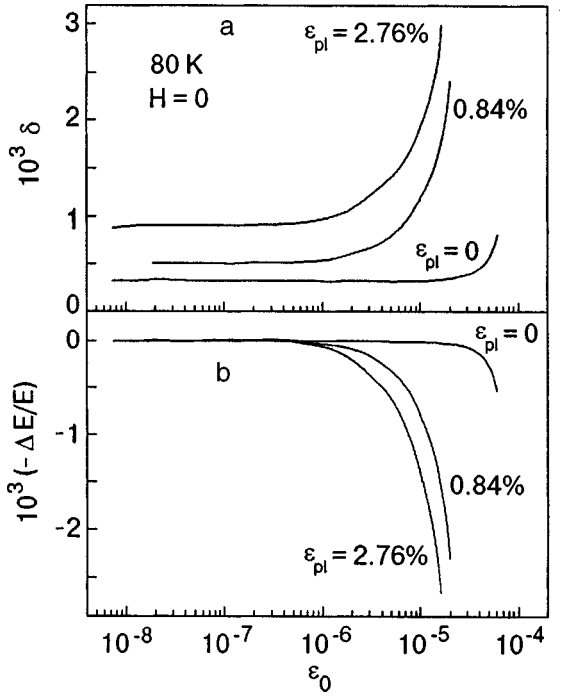

FIG. 3. Effect of plastic deformation on the amplitude dependences of decrement (a) and modulus defect (b) at 80 K for different values of preliminary plastic deformation in zero field.

an undeformed sample. The critical amplitude ε_{0c} at the onset of amplitude dependences increases with decreasing temperature, i.e., the curves are displaced towards higher amplitudes.

Preliminary plastic deformation $\varepsilon_{\rm pl}=0.84\%$ decreases ε_{0c} considerably at all temperatures. Subsequent deformation to the value $\varepsilon_{\rm pl}=2.76\%$ results in a further decrease in ε_{0c} which, however, is not so sharp as in the case of the first deformation. The effect of preliminary plastic deformation is demonstrated in Fig. 3 for the amplitude dependences measured at $T=80$ K.

2.2. Effect of the applied magnetic field

Figure 4 shows the dependences of the decrement δ and the relative variation $\Delta f_r/f_r$ of the resonance oscillator frequency on the applied field strength H, which were measured in the amplitude-independent region at a deformation amplitude $\varepsilon_0 \sim 1\cdot 10^{-7}$ and a temperature of 5.5 K. It can be seen that the decrement becomes considerably smaller and the resonance frequency increases with increasing H. The maximum relative variation $\sim 4.5\times 10^{-4}$ of the resonance frequency considerably exceeds the maximum variation ($\sim 6\times 10^{-5}$) of the decrement.[2)] Moreover, the resonance frequency attains saturation for much lower values of the applied magnetic field. As the magnetic field decreases to lower values of H, a small hysteresis observed in δ and $\Delta f_r/f_r$ points towards irreversible variations in the magnetization of samples upon removal of the magnetic field. The large values of the saturating fields for δ and $\Delta f_r/f_r$ is worth noting. Iron displays a clearly manifested anisotropy of the saturation field: the ⟨100⟩ axis is the easy magnetization axis while the ⟨110⟩ and ⟨111⟩ axes are the crystallographic directions of the moderate and difficult magnetizations.[26,32] According to Ref. 32, however, even for these directions the

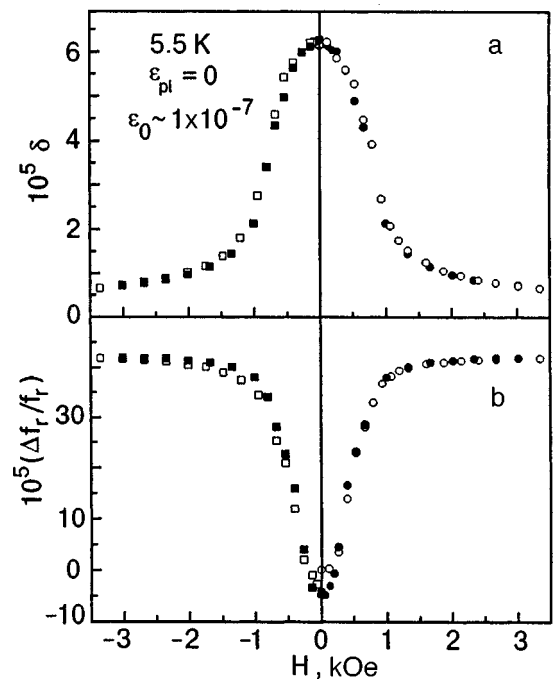

FIG. 4. Dependence of decrement (a) and resonance frequency (b) on the magnitude and direction of the applied magnetic field. The vector **H** is parallel (●,○) and antiparallel (■,□) to the wave vector **q** of ultrasound in the amplitude-independent region at 5.5 K. Light and dark symbols correspond to an increase and subsequent decrease respectively in the absolute value of **H**; $\Delta f_r = f_r(H) - f_r(0)$.

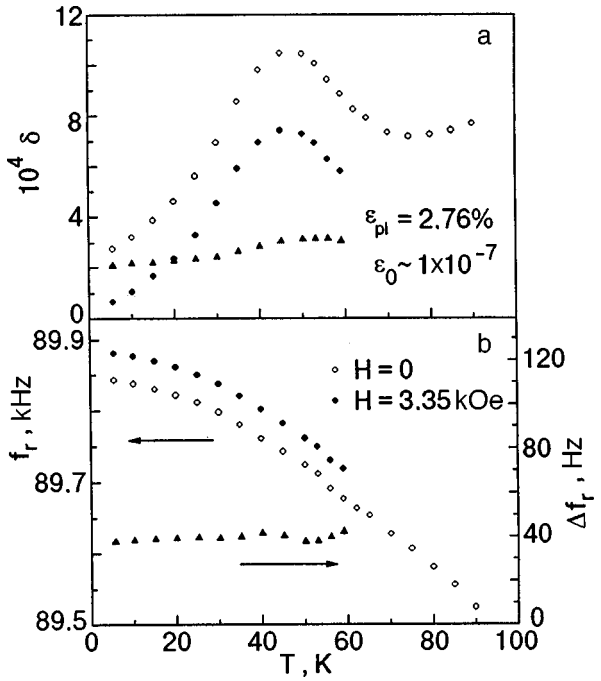

FIG. 5. Effect of saturating magnetic field on the temperature dependences of decrement (a) and resonant frequency (b) near the α-peak (magnetomechanical effects are shown by dark triangles): $\delta(3.35)-\delta(0)$ (a) and $f_r(3.35)-f_r(0)$ (b).

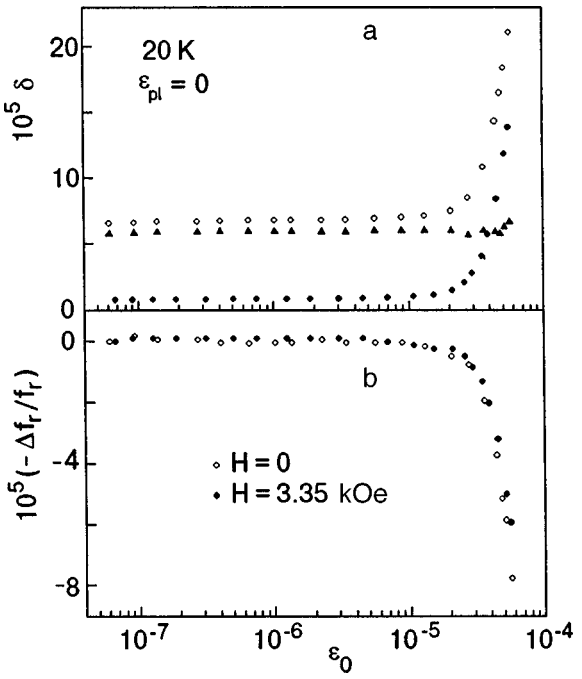

FIG. 6. Effect of saturating magnetic field on the amplitude dependences of decrement (a) and resonant frequency (b) in an undeformed sample at 20 K (notation is the same as in Fig. 5).

saturating field does not exceed 0.5–0.6 kOe. In our samples having the ⟨731⟩ orientation, saturation of δ and $\Delta f_r/f_r$ is attained in fields 1.5–2 kOe, which are 2–3 times stronger.

In order to separate the magnetoacoustic and dislocation effects, we studied the effect of the saturating magnetic field on the temperature and amplitude dependences of the decrement and resonance frequency of the samples. Figure 5 shows the temperature dependence regions in the vicinity of the $\delta(T)$ peak in a sample deformed up to $\varepsilon_{pl}=2.76\%$. Measurements were made in zero field and in an applied field $H=3.35$ kOe. It can be seen that the application of an external magnetic field leads to a lowering of the entire $\delta(T)$ curve without any significant displacement of the peak along the temperature axis and a variation in the height of the peak relative to the background. The saturating magnetic field also changes the amplitude dependences in an identical manner, as can be seen from Figs. 6a and 6b showing the dependences $\delta(\varepsilon_0)$ and $(\Delta f_r/f_r)(\varepsilon_0)$ measured for one of the undeformed samples of the series at 20 K. Application of the saturating magnetic field lowers the decrement by about the same amount in the entire range of amplitudes including the amplitude-dependent region (Fig. 6a). The amplitude dependences of the relative variation in the resonance frequencies $(\Delta f_r/f_r)(\varepsilon_0)$ are practically identical in a saturating magnetic field and in zero field (Fig. 6b).

3. DISCUSSION OF RESULTS

3.1. Effect of spontaneous magnetization on acoustic effects in iron

Because of the presence of spontaneous magnetization regions (domain structure), ferromagnets may display magnetoacoustic effects which are associated with reversible and irreversible motion of domain walls, micro- and macroeddy currents, and have in the general case a complex dependence on the vibrational frequency, deformation amplitude, domain wall features, and several other characteristics of the ferromagnet.[26] The present research does not aim specifically at the investigation of magnetomechanical effects, and measurements in a saturating magnetic field were made for a correct separation of dislocation and magnetoacoustic contributions to the measured decrement and the elastic modulus. It was found that although magnetoacoustic contributions in the given frequency region and in samples with the given microstructure are quite significant, they depend weakly and monotonically on temperature (at least in the region of the ultrasonic absorption peak initiated by plastic deformation) and are practically independent of the amplitude of ultrasonic vibrations (see Figs. 5 and 6). Thus the magnetoacoustic contributions the present case can be considered to be free of the specific anomalies and can be regarded as some background components of the decrement and the dynamic elastic modulus which can be subtracted together with other components from measured values while separating the dislocation contributions.

3.2. Dislocation acoustic effects in the amplitude-independent region

Changes occurring in the temperature dependences of the decrement and dynamic elastic modulus as a result of plastic deformation and subsequent prolonged holding of the samples at room temperature are a consequence of the introduction of fresh dislocations resulting in the formation of a nonequilibrium defect structure in the crystal. According to

the string dislocation model,[1] the increase in the decrement δ_d and the relative decrease in the Young's modulus $(\Delta E/E)_d$ caused by the introduction of dislocations in the frequency range under consideration are described by the relations

$$\delta_d = 120\Omega\Delta_0\Lambda L_c^4\frac{\omega B}{\pi C}, \tag{1}$$

$$\left(\frac{\Delta E}{E}\right)_d = \frac{6\Omega\Delta_0\Lambda L_c^2}{\pi}, \tag{2}$$

where Ω is the orientational factor for taking into consideration the relative contribution of dislocations belonging to different slip systems, $\Delta_0 = 8Gb^2/\pi^3 C$, G is the shear modulus, b the modulus of the Burgers vector, C the linear tension of a dislocation, Λ the dislocation density, L_c the average length of dislocation segments, $\omega = 2\pi f_r$, and B the dislocation drag coefficient.

For small plastic deformations, changes are mainly observed in the dislocation density and the average length of dislocation segments. The value of Λ can only increase with $\varepsilon_{\rm pl}$, while the value of L_c depends on strain nonmonotonically: first it increases due to the formation of new long dislocation loops and the liberation of growth dislocations from Cottrell impurity ''atmospheres,'' and then decreases as a result of interaction of dislocations with one another as well as with other defects when the dislocation density is high. Experiments in the amplitude-independent region do not permit a correct separation of these effects. The results presented in Fig. 1 only suggest that the values of $\varepsilon_{\rm pl}$ attained in our experiments are still accompanied by an increase in the product ΛL_c, which leads to a significant increase in the decrement and a considerable decrease in the elastic modulus. Prolonged holding of the samples at room temperature (low-temperature recovery) stabilizes the emerging defect structure which is mainly a result of migration of impurities in the long-range elastic fields of dislocations and the formation of Cottrell's impurity ''atmospheres,'' as well as a partial relaxation of internal stresses owing to thermally activated movement of dislocation loops to more advantageous positions (from the energy point of view) under the effect of these stresses. These processes reduce the average length of dislocation segments and lead to a considerable decrease in δ_d as well as in $(\Delta E/E)_d$.

The most interesting effect caused by plastic deformation is the emergence of a peak (known as the α-peak[16]) on the $\delta(T)$ curve near the temperature 52 K, steps on the $E(T)$ curve (modulus defect), and enhancement of these anomalies upon an increase in $\varepsilon_{\rm pl}$. Such a peak was observed earlier at nearly the same temperature for high-purity iron samples having an orientation ⟨100⟩ and deformed by 0.82%.[23,24] The relaxation origin of the peak was established, and the activation parameters of the corresponding relaxation process were determined. In view of a comparatively low activation energy $U \approx 0.07$ eV for a large value of the attack frequency $\nu_0 = 5\times 10^{12}\,{\rm s}^{-1}$, it was proposed that the microscopic relaxation mechanism involves the formation of a pair of kinks on the nonscrew components of dislocations. This hypothesis is in line with the computer simulation data and the results obtained by transmission electron microscopy,[33] according to which a system of dislocation loops in the shape of ellipses elongated in the direction ⟨111⟩ of the Burgers vector and having segments with edge components constituting the significant part of the total length of the loops (up to 20%) are formed in iron crystals under plastic deformation at room temperatures. The energy parameters of screw and edge dislocations differ considerably. In particular, the ratio of their linear tensions is $C_{\rm screw}/C_{\rm edge} \approx 6$. The formation of a pair of kinks on screw dislocations obviously corresponds to the so-called γ-peak in iron with an activation energy ~ 0.72 eV.[34]

As for samples having the orientation ⟨100⟩, the prolonged holding of deformed samples at room temperature reduces the height and slightly decreases the temperature T_p of the α-peak. This is illustrated in Fig. 2a for a sample deformed preliminarily by 2.76%. The decrease in the peak height can naturally be attributed to the decrease in the average length of dislocation segments on which pairs of kinks can be formed. The decrease in the temperature T_p corresponding to the peak, which is determined by the condition $2\pi f_r \tau_p = 1$ is less obvious [$\tau_p = \nu_0^{-1}\exp(U/kT_p)$] is the relaxation time at the peak temperature). Since the resonance frequency f_r of the vibrator changes (*increases*) insignificantly during low-temperature recovery, the observed decrease in T_p indicates either a decrease in the activation energy U of the given relaxation process, or an increase in the attack frequency ν_0, or a combination of both effects. According to Louchet *et al.*,[35] the attack frequency ν_0 during the formation of kink pairs is a function of L_c:

$$\nu_0 = \frac{b\nu_D L_c}{l_0^2}, \tag{3}$$

where ν_D is the Debye frequency and l_0 is the critical separation between kinks of opposite signs, which corresponds to the saddle configuration for a given pair. It can be seen that a decrease in the average length of the segment must lead to a decrease in the attack frequency. Thus, the decrease in the peak temperature can be attributed to a decrease in the activation energy U, whose origin remains unclear.

Another possible explanation for the decrease in T_p may be a variation of the type and parameters of distribution of U and/or ν_0 upon a prolonged low-temperature recovery of the samples. As a matter of fact, the observed peaks of sound absorption and ''steps'' (modulus defect $\Delta E/E$) on the $E(T)$ curve are found to be much broader (see also Ref. 22) than what is predicted by the theory for a thermally activated relaxation process with a single relaxation time $\tau = \nu_0^{-1}\exp(U/kT)$:[36]

$$\delta(T) = \pi\Delta_M\frac{\omega\tau(T)}{1+[\omega\tau(T)]^2}, \tag{4}$$

$$\frac{\Delta E}{E}(T) = \Delta_M\frac{1}{1+[\omega\tau(T)]^2}. \tag{5}$$

Here Δ_M is the maximum value of modulus defect. It was shown earlier[36] that the broadening of the peak may be due to the distribution of U and/or ν_0. Preliminary results of a

more detailed analysis indicate that the change in the distribution parameters for these quantities may lead not only to a change in the breadth and height of the peak, but also to a displacement of T_p.

3.3. Amplitude dependences

In the absence of a noticeable amplitude dependence of magnetomechanical effects (see Fig. 6), nonlinear effects associated with the movement of dislocations through local potential barriers created by point defects in crystals (such as interstitial and substitutional impurities and their clusters, intrinsic interstitial atoms, and vacancies) are the probable reasons behind the dependence of decrement and dynamic elastic modulus on ε_0. A convincing argument supporting this is the nature of variation of amplitude dependences following the preliminary plastic deformation of the samples and, first of all, a significant decrease in ε_{0c}. Such an effect of plastic deformation was observed earlier in high-purity single crystals of Mo[37,38] and W.[39] At the same time, the results presented in the present work do not match with the data obtained by Higgins and Carpenter,[40] who studied the effect of plastic deformation on the amplitude dependences in a polycrystalline armco-iron of 99.74 wt. % purity at a frequency ~ 50 kHz. They found that preliminary plastic deformation in their samples almost does not affect the value of ε_{0c}. Without carrying out measurements in a saturating magnetic field, they concluded that the amplitude dependences of sound absorption are associated with the magnetomechanical hysteresis. As a matter of fact, the shape of the amplitude dependences obtained in Ref. 40 (an extended amplitude-independent region and a monotonic increase in absorption in the amplitude-dependent region) points towards their dislocation origin, while the weak effect of the preliminary plastic deformation is due to a comparatively low purity and structural imperfections in the investigated samples.

A microscopic picture and the corresponding theoretical description of nonlinear dislocation acoustic effects remain incomplete so far in spite of the efforts of a large number of researchers and apparent simplicity of the phenomenon. In the initial approximation, the correctness of any theory of amplitude-dependent dislocation losses and the variation of the elastic modulus can be verified by comparing the shape of the actually measured amplitude dependences with the dependences $\delta(\varepsilon_0)$ obtained from this theory.

The first generally accepted theory of the amplitude-dependent dislocation absorption of ultrasound is the Granato–Lücke hysteresis model[1] in which an exponential dependence of the amplitude-dependent component of decrement $\delta_H=\delta-\delta_i$ on the amplitude of the applied stress $\sigma_0=G\varepsilon_0$ was obtained under the assumption of ''catastrophic'' breakaway (i.e., the breakaway of a dislocation loop from all ''weak'' stoppers in the gap between unsurmountable ''strong'' stoppers in the case of the breakaway from at least one of the ''weak'' stoppers) and for an exponential distribution of dislocation segment lengths:

$$\delta_H=\frac{\Lambda L_N^3\overline{\sigma}_M}{6L_c\sigma_0}\exp\left(-\frac{\overline{\sigma}_M}{\sigma_0}\right), \tag{6}$$

where L_N is the separation between unsurmountable pinning centers, $\overline{\sigma}_M=F_M/bL_c$, F_M the maximum binding force between an impurity atom and a dislocation, and δ_i the amplitude-independent decrement.

Indenbom and Chernov[13,14] used slightly different model concepts to prove that the form of the $\delta_H(\varepsilon_0)$ dependence is determined by the distribution of dislocation segment lengths. In the case of an exponential segment-length distribution, the amplitude dependence is also exponential:[14]

$$\delta_H=\Lambda L_{\min}^2\left(1+\frac{L_{\min}}{L_c}\right)\exp\left(-\frac{L_{\min}}{L_c}\right), \tag{7}$$

where $L_{\min}=F(T)/(b\sigma_0)$ for long segments, and $F(T)$ is the total force of interaction between a dislocation and a defect (''binding energy'' approximation[41]).

For a power segment-length distribution function with an index $-m$, the amplitude dependence acquires the form

$$\delta_H=\frac{\Lambda L_c^2}{m-2}\left(\frac{L_{\min}}{L_c}\right)^{-m+4}, \tag{8}$$

i.e., is also a power function for long segments.

Finally, Kharitonov[10] made an attempt to take into account not only the distribution of dislocation segment lengths, but also the intensity distribution of local barriers and obtained the following second-power dependence of decrement on stress (independent of the segment-length distribution function):

$$\delta_H=\frac{3\Omega K b^2\Lambda L_c^4 E}{8GF_M^2}\sigma_0^2, \tag{9}$$

where K is the dimensionless coefficient whose magnitude varies from $K=1$ for segments of equal length to $K\approx 3$ for a random distribution of pinning centers at dislocations.

An analysis of the dependences $\delta_H(\varepsilon_0)$ obtained in the present work shows that these dependences are described most correctly by power functions. Figure 7 shows the results obtained for undeformed (a) and deformed (b,c) samples in log–log coordinates. It can be seen that the experimental points fit well into straight lines corresponding to the dependences $\delta_H\sim\varepsilon_0^n$. The amplitude dependences of modulus defect exhibit a similar behavior. The only exceptions are large-amplitude segments at high-temperatures at which irreversible changes in the dislocation structure of the samples obviously take place. Table I gives the values of n obtained for the dependences $\delta_H\sim\varepsilon_0^n$ as well as for $(\Delta E/E)_H\sim\varepsilon_0^n$. It is worth noting that the value of n for undeformed samples increases upon cooling and is twice as large as the corresponding values for deformed samples at temperatures below ~ 80 K. According to Indenbom and Chernov,[14] the power dependence of the decrement on the amplitude of deformation indicates the presence of a power distribution of dislocation segment lengths in the crystals. Using expression (8), we find that the exponent in the power dependence of the segment-length distribution for undeformed samples changes with cooling from $m\approx -5.5$ to $m\approx -7$. The temperature dependence of m in deformed samples is weak.

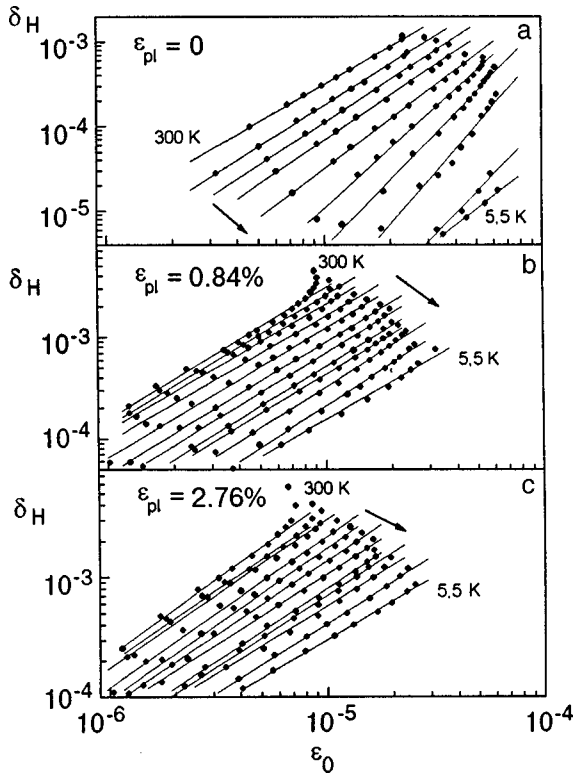

FIG. 7. Dependence of the amplitude-dependent decrement component on the amplitude and temperature in log–log coordinates for various degrees of plastic deformation.

The ratio of the amplitude-dependent component of decrement to the corresponding value of modulus defect $r = \delta_H/(\Delta E/E)_H$ is another parameter that can be used to draw certain conclusions concerning the adequacy of a theory to real dislocation processes in amplitude-dependent region. By way of an example, Fig. 8 shows the values of r at 80 K as a function of ε_0 for undeformed and deformed samples. Table I gives the values of $\bar{r}$ averaged over the amplitude interval for various temperatures and degrees of plastic deformation.

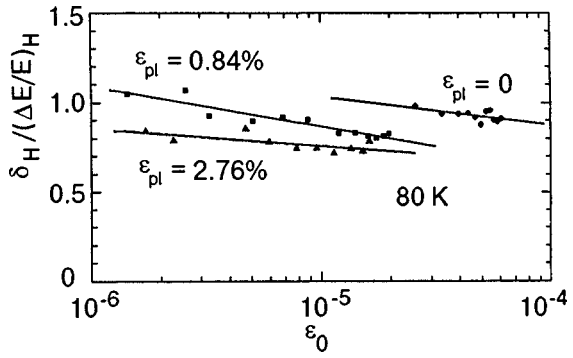

FIG. 8. Dependence of the ratio of the amplitude-dependent decrement component to the corresponding modulus defect on the amplitude and magnitude of preliminary plastic deformation.

A detailed analysis of the available experimental and theoretical results on the value of r can be found in Ref. 42. Unfortunately, this publication contains no information for bcc metals, although such results have been reported earlier (see, for example, Refs. 24 and 43). According to Lebedev,[42] a definite relation between the values of n and r in the case of power dependences $\delta_H \sim \varepsilon_0^n$ and $(\Delta E/E)_H \sim \varepsilon_0^n$ allows us to make a choice between different models of amplitude-dependent acoustic effects (see Table 1 in Ref. 42). The model of breakaway of dislocation segment from pinning centers (see Refs. 1, 10, 12–14) and the generalized frictional model[15,44] were proposed as alternatives. In our case, the values of $1.5<n<3$ correspond to the values of $1.1>\bar{r}>1$ for an undeformed sample, $1.2<n<1.4$ corresponds to $0.98>\bar{r}>0.67$ for a sample deformed by 0.84%, and $1.1<n<1.4$ corresponds to $0.85>\bar{r}>0.62$ for a sample deformed by 2.76%. None of these combinations is in accord with the pairs of values of n and r given in Table 1 in Ref. 42. The values of r for given values of n lie in the interval between the values predicted by the above-mentioned alternative models. Some peculiarities in the behavior of r are also worth noting. It is shown in Fig. 8 that the value of r for all samples decreases with increasing amplitude. A similar

TABLE I. Exponents n for amplitude dependences δ_H, $(\Delta E/E)_H$ and the ratio $\delta_H/(\Delta E/E)_H$ for various temperatures T and degrees of preliminary deformation ε_{pl}.

	$\varepsilon_{pl}=0$			$\varepsilon_{pl}=0.84\%$			$\varepsilon_{pl}=2.76\%$		
	n			n			n		
T, K	δ_H	$(\Delta E/E)_H$	$\bar{r}$	δ_H	$(\Delta E/E)_H$	$\bar{r}$	δ_H	$(\Delta E/E)_H$	$\bar{r}$
5.5	2.0	2.6	0.89	1.2	1.3	0.98	1.1	1.1	0.85
20	2.6	1.9	0.70	1.4	1.4	0.90	1.2	1.2	0.78
37	–	–	–	1.4	1.4	0.88	1.1	1.2	0.71
50	3.0	2.5	1.0	1.3	1.4	0.90	1.2	1.3	0.75
60	–	–	–	1.3	1.4	0.89	1.2	1.3	0.77
80	2.6	2.4	0.89	1.3	1.4	0.88	1.2	1.2	0.82
100	–	–	–	1.3	1.4	0.89	–	–	–
110	2.3	2.1	0.91	–	–	–	1.2	1.4	0.83
140	1.9	2.1	1.1	1.3	1.4	0.79	1.3	1.4	0.76
180	1.7	1.8	1.2	1.2	1.4	0.76	1.3	1.2	0.61
220	1.7	1.8	1.2	1.2	1.4	0.71	1.2	1.3	0.67
260	1.6	1.8	1.3	1.3	1.4	0.64	1.3	1.2	0.57
300	1.5	1.5	1.1	1.4	1.4	0.67	1.4	1.4	0.62

regularity was noted earlier[45] for Zn single crystals. Another peculiarity is a systematic decrease in $\bar{r}$ with increasing plastic deformation. In other words, in both cases the modulus defect increases at a higher rate than the amplitude-dependent component of decrement both in the deformation amplitude, and in the magnitude of plastic deformation.

CONCLUSIONS

(1) Linear and nonlinear acoustic properties of iron single crystals of the given purity and orientation are mainly determined by the state and parameters of the dislocation structure of the samples, which can be varied over a wide range by preliminary plastic deformation of the samples, followed by their ''ageing'' at room temperature.

(2) An increase in the dislocation density and the average length of dislocation segment in the linear region leads to a considerable enhancement of sound absorption and to a decrease in the elastic modulus. Besides, deformed samples exhibit at $T \sim 52$ K relaxation peak in sound absorption and modulus defect, which increase significantly with the extent of deformation. It is assumed that like in high-purity Fe single crystals with the $\langle 100 \rangle$ orientation, the corresponding relaxation process is due to the thermoactivated formation of kink pairs on nonscrew dislocation components. The decrease in the peak height and temperature upon ''ageing'' can be due to a change in the distribution of dislocation segment lengths.

(3) For the nonlinear region, it is found that the amplitude dependences of decrement and modulus defect are power functions with typical values of exponents $1.1 < n < 2.5$. Lower values of n were obtained for deformed samples. The power form of the amplitude dependences indicates that the distribution of dislocation segment length is a power function.

(4) The ratio $r = \delta_H / (\Delta E/E)_H$ of the amplitude-dependent component of decrement to the corresponding modulus defect is smaller than or of the order of unity, depends on the amplitude of vibrations only slightly, and decreases systematically upon an increase in plastic deformation. The values of r are quite inconsistent with the values of n predicted by the available models of hysteresis internal friction, indicating the inadequacy of the existing theories to the obtained experimental data.

(5) In the investigated region of vibrational amplitudes and temperatures, magnetoacoustic effects in a saturating external magnetic field are strong, virtually independent of the amplitude, and exhibit a weak monotonic dependence on temperature.

The author is grateful to V. Ya. Platkov and V. D. Natsik for their interest to this work and valuable discussions as well as to S. Kadeckova and L. N. Pal-Val for their help in setting up experiments and in preparing the manuscript.

This research was partly financed by the Swiss National Science Foundation (Grant No. 7UKPJ048645).

*E-mail: palval@ilt.kharkov.ua

[1] A. Granato and K. Lücke, in *Physical Acoustics*, Vol. 4A, Academic Press, NY, 1966.
[2] V. S. Postnikov, *Internal Friction in Metals* [in Russian], Metallurgiya, Moscow (1969).
[3] R. De Batist, *Internal Friction of Structural Defects in Crystalline Solids*, Elsevier, New York (1972).
[4] V. D. Natsik and P. P. Pal-Val, Mater. Sci. Eng., A **164**, 312 (1993).
[5] A. T. Marchenko, I. V. Ostrovskii, and A. I. Polovina, Ukr. Fiz. Zh. **31**, 1577 (1986).
[6] I. V. Ostrovskii and O. A. Korotchenko, Ukr. Fiz. Zh. **33**, 385 (1988).
[7] J. C. Swartz and J. Weertman, J. Appl. Phys. **32**, 1860 (1961).
[8] G. Alefeld, J. Appl. Phys. **36**, 2642 (1965).
[9] M. Koiwa and R. R. Hasiguti, Acta Metall. **13**, 1219 (1965).
[10] A. V. Kharitonov, Akust. Zh. **XI**, 226 (1965).
[11] A. Seeger and P. Schiller, in *Physical Acoustics* Principles and Methods (Ed. by W. P. Mason) Acad. Press, N. Y. (1986).
[12] D. G. Blair, T. S. Hutchison, and D. H. Rogers, Can. J. Phys. **49**, 633 (1971).
[13] V. L. Indenbom and V. M. Chernov, Phys. Status Solidi A **14**, 347 (1972).
[14] V. L. Indenbom and V. M. Chernov, in *Mechanisms of Relaxation Phenomena in Solids* [in Russian], Nauka, Moscow (1972).
[15] S. Asano, J. Phys. Soc. Jpn. **29**, 952 (1970).
[16] A. Seeger and C. Wüthrich, Nuovo Cimento B **B33**, 38 (1976).
[17] A. V. Granato and K. Lücke, J. Appl. Phys. **52**, 7136 (1981).
[18] H. L. Caswell, J. Appl. Phys. **29**, 1210 (1958).
[19] R. H. Saul and C. L. Bauer, J. Appl. Phys. **39**, 1469 (1968).
[20] P. P. Pal-Val and V. Ya. Platkov, Metallofizika (Kiev) **8**, 58 (1986).
[21] A. B. Lebedev, V. I. Ivanov, and B. K. Kardashev, Fiz. Tverd. Tela (Leningrad) **29**, 1514 (1987) [Sov. Phys. Solid State **29**, 866 (1987)].
[22] P. P. Pal-Val, Fiz. Nizk. Temp. **23**, 1250 (1997) [Low Temp. Phys. **23**, 938 (1997)].
[23] P. P. Pal-Val and S. Kadeckova, Phys. Status Solidi A **94**, K29 (1986).
[24] P. P. Pal-Val, V. D. Natsik, and S. Kadeckova, Philos. Mag. A **56**, 407 (1987).
[25] P. P. Pal-Val, V. D. Natsik, and S. Kadeckova, Phys. Status Solidi A **105**, K37 (1988).
[26] U. Bratina, in *Physical Acoustics*. Principles and Methods (Ed. by W. P. Mason) Acad. Press, N. Y. (1966).
[27] K. Z. Saleeb and S. Kadeckova, Krist. Tech. **9**, 1265 (1974).
[28] T. Hejnal, S. Kadeckova, V. Novak, and B. Sestak, Czech. J. Phys. **B27**, 1263 (1977).
[29] P. P. Pal-Val and H.-J. Kaufmann, Fiz. Nizk. Temp. **9**, 325 (1983) [Sov. J. Low Temp. Phys. **9**, 163 (1983)].
[30] V. D. Natsik, P. P. Pal-Val, and S. N. Smirnov, Akust. Zh. **49**, 896 (1998).
[31] B. Sestak, V. Novak, and S. Libovicky, Philos. Mag. A **57**, 353 (1988).
[32] K. Hoselitz, in *Physical Metallurgy* [Russian transl.], Mir. Moscow (1967).
[33] H. O. K. Kirchner, H. Mughrabi, F. Prinz, and H. Schmid, Phys. Status Solidi A **49**, 539 (1978).
[34] P. Astie, in *Proc. Summer School on Internal Friction in Solids* (Ed. by S. Gorczyca and L. B. Magalas), Krakow (1984).
[35] F. Louchet, L. P. Kubin, and D. Vesely, Philos. Mag. A **39**, 433 (1979).
[36] A. S. Nowick and B. S. Berry, *Inelastic Relaxation in Crystalline Solids* Acad. Press, N. Y. (1972).
[37] P. P. Pal-Val and H.-J. Kaufmann, Cryst. Res. Technol. **19**, 1049 (1984).
[38] P. P. Pal-Val, H.-J. Kaufmann, and V. I. Startsev, Fiz. Tverd. Tela (Leningrad) **27**, 852 (1985) [Sov. Phys. Solid State **27**, 522 (1985)].
[39] G. S. Baker and S. H. Carpenter, J. Appl. Phys. **38**, 3557 (1967).
[40] F. P. Higgins and S. H. Carpenter, Mater. Sci. Eng. **37**, 173 (1979).
[41] V. M. Chernov and V. L. Indenbom, Fiz. Tverd. Tela (Leningrad) **10**, 3331 (1968) [Sov. Phys. Solid State **10**, 2632 (1968)].
[42] A. B. Lebedev, Philos. Mag. A **74**, 137 (1996).
[43] H.-J. Kaufmann and P. P. Pal-Val., Phys. Status Solidi A **62**, 569 (1980).
[44] Y. Nishino and S. Asano, Phys. Status Solidi A **138**, K9 (1993).
[45] V. Ya. Platkov and I. K. Nosolev, Izv. Ross. Akad. Nauk, Ser. Fiz. **57**, 26 (1993).

Translated by R. S. Wadhwa

BRIEF COMMUNICATIONS

Time evolution of the density of vibrational states in the crystal lattice of the system La–Sr–Cu–O

A. G. Chirkov and V. G. Chudinov

*Physicotechnical Institute, Ural Branch of the Russian Academy of Sciences, 426001 Izhevsk, Russia**)
(Submitted July 9, 1998; revised August 17, 1998)
Fiz. Nizk. Temp. **25**, 94–96 (January 1999)

The molecular dynamics method is used for studying the dynamic properties of the crystal lattice of La–Sr–Cu–O system. It is shown that the density of vibrational states of the system undergoes an evolution, viz., a periodic redistribution between (phonon and soliton) peaks. Such an effect is associated with nonlinear resonance processes in the system. © *1999 American Institute of Physics.* [S1063-777X(99)01301-8]

1. In recent years, there has been a considerable growth in the interest towards the investigation of the properties of anharmonic crystal lattices. This interest has been triggered, in particular, by the possibility of emergence of self-trapped modes in such systems with frequencies higher than the maximum frequency of a harmonic crystal.[1,2] Vibrations in the one-dimensional case are localized at three[2] or two[3] atoms and have the same probability at any site in the lattice. The introduction of an inhomogeneity leads to their spatial localization.[4] The results were obtained mainly from analytic and numerical analysis of one-dimensional systems.

The lattice dynamics of nonlinear three-dimensional systems can be studied in a computer experiment using the molecular dynamics method (MMD). The system $La_{2-x}Sr_xCuO_4$ was studied by us earlier.[5] The introduction of Sr impurity atoms into the La_2CuO_4 lattice results in the excitation of local high-frequency vibrations (LHFV) in four oxygen atoms in the CuO_2 layer in the vicinity of the Sr atoms. For low Sr concentrations,, LHFV are spatially localized and lead to spatial redistribution of the kinetic energy of the atoms in the system, i.e., to the formation of ''hot'' regions and a ''cold'' matrix. In the model object Sr_2CuO_4, LHFV are not localized in space and the kinetic energy is not redistributed. The results obtained by us in Ref. 5 are essentially similar to those obtained for one-dimensional systems in the above-mentioned works. An analytic solution of such a problem has not been obtained so far. The stability of such excitations becomes a subject for investigation. Among other things, the possibility of decay of self-trapped modes into phonons was studied by Malomed.[6] It is also known that interaction between solitons can considerably affect the number of excited states in the system, including the density of phonon states.[7] All this is reflected in the superconducting properties of the system.

Hence the present communication aims at the investigation of the evolution of dynamic properties of the $La_{2-x}Sr_xCuO_4$ crystal lattice over a long time (on the computer experiment scale, viz., $\sim 10^{-10}$ s).

2. The experimental technique is described in our earlier works.[5,8] The present paper studies the same objects and employs the same computational technique.

The model crystallite consisted of three layers, viz., La(Sr)–O, Cu–O_2, La(Sr)–O, and contained up to about 2000 atoms. Atoms in the La(Sr)–O layers were rigidly fixed. The Cu–O_2 layer contained up to $\sim$800 mobile atoms. Cyclic boundary conditions were specified along the axes **a** and **b**. The interaction potentials were borrowed from Ref. 9.

In this work, we calculate the density of vibrational states (DVS) $G(w)$ at various instants of time with equal intervals $\Delta \sim 3\times 10^{-13}$ s. Calculations were made for crystallites with Sr concentration $x=0$, 0.03, 0.12, 0.17, 0.25, and 2.0 at $T=70$ K. LHFV are excited for all values of x except zero. This is manifested in DVS in the form of local high-frequency peaks (LHFP) in the vicinity of $\sim$0.4 eV. The LHFP are solitary for $x=0.03$ and 2.0, while in all other cases they are split into two. Except for $x=0$, the time evolution of DVS is in the form of ''pumping'' (redistribution): a periodic variation of the ratio of heights of LHFP and phonon peaks, indicating a fluctuation of the number of normal modes. By way of an example, Fig. 1 shows the DVS for Sr concentration $x=0.12$ at various instants of time. Such a pattern is characteristic of LHFP splitting. The ratio of the peaks varies between two LHFP and phonon peaks. Figure 2 shows the time dependence of the areas (number of normal modes) described by the curve coresponding to the phonon component of DVS and LHFV for $x=0.03$ (in this case, the LHFP is solitary and the process can be visualized most clearly). It was estimated from this figure that the characteristic time of the ''pumping'' period does not exceed 10^{-12} s. Methodical impediments do not allow us to determine the exact value of the period of this vibrational process. Note that the ''pumping'' process is observed only in the presence of LHFV.

In order to determine qualitatively the role of crystal lattice imperfections in a model crystallite with $x=0.17$, we constructed a model grain boundary in which the stoichiom-

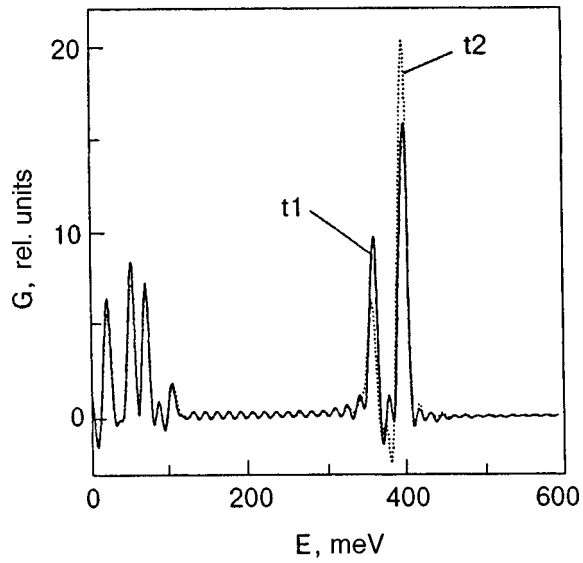

FIG. 1. Density of vibrational states in the $Cu-O_2$ layer of the system $La_{1.88}Sr_{0.12}CuO_4$ at the instants $t1$ and $t2=t1+2\Delta$.

etry of the Sr atomic concentration is violated. In this case, the DVS acquired two additional high-frequency peaks with energy ~ 0.49 and 0.54 eV. The deformation of the phonon part of DVS was terminated. The ''pumping'' effect was observed only between four LHFP. The presence of such a defect formed by oxygen atoms does not lead to the emergence of additional LHFP, and the overall pattern of DVS evolution is preserved.

3. In all probability, the observed instability in the DVS is a consequence of nonlinearity of the system and is caused by a strong interaction between solitons.[7] On the one hand, there is a tendency on the part of LHFP to disintegrate into delocalized low-frequency vibrations (phonons), while on the other hand it leads to the excitation of LHFV since their presence in a nonlinear system is advantageous from the energy point of view.[2] These two trends result in the establishment of a periodic steady-state process of variation of the number of delocalized and soliton-bounded elementary excitations.

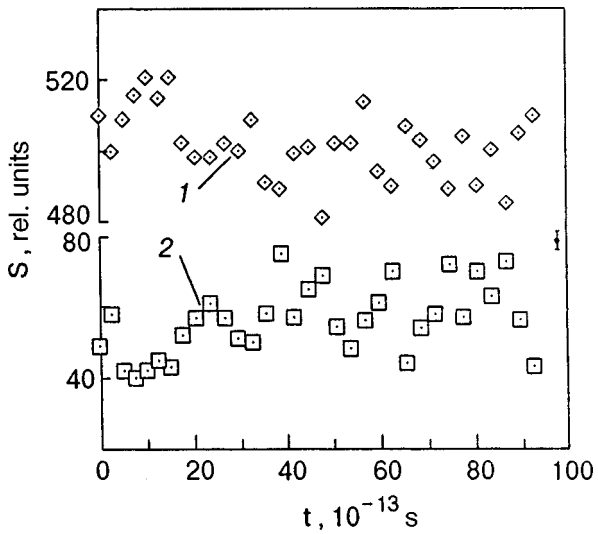

FIG. 2. Time dependence of the areas bounded by the curves corresponding to low-frequency (phonon)(*1*) and local high-frequency (*2*) components of the density of vibrational states for the $Cu-O_2$ layer of the system $La_{1.97}Sr_{0.03}CuO_4$.

It should also be interesting to note that according to Katsnel'son and Trefilov,[10] nonlinear resonance can emerge in anharmonic systems (for multiple values of the frequency ratio) and lead to energy transfer from the oscillator of one frequency to others whose characteristic times differ from phonon times ($\sim 10^{-11}$ s). This was associated by the authors with the ''central peak'' problem, i.e., with quasielastic scattering of neutrons near structural phase transitions. This problem remains unsolved so far, and phonon density fluctuation is considered to be one of the possible reasons behind the phenomenon.[11] A ''central peak'' was also detected in $La_{2-x}Sr_xCuO_4$.[12] The results obtained by us are reminiscent of nonlinear resonance: the change in the ratios of the DVS peak heights indicates a variation of the number of oscillators with the same energy due to resonance interaction with the others. In this case, we should speak of resonance not only in the phonon subsystem, but also between phonons and solitons (if solitons are present in the system). The interesting results presented in Ref. 13 were obtained on the basis of an analysis of experiments on the measurement of the velocity of sound and tempering in high-temperature superconductors. It was concluded that these systems contain defects with internal degrees of freedom (''fluctuators''), and several experimental results were explained as a result of such an analysis. In this sense, the defect complex in the vicinity of Sr atoms, which is responsible for DVS fluctuations, is considered just like a ''fluctuator'' in our work.

4. Thus, it has been established in this work on the basis of molecular dynamics that the density of states in the crystal lattice of the system La–Sr–Cu– O displays nonlinear resonance effects involving a periodic exchange of energy between different (phonon and soliton) vibrational degrees of freedom with a characteristic time not exceeding 10^{-12} s. The resonance conditions may change upon the introduction of certain types of defects.

In our earlier works,[5,8,14,15] we used the same object of investigation to show the correlation between the presence of LHFV (which causes the separation of the system into ''cold'' and ''hot'' regions) and the superconducting transition temperature of the system. The obtained result, viz., a periodic deformation of the DVS, can account in the same model for the existence of a ''central peak'' in the system in keeping with the hypothesis on the fluctuation of the phonon density of states. It also specifies the possible type of ''fluctuator'' defects. Moreover, the observed vibrational process can be juxtaposed with quasiparticles with the corresponding energy (in units of meV), which can participate in the formation of high-temperature superconductivity.

The authors are grateful to E. I. Salamatov and E. P. Chulkin for fruitful discussions and valuable remarks.

*)E-mail: uufti@fti.udmurtia.su

[1] A. M. Kosevich and A. S. Kovalev, Zh. Éksp. Teor. Fiz. **67**, 1793 (1974) [Sov. Phys. JETP **40**, 891 (1974)].
[2] A. J. Sievers and S. Takeno, Phys. Rev. Lett. **61**, 970 (1988).
[3] J. B. Page, Phys. Rev. B **B41**, 7835 (1990).
[4] R. F. Wallis, A. Franchini, and V. Bortolani, Phys. Rev. B **B50**, 9851 (1994).
[5] V. G. Chudinov, A. G. Chirkov, E. B. Dolgusheva, and V. M. Dyadin, Sverkhprovodimost: Fiz., Khim., Tekh. **6**, 204 (1993).
[6] B. A. Malomed, Phys. Rev. B **49**, 5962 (1994).
[7] A. M. Kosevich and A. S. Kovalev, *Introduction to Nonlinear Physical Mechanics* [in Russian], Naukova Dumka, Kiev (1989).
[8] A. G. Chirkov and V. G. Chudinov, Sverkhprovodimost: Fiz., Khim., Tekh. **7**, 800 (1994).
[9] V. G. Chudinov, E. B. Dolgusheva, and A. A. Yur'ev, Sverkhprovodimost: Fiz., Khim., Tekh. **4**, 2086 (1991).
[10] M. I. Katsnel'son and A. V. Trefilov, Fiz. Met. Metalloved. **64**, 629 (1987).
[11] A. Bruce and R. Cawley, *Structural Phase Transitions*, Taylor & Francis, Philadelphia, PA, 1981.
[12] P. Boni, J. D. Axe, G. Shirane *et al.*, Phys. Rev. B **38**, 185 (1988).
[13] V. I. Kozub, Phys. Rev. B **B49**, 6895 (1994).
[14] V. G. Chudinov, A. G. Chirkov, and R. R. Nurgayanov, Fiz. Nizk. Temp. **24**, 13 (1998) [Low Temp. Phys. **24**, 9 (1998)].
[15] V. G. Chudinov, A. G. Chirkov, and F. A. Sautin, Fiz. Tverd. Tela (St. Petersburg) **40**, 984 (1998) [Phys. Solid State **40**, 901 (1998)].

Translated by R. S. Wadhwa

Anomalous transport behavior of $La_{0.825}Sr_{0.175}MnO_{3-\delta}$ polycrystalline samples below Curie temperature

A. N. Pogorilyi, N. A. Belous, and A. I. Tovstolytkin

*Institute of Magnetism, 36-b Vernadskii St., Kiev, 252680, Ukraine**

A. G. Belous and O. Z. Yanchevski

Institute of General and Inorganic Chemistry, 32/34 Palladina Pr., Kiev, 252680, Ukraine
(Submitted July 9, 1998; revised August 25, 1998)
Fiz. Nizk. Temp. **25**, 97–99 (January 1999)

The temperature (T) dependencies of resistivity (ρ_0) and magnetoresistance (MR) in the range of 100–300 K have been investigated in $La_{0.825}Sr_{0.175}MnO_{3-\delta}$ polycrystalline samples with different sintering temperatures T_S (1300 °C and 1360 °C). Two peaks on the $\rho_0(T)$ curve were found in the sample with the lower value of T_S. Inhomogeneity of the spin configuration and multiply-connectedness of ferromagnetic phase is believed to give rise to anomalous behavior of resistivity below the Curie temperature. © *1999 American Institute of Physics.* [S1063-777X(99)01401-2]

Recent observations of colossal negative magnetoresistance (CMR) in thin films and bulk materials of doped manganites $La_{1-x}A_xMnO_3$ (A—divalent ions, e.g., A=Ca, Sr, Ba, and Pb) have generated renewed interest in this system, especially due to its potential technological application.[1,2] The end members, $x=0$ and $x=1$, are antiferromagnetic insulators but intermediate compositions with mixed Mn^{3+}/Mn^{4+} are ferromagnetic with metallic behavior below the Curie temperature T_C.[3] The ferromagnetic state in these compounds is stabilized by a double-exchange mechanism originating from the strong coupling between the charge carriers and local spins which are both dominantly of the $3d$ character.[4] Among the four $3d$ electrons on the Mn site, t_{2g}^3 electrons are localized, while the e_g^{1-x} state, being strongly hybridized with O $2p$ orbitals, is itinerant below T_C and localized in the paramagnetic-semiconducting state above T_C.[5]

The latest Mössbauer and pulsed neutron diffraction experiments show that local structural and magnetic inhomogeneity is responsible for the peculiar properties of low-doped manganites ($x<0.4$) not only at high temperatures, but also at $T<T_C$.[5,6] Down to the lowest temperatures measured ($T=10$ K), such materials consist of a mixture of paramagnetic and ferromagnetic regions within the same matrix, the fraction of the latter phase growing as the temperature decreases. Since the resistivity in the ferromagnetic state differs from that in the paramagnetic one,[5] the resulting transport properties below T_C strongly depend on spatial distribution and temperature evolution of the ferromagnetic phase. In that case local structural disorder, especially one induced by intergrain boundaries in polycrystalline samples, can cause not only additional charge carrier scattering, but also drastic changes in the temperature dependence of the resistivity below the Curie temperature. The increased role of such effect in $La_{1-x}Sr_xMnO_3$ is expected at those strontium concentrations, where antiferromagnetic-ferromagnetic transition occurs and the ferromagnetic metallic phase begins to be established, i.e., at $x\cong 0.175$.[3] In this paper, we have revealed the profound influence of the preparation conditions on the transport and magnetoresistive properties of $La_{0.825}Sr_{0.175}MnO_{3-\delta}$ polycrystalline samples, the effect, we believe, having the mechanism described above.

The perovskite samples of $La_{0.825}Sr_{0.175}MnO_{3-\delta}$ were prepared through two-stage solid-state reaction processing in air. The starting mixture of La_2O_3, Mn_2O_3 and $SrCO_3$ was annealed for 2 hours at a temperature of 1100 °C. After subsequent grinding and pressing in pellets, the obtained products were sintered for 2 hours and then slowly cooled down to room temperature. Two values of the sintering temperature T_S (1300 °C and 1360 °C for samples 1 and 2, respectively) were chosen to compare the effects of grain size and intergrain connectedness. X-ray diffraction study showed a single-phase perovskite structure, the diffraction pattern for both samples being identical. In order to make sure of the result's reproducibility, the specimens with the lower sintering temperature were synthesized repeatedly in exactly the same way, as was described above. All investigated properties of the samples prepared at the same conditions are found to be very similar ones. DC resistance measurements were performed using standard four-probe method in the temperature range 100–295 K. The samples for resistivity measurements were cut into rectangular bars, with the typical dimensions of $2\times3\times10$ mm. Electrodes were formed with a heat treatment type silver paste. The magnetoresistance (MR) was measured in fields up to 5 kOe and is defined as $(\rho_0-\rho_H)/\rho_0$, where ρ_0 and ρ_H are the resistivity in zero field and applied field, respectively. AC magnetic susceptibility (χ) measurements were performed at a frequency 1000 Hz by a mutual inductance bridge.

Figure 1 shows the temperature (T) dependencies of the resistivity (ρ_0) and magnetoresistance (MR) in the field $H=5$ kOe for the $La_{0.825}Sr_{0.175}MnO_{3-\delta}$ polycrystalline

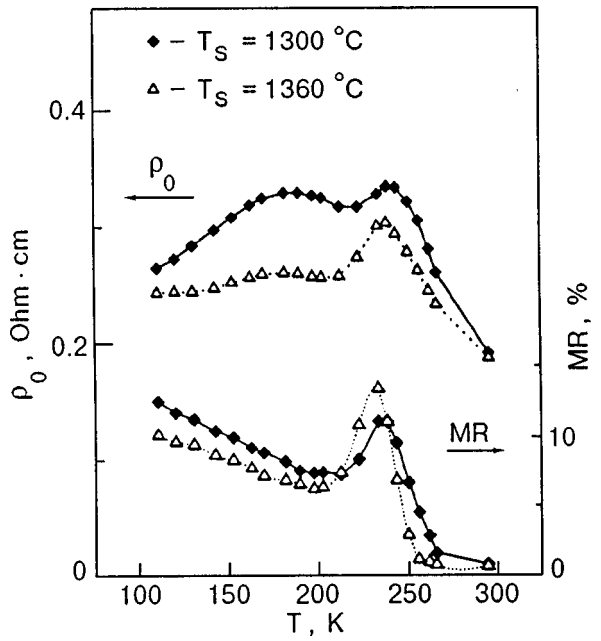

FIG. 1. The temperature dependencies of the resistivity ρ_0 and magnetoresistance MR in a field $H=5$ kOe for the $La_{0.825}Sr_{0.175}MnO_{3-\delta}$ polycrystalline samples with two different values of sintering temperature T_S.

samples with different values of T_S. The resistivity peak occurs at about the same $T_m \cong 240$ K for both samples studied. At a T slightly below T_m each MR(T) curve also has a peak caused by the paramagnetic to ferromagnetic transition and located close to $T_C \cong 237$ K. The magnetoresistive behavior near T_C good correlates with the results of AC susceptibility measurements, showing a sharp magnetic transition in the sample 2 ($T_S=1360$ °C) and a relatively broadened one in the sample 1 with the lower T_S.

The low-temperature ($T<200$ K) magnetoresistance effect, which increases with decreasing T in our case but is generally absent in single crystals, can be understood in terms of spin polarized tunneling across intergrain boundaries.[7,8] This effect, being appreciably greater in the sample with $T_S=1300$ °C, is indicative of increased influence of grain boundaries in the sample 1 compared to the sample 2. The lower sintering temperature seems to have resulted in smaller grain sizes or worse intergrain connectedness, as was expected initially. The resistivity ρ_0 of the sample 1 is greater than that of the sample 2, consisting with increased influence of intergrain boundaries which act as the regions of enhanced scattering for the charge carriers. The main features of the transport behavior of both samples are similar in the paramagnetic phase but differ essentially in the ferromagnetic region. In addition to the peak at T_m, a second broad peak at $T_{ma} \cong 180$ K is clearly visible for the sample with $T_S=1300$ °C. It is noteworthy that there are no anomalies below the Curie point on the temperature dependencies of magnetoresistance and magnetic susceptibility for both samples. Thus, it is unlikely that the peak at T_{ma} is caused by any kind of a magnetic transition (e.g., by partial antiferromagnetic ordering originating from local chemical inhomogeneity of the grains).

It should be noted that two peaks on the $\rho_0(T)$ dependence were observed by other authors in $La_{1-x}Sr_xMnO_3$ polycrystalline samples near $x=0.20$,[9] but no reasons were given for such behavior. Our work seems to clarify the origin of such a phenomenon.

As was noted above, the spin configuration of perovskite manganites is sufficiently inhomogeneous below Curie temperature and the charge carriers are not completely delocalized in this temperature range.[4,6] The coexistence of ferromagnetic and paramagnetic regions far below T_C distinguishes such materials from conventional ferromagnetics and is believed to be responsible for their unusual transport and magnetic properties.[5] As the temperature decreased through T_C, the transition into the magnetically ordered state, being at the same time accompanied by a delocalization of charge carriers, initially occurs only in some confined regions.[4] Intergrain boundaries in polycrystalline samples obviously makes difficulties in forming channels between these regions and, thus, the multiply-connected ferromagnetic phase is believed to be formed down to a certain temperature T^{mc} below T_C. The lowering of the sintering temperature T_S can sufficiently decrease T^{mc} value due to increased influence of the boundaries. In this case down to T^{mc} the current has to flow through the paramagnetic regions, the resistivity of which has a thermally activated character. As the temperature decreases, the competition between increasing conductivity with growing ferromagnetic fraction and its decreasing in paramagnetic phase can result in shaping peak on the $\rho_0(T)$ dependence in the low-temperature region. This picture seems to take place in one of our $La_{0.825}Sr_{0.175}MnO_{3-\delta}$ samples as well as in some other cases.[9]

The authors would like to thank S. V. Cherepov for performing magnetic susceptibility measurements. The research described in this publication was made possible in part by Award No. UP1-370 of the U.S. Civilian Research and Development Foundation for the Independent States of the Former Soviet Union.

*E-mail: apogor@imag.kiev.ua

[1] S. Jin, M. McCormack, T. H. Tiefel, and R. Ramesh, J. Appl. Phys. **76**, 6929 (1994).
[2] R. von Helmolt, J. Wecker, K. Samwer, L. Haupt, and K. Bärner, J. Appl. Phys. **76**, 6925 (1994).
[3] A. Urushibara, Y. Moritimo, T. Arima, A. Asamitsu, G. Kido, and Y. Tokura, Phys. Rev. B **B51**, 14103 (1995).
[4] J. B. Godenough, J. Appl. Phys. **81**, 5330 (1997).
[5] V. Chechersky, K. Nomura, A. Nath, H. Ju, and R. L. Greene, Fiz. Nizk. Temp. **23**, 732 (1997) [Low Temp. Phys. **23**, 539 (1997)].
[6] D. Louca and T. Egami, J. Appl. Phys. **81**, 5484 (1997).
[7] A. Gupta, G. Q. Gong, G. Xiao, P. R. Duncombe, P. Lecoeur, P. Trouilloud, Y. Y. Wang, V. P. Dravid, and J. Z. Sun, Phys. Rev. B **B54**, R15629 (1996).
[8] H. Y. Hwang, S.-W. Cheong, N. P. Ong, and B. Batlogg, Phys. Rev. Lett. **77**, 2041 (1996).
[9] Yi Tang, I. Shaltout, R. Braunstein, R. v. Helmolt, L. Haupt, and K. Bärner, Phys. Status Solidi B **B182**, 509 (1994).

This article was published in English in the original Russian journal. It was edited by R. T. Beyer.

LETTERS TO THE EDITOR

Magnetic-field-induced phase transitions between helical structures in noncentrosymmetric uniaxial antiferromagnets

A. N. Bogdanov and A. A. Shestakov

*A. Galkin Physicotechnical Institute, National Academy of Sciences of the Ukraine, 340114 Donetsk, Ukraine**

(Submitted September 14, 1998)
Fiz. Nizk. Temp. **25**, 100–104 (January 1999)

Two symmetrically different types of one-dimensional modulated structures (*cycloids* and *conical helicoids*) can exist in noncentrosymmetric uniaxial antiferromagnets. An applied magnetic field induces a first-order phase transition between these phases. The equilibrium parameters of the modulated structures are determined from the solution of the corresponding differential equations, and the phase diagram of the antiferromagnet in a bias magnetic field is calculated numerically. An analysis of experimental results leads to the conclusion that the predicted phase transition occurs in $Ba_2CuGe_2O_7$. © *1999 American Institute of Physics.* [S1063-777X(99)01501-7]

1. Long-periodic modulated structures formed in magnets without an inversion center[1] are in fact chiral systems in magnetically ordered materials. Such structures are observed in cubic helimagnets and in a number of uniaxial hexagonal magnets without an inversion center.[2] In contrast to exchange spirals with a period of a few unit cells and with an arbitrary direction of spin rotations, chiral helicoids are characterized by a long period (from tens to hundreds of lattice constants) and a definite direction of rotation of magnetic moments.

Helicoidal structures were discovered recently in noncentrosymmetric uniaxial antiferromagnets $BiFeO_3$ [Ref. 3] and $Ba_2CuGe_2O_7$.[4–7] Owing to the orienting effect of uniaxial anisotropy, the structure and properties of such spirals differ significantly from those for helicoids in cubic helimagnets and uniaxial systems.

In this communication, a theory of one-dimensional modulated structures in uniaxial noncentrosymmetric antiferromagnets is developed. The solution of the system of differential equations shows that for different magnitudes and orientations of the magnetic field, helicoids with different structures are stable, and first-order phase transitions occur between them.

2. As in Ref. 8, we write the energy functional for a two-sublattice antiferromagnet without an inversion center in terms of the components of the vectors $\mathbf{l}=(\mathbf{M}_1-\mathbf{M}_2)/(2M_0)$ of antiferromagnetism and $\mathbf{m}=(\mathbf{M}_1+\mathbf{M}_2)/(2M_0)$ of total magnetization ($\mathbf{M}_i$ are the magnetizations of the sublattices, $M_0=|\mathbf{M}_i|$):

$$W=\int wdV=M_0^2\int dV\left(A\sum\left(\frac{\partial\mathbf{l}}{\partial x_i}\right)^2+w_0+w_D\right), \quad (1)$$

where A is the constant of the nonuniform exchange interaction. The homogeneous energy component

$$w_0=2\lambda\mathbf{m}^2-Bl_z^2-2\mathbf{H}\cdot\mathbf{m}/M_0 \quad (2)$$

includes the exchange interaction with the constant λ, the energy of uniaxial anisotropy, and the energy of interaction with the applied field $\mathbf{H}$. For a positive anisotropy constant B, the z-axis is the easy magnetization axis. The energy w_D contains invariants linear in the first spatial derivatives with respect to $\mathbf{l}$. For example, for the tetragonal antiferromagnet $Ba_2CuGe_2O_7$ (having the Néel temperature $T_N=3.26$ K and the space group $P42_1m-D_{2d}^3$),[5] we have

$$w_D=D\left(l_z\frac{\partial l_x}{\partial y}-l_x\frac{\partial l_z}{\partial y}+l_z\frac{\partial l_y}{\partial x}-l_y\frac{\partial l_z}{\partial x}\right) \quad (3)$$

(the invariants of this type for other noncentrosymmetric classes are written in Ref. 8) Depending on the sign of D, the energy w_D stabilizes one of alternative directions of rotation of the vector $\mathbf{l}$. For definiteness, we assume that $D<0$. In the field region much lower than the exchange field $H_E=2\lambda M_0$, the magnetization vector is small ($m\ll 1$), and the energy of inhomogeneous states is mainly associated with the rotation of the vector $\mathbf{l}$. For this reason, in formulas (1) and (3) we omit terms nonuniform in $\mathbf{m}$. Neglecting the paraprocess and minimizing $w_0(2)$ in $\mathbf{m}$, we obtain the following result:

$$m=[\mathbf{H}-\mathbf{l}(\mathbf{l}\cdot\mathbf{H})/l^2]/H_E. \quad (4)$$

Let us consider modulated states inhomogeneous in the spatial variable x (*helicoids* as such) in a magnetic field tilted from the easy axis by the angle ψ. Since the energy w_D stabilizing inhomogeneous states does not contain derivatives with respect to z, the propagation vector of the helix lies in the basal plane xy, forming a certain angle γ with the x-axis. Substituting (4) into (1), we can write the energy functional in the form

$$w/\tilde{w}=\left(\frac{\partial\theta}{\partial\xi}\right)^2+\sin^2\theta\left(\frac{\partial\varphi}{\partial\xi}\right)^2-\frac{4}{\pi}\Bigg\{(\cos\varphi\cos\gamma-\cos\psi\sin\varphi\sin\gamma)\frac{\partial\theta}{\partial\xi}-\sin\theta[\sin\psi\sin\theta\sin\gamma-\cos\theta(\sin\varphi\cos\gamma+\cos\psi\cos\varphi\sin\gamma)]\frac{\partial\varphi}{\partial\xi}\Bigg\}-h^2\sin^2\theta-\beta(\cos\psi\cos\theta-\sin\psi\sin\theta\cos\varphi)^2. \tag{5}$$

The components of the vector **l** are written here in the polar system of coordinates with the polar axis directed along the applied field vector

$$l_x=l(\cos\theta\sin\psi+\sin\theta\cos\psi\cos\varphi),$$
$$l_y=l\sin\theta\sin\varphi, \tag{6}$$
$$l_z=l(\cos\theta\cos\psi-\sin\theta\sin\psi\cos\varphi);$$

new units are introduced for the spatial variable $\xi=\tilde{x}/x_0$, magnetic field $h=H/H_0$, and energy:

$$x_0=\frac{\pi A}{4|D|},\quad H_0=\frac{\pi|D|M_0}{2}\sqrt{\lambda/2A},\quad \tilde{w}=\frac{\pi^2D^2}{16A}, \tag{7}$$

and the parameter $\beta=16AB/(\pi D)^2$ plays the role of effective anisotropy.

The equilibrium states of a helicoid are determined from the solution of Euler's equations for functional (6) with periodic boundary conditions and subsequent minimization of energy in the period of the structure and the parameter γ. A complete analysis of these solutions will be carried out in a separate publication. Here we write the solutions for systems with weak anisotropy ($\beta\ll1$) including the antiferromagnet $Ba_2CuGe_2O_7$.

3. An analysis of the functional (5) including analytic and numerical methods allowed us to find the following two solutions for helicoidal structures in a weakly anisotropic antiferromagnet.

A. $\theta=\pi/2+\theta_1(\xi)$ ($\theta_1\ll1$), $\varphi=\varphi(\xi)$. In this phase, vector **l** deviates insignificantly during its rotation from the direction perpendicular to the field under the action of anisotropy. The deviation θ_1 has the maximum value when the vector **l** lies in the plane formed by the field vector and the easy axis and is equal to zero when vector **l** is perpendicular to this plane. In the helicoid under consideration, the sublattice magnetization vectors describe in the space the surfaces close to conical. For this reason, we shall refer to this structure as a *conical helicoid*.

For small $\theta_1(\xi)$, Euler's equations for energy (5) have the form

$$\frac{d^2\theta_1}{d\xi^2}-h^2\theta_1+\frac{\beta}{4}\sin2\psi\cos\varphi=0,$$
$$2\frac{d^2\varphi}{d\xi^2}-\beta\sin^2\psi\sin2\varphi=0. \tag{8}$$

Solving the system (8) with the boundary conditions $\theta_1(0)=0$, $\theta_1(R_1)=0$, $\varphi(0)=0$, $\varphi(R_1)=0$ and minimizing the energy in γ and R_1, we obtain

$$L_I=\frac{16}{\sin\psi},\quad \varphi=\frac{2\pi\xi}{L_I},\quad \theta_1=\Xi\cos\left(\frac{2\pi\xi}{L_I}\right),$$
$$\left(\Xi(h,\psi)=\frac{\beta\sin\psi\cos\psi}{h^2+(2\sin\psi/\pi)^2}\right). \tag{9}$$

Condition $\theta_1\ll1$ is satisfied for $\Xi\ll1$. This inequality defines the limits of applicability of the approximation used here. For $\beta\ll1$, this inequality is violated only in the region in which both the field and the angle ψ are small simultaneously ($h\ll1$, $\psi\ll1$). Substituting (9) into (4), we obtain the following expressions for the magnetization components $m_\parallel^{(I)}$ and $m_\perp^{(I)}$ parallel and perpendicular to the field:

$$m_\parallel^{(I)}=\eta h(1-\Xi^2),\quad m_\perp^{(I)}=\eta h\Xi\quad(\eta=H_0/H_E). \tag{10}$$

It follows from formulas (9) that the equilibrium period of a conic helicoid is independent of the field, and is determined entirely by the magnitude of the angle ψ. The minimum period of the helicoid observed in a magnetic field perpendicular to the easy axis. As the angle ψ decreases, the pitch of the conical spiral unwinds unlimitedly, and the conical helicoid in a field parallel to the easy axis is transformed into a homogeneous state.

B. $\theta=\theta(\xi)$, $\varphi=0,\pi$. These solutions describe a helicoid in which the vector **l** rotates in a plane formed by the vector of the applied magnetic field and the easy axis (*cycloid*). Equilibrium parameters for a cycloid can be obtained without imposing any constraints on the value of β. An analysis of the functional (5) shows that the cycloid exists in the region bounded by the curve

$$B^*=\sqrt{(h^2-\beta\cos2\psi)^2+(\beta\sin2\psi)^2}=1, \tag{11}$$

and its structure is described by solutions of the equation for a ''nonlinear pendulum'':

$$2\frac{d^2\theta}{d\xi^2}-B^*\sin2(\theta-\theta_0)=0,\quad \tan2\theta_0=\frac{\beta\sin2\psi}{h^2-\beta\cos2\psi}. \tag{12}$$

The solutions of Eq. (12) can be expressed in terms of elliptical functions and have been studied comprehensively (see, for example, Ref. 9). The magnetization components and the equilibrium period of the cycloid L_{II} can be written in the parametric form:

$$m_\parallel^{(II)}=\frac{\eta h}{2}\left\{1+\left[1+\frac{1}{k^2}\left(\frac{E(k)}{K(k)}-1\right)\right]\frac{(h^2-\beta\cos2\psi}{B^*}\right\},$$
$$m_\perp^{(II)}=\frac{\eta\beta h\sin2\psi}{B^*k^2}\left(\frac{E(k)}{K(k)}-1+\frac{k^2}{2}\right), \tag{13}$$
$$L_{II}=\frac{16k}{\pi}\sqrt{\beta/B^*}K(k),$$

where the parameter k is determined from the equation $(B^*)^{1/2}E(k)=k$ [$K(k)$ and $E(k)$ are complete elliptical integrals of the first and second kind respectively]. As we approach the boundary (11) of the region, the period of the

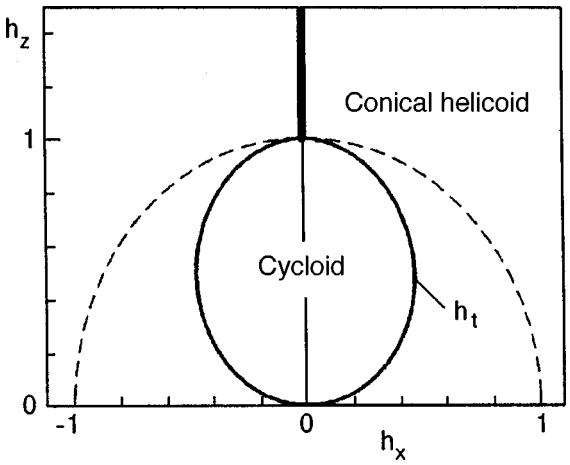

FIG. 1. The $h_x h_z$ phase diagram for $\beta=0.01$. The curve $\mathbf{h}_t$ corresponding to the first-order phase transition bounds the stability region for the cycloid. A conical helicoid is stable outside this region. The bold curve bounds the region in which the period of the conical helicoid is infinitely large. The dashed curve marks the critical line (11).

cycloid increases indefinitely, and the system goes over to a homogeneous state with θ_0 (12) for $B^*=1$. For $\beta \ll 1$, the critical curve (11) is an arc of the circle of unit radius (Fig. 1).

The region of thermodynamic stability of the cycloid on the (h_x, h_z) phase diagram (Fig. 1) is bounded by a closed curve $\mathbf{h}_t$ describing a first-order phase transition. Outside this region, the stable state of the system corresponds to a conical helicoid. Figure 2 shows field dependences of parallel magnetization components in individual phases upon a change in the field along the line $h_z=0.6$. If we assume that thermodynamically stable states are formed in the system, magnetizations experiences jumps on the phase-transition curve $\mathbf{h}_t$.

For $\psi=0$, the phase transition occurs in the field $h=1$. It follows hence that the field H_0 introduced in (7) is numerically equal to the field of phase transition in a magnetic field directed along the easy axis. Since the period of a conical helicoid tends to infinity as $\psi \to 0$, the line $\psi=0$, $h>1$ can be formally regarded as the range of a homogeneous state and the point $\psi=0$, $h=1$ as an isolated point of phase transition of the cycloid to a homogeneous state. Under actual experimental conditions, a homogeneous state cannot be formed in view of the nonuniformity of the magnetic field and uncontrolled disorientation of the sample. Even in the case of strict orientation of the field along the easy axis, a conical helicoid with a large spiral pitch will be formed above the transition field. (In this case, we disregard the effects associated with the finite size of the sample.) Thus, a magnetic field induces in noncentrosymmetric uniaxial antiferromagnets a phase transition from a cycloid to another modulated state, viz., conical helicoid. Modulated states exist in this class of crystals up to exchange fields. It was assumed earlier on the basis of the results of model calculations[1,3,8,9] that modulated structures (cycloids) are destroyed even in comparatively weak fields of the order of H_0, and the system goes over to a homogeneous state.

4. At present, helicoidal structures have been investigated thoroughly in $Ba_2CuGe_2O_7$ both in a magnetic field parallel to the easy axis,[5,6] and in a field oriented in the basal plane.[7] In zero field and in weak fields, the period of a helicoid in $Ba_2CuGe_2O_7$ is equal to 222 Å and includes 37 magnetic ions. It follows from (9) that the characteristic length x_0 (7) in a given crystal is 14 Å. Zheludev *et al.*[6] describe the field dependences of the period of the structure in the vicinity of H_0 for two cases of sample disorientation ($\psi=1°$ and $\psi<0.3°$). In both cases, modulated states were observed above the transition field, which confirms our conclusions concerning the existence of phase transitions between modulated structures.

The authors are grateful to the Alexander von Humboldt Foundation for providing computers and A. Zheludev for fruitful discussions of some topics considered in this paper.

*E-mail: bogdanov@host.dipt.donetsk.ua

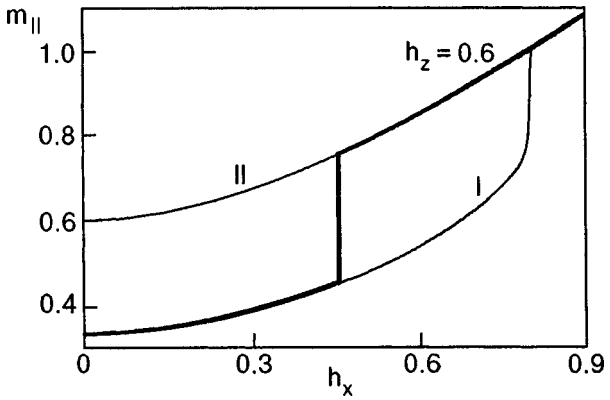

FIG. 2. Magnetization components parallel to the field for a cycloid (I) and a conical helicoid (II) as functions of the planar field h_x for $h_z=0.6$. The field of phase transition is attained for $h_x=0.456$. Bold curves mark the regions corresponding to thermodynamically stable states. Magnetization is measured in the units of η.

[1] I. E. Dzyaloshinskii, Zh. Éksp. Teor. Fiz. **46**, 1420 (1964) [Sov. Phys. JETP **19**, 960 (1965)].
[2] B. Lebech, in *Recent Advances in Magnetism of Transition Metal Compounds* (ed. by A. Kotani and N. Suzuki), World Scientific, Singapore (1992).
[3] Yu. F. Popov, A. K. Zvezdin, and G. P. Vorob'ev, Pis'ma Zh. Éksp. Teor. Fiz. **57**, 65 (1993) [JETP Lett. **57**, 69 (1993)].
[4] A. Zheludev, G. Shirane, Y. Sasego *et al.*, Physica B **234-236**, 546 (1996); Phys. Rev. B **54**, 15163 (1996).
[5] A. Zheludev, S. Maslov, G. Shirane *et al.*, Phys. Rev. Lett. **78**, 4857 (1997).
[6] A. Zheludev, S. Maslov, G. Shirane *et al.*, Phys. Rev. B **57**, 2968 (1998).
[7] A. Zheludev, S. Maslov, G. Shirane *et al.*, Phys. Rev. B **56**, 14006 (1997).
[8] A. N. Bogdanov and D. A. Yablonskii, Zh. Éksp. Teor. Fiz. **96**, 253 (1989) [Sov. Phys. JETP **69**, 142 (1989)].
[9] Yu. A. Izyumov, *Neutron Diffraction at Long-Periodic Structures* [in Russian], Energoizdat, Moscow (1987).

Translated by R. S. Wadhwa

Amorphous–crystalline films of fullerite C_{60}

N. I. Gorbenko, E. N. Zubarev, S. A. Medvedev, A. T. Pugachev, and N. P. Churakova

Kharkov State Polytechnical University, 310002 Kharkov, Ukraine
(Submitted September 25, 1998)
Fiz. Nizk. Temp. **25**, 105–107 (January 1999)

Fullerite C_{60} films obtained by evaporation and condensation of C_{60} molecules on a cooled glass surface are investigated by high-resolution electron-optical methods (including direct lattice resolution and selected area diffraction). It is found that the films have an amorphous–crystalline structure, the amount of amorphous phase reaching 70%. Diffraction patterns of amorphous fullerite are obtained. The values of $4\pi(\sin\theta)/\lambda$ are determined for the first three halos. The positions of halos indicate that the structure of amorphous fullerite can be described by the hard spheres liquid model. © *1999 American Institute of Physics.* [S1063-777X(99)01601-1]

Starting from the time of discovery of fullerenes and the methods of their obtaining in macroscopic amounts, these materials have become an object of numerous investigations.[1,2] Fullerene C_{60} and its condensed state (fullerite) is the most popular among these materials. At room temperature and under normal pressure, pure fullerite is a crystal with a face-centered cubic (fcc) lattice. At $T=260$ K, the lattice is transformed to a simple cubic (sc) lattice. Fullerite C_{60} can be transformed into conventional phases of carbon as well as into other structures with one- and two-dimensional polymerization upon an increase in temperature and pressure as well as a result of illumination by visible and ultraviolet light. The growth and structure of thin C_{60} films are being studied by many authors. Special attention is paid to the obtaining of amorphous fullerite films since they are convenient for verifying many models in the physics of amorphous state as one-component objects with the known type of molecular interaction. To our knowledge, no results on amorphous fullerite films have been reported as yet.

The results of our preliminary investigations proved that the nanocrystalline structure was formed during the vacuum deposition of C_{60} films on the (100) surface of NaCl crystals at room temperature. The size of crystallites in such films, which was measured by using dark-field electron-microscopic photographs, was ~ 50 Å. These results suggest that amorphous fullerite films must be formed during the deposition of fullerene C_{60} on an amorphous substrate being cooled. This is justified the more so since fullerene molecules have a large mass, and hence must be characterized by low values of the surface diffusivity.

In this communication, we report on the results of electron diffraction and electron-microscopic studies of C_{60} films at room temperature, which were deposited in vacuum on the glass surface being cooled.

The C_{60} fullerite films were obtained by evaporation and deposition of C_{60} single crystals with a purity not worse than 99.9% in a $\sim 10^{-3}$ Pa vacuum. The substrate was quartz glass cooled by liquid nitrogen vapor and having the temperature in the range from 243 to 293 K. The film thickness determined from frequency variation of a quartz-crystal microbalance was 300 Å.

The films were separated from the substrate for subsequent electron-optical investigations. For this purpose, gelatine is used, but this requires a heating of the film to 40–50 °C. In order to avoid additional heating of the films, we proposed an original technique for separating films from the glass surface, whose essence is as follows. A drop of water is placed on a C_{60} film at room temperature. Then the substrate with the film and the drop of water is cooled to 273 K, and the ice with the film is separated mechanically from the glass and is placed in water. Then the film is scooped into the copper sieve of the electron microscope.

Electron diffraction measurements of the films were made on an electron diffraction instrument EVR with an accelerating voltage 40 kV and the electron beam density not higher than $j=10^{-6}$ A/cm^2. Electron-microscopic studies of the films were carried out on an electron microscope PEM-U. The resolution of the microscope was 2 Å, which was confirmed by direct resolution of atomic planes (200) in thin monocrystalline gold films. Selected area diffraction patterns were obtained by using a selector diaphragm of diameter 0.7 μm.

According to the results of electron diffraction studies, the films were amorphous–crystalline. Electron diffraction patterns contained both reflexes from the fcc fullerite C_{60} crystal with the lattice constant 14.18 Å and a halo-type pattern typical of amorphous or nanocrystalline structures. The maximum amount of the amorphous phase was observed in films deposited at the substrate temperatures 278 K. The amount of the crystalline phase was larger at lower and higher temperatures. The films with the minimum amount of the crystalline phase served as objects for subsequent electron-microscopic experiments.

Figure 1 shows a typical electron-microscopic photograph of fullerite C_{60} film with a magnification of 2000000.

The dark regions on the photograph correspond to the crystalline phase. This follows from the microscopic diffraction pattern for these regions, which is typical of the fcc fullerite C_{60} crystal with a lattice period of 14.18 Å. Dark

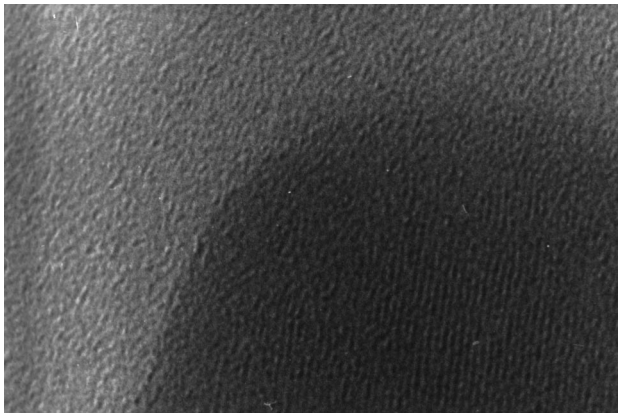

FIG. 1. Light-field electron-microscopic photograph of an amorphous–crystalline fullerite C_{60} film ($\times 2000000$). Dark regions correspond to the crystalline phase and light regions to the amorphous phase.

regions show the resolution of crystalline planes with a spacing of 8.2 Å, which corresponds to the fcc planes (111) of the fcc fullerite C_{60} crystal.

Light regions on the photograph correspond to the amorphous phase and occupy approximately 70% of the photograph area. The resolution of the crystalline planes in light regions is not observed. The microdiffraction patterns from these regions have the form of halos typical of diffraction at amorphous structures.

For a quantitative analysis of electron diffraction pattern of light regions, a series of microdiffraction patterns were photographed under different exposure times for a constant electron beam density. The results of a photometric treatment of microdiffraction patterns were used to plot the intensity I of electron scattering as a function of the wave vector $K=4\pi(\sin\theta)/\lambda$ shown in Fig. 2. The same figure shows the line electron diffraction pattern of the fcc fullerite C_{60} crystal. The (200) line is not shown since it is absent on the electron diffraction patterns in view of the size relations between the radius of the fullerene molecule and the fcc lattice parameter of fullerite.[3] It follows from Fig. 2 that the obtained diffraction pattern cannot be regarded as a superposition of blurred diffraction peaks of nanocrystalline C_{60}. The intensity peaks of $I(K)$ correspond to the points $K_{\max 1}=0.71$ Å^{-1}, $K_{\max 2}=1.42$ Å^{-1}, $K_{\max 3}=2.14$ Å^{-1}. It should be noted that the first peak lying in the region of strong background is displaced slightly towards small angles θ. In order to determine the position of this peak, the background was approximated by a linear function and the diffraction peak by the Gauss function.

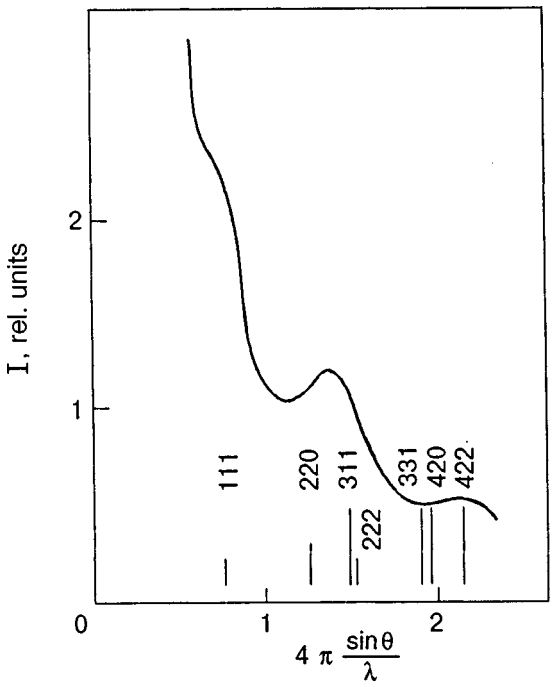

FIG. 2. Intensity (in relative units) of the electron diffraction patterns of amorphous fullerite as a function of $K=4\pi(\sin\theta)/\lambda$ and line electron diffraction pattern of the fcc fullerite C_{60} crystal.

It is well known (see, for example, Ref. 4) that the structural factors $a(K)$ for most liquid metals in the reduced coordinates $K/K_{\max 1}$ ($K_{\max 1}$ is the position of the first peak) virtually coincide. The positions of the peaks of the function $a(K)$ correspond to the ratios $K_{\max i}/K_{\max 1}$ $(i=1,2,3)$ equal to 1, 2, and 3. The positions of the halos in our diffraction patterns satisfy these relations, indicating the possibility of describing the structure of amorphous fullerite films on the basis of the model of a hard spheres liquid.

This research was carried out under the financial support from the Ukrainian Ministry of Education.

[1] H. W. Kroto, J. R. Heath, S. C. O'Brien *et al.*, Nature (London) **318**, 162 (1985).
[2] G. Meijer and D. S. Bethune, J. Chem. Phys. **93**, 7800 (1990).
[3] S. Amelinckx, C. van Heurck, and D. van Dyck, Phys. Status Solidi A **131**, 589 (1992).
[4] E. I. Khar'kov, V. I. Lysov, and V. E. Fedorov, *Physics of Liquid Metals* [in Russian], Vishcha Shkola, Kiev (1979).

Translated by R. S. Wadhwa